MASS TRANSFER ON SOLUBLE WALLS WITH DEVELOPING ROUGHNESS IN PIPES AND BENDS

MASS TRANSFER ON SOLUBLE WALLS WITH DEVELOPING ROUGHNESS IN PIPES AND BENDS

BY

DONG WANG, M. Eng., B.Eng.

A Thesis
Submitted to the School of Graduate Studies
in Partial Fulfillment of the Requirements
for the Degree
Doctor of Philosophy
McMaster University

Doctor of Philosophy (2016) McMaster University
(Mechanical Engineering) Hamilton, Ontario, Canada

TITLE: Mass transfer on soluble walls with developing roughness in pipes and bends

AUTHOR: Dong Wang
M. Eng., B. Eng., Mechanical Engineering
Nanjing University of Science and Technology, Nanjing, China

SUPERVISOR: Dr. Chan Y. Ching

NUMBER OF PAGES: xiv; 225

ABSTRACT

Flow accelerated corrosion is a piping degradation mechanism that results in pipe wall thinning due to the dissolution of the magnetite oxide layer on carbon steel surfaces to the bulk flow. The rate limiting process of flow accelerated corrosion in piping system is the diffusion-controlled mass transfer. The surface roughness develops due to the mass transfer and can subsequently have a significant effect on the mass transfer. The naturally developing surface roughness in many dissolving surfaces, including carbon steel pipes, is a densely packed array of saucer shaped depression called scallops, which can have several length scales. Heretofore, the developing roughness on soluble walls has not been quantified, mainly due to the lack of a reliable measurement methodology.

The overall objective of this research is to investigate the developing roughness and the corresponding mass transfer on soluble walls in different piping geometries. A wall dissolving method using gypsum test sections dissolving to water in a closed flow loop was used to mimic the mass transfer in carbon steel pipes due to a similar Schmidt number of 1200. A novel non-destructive measurement technique using X-ray CT scans was developed to measure the development of surface roughness and the corresponding mass transfer. The method was validated by performing experiments using straight pipe test sections and comparing against traditional measurements method using ultrasonic sensors, coordinate measurement machine and laser scans.

The time evolution of surface roughness and the corresponding mass transfer were measured in pipe test sections at Reynolds number of 50,000, 100,000 and 200,000. The roughness scallops were observed to initiate locally and then develop until the surface is spatially saturated. The surface roughness was characterized by the RMS height, peak-to-valley height, integral length scale, density and spacing of the scallops. Two time periods of roughness development were identified: an initial period of slower growth in the roughness height followed by a relatively higher growth rate that corresponded to the period before and after the surface saturates with the scallops. The mass transfer enhancement due to the roughness in each of these time periods was also found to be different, with a higher increase in the first period followed by a slower increase once the streamwise spacing was approximately constant. Both the height and spacing of the roughness elements was found to affect the mass transfer enhancement. A new correlation is proposed for the mass transfer enhancement as a function of the height-to-spacing ratio of roughness, with a weak dependence on Reynolds number.

The measurement methodology was extended to study the mass transfer and developing roughness in a complex S-shaped back to back bend at Reynolds number of 200,000. The mass transfer in bend geometry can be enhanced by both the local flow due to the geometry effect and the developing roughness. Two high mass transfer regions were identified: at the intrados of the first and second bends. The height-to-spacing ratio of the roughness was found to increase more rapidly in these high mass transfer regions. An additional one-time experiment was performed at a Reynolds number of 300,000. A higher surface roughness with smaller values of spacing-to-height ratio was found in the regions with high mass transfer.

ACKNOWLEDGEMENTS

I would like to express my great appreciation to my supervisor, Dr. Chan. Y. Ching, for giving me the opportunity to work with him in “the best city in the world”, Hamilton. I was encouraged and motivated by his great enthusiasm, insight and rigor for academic research. I was also deeply impressed by Dr. Ching’s attitude, humor and wisdom about personal life. Without his guidance and support, the completion of this Ph.D. thesis and the accomplishments made for the academic community might be impossible.

Great appreciations are also expressed to Dr. Dan Ewing for his invaluable guidance and help through my research, as a co-supervisor in my mind. With his great academic enthusiasm and dedication, he has always been providing helpful suggestions and comments to my experiments and data reduction. He has set a perfect model of a great scientist for me.

I would also like to thank my supervisory committee members, Dr. Lightstone and Dr. Cotton and for their time and interest, and for their great suggestions through my research. I would like to thank the all the members in the Flow Accelerated Corrosion (FAC) group and the TMRL group for offering kind help and advices, particularly Yong Huang, Thuan Le and Akshay Jain. I would also like to extend my thanks to the mechanical engineering technicians for their technical supports for my experiments: Mr. Ron Lodewyks, Mr. Mark Mackenzie, Mr. Jim Mclaren, Mr. Michael Lee and Mr. John Colenbrander. Special thanks also go to Dr. Tom Chow from Medical Physics, Juravinski Cancer Center for providing the CT scan images of the test sections.

Last but not least, I would like to thank my parents for their unconditional love and support during my study abroad. I would also like to extend special thanks to my girlfriend, Yiqiu, who has taught me how to pursue the true happiness and love bravely.

TABLE OF CONTENTS

LIST OF FIGURES

LIST OF TABLES

Chapter 1

Introduction

Flow Accelerated Corrosion (FAC) is a serious safety and reliability issue in power generation plants, especially nuclear power plants (NPP). FAC causes wall thinning and weakening in carbon steel piping components, which can result in catastrophic failure if not detected and rectified as evidenced in accidents at Surry (1986), Pleasant Prairie (1996), Mihama (2004) and Latan (2007). While the fluid chemistry and materials determine the overall potential for FAC, flow and mass transfer conditions determine the local distribution of the wall thinning rates. Among these factors are the geometrical configuration and orientation of the piping components, flow rate, local turbulence, fluid temperature, and surface roughness (Poulson, 1999). Essentially, FAC is a multi-step process which is schematically shown in Fig. 1.1 (Kain *et al.*, 2011): (i) a series of electrochemical reactions at the metal-oxide interface, (ii) chemical erosion and dissolution of the oxide layer of carbon steel pipe walls and (iii) convective mass transfer of ferrous ions from the oxide-water interface through the boundary layer into the bulk flow (Pietralik & Schefski, 2011).

The model proposed by Berge et al. (1980) is commonly used to determine the FAC wear rate and can be presented in the following form (Remy et al., 1992; Lister *et al.*, 2008):

$$CR = \frac{2h_m k_d \Delta C}{(h_m + 2k_d)} \tag{1.1}$$

where CR is the corrosion rate, h_m is the mass transfer coefficient, k_d is the dissolution kinetic constant and ΔC is the concentration gradient. In typical FAC situations, the dissolution kinetic constant is very much greater than the mass transfer coefficient ($k_d \gg h_m$), and the corrosion rate could be expressed as

$$CR = h_m \Delta C \tag{1.2}$$

Thus, the diffusion-controlled mass transfer can be considered the rate limiting process, and is of significant interest to the FAC community.

The control of FAC in practical applications requires the identification of regions of high local mass transfer. The piping component or geometry can have a significant influence on the local flow patterns and hence mass transfer rates. For example, piping components with singularities, such as sudden expansions, orifices and valves have

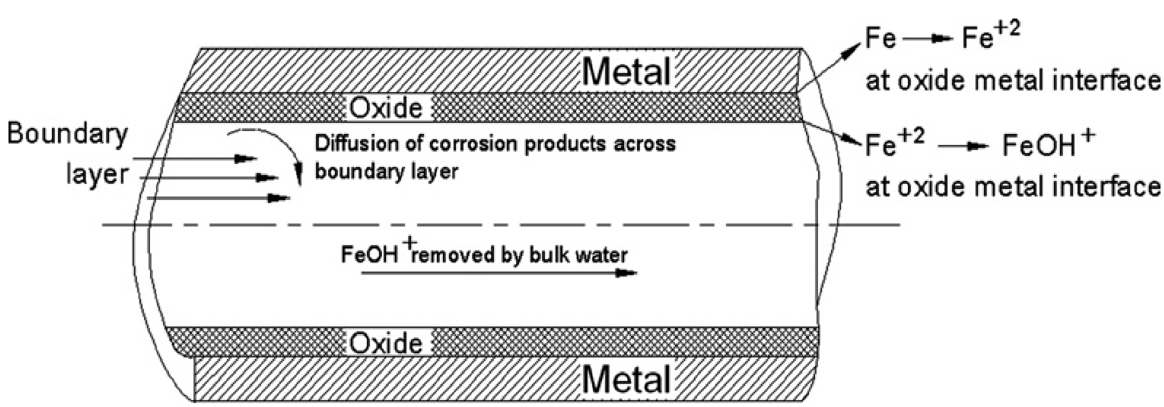

Fig. 1.1: Schematic mechanism of Flow Accelerated Corrosion (Kain *et al.* 2011)

shown higher rates of FAC due to flow separation and reattachment downstream of these elements. The local mass transfer rates in bend geometries is also important because these are some of the most common elements in a piping system and the mass transfer in bends is enhanced relative to that in straight pipes. The problem is exacerbated when bends are attached back-to-back because of the sudden changes in flow direction and complex secondary flows that can develop in these geometries. One important parameter that affects mass transfer is the surface roughness, which develops naturally due to mass transfer in FAC applications.

1.1 Motivation and Research Objectives

The mass transfer on smooth surfaces has been studied for different piping geometries. Surface roughness has been shown to significantly increase the mass transfer. Most previous studies on the effect of roughness on mass transfer, however, have been studied using predefined surface roughness that have been machined or cast onto the surface. On soluble walls, including carbon steel pipes due to FAC, the surface roughness develops naturally with time due to mass transfer to the bulk flow. The developing roughness can subsequently affect the mass transfer and vice versa. The effect of the developing roughness on the mass transfer is less understood as there have been only very few studies on how the roughness develops in soluble walls and on the effect of the developing roughness on mass transfer. The most common natural roughness pattern that has been observed in many systems, including carbon steel piping due to FAC, is a densely packed array of intersecting saucer shaped depressions usually called scallops.

The roughness or scalloped patterns that naturally develop on these surfaces can have very different characteristics to predefined machined or cast roughness. The main difficulty with characterizing the development of roughness on a surface has been the lack of a reliable non-destructive measurement technique to measure the surface topography. Thus, the overall objective of this thesis is to develop a robust and reliable non-destructive measurement technique to measure the developing roughness and corresponding mass transfer on a soluble wall, and use the technique to characterize the effect of roughness on mass transfer in pipes and bend geometries. The specific objectives can be articulated as:

1. To develop a non-destructive measurement technique to characterize the development of surface roughness and mass transfer over a soluble surface with time.
2. To measure and characterize the development of surface roughness in straight pipes at different Reynolds numbers.
3. To determine the effect of the developing surface roughness on the mass transfer in straight pipes at different Reynolds numbers.
4. To measure and characterize the local development of surface roughness and mass transfer in a back-to-back bend arranged in an S-configuration.

1.2 Thesis Outline

The main body of this thesis consists of five journal articles that address the above objectives. An introduction chapter and a final chapter with the overall conclusions and recommendations are added. The chapters consisting of the 5 journal articles are arranged as:

Chapter 2: This contains the first published journal article titled “On the non-destructive measurement of local mass transfer using X-ray computed tomography”. This article describes the development and validation of a novel non-destructive measurement methodology for quantifying the local mass transfer and surface roughness using X-ray computed tomography using a dissolving wall technique. Pipe sections using a gypsum lining dissolving to water in a closed flow loop was used here. The methodology developed here is unique and a first in the world.

Chapter 3: The second published journal article titled “Time evolution of surface roughness in pipes due to mass transfer under different Reynolds numbers" is presented in chapter 3. Pipe test sections with a dissolving gypsum lining to water at a Schmidt number of 1200 were tested at Reynolds numbers of 50,000, 100,000 and 200,000 over multiple time intervals. The Schmidt number here is similar to that for the diffusion of the iron magnetite layer of carbon steel piping in water, and provides an analogous mass transfer environment to FAC in power generation plants. The time evolution of roughness due to the mass transfer was characterized and quantified. This is the first instance that the developing roughness on a surface has been quantified.

Chapter 4: This chapter contains the article “The effect of naturally developing roughness on the mass transfer in pipes under different Reynolds numbers” which has been submitted to a journal for review. This article focuses on the mass transfer variations with the developing roughness characterized in chapter 4. A correlation for the mass transfer enhancement in terms of the roughness parameters is proposed here.

Chapter 5: The published journal article titled “Measurement of local mass transfer and the resulting roughness in a large diameter S-bend at high Reynolds number” is presented in this chapter. The measurement technique developed in Chapter 2 was extended to an S-bend geometry at a high Reynolds number of 300,000. Most previous measurement of mass transfer in bends have been performed at Reynolds number on the order of 100,000. The local distribution of the roughness within the S-bend and the resulting mass transfer was characterized.

Chapter 6: The article titled "Development of surface roughness and its effect on the mass transfer in an S-shaped back to back bend” is presented in chapter 6, which has been submitted to a journal for review. This article investigates the roughness development and mass transfer in an S-shape back to back bend using the non-destructive X-ray CT scan measurement methodology. Both the geometry effect and roughness effect on the mass transfer are identified in this paper.

There are four appendices in this thesis. Appendix A provides more details about the calculation of the modified time. Appendix B and C provide supplementary figures for the mass transfer in chapter 3 and chapter 5. Appendix D outlines the main data reduction routines using Matlab to obtain the mass transfer and characterize the corresponding surface roughness from the X-ray CT scans.

1.3 A Note to the Reader

Since this thesis consists of a series of journal articles, there is some overlap and repetition of material. In particular, the sections of each journal article pertaining to the experimental facility and measurement methodology contain significant repetition since the same facility was used in all experiments. There is also some overlap of material in the introduction section of each article; however, each introduction section contains more specific references related to the work presented in each paper.

1.4 References

Berge, P., Ducreux, J. and Saint-Paul, P. 1980. Effects of Chemistry on Erosion Corrosion of Steels in Water and Wet Steam, Proc. 2nd. BNES Internl. Conf. on Water Chem. of Nucl. Reactor Systems, Bournemouth, UK.

Kain, V., Roychowdhury S., Ahmedabadi P., Barua D.K. 2011. Flow accelerated corrosion: Experience from examination of components from nuclear power plants. *Engineering Failure Analysis*. 18: 2028-2041.

Lister, Derek H., Liu, Lihu, & Feicht, Andrew, D. 2008. A fundamental study of flow-accelerated corrosion in feedwater systems. Power Plant Chemistry, 10(11), 659-667.

Pietralik, JM., Schefski, CS. 2011. Flow and mass transfer in bends under Flow-Accelerated Corrosion Wall Thinning Conditions. *Journal of engineering for gas turbines and power*. 133(1) 012902: 1-7.

Poulson, B. 1999. Complexities in predicting erosion corrosion. *Wear*. 233-235(1999): 497-504.

Remy, F.N., Bouchacourt, M. 1992. Flow-assisted corrosion: a method to avoid damage, Nuclear Engineering and Design, 133(1): 23-30.

Chapter 2

On the non-destructive measurement of local mass transfer using X-ray computed tomography

Complete citation:

Wang, D., Huang, Y., Ewing, D., Chow, T., Cotton, J., Noseworthy, M.D., Ching, C.Y., 2015. On the non-destructive measurement of local mass transfer using X-ray computed tomography. *Int. J. Heat Mass Transfer*. 81: 531-541.

Copyright:

Relative Contributions:

Wang D.: Performed all experiments, interpretation and analysis of the data and wrote the first draft of the manuscript including all figures and text.

Huang Y.: Performed CMM measurements for test sections.

Ewing D.: Assisted in the interpretation and discussion of results.

Chow T.: Performed the CT scans of test sections.

Cotton J. S.: Offered help and suggestions for the CT scan measurements.

Noseworthy M. D.: Offered help and suggestions for the CT scan measurements.

Ching C. Y.: Supervisor and was responsible for the final draft submittal to the journal.

Abstract

A novel methodology is developed here to measure wall mass transfer rates non-destructively using X-ray computed tomography (CT). The mass transfer was measured using a gypsum lined 203mm diameter straight pipe section using a dissolving wall method to water. The measurements were performed at a Reynolds number of 86,000 and Schmidt number of 1200. The local wear of the internal surface is obtained from the CT scans by aligning and analyzing the cross-sectional scanned images of the test section before and after the experiment. The full surface wear contours and the corresponding mass transfer rates are obtained by a three-dimensional reconstruction of the entire test section. The measurements from the CT scans are compared to results obtained from Ultrasonic (UT) measurements of the wall thickness and internal surface measurements using a Coordinate Measuring Machine (CMM) and digital laser scans. The results from the CT scan methodology are in good agreement with the other methods, indicating that the method is robust and can be used to obtain the local mass transfer and roughness over the entire surface. Thus, it can be used as a principal method to investigate mass transfer non-intrusively in complex piping geometries.

2.1 Introduction

Flow Accelerated Corrosion (FAC) causes wall thinning and weakening of carbon steel piping components in power generation plants. If this is not predicted or detected in planned outages, there is the danger of sudden rupture and failure of the piping system. FAC consists of electrochemical reactions at the metal-oxide interface, chemical erosion at the oxide layer and convective mass transfer of the ferrous ions from the oxide-water interface into the bulk flow [1]. The mass transfer rate from the wall to the bulk flow plays a limiting role in the wall thinning rates. Thus, control of FAC in practical applications requires the identification of regions of high local mass transfer in the piping systems.

The mass transfer in piping components has been measured using a variety of methods, including: (i) dissolving wall methods [2-7], (ii) electrochemical techniques [8-11], and (iii) through analogy with heat transfer [12-13]. The advantages and drawbacks of these methods are reviewed in [6]. The drawback of the limiting current density electrochemical technique (LCDT) is that it can not be used to study the change in mass transfer rates over a dissolving surface. The use of the analogy between heat and mass transfer [12] to infer mass transfer coefficients can be problematic, since most heat transfer measurements are performed at relatively low Prandtl numbers, typically less than 10, while the diffusion of the iron magnetite layer of carbon steel piping in water occurs at a Schmidt number of about 1200. Furthermore, in heat transfer applications there is little change to the surface topography. In mass transfer applications, however, the surface will change with the development of roughness due to the mass transfer, which can significantly affect the mass transfer rates. Dissolving wall methods are well suited in these instances, since the surface roughness will develop due to the flow.

The local wall thinning rates in the dissolving wall method have been measured using Ultrasonic transducers (UT) [5, 17], Coordinate Measuring Machine (CMM) measurements [7, 18], laser scans of the internal surface [19, 20] and through X-rays of the test section [5]. Ultrasonic sensors are commonly used for local wall thickness measurements or flaw inspection [14-16], and has been used to measure the local mass transfer rates at selected locations in straight pipes and downstream of an orifice [5, 17]. Goldstein and Cho [7] used an automated surface measuring system, akin to a CMM, to measure the mass transfer on a flat surface using the naphthalene sublimation method. Yamagata *et al*. [18] measured the mass transfer downstream of an orifice in a circular pipe by measuring the surface height of a layer of benzoic acid before and after the experiment on two sectioned halves of a test specimen using a CMM. Mazhar *et al.* [19] and Le *et al.* [20] measured the local mass transfer and roughness in single and back-to-back bends using gypsum test sections, where the test section was sectioned and the surface topography was obtained by laser scanning of the worn surface.

The objective here is to develop a non-intrusive methodology using X-ray Computed Tomography (CT) for measurements of the mass transfer and surface roughness. CT has been used for dimensional metrology in other fields, including engineering design and manufacturing for quality control, because it can be used non-destructively to generate high-resolution images for both the internal and external surfaces [21, 22]. Wilkin *et al.* [5] measured the local mass transfer in pipes and elbows by analyzing X-ray photographs of two perpendicular planes on the test section at different run times. This method did appear to be effective but the analysis tools were limited at that time. The CT technique overcomes these difficulties, since it can provide a full 3-dimensional image of the test sections. Experiments were performed for mass transfer using a gypsum lined straight pipe section in water, which provides a Schmidt number of 1200, similar to dissolution of ferrous ions Fe^{2+} in water [10]. The results from the CT scan methodology were compared to those from UT, CMM and laser scans. The experimental facilities and data reduction techniques are presented in the next section, followed by a discussion and presentation of the results and ends with the conclusions of the study.

2.2 Experimental Facility and Measurement Methodologies

The mass transfer experiments were performed in the test facility shown schematically in Fig. 2.1. The water in the facility flows from a 1.5 m^3 reservoir through a 101.5mm diameter, 9m long downcomer before entering a centrifugal pump at the bottom of the loop. The flow exits the pump to a 203mm diameter, 9.5m long acrylic riser through a sudden expansion at the bottom of the riser. The flow passes through the riser with a length of 36 diameters before entering the gypsum lined test section. The flow exits the test section to a 9 diameter long downstream pipe before flowing back into the reservoir. The flow rate was controlled using a pump speed controller and was

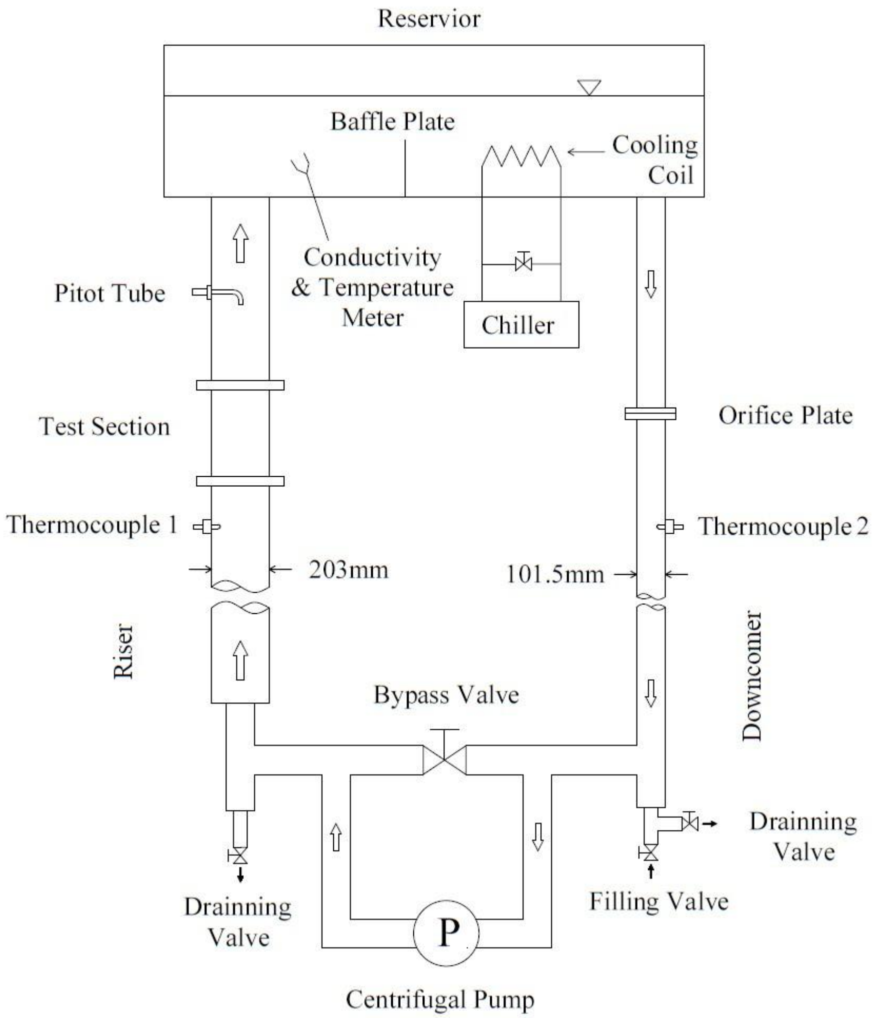

Fig. 2.1: Schematic of experimental test facility

measured using a Pitot tube in the riser downstream of the test section and an orifice plate (β = 0.6) installed in the downcomer. The temperature of water throughout the testing time was measured at three locations along the loop: (i) in the riser upstream of the test section, (ii) in the main reservoir and (iii) in the downcomer. The water temperature just upstream of the test section was maintained at 25±0.5℃ using a cooling coil in the reservoir. The electric conductivity of water in the reservoir was measured by a conductivity probe and recorded with a dedicated computer. Calibration tests were performed offline to correlate the concentration of dissolved gypsum to the electric conductivity of the water at 25℃.

The test section was a gypsum lined straight pipe that was 203mm in diameter and 406mm long. The test section was manufactured using a collapsible maple wooden core and an acrylic casing as shown in Fig. 2.2(a). The wooden core (which forms the inner surface of the test section) has an outer diameter of 203mm and the acrylic casing has an inner diameter of 235 mm, which leads to a 16mm thick gypsum liner. Four acrylic strips were machined and glued to the outer casing of the test section shown in Fig. 2.2(b). Five holes that were equally spaced at 50.8mm were drilled on each strip to accommodate ultrasonic transducers to measure the thickness of the gypsum lining. The holes along the four acrylic strips was offset by 12.7mm along the axial direction. The acrylic casing and wooden core were held concentrically during the casting process, using fixtures including the base plate, and end cap. The inside of the wooden core was braced with wooden inserts along its length. The gypsum was generated by mixing hydrocal ($CaSO_4 \cdot 1/2H_2O$)

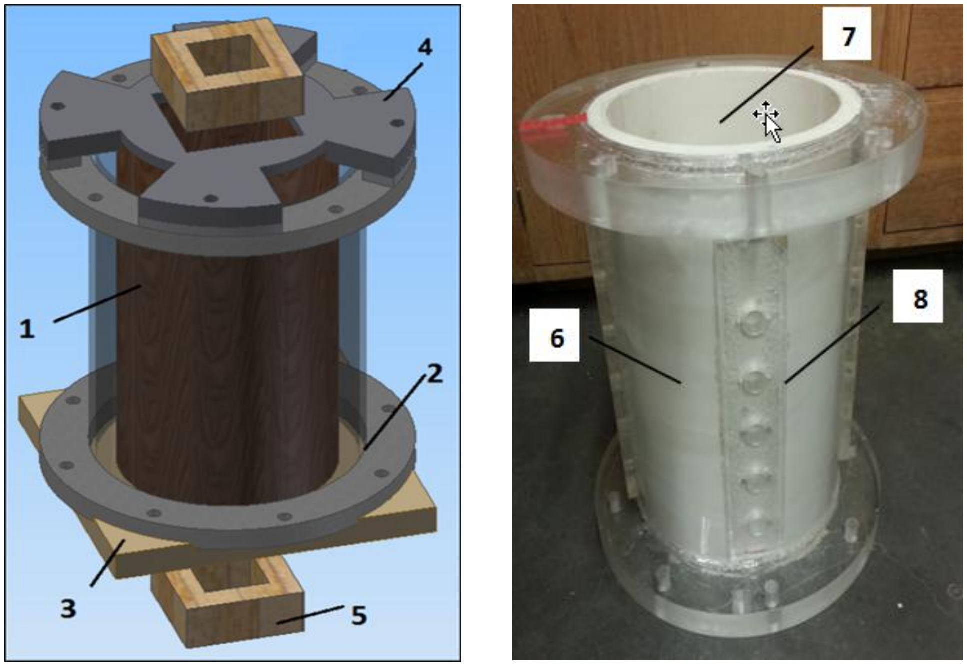

Fig. 2.2: (a) Assembly of mold for casting the gypsum lining and (b) fabricated test section (1. Inner Core 2.&6. Outer Acrylic Casing 3. Base Plate 4. End Cap 5. Wooden Insert 7. Gypsum Liner 8.Acylic Strip for UT sensors)

with water that yields gypsum with a density of 1580 kg/m^3. A small ratio of citric acid was added during the mixing stage to slow the curing process to facilitate the casting. The casting was left to cure under ambient conditions for approximately 20 days until the weight measured by a scale accurate to $\pm$25g reached steady state.

The test section was CT scanned before the experiment to obtain the inner surface topography of the unworn gypsum lining. The test section was installed in the riser and water was allowed to flow through the test section at a Reynolds number of 86,000. The experiments were performed for time intervals of 9, 6, 6, 6, 6 hours for a total run time of 33 hours. At the end of each time interval, the thickness of the gypsum lining at the selected locations was measured using the ultrasonic transducer. At the conclusion of the test, the test section was CT scanned once more to obtain the worn surface topography. The inner surface was also measured before and after the tests using a CMM. Once all the non-destructive measurements were obtained, the test section was cut along the axial direction into two halves and the inner surface laser scanned to obtain an independent measurement of the worn surface topography.

The CT scans were obtained with an image resolution of 1024×1024 pixels over a field of view (FOV) of 26cm, which yielded a physical resolution of 0.25×0.25mm. The through-plane resolution (i.e. slice thickness) was 1mm. The intensity level of the CT scans was adjusted so that both the gypsum lining and acrylic outer shell were captured clearly, as shown in Fig. 2.3(a). The inside and outside surfaces of the gypsum liner, and the outside surface of the acrylic casing were demarcated using edge detection techniques that were based on the Sobel method [23, 24]. This method detects the edges based on the maximum of the gradient of gray scale in the images, as shown in Fig. 2.3(b). The two-dimensional cross sectional profiles of the test section were combined into a three-dimensional array of points corresponding to the inner and outer surface of the gypsum liner and the outside of the acrylic casing, as shown in Fig. 2.3(c). The axis along the center of the test section was re-constructed based on a best fit of the outer surfaces of the gypsum liner through the center. The unworn and worn surfaces were aligned along the axial direction based on common streamwise features, including the acrylic strips and ultrasonic holes. The local radius of the inner surface was computed on a spatially uniform grid with a resolution of 0.5×1mm, that corresponded to approximately 0.3^o in circumferential direction (θ) and 1mm in spacing along the streamwise direction (z). The

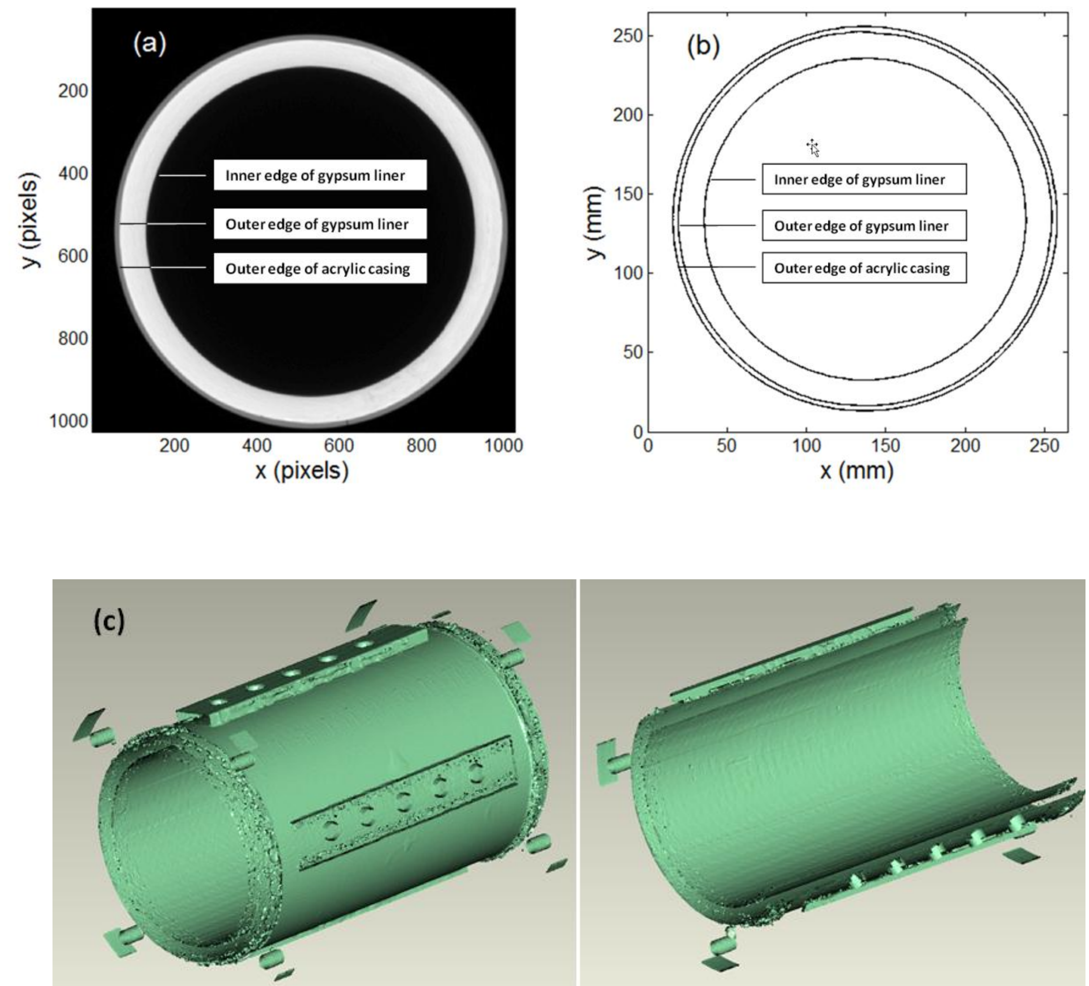

Fig. 2.3: (a) Representative CT scan image of an unworn cross section (b) Edges of local radii detected from the CT scan image (c) Complete 3-D reconstruction of the test section from the CT scan

center for this calculation was based on a best fit to the inside of the gypsum liner in the unworn test section.

A Coordinate Measuring Machine (Zeiss Prismo 900) with Vast measuring head and contact probe was used to obtain the internal surface dimensions of the test section. The test section here was short enough and large enough in diameter to allow the probe to be placed within the entire unsectioned pipe. The inner surface was detected by a 1mm diameter measuring stylus at twelve axial locations along the test section spaced 25.4mm apart. The CMM could measure approximately 55^{o} in the circumferential direction. Thus, the measurements were performed for eight separate orientations with an overlap of approximately 5^{o} at both ends of each curve. The curves measured from different angles at the twelve axial locations were aligned to a common coordinate system by referencing a fixture and holes in the flange on the outer casing. The axis of the inner surface of the gypsum liner was determined from a best fit to the centers using a least squares circle fit at each location.

The laser scan measurements were performed using a hand-held laser digitizer with a resolution of 0.5 mm. The test section was cut into two halves along the axial direction after the experiment using a thin blade band saw and the entire inner surfaces were scanned. The scanned worn surface was initially aligned to a cylindrical coordinate system using commercial image processing software and the data re-gridded to a spatially uniform grid of 1×1mm.

The ultrasonic measurements were performed using a Panametrics 5052UA ultrasonic analyzer and an Olympus M106-SM contact ultrasonic transducer operating at

2.25MHz. The analog output signals were recorded using a National Instrument data acquisition board at a sampling frequency of 10MHz and analyzed using in-house routines in MATLAB. The wall thickness of the gypsum lining is calculated as [25, 26]

$$L = V\,t\,/\,2 \tag{2.1}$$

where t is the transit time for the ultrasonic wave to travel to and from the other wall of the sample and V is the speed of the ultrasonic wave travelling in the material. The transit time was determined by the Pulse-Echo Method [25, 26], which measures the round trip transit time between the initial pulse and first echo reflected from the other side of the gypsum lining. A threshold method was used to filter out the noise and detect the reflected waves of multiple echoes. Two thousand pulses and reflected echoes were analyzed to obtain an average transit time for each measurement. The speed of the ultrasonic wave in the gypsum was determined using a 23mm thick square cross-section gypsum block. The calibration experiment was performed for the dry sample and for the same sample after it was soaked in water over 10 minute time intervals. The result indicated the speed initially decreased with the soaking time, but was approximately constant (2940 m/s) after one hour. The gypsum test section was soaked in water for two hours prior to the experiment for the initial ultrasonic measurements to ensure it was saturated.

The uncertainty of the wear measurement using the CT scans was quantified by examining the deviation between the outer edges of the gypsum liner from the scans before and after the test. As shown in Figure 2.4, the deviation is within $\pm$0.2mm over most of the test section due to misalignment of the two scans, with a maximum of

0.5mm, and is the major contributing factor to the overall uncertainty. The overall uncertainty for the wear measurements from the CT scans is approximately ±6.4% at a 95% confidence level, estimated as two standard deviations due to the misalignment normalized by the mean wear. The accuracy of the CMM measurement is ±5μm, which corresponds to an error of less than ±0.2%. However, the alignment of the worn and unworn surfaces to obtain the wear introduces a much larger uncertainty. In this case, only 12 circumferential measurements are available along the axial direction, as opposed to a complete internal surface from the CT scans. The overall uncertainty in the wear rates from the CMM measurements is estimated as ±5% to 95% confidence level. The uncertainty of the UT thickness measurement is mainly due to the uncertainty of the

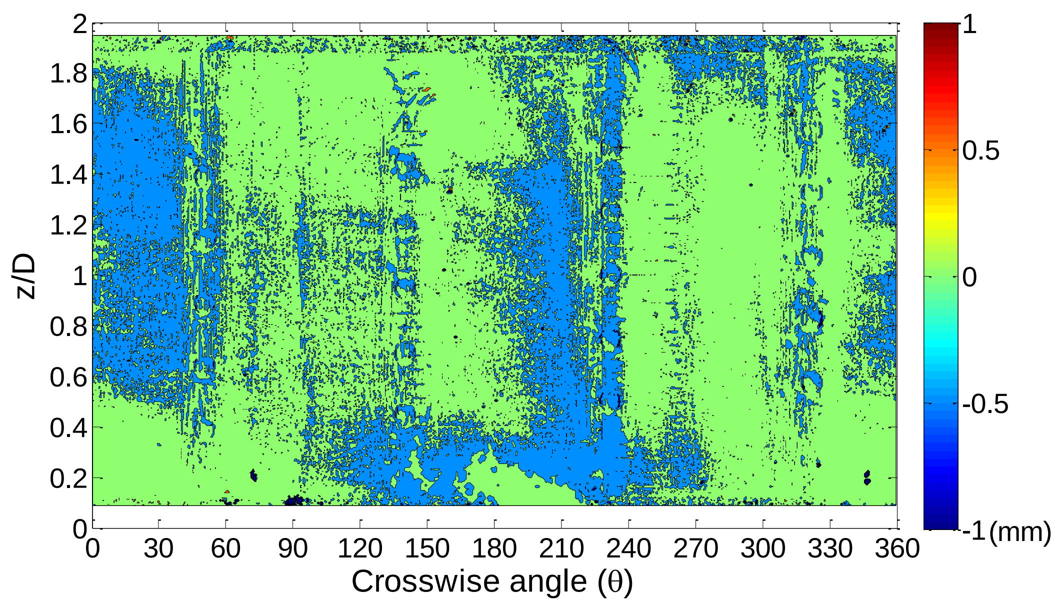

Fig. 2.4: Deviation of local radius between outer surfaces of the gypsum liner before and after experiment from the CT scans

acoustic speed through the gypsum test section. The uncertainty of the wear rates from the UT measurements is estimated to be $\pm 14\%$. This is relatively large compared to both the CT scan or the CMM due to the change in the acoustic speed with the degree of saturation of the gypsum liner. The laser scanning technique was only used to obtain the surface topography of the worn test section. The uncertainty of the worn local radius from the laser scan was estimated to be $\pm 10\%$.

2.3 Results and Discussion

An evaluation of the CT scan measurements was initially performed by comparing the inner radius of the unworn and worn test sections with the other methods. The local radius of the unworn test section from the CT scans at different axial locations is compared to those obtained from the CMM in Fig. 2.5. Here, only every fifth data point from the CT scan is shown to improve the clarity of the figures and better show the comparison between the two measurement techniques. The deviation between the two measurements is within ± 0.2mm, and within the measurement uncertainty. The magnitude of the unworn radius is approximately 101.5 ± 0.5mm, indicating a good cast quality. There are some minor discontinuities in the CMM measurements along the circumferential direction. This is because the measurement was not performed continuously, and the test section had to be rotated for each 45° sector for this measurement. A comparison of the worn radius measured by the CT scan, CMM and laser scan is presented in Fig. 2.6. The results from the CT scan are again in good agreement with the CMM measurements, and to within the expected uncertainty. The

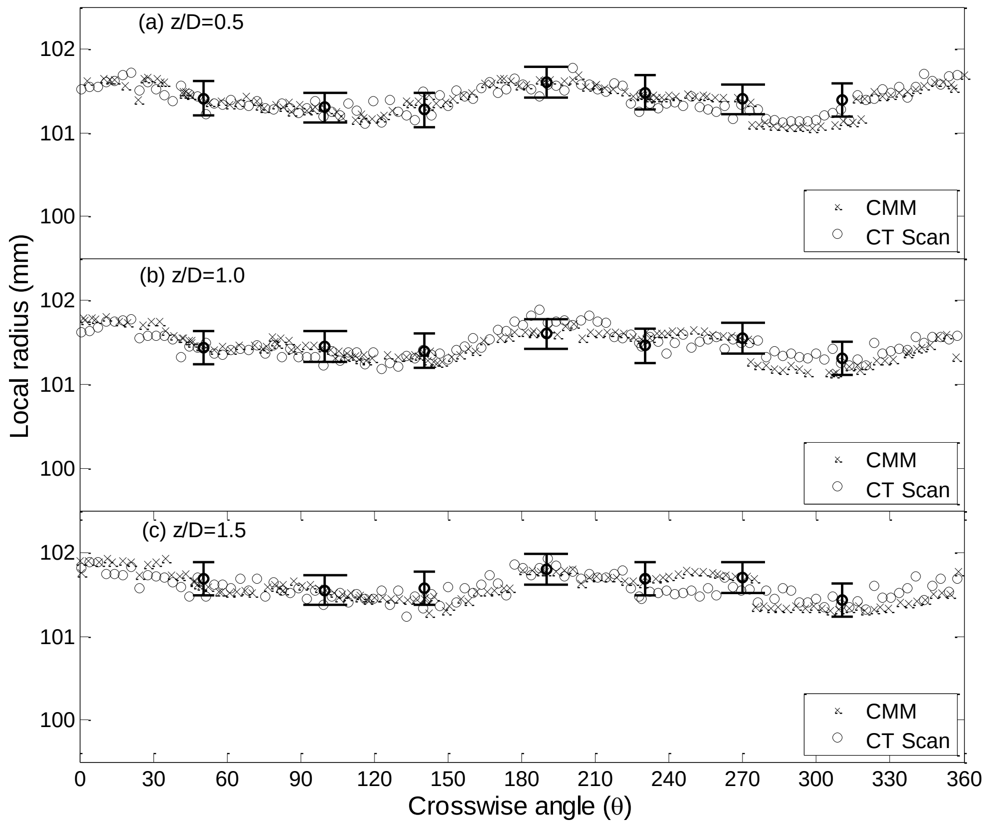

Fig. 2.5: Comparison of local unworn radius measurements from CMM and CT scan at typical streamwise locations

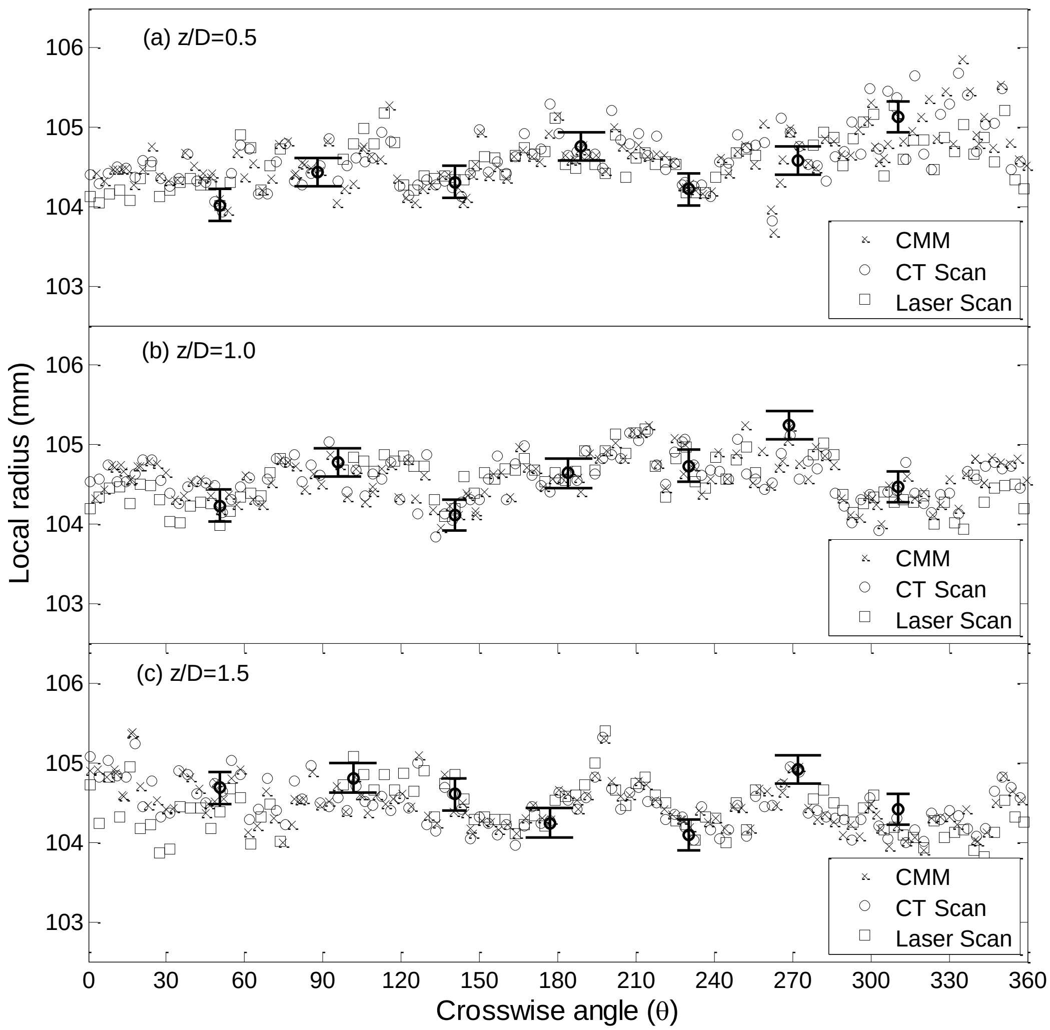

Fig. 2.6: Comparison of local worn radius measurements from CMM, CT scan and laser scan at typical streamwise locations

laser scan measurements are also in reasonable agreement with the results from the CT scan and CMM, but with larger deviations of approximately 0.3mm in the circumferential regions 0° to 60° and 300° to 360°. The deviations of the laser scan measurements to those from the CT scan and CMM can be attributed to the different methods of locating the central axis of the section from the laser scans. The laser scans are performed after cutting the test section axially into two halves. The central axis in this case was determined by assuming that each half was axi-symmetric; for the CMM and CT scan measurements, this is determined based on the complete unworn surface of the test sample. The local wear profiles from the CT scan and CMM were obtained by subtracting the local unworn radius of the inner surface from the worn radius, and are shown in Fig. 2.7. The wear profiles from the CT scan and CMM are in good agreement, with the trends similar to the local worn radius profiles of Fig. 2.6, as expected. The average local wear is approximately 3mm, with the wear slightly higher and less uniform in the entrance region at z/D=0 to 0.5.

The ultrasonic measurements for the wall thickness of the gypsum lining were made at 4 circumferential locations and a total of 20 streamwise locations from z/D of 0.375 to 1.5625. The thickness measurements were made at test times of 0 (unworn), 9, 15, 21, 27 and 33 hours, so that the progression of the wear with time could be evaluated. The final wear profiles from the UT measurements are compared with the CT scan results at the four azimuthal locations in Fig. 2.8. The UT measurements have a much higher uncertainty (±14%), but are still within reasonable agreement with the CT scan measurements. In general, the UT measurements show a lower wear than the CT scan

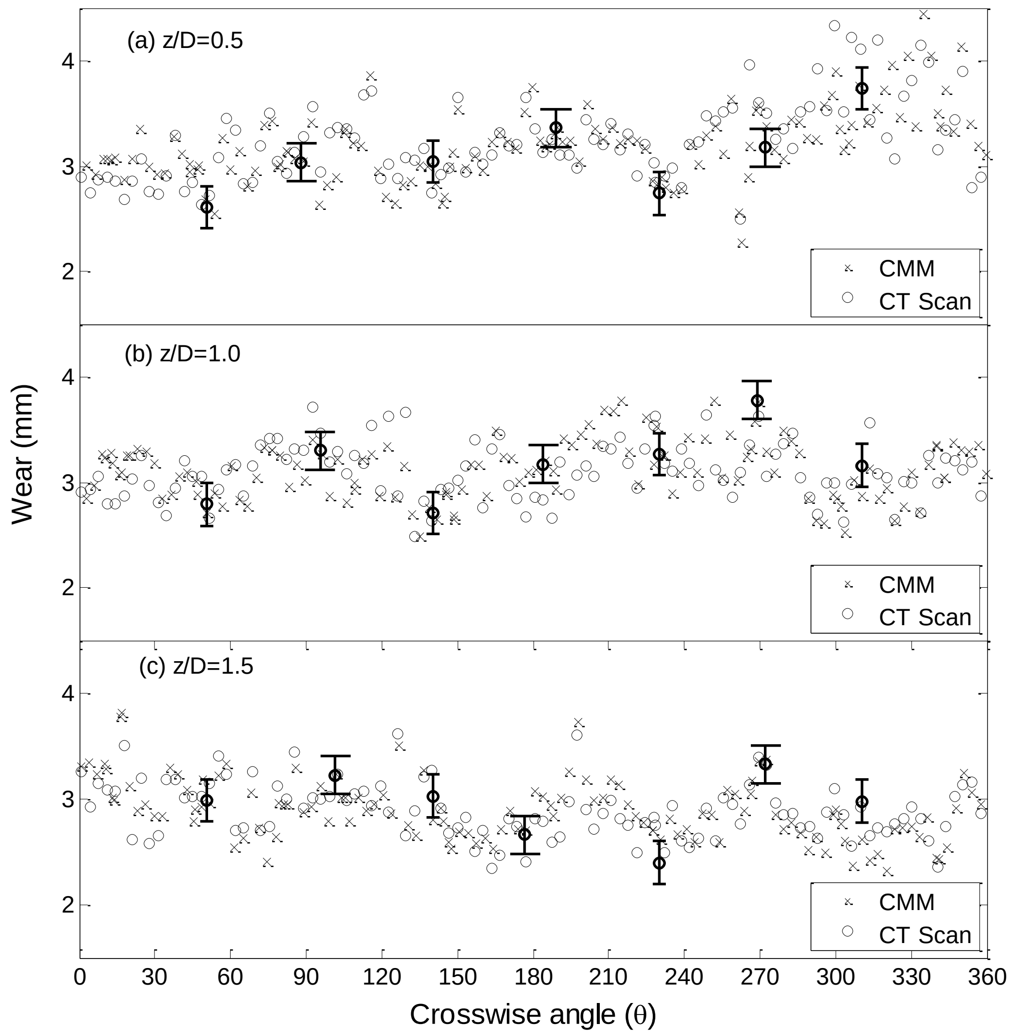

Fig. 2.7: Comparison of local wear profiles obtained from CMM measurement and CT scan at typical streamwise locations

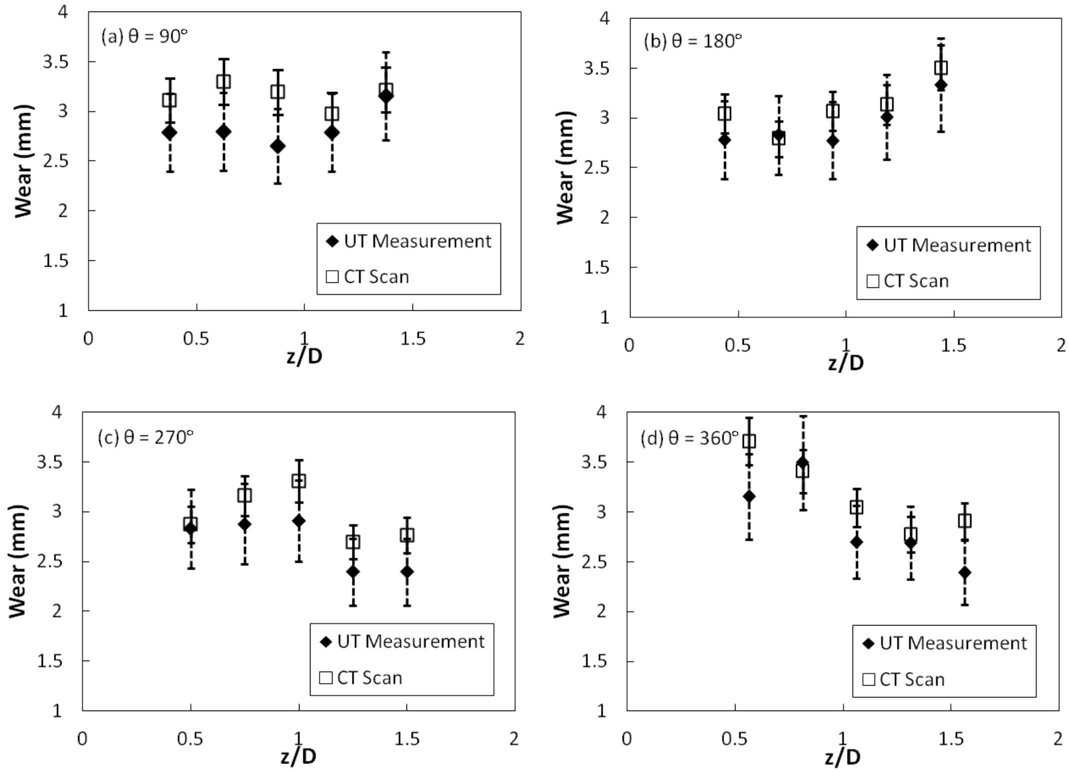

Fig. 2.8: Comparison of final wear obtained from UT measurement and CT scan at different azimuthal locations (θ = 90°, 180°, 270°, 360°)

measurements, which likely could be due to an underestimation of the acoustic speed in the gypsum lining.

The local mean radius was determined by running an average over a larger grid cell to eliminate variations due to local roughness. The effect of the cell size on the local mean radius is shown in Fig. 2.9. The grid cell of $15\times15\text{mm}^2$ still encompasses the variations due to local roughness, while the larger grid cell of $40\times40\text{mm}^2$ is seen to filter the variation of the local mean radius. A cell size of $25\times25\text{mm}^2$ is seen to capture the

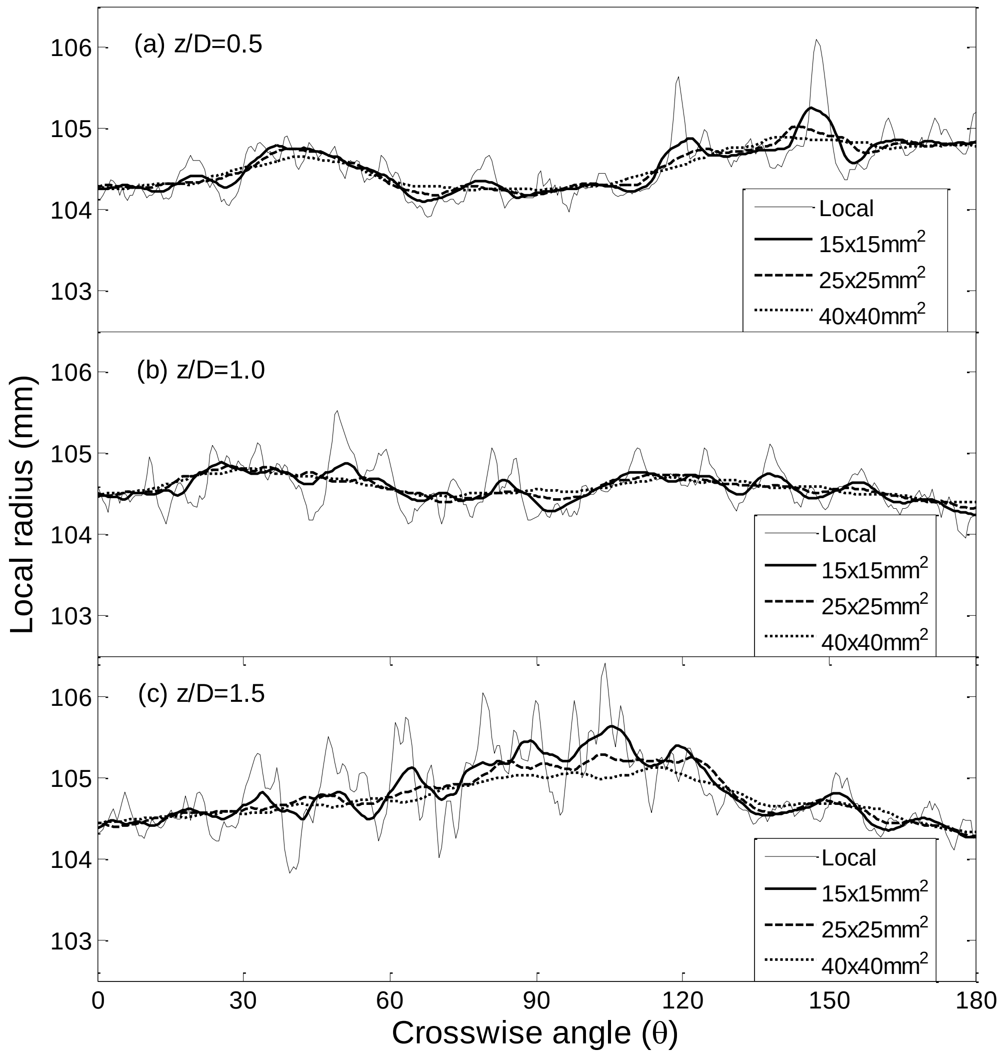

Fig. 2.9: Profiles of local worn radius evaluated by averaging over different grid cell sizes from CT scan at typical streamwise locations

local variation of the mean radius, while eliminating variations due to local roughness, and is used here to obtain the mean radius for each data point.

The absolute roughness height (*e*) used to characterize the surface roughness was determined by evaluating the deviations of the roughness peaks and valleys from the local mean surface. A minimum threshold value of 0.07mm was set to exclude the noise when evaluating the peaks and valleys. The roughness height is estimated based on the mean positive and negative values of the local maxima and minima within a cell of $25\times25\text{mm}^2$. The histograms of the local deviations over the entire cell and the local maxima and minima after the thresholding at typical locations are shown in Fig. 2.10. The histograms illustrate that the local maxima and minima found within each grid cell does represent the typical values of roughness height. The variation of the local maxima and minima from the mean radius, identifying the peaks and valleys of the roughness of the worn surface, are shown in Fig. 2.11 at three typical streamwise locations. The mean values over the grid cell of the local maxima and minima are also shown in these figures. The local maxima and minima are, in general, within ±1mm. The local maxima and minima at z/D=0.5 are relatively larger than those downstream, particularly at crosswise angles between 30° and 120°. The difference between the mean values of the local maxima and minima within each grid cell was used to obtain the absolute roughness height (*e*).

The distribution of the relative roughness (e/D) evaluated from the CT and laser scans are shown in Fig. 2.12. The data missing from the laser scans along θ=40° and 220° are due to the cut lines to section the pipe for the laser scans. There is good

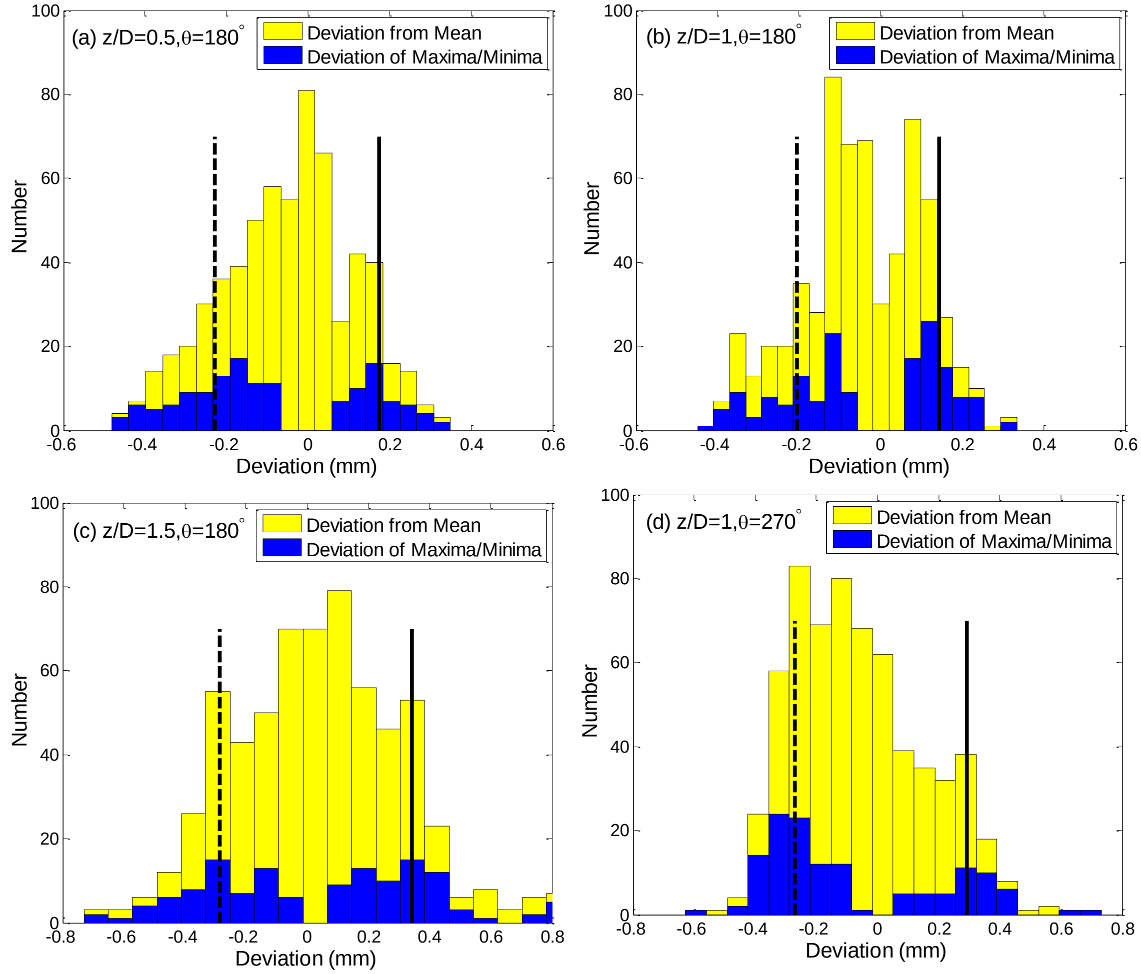

Fig. 2.10: Histograms of local deviation from mean and deviation of maxima/minima over a $25 \times 25 mm^2$ grid cell at typical locations. The mean value of the maxima (—) and minima (----) are also shown.

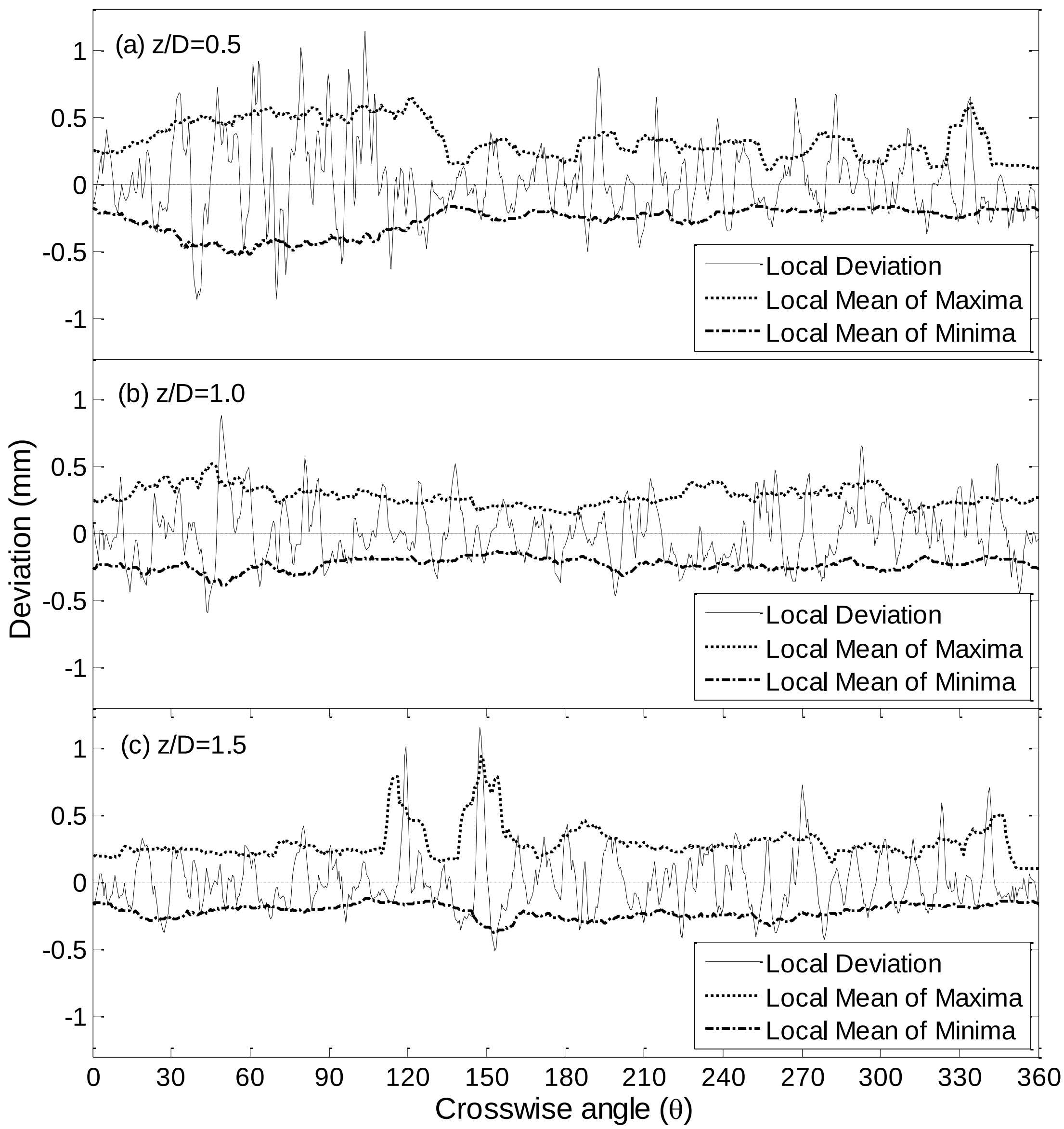

Fig. 2.11: Distribution of local maxima and minima and local mean of the maxima and minima averaged over a $25 \times 25 mm^2$ grid cell at typical streamwise locations

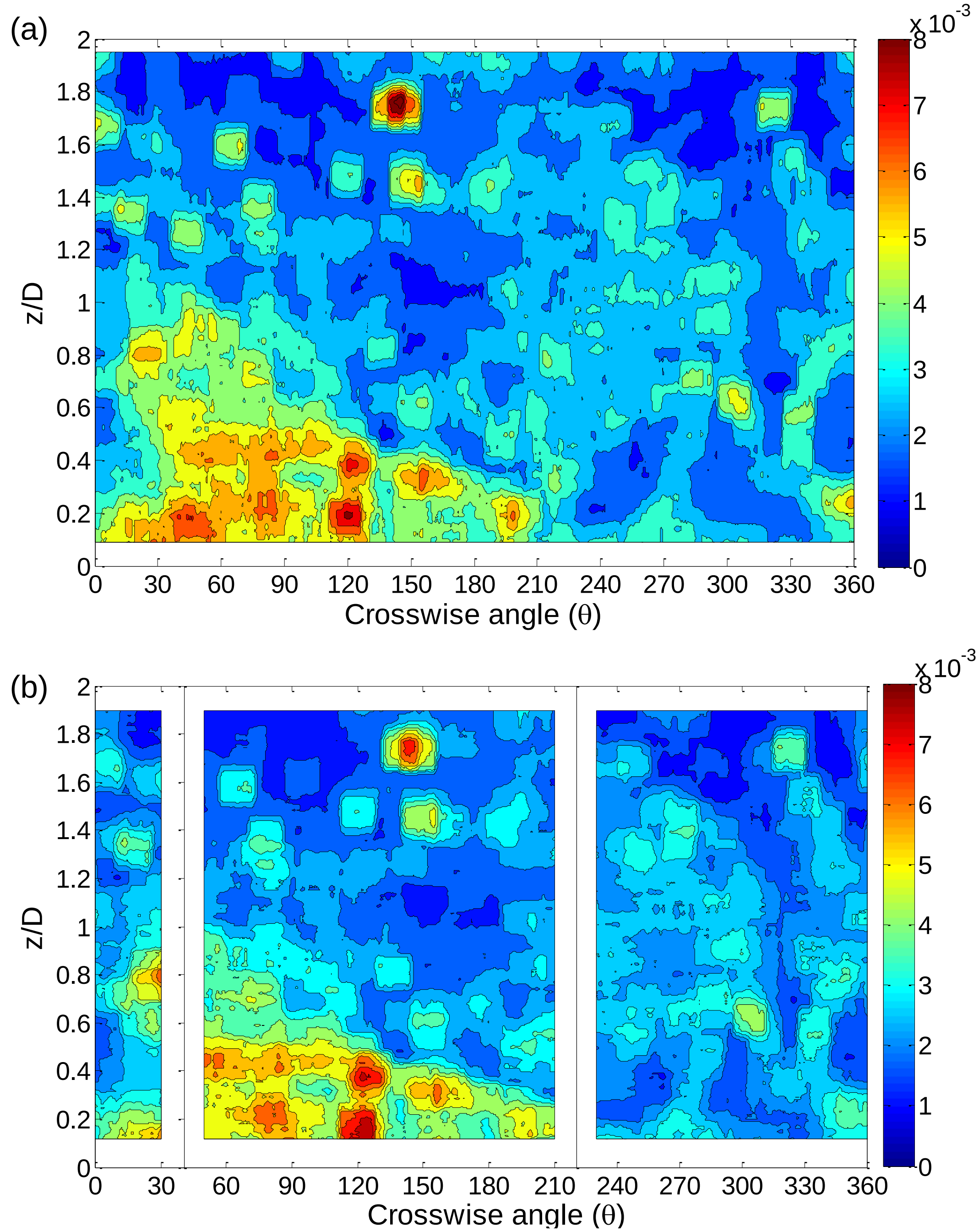

Fig. 2.12: Comparison of distribution of the relative roughness height (*e/D*) from (a) CT scan and (b) laser scan

correspondence and agreement in the relative roughness from the two methods. Both methods show a relatively rougher region near the inlet at crosswise angle at θ=0°~210°. The overall distribution of the relative roughness further downstream of the inlet is relatively uniform, with a value of about 3×10^{-3}, and lower than that in the inlet region that had values in the range 5 to 7×10^{-3}. A small region of high roughness is observed around $\theta\approx140°$ and $z/D\approx1.8$. This is likely due to the presence of an isolated scallop due to a casting defect, and this region could be neglected for further analysis. The dimensionless roughness height (e^+) is calculated by $e^+ = eu_\tau/v$ using the absolute roughness height (e) and friction velocity (u_τ) estimated from the Moody diagram [27]. The typical value of e^+ over the entire worn surface is in the range 12 to 18, which corresponds to the transient region of roughness for mass transfer. The transient roughness region has been recognized as a critical region where the roughness has the maximum effect on mass transfer [28].

Following Mazhar *et al*. [19], the mass transfer coefficient is determined by

$$h_m = \frac{1}{(c_w - c_{b0})}\rho\frac{\partial\delta}{\partial\tilde{t}} \tag{2.2}$$

where δ is the local wear, ρ is the density of gypsum and $\tilde{t}$ is a modified time to compensate for the increase in concentration of the bulk fluid over the run time, and given by

$$\tilde{t} = \frac{\int_0^T (c_w - c_b(t))dt}{(c_w - c_{b0})} \tag{2.3}$$

and $\Delta c_0 (= c_w - c_{b0})$ is the initial concentration difference (2.6g/l). The wear rate was calculated by dividing the local wear (δ) measured from the CT scan and CMM by the final modified time. The local wear rates from the UT measurements were obtained by a linear fit to the variation of the wear with modified time. The local Sherwood number is obtained as

$$Sh = \frac{h_m D}{D_m} \tag{2.4}$$

where D is the diameter of the pipe, and D_m (7.42×10^{-10} m^2/s) is the mass diffusivity of gypsum at 25℃. The value for the mass diffusivity is obtained by correcting the value from Wilkin *et al*. [5] at 20℃ to 25℃ using the Stokes-Einstein Equation [29].

The wear averaged over a grid cell of the same size as that used to estimate the roughness was used to evaluate the local Sherwood number. The distribution of the local Sherwood number over the entire test section from the CT scan is shown in Fig. 2.13. The mass transfer was relatively larger in the pipe entrance region (z/D < 0.5), with a maximum Sherwood number between 6000 and 8000. This is likely due to the entrance effects and a slight sudden expansion as the flow enters the larger diameter worn test section. The Sherwood number decreases downstream as the flow develops and becomes relatively uniform downstream of the test section. The average Sherwood number over the entire test section is approximately 5000. There is some correspondence between the distribution of the local Sherwood number and the roughness (Fig. 2.12), with both decreasing along the streamwise direction. However, the local Sherwood number in the high mass transfer region is not exactly consistent with the high roughness region, indicating that the relationship between mass transfer and development of roughness is not direct.

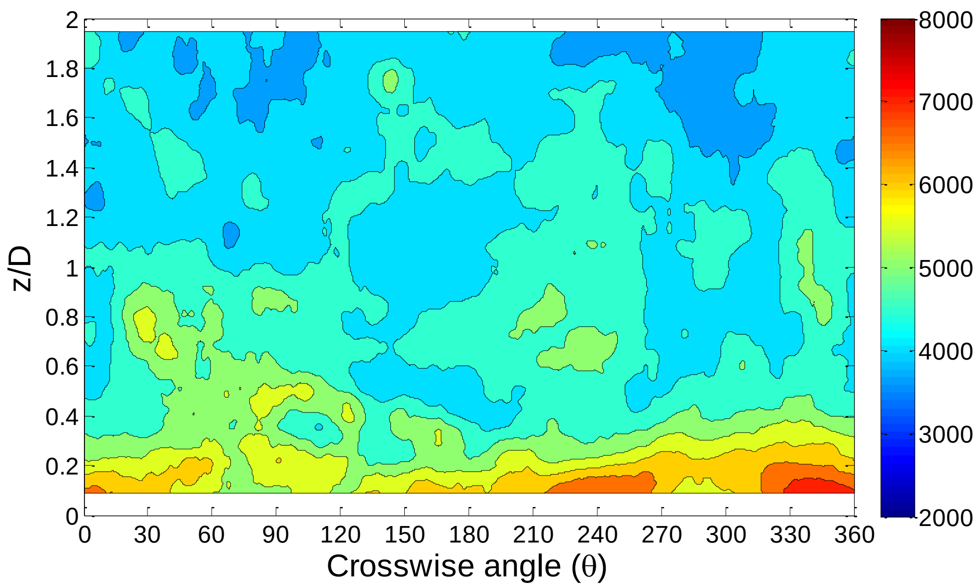

Fig. 2.13: Distribution of the local Sherwood number over the test section from the CT scan

The Sherwood number profiles along the streamwise direction for different circumferential locations are shown in Fig. 2.14(a). The Sherwood number decreases from about 6000 at the entrance to reach a relatively uniform value beyond $z/D\approx0.6$. The Sherwood number in the uniform region is 20% higher than the results from Postlethwaite and Lotz [10] for fully rough pipes. This could be due to the current roughness being in the transition region, where the mass transfer is a maximum due to the roughness [28]. The Sherwood number profiles in the azimuthal direction at selected streamwise locations are shown in Fig. 2.14(b). The profiles indicate that the mass transfer is relatively uniform along the azimuthal direction. The agreement in the Sherwood number determined from the CMM and UT measurements with those from the

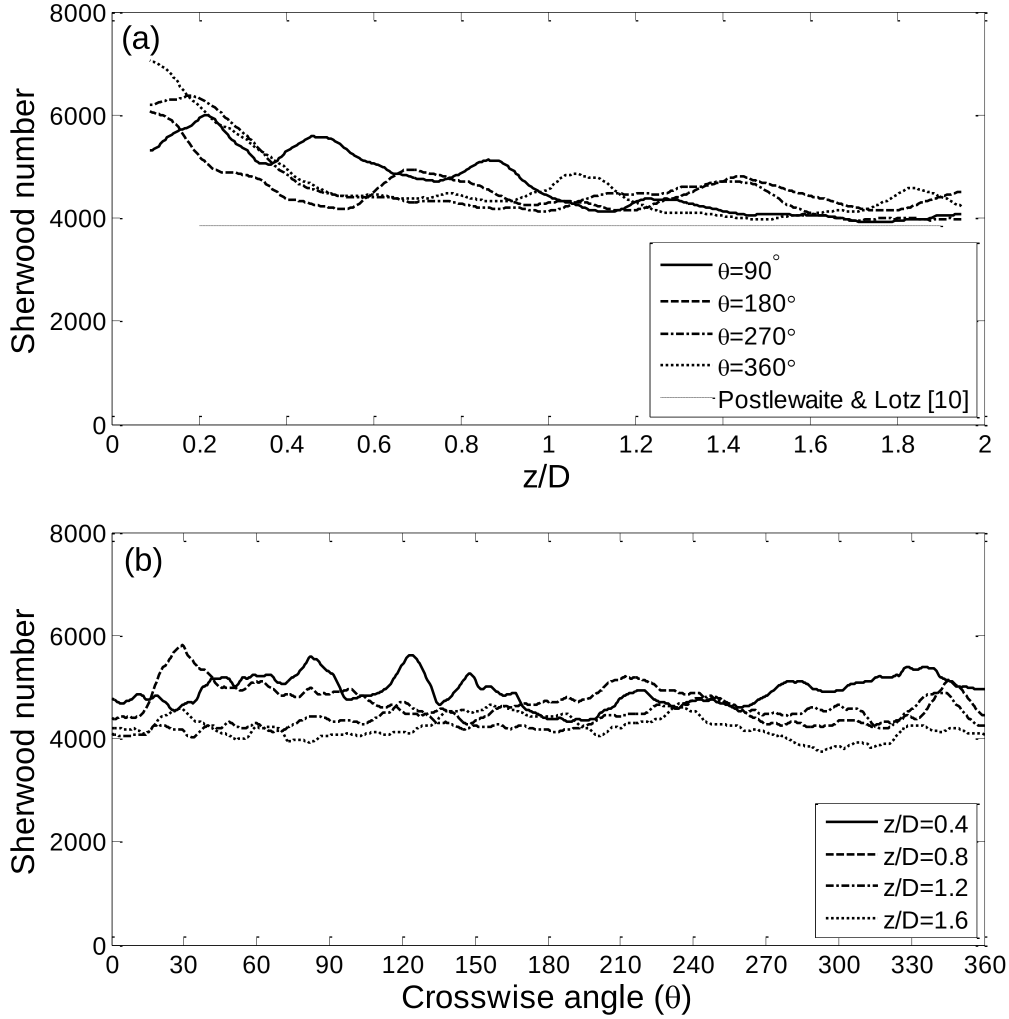

Fig. 2.14: Local Sherwood number profiles at **(a)** typical azimuthal locations (θ=90°, 180°, 270°, 360°) along streamwise direction and **(b)** typical streamwise locations (*z/D*=0.4, 0.8, 1.2, 1.6) along azimuthal direction

CT are similar to those of the wear, and hence are not shown here.

2.4 Conclusions

A novel non-intrusive method for measuring the mass transfer using a dissolving wall method has been developed using X-ray Computed Tomography (CT). The tests were performed using a 203 mm cylindrical test section with a gypsum lining in a flow loop with water as the working fluid. The CT scan measurements were benchmarked against measurements using a CMM machine, Ultrasonic sensors and laser scans. The local wear profiles were obtained by subtracting the local worn radius from the unworn case from the CMM measurements and X-ray CT scan. The worn surface topography and wear distribution over the entire test section was obtained by the CT scan. The local wear obtained from the CT scan was in good agreement with the CMM measurements. The ultrasonic sensors were used to measure the variation of the thickness of the gypsum lining over the test time, and hence the mass transfer rates, at selected locations along the test section. The mass transfer estimated from the UT measurements was in agreement with the CT scan data to within the experimental uncertainty. The laser scanning for the worn surface topography was performed at the end of the experiment by cutting the test section in half along the streamwise direction. Comparison of the surface topography and the roughness evaluation from the laser scans was in good agreement with that from the CT scan. The Sherwood number in the straight pipe for this experiment is slightly higher than previous results for fully rough pipes. This can be attributed to the surface roughness being in the transition region, which has the highest effect on the mass transfer. The results here show that the CT scan methodology is an effective non-intrusive measurement technique that can be used to investigate the evolution of the roughness and mass transfer on dissolving walls in complex piping geometries.

2.5 References

[1] Pietralik JM., Schefski CS. 2011. Flow and mass transfer in bends under Flow-Accelerated Corrosion Wall Thinning Conditions. *Journal of engineering for gas turbines and power*. 133(1) 012902: 1-7.

[2] Sherwood T. K., Ryan J. M. 1959. Mass transfer to a turbulent fluid with and without chemical reaction. *Chemical Engineering Science*. 11(2): 81-91.

[3] Meyerink E. S. C., Friedlander S.K. 1962. Diffusion and diffusion controlled reactions in fully developed turbulent pipe flow. *Chemical Engineering Science*. 17:121-135.

[4] Harriott Peter, Hamilton R. M. 1965. Solid-liquid mass transfer in turbulent pipe flow. *Chemical Engineering Science*. 20:1073-1078.

[5] Wilkin SJ., Oates HS., Coney M. 1983. Mass transfer on straight pipes and 90°bends measured by the dissolution of plaster (1st Edition). *Central Electricity Research Laboratories Report*. TPRD/L/2469/N83.

[6] Poulson Bryan, Robinson Russel. 1986. The use of a corrosion process to obtain mass transfer data. *Corrosion Science*. 26:265-280.

[7] Goldstein R.J. & Cho H.H. 1995. A review of mass transfer measurements using naphthalene sublimation. *Experimental thermal and fluid science*. 10:416-434.

[8] Berger FP., Hau KFFL. 1977. Mass transfer in turbulent pipe flow measured by the electrochemical method, *Int. J. of heat and mass transfer*. 20:1185-1194.

[9] Shaw D. A., Hanratty T. J. 1977. Mass Transfer Rates to a Wall at large Schmidt number. *AIChE Journal*. 23(1): 28-37.

[10] Postlethwaite J., Lotz U. 1988. Mass transfer at erosion-corrosion roughened surfaces. The *Canadian Journal of Chemical Engineering*. 66: 75-78.

[11] Zhao W., Trass O. 1997. Electrochemical mass transfer measurements in rough surface pipe flow. *Int. J. Heat Mass Transfer*. 40(12):2785-2797.

[12] Chilton T.H. & Colburn A.P. 1934. Mass transfer (absorption) Coefficients. *Industrial and engineering chemistry*. 26(11): 1183-1187.

[13] Coney M. 1980. Erosion Corrosion: The calculation of mass transfer coefficients. *Central Electricity Research Laboratories Report*. RD/L/N197.

[14] Jukka S. Jurvelin, Tuomas Rasanen, Pekka Kolmonen, Tiina Lyyra. 1995. Comparison of optical, needle probe and ultrasonic techniques for the measurement of articular cartilage thickness. *Journal of biomechanics*. 28(2): 231-235.

[15] Dixon S, Edwards C, Palmer S.B. 2001. High accuracy non-contact ultrasonic thickness gauging of aluminum sheet using electromagnetic acoustic transducers. *Ultrasonics*. 39(6): 445-453.

[16] Renaldas Raisutis, Rymantas Kazys, Liudas Mazeika. 2008. Ultrasonic Thickness Measurement of Multilayered Aluminum Foam Precursor Material. *IEEE transactions on instrumentation and measurement*. 57(12): 2846-2855.

[17] Wang D. 2012. Characterization of local mass transfer rate downstream of an orifice. *Master's Thesis*. McMaster University, ON, Canada.

[18] Yamagata T., Ito A., Sato Y., Fujisawa N. 2014. Experimental and numerical studies on mass transfer characteristics behind an orifice in a circular pipe for application to pipe-wall thinning. *Experimental thermal and fluid science*. 52: 239-247.

[19] Mazhar H., Ewing D., Cotton J.S., Ching C.Y. 2013. Experimental investigation of mass transfer in 90^o pipe bends using a dissolvable wall technique. *International Journal of Heat and Mass Transfer*. 65: 280–288.

[20] Le T., Ewing D., Schefski C., Ching C.Y. 2014. Mass transfer in back-to-back elbows arranged in an out of plane configuration. *Nuclear engineering and design*. 270: 209-216.

[21] Kruth J. P., Bartscher M., Carmignato S., Schmitt R., Chiffre L. De, Weckenmann A. 2011. Computed tomography for dimensional metrology. C*IRP Annals Manufacturing Technology*. 60: 821-842.

[22] Ontiveros S., Yague-Fabra J. A., Jimenez R., Tosello G., Gasparin S., Pierobon A., Carmignato S. and Hansen H. N. 2012. Dimensional measurement of micro-moulded parts by computed tomography. *Measurement science and technology*. 23:125401.

[23] Sobel I. 1970. Camera Models and Perception. *Ph.D. thesis*. Stanford University, Stanford, CA.

[24] Sobel I. 1990. An Isotropic 3×3 Gradient Operator. *Machine vision for three dimensional scenes,* Freeman, H., Academic Pres, NY, 376-379.

[25] Truell R., Elbaum C. & Chick, B.B. 1969. Ultrasonic Methods in Solid State Physics. Academic Press. Chapter 2.

[26] Krautkramer J., Krautkramer M. 1983. Ultrasonic Testing of Materials: Third Edition. Springer-Verlag. Chapter 10-11.

[27] Moody Lewis F. 1944. Friction factors for pipe flow. *Transaction of the ASME*. 66: 671-84.

[28] Dawson D. A., Trass O. 1972. Mass transfer at rough surfaces. *Int. J. of heat and mass transfer*. 15:1317-1336.

[29] Simpson J. H., Carr H. Y. 1958. Diffusion and Nuclear Spin Relaxation in Water. *The physical review*. 111(5): 1201-1202.

Chapter 3

Time evolution of surface roughness in pipes due to mass transfer under different Reynolds numbers

Complete citation:

Wang D., Ewing D., Ching C.Y. 2016. Time evolution of surface roughness in pipes due to mass transfer under different Reynolds numbers. *Int. J. Heat Mass Transfer*. 103:661-671.

Copyright:

Relative Contributions:

Wang D.: Performed all experiments, interpretation and analysis of the data and wrote the first draft of the manuscript including all figures and text.

Ewing D.: Assisted in the interpretation and discussion of results.

Ching C. Y.: Supervisor and was responsible for the final draft submittal to the journal.

Abstract

Experiments were performed using a dissolving wall method to characterize the development of surface roughness in pipes at Reynolds number from 50,000 to 200,000. The test sections had a lining of gypsum that dissolved to flowing water in a closed flow loop. The tests were run over sequential time periods for each Reynolds number. At the end of each time period, the inner surface topography was measured using X-ray CT scans. Scallops are seen to initiate on the surface over time and then subsequently grow spatially and in depth with time. The surface was divided into smaller local areas and a scallop initiation time was introduced so that a common time datum from initiation could be used to characterize the time development of the roughness. The peak-to-valley roughness height was found to scale well with time when normalized by the turbulent inner scales. There is an initial period of slower growth rate in the roughness height, followed by a period of relatively higher growth rate. The growth of the integral length scale of the scallops is different, with an initial rapid growth followed by a much slower growth rate. The streamwise spacing of the scallops estimated from the density is approximately 1000 wall units as the scallops saturate the surface. There is a good correlation between the roughness height and the wear when normalized by the turbulent inner scales.

3.1 Introduction

Surface roughness plays an important role in the momentum and mass transfer at the wall, with a significant enhancement in the mass transfer rates for flow over rough walls [1-4]. Experimental studies have been performed to investigate the roughness effect on mass transfer using different types of predefined surface roughness, mainly using electrochemical methods for the mass transfer measurements. The artificial surface roughness includes V-grooves [1], sandpaper-roughened [2], square rib [3] and erosion-corrosion roughened surfaces [4]. In addition to the roughness height, the ratio of pitch to height, size and frequency of the roughness elements were found to affect the mass transfer.

For the case of mass transfer on a soluble surface, the surface roughness develops naturally due to the mass transfer to the bulk flow, which subsequently affects the momentum and mass transfer and vice versa. The most common natural roughness pattern is a densely packed array of intersecting, saucer-shaped depressions or pits, usually called ‘scallops’ [5]. In geological fields, scalloped cave channel walls are commonly seen in karst systems or ice caves due to the fluid flow [6]. Early studies indicated that the natural physical scallop length was correlated to the fluid flow velocity during the scallop development [5-7]. Surface defects or imperfections on the surface are thought to be responsible for initialization of scallops. Goodchild and Ford [7] found the mean length of stable scallops (L) correlated with the mean flow velocity with a value (LU/ν) of approximately 11,500, showing that the scallop length was inversely proportional to the flow velocity. Blumberg & Curl [6] performed experiments on soluble gypsum surfaces and found the normalized wavelength (Lu_τ/υ) to be approximately 2200. Thomas [8] later analyzed roughness data from a large variety of sources in both natural geological fields (granular bed, rock, ice, plaster) and man-made industrial plants (metal pipes) and proposed the dimensionless average streamwise spacing ($\lambda u_\tau/\upsilon$) of ripples or scallops was approximately 1000. The streamwise spacing proposed by Thomas [8] is close to the scallop characteristic length when the scallops or ripples are fully developed.

In industrial piping systems, the scalloped patterns formed in metal pipes [9, 10] due to flow accelerated corrosion (FAC) are very similar to those found in geological fields. The pipe wall thinning rates are found to be enhanced by the increase in mass transfer due to the scallops developing on the surface. The mass transfer on surfaces with naturally developing roughness has been experimentally studied using dissolving wall methods with naphthalene sublimation in air [11, 12] and gypsum dissolution in water [13, 14]. The mass transfer results with predefined roughness [1-4] have not been compared to those on dissolving walls, primarily because of the difficulties of characterizing the temporal development of the roughness and mass transfer. Thus, there is uncertainty when using correlations developed for predefined roughness to predict the mass transfer on surfaces with naturally developing roughness. Mazhar et al. [14] investigated the change of roughness and mass transfer by using different gypsum test sections tested for different times. The roughness height was found to decrease slightly with increasing Reynolds number. Using a dissolving gypsum surface, Villien et al. [15]

observed the length scale of scallops decreased, while the density of scallops increased with increasing flow rate; however, this was not quantified. Wang et al. [16] recently developed a non-destructive measurement technique to quantify the scalloped surface and the corresponding mass transfer using X-ray CT scans. They used the method for flow in a S-bend at a Reynolds number of 300,000 [17] and determined that regions of high mass transfer corresponded to regions of higher roughness and the ratio of streamwise spacing to roughness height was very different in the different regions.

One challenge in quantifying the temporal development of the roughness is in selecting the appropriate roughness parameters to characterize the surface. A typical surface contains a range of spatial wavelengths, which can be decomposed to surface form, waviness and roughness. The decomposition can be done using a number of surface filtering methods, such as 2RC, Gaussian, spline, morphological, and wavelets [18]. Wavelet analysis allows space-frequency localization, which is well suited for multi-scale analysis of surface roughness [19, 20]. The proper selection of the local sampling area is also important so that it provides both local information as well as be sample independent [21]. The roughness height is typically characterized by the arithmetic mean deviation, root-mean-square deviation and ten point peak to valley height while the topography is often characterized by the skewness and kurtosis [21, 22]. The spatial length scales of roughness can be characterized by the autocorrelation lengths from two-dimensional autocorrelation functions [21], while the spatial distribution can be characterized by the number of roughness elements or scallops in a unit area.

The objective here is to investigate the time evolution of the roughness due to dissolution from a solid soluble pipe wall under different Reynolds numbers. Experiments were performed using 203mm diameter straight pipe test sections at Reynolds numbers of 50,000, 100,000 and 200,000. The wall dissolving method using gypsum dissolution to water at 25 ℃ was used, with a Schmidt number of 1200. The surfaces before and after each run time were measured non-destructively using X-ray CT scans.

3.2 Experimental Methodology and Data Reduction

The experiments were performed in the test facility shown schematically in Fig. 3.1. The water in the facility flows from a 1.5 m^3 reservoir through a 101.5 mm diameter, 9 m long downcomer before entering a centrifugal pump at the bottom of the loop. The flow exits the pump to a 203 mm diameter (*D*), 9.5 m long acrylic riser through a sudden expansion at the bottom of the riser. The flow passes through the riser with a length of 7.3 m (36*D*) before entering the straight gypsum lined test section. The flow exits the test section to a 1.4 m (7*D*) downstream pipe back to the reservoir. The flow rate is adjusted using a variable speed controller for the pump and measured using two Pitot tubes; one in the 203 mm riser downstream of the test section and the other in the 101.5 mm downcomer. Detailed velocity profiles in the 203 mm riser were measured upstream of the test section by traversing a Pitot tube in two orthogonal directions to confirm the flow entering the test section is fully developed. The two pitot tubes in the riser and downcomer were calibrated against the flow rate from the complete traverse. The

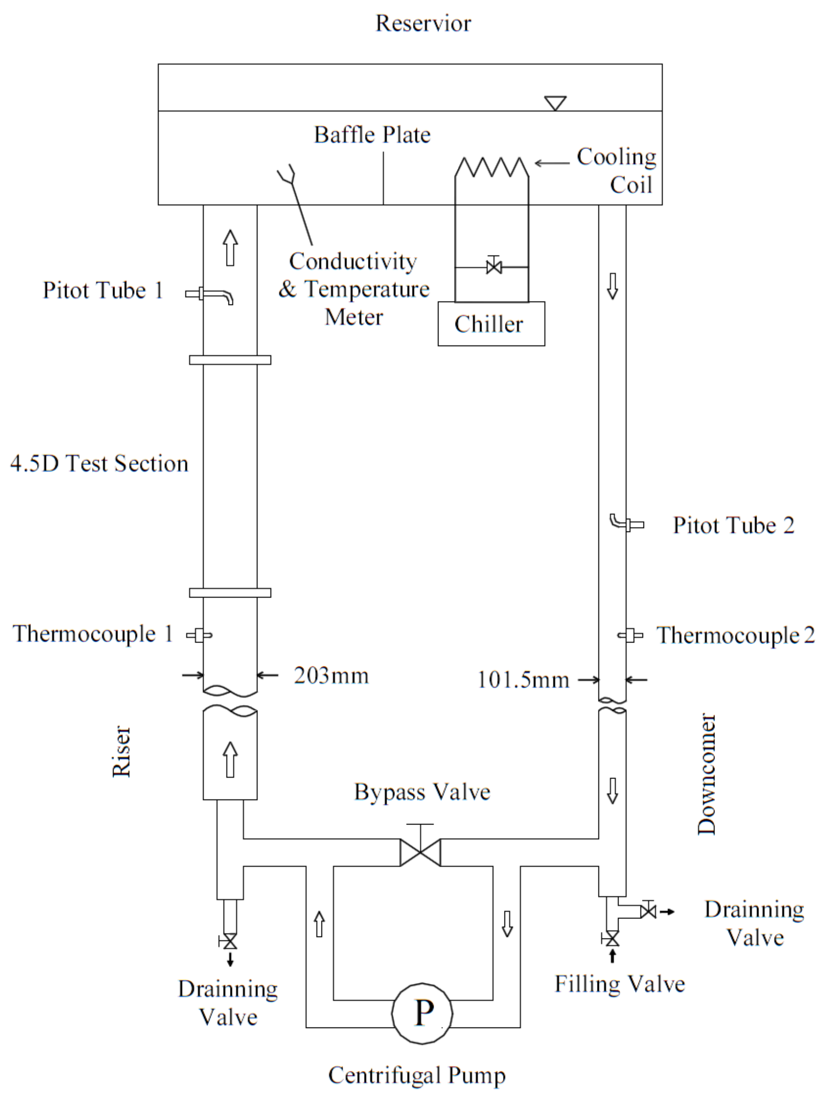

Fig. 3.1: Schematic of test facility

temperature of water throughout the tests was measured at three locations along the loop: (i) in the main reservoir, (ii) the riser and (iii) the downcomer. The water temperature was maintained at 25 $\pm$0.5 ℃ using a cooling coil in the reservoir. The electrical conductivity of water was measured by a conductivity probe in the reservoir and recorded with time. A calibration test was performed to correlate the concentration of dissolved gypsum to the electrical conductivity of the water at 25 ℃ before the experiment.

The experiments were performed using three 203 mm inner diameter straight test sections that had 14 mm, 14 mm, and 22 mm thick gypsum linings. The larger gypsum lining on one test section was due to a slightly larger outer diameter shell for that particular section. The test sections were cast using a three-dimensional printed collapsible inner core and a polycarbonate outer shell. The gypsum was generated by mixing hydrocal ($CaSO_4$•$1/2H_2O$) with water that yields gypsum with a density of 1580 kg/m^3. A small ratio of citric acid was added during the mixing stage to slow the curing process to facilitate the casting. The inner core was removed shortly after casting and the gypsum was left to cure under ambient conditions for approximately 15 days until the weight of the test section reached steady state using a scale accurate to $\pm$25g.

The experiments were performed by flowing water through the test sections with mean velocities of 0.85 m/s, 1.7 m/s and 3.4 m/s. The corresponding Reynolds numbers were 50,000 100,000 and 200,000. The experiments were performed as a series of consecutive trials to capture the time evolution of surface roughness for each Reynolds number. In each case, the test sections were exposed to the flowing water for a set period of time and then the surface characteristics were measured. Each test section was then put back into the facility and the process repeated. In total, eight experiments for each Reynolds number were performed with different time periods, as shown in Table 3.1, for total experimental times of 112, 64, 44 hours for the three Reynolds number. A modified time (t_{mod}) given by

$$t_{mod} = \frac{\int_0^{t_{exp}} (c_w - c_b(t))dt}{c_w - c_{b0}} \tag{3.1}$$

was used to correct the experimental time to account for the change in bulk concentration of the flow during the testing period, where t_{exp} is the actual experimental time, c_w is the wall concentration, c_b is the bulk concentration as a function of time and the initial bulk concentration $c_{b0} = 0$.

The surfaces of the test sections were measured using X-ray CT scans for the unworn initial surface and worn surfaces after each test. Details of the measurement methodology can be found in [16]. The image resolution at each cross-section was 1024×1024 pixels, which yielded a physical resolution of 0.25×0.25 mm^2. The through plane resolution (i.e. slice thickness) was 1mm along the test section. A Sobel edge detection method was used to analyze the two-dimensional CT raw images [23], and then the cross sectional profiles were combined into a three-dimensional array of points corresponding to the inner and outer surfaces of the gypsum liner, as well as the outer surface of the shell. The data points of the inner surface profiles were reconstructed by a three-dimensional data processing software to obtain the three-dimensional roughness.

Table 3.1: Experimental conditions for the three test sections

Re	*Sc*	No. of Expts.	Total Time (hrs)	Time Periods (hrs)
50,000	1200	8	112	8, 8, 16, 16, 16, 16, 16, 16
100,000	1200	8	64	8, 8, 8, 8, 8, 8, 8, 8
200,000	1200	8	44	4, 4, 4, 4, 4, 8, 8, 8

The inner surfaces were finally computed on a uniformly distributed sampling interval of 1×1 mm^2 in the axial and circumferential directions. The axis along the center of the test section was initially determined on a best fit of the outer surfaces through the center for each case. The axis was then refined on a best fit of the unworn inner surface to ensure it followed the inner surface. The surfaces at different times were aligned by computing the maximum two-dimensional cross-correlation functions between the surfaces. A 2-D Discrete Wavelet Transform (DWT) was used to decompose the surface based on different wavelengths using the Daubechies wavelet [24] of order 5. The surface roughness was then characterized in smaller sampling areas of 240×80, 160×80, 80×80 mm^2 for Reynolds number at 50,000, 100,000 and 200,000, respectively, which are approximately five times the physical length scales of the roughness in each direction.

The height of the roughness was characterized by computing the root mean square roughness height (e_{rms}) and five maximum peak to valley roughness height (e_{p-v}) in a given sampling area [21]. Eight neighboring points were used to identify the true valleys of the scallops from other roughness features [25]. In sampling areas with less than five peaks or valleys due to late initiation, only the total number of valleys and peaks found in these areas is used. The scallop size was characterized by the integral length scales from the normalized two-dimensional autocorrelation function. The height and length scales were normalized by the near-wall (inner) length scale

$$\frac{\nu}{u_\tau} = \frac{D}{Re} * \sqrt{\frac{8}{f_D}} \tag{3.2}$$

where f_D is the Darcy friction factor. The Darcy friction factor is obtained from the Colebrook equation [26]:

$$\frac{1}{\sqrt{f_D}} = -2.0 \log_{10}\left(\frac{e_s/D}{3.7}\right) + \frac{2.51}{Re\sqrt{f_D}} \tag{3.3}$$

where e_s is the equivalent sand-grain roughness height defined by Nikuradse [27]. Here, the equivalent sand-grain roughness is evaluated as three times RMS roughness height [28, 29].

3.3 Results and Discussion

The physical change in the surface roughness with modified time from the CT scan images for one half of the pipe are shown in Fig. 3.2. Scallop-shaped pits or depressions are clearly seen to develop on the surfaces with time, consistent with other studies [5-8]. Initially, the scallops are sparse and non-uniformly distributed, and then grow in physical size and spatial density (number of scallops per unit area) with time. The Reynolds number is seen to have a significant effect in the roughness development. The surface roughness at higher Reynolds number develops more rapidly and is longer on the surface at lower Reynolds number. The density of scallops increases with time and varies distinctly with Reynolds number, with a higher density for high Reynolds numbers, consistent with Villien et al. [15].

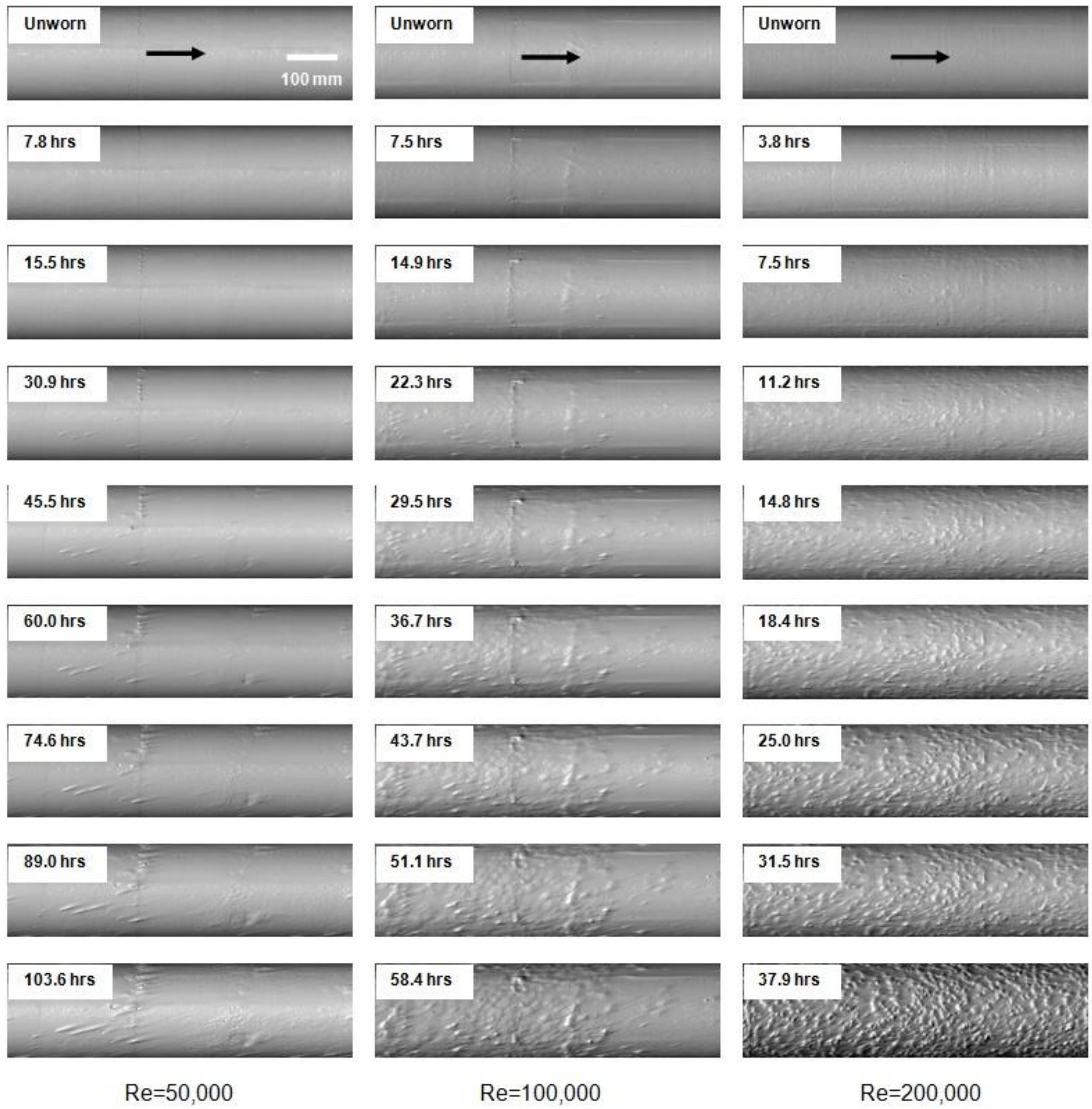

Fig. 3.2: Images showing the roughness development on the inner surfaces (0~180 °) with modified time for Reynolds number of 50,000, 100,000 and 200,000

A wavelet analysis was used to separate the surface topography into waviness, roughness and noise based on length scales. A total of 6 levels of wavelet decomposition for the surfaces were performed and three regrouped-levels representing the three main surface features were estimated: noise (level 2 and below), roughness (level 2 - 6), waviness and form (level 6 and above). The original surface and the three components for the surface at Re=200,000 at the last time are shown in Fig. 3.3. The results show that the wavelet analysis can separate surface roughness, shown in Fig. 3.3(c), from other surface details. Contours of the surface roughness from the wavelet decomposition for all the surfaces are shown in Fig. 3.4. The positive values represent roughness peaks or protrusions, and the negative values represent the roughness valleys or depressions. The results show long linear features at the initial times that reflect the seams that occur during the casting process. The compact blue features represent the scallops. The scallops are distributed more densely and uniformly and appear to saturate the surface at the latter times for the flow Reynolds number of 200,000. The surface roughness develops non-uniformly, particularly for the lower Reynolds numbers where the scallops are not initiated at the same time and vary in size.

The change of the roughness height (e_{rms} and e_{p-v}) within the local sampling areas with the modified time for *Re* = 200,000 as a representative case is shown in Fig. 3.5. Due to entrance and exit effects, only the axial distance (z) from 0.5 to 4 diameters of the entire test sections was used to characterize the surface roughness. Each line in the figure represents the variation within that local sampling area. Both e_{rms} and e_{p-v} grow

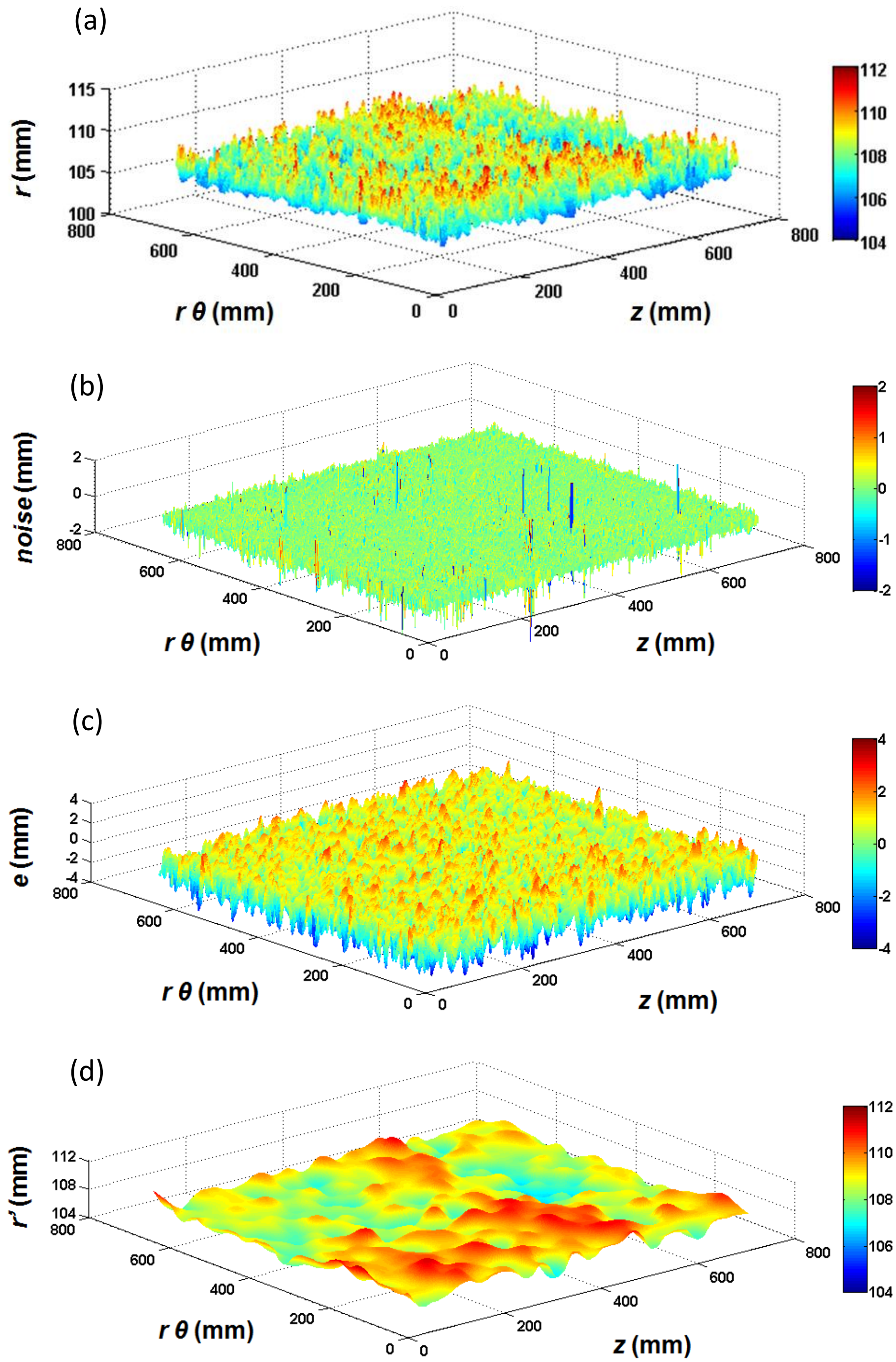

Fig. 3.3: Illustration of three regrouped-level wavelet decomposition of surface for Re = 200,000 at 37.9 hours: (a) Original surface (b) noise/uncertainty level (level 2 and below) (c) surface roughness level (level 2 - 6) (d) surface waviness + form level (level 6 and above)

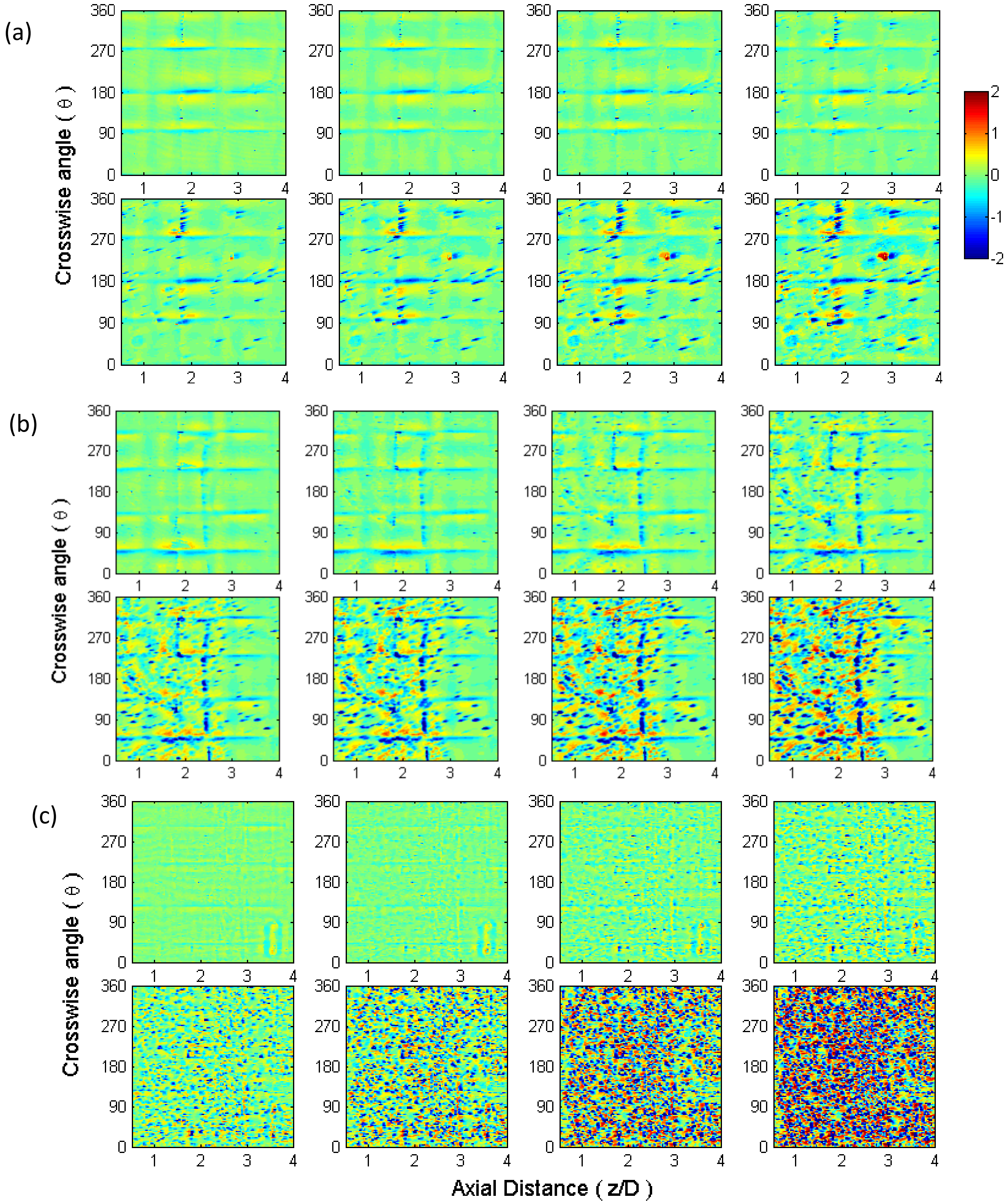

Fig. 3.4: Contours showing surface roughness height (mm) with modified time (same as Fig. 2) at (a) *Re* = 50,000 (b) *Re* = 100,000 (c) *Re* = 200,000

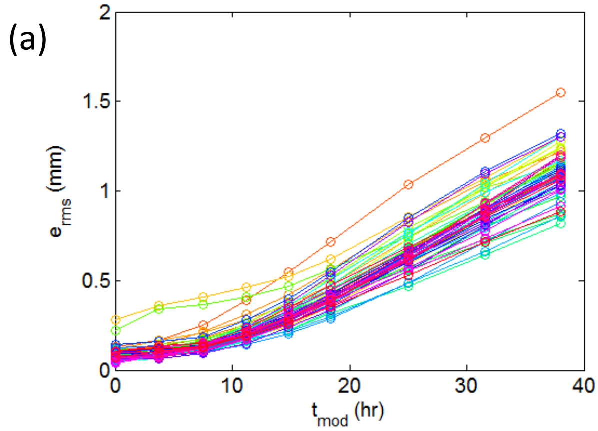

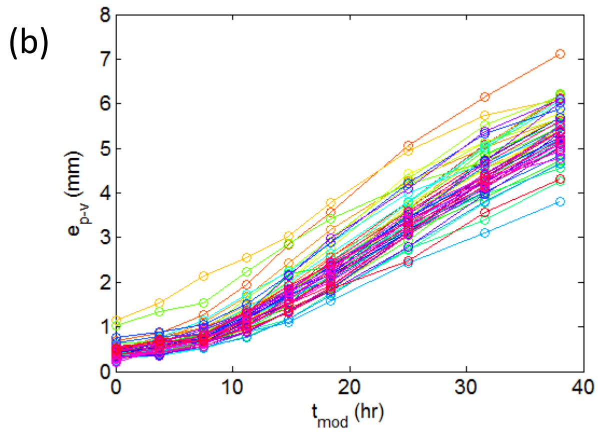

Fig. 3.5: Change in (a) RMS and (b) peak to valley roughness height as a function of modified time in the different local sampling areas for Re = 200,000

with time, with larger growth rates at later times. The e_{p-v} is approximately five times larger than e_{rms} towards the end of the modified time. The change in e_{p-v} with time is similar for the different local sampling areas, but with a time shift, reflecting the different initiation times of the scallops within each local sampling area. The modified time was shifted by the initiation time to establish a common time datum relative to initiation. Thus, the time (t) from scallop initiation, which is used here, is computed as,

$$t = t_{mod} - \Delta t \tag{3.4}$$

The time shift (Δt) for the initiation was estimated from the intercept on the time axis by a best fit to the growth of the peak to valley roughness height. The change in e_{rms} and e_{p-v} as a function of the time relative to the initiation time is shown in Fig.3.6 (a-b). There is a clear Reynolds number dependence, with an increasing growth rate with increasing Reynolds number. The roughness heights, normalized by the near-wall (inner) length scale (ν/u_τ) with the adjusted time normalized by the inner time scale $(\nu/{u_\tau}^2)$

$$t^+ = \frac{t}{\nu/{u_\tau}^2} \tag{3.5}$$

and the mixed time scale of inner and outer time scales (D/U) [30]

$$t/t_m = \frac{t}{\sqrt{\nu/{u_\tau}^2 * (D/U)}} \tag{3.6}$$

are shown in Fig. 3.6 (c-f). The profiles of e_{rms}^+ and e_{p-v}^+ for the different Reynolds numbers collapse when compared in terms of the inner time scale (Fig. 3.6 c-d), but not the mixed time scale, indicating the development of the roughness height of the scallops is strongly related with the near-wall turbulent flow. There appears to be two regions of growth, particularly in the peak to valley height: (i) a slower growth rate up to $t^+ \approx 2 \times 10^8$

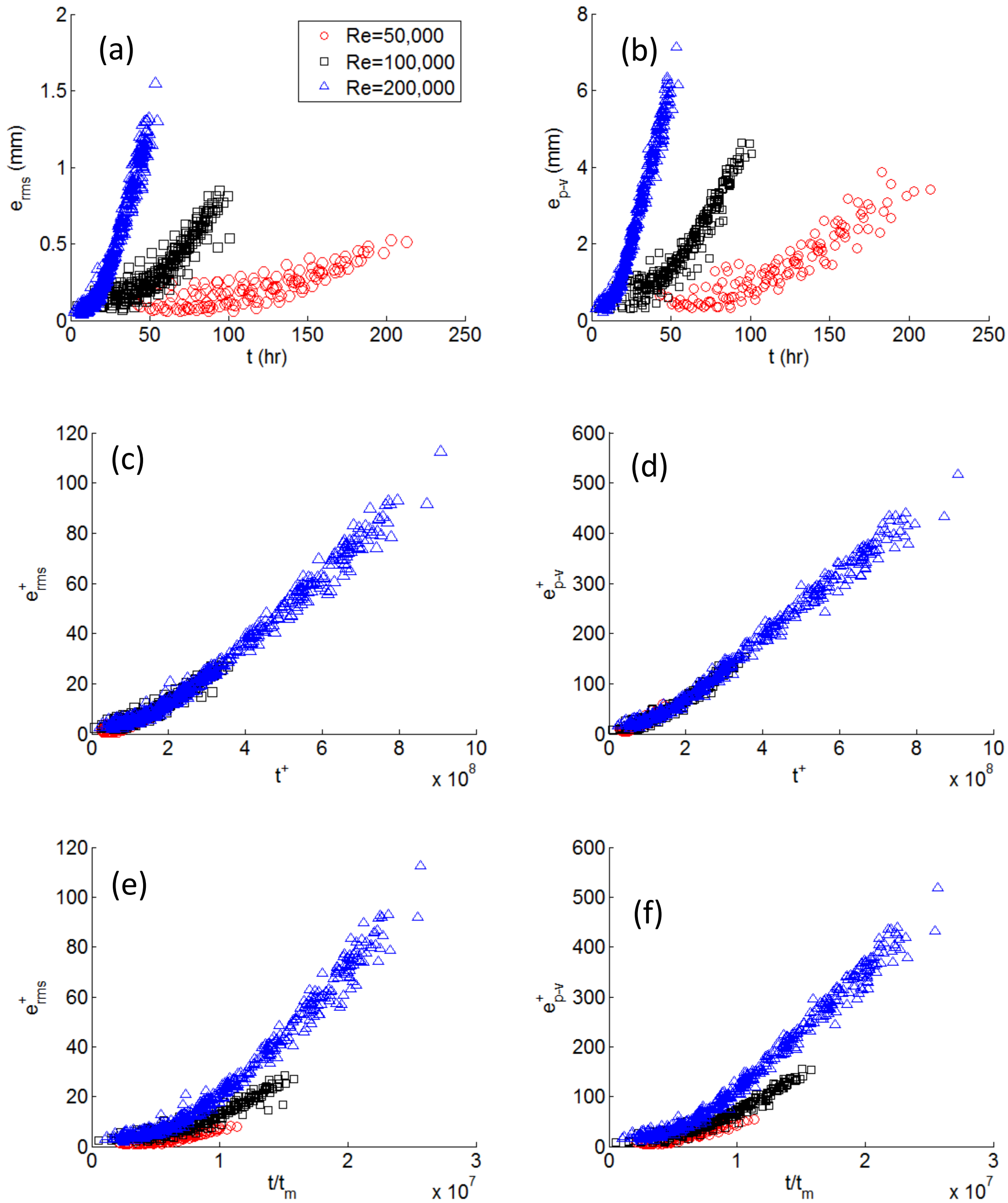

Fig. 3.6: Variation of (a) RMS and (b) P-V roughness height with time, (c) and (d) Normalized roughness height with time normalized by inner scale and (e) and (f) with time normalized by mixed time for Reynolds number of 50,000, 100,000 and 200,000

and (ii) a higher growth rate at $t^+ \geq 2\times10^8$. Both the slower and higher growth rates are approximately constant. The higher growth rate continues for the time period considered here, even up to e^+_{p-v} of approximately 500 at the highest Reynolds number at the last time of the current experiment.

The three-dimensional profiles showing the growth of a typical scallop with time at *Re*=200,000 is shown in Fig. 3.7(a). The corresponding two-dimensional contour plot showing the deviation and 2-D autocorrelation function are shown in Fig. 3.7(b) and 3.7(c). The normalized autocorrelation functions along the direction of maximum autocorrelation length were used to obtain the integral length scales. At short times, the autocorrelation function is affected by other surface features. At longer times, once the scallops become the dominant feature, the autocorrelation function is similar to the scallop growth. The integral length scale (L) of the scallops was determined here by fitting a Gaussian curve to the initial decay of the autocorrelation function. The integral length scales were obtained by integrating the Gaussian function as $\sqrt{\pi/4a}$, where a is the constant coefficient of the Gaussian function. A similar approach was applied to the autocorrelation function normal to this direction to determine the width (W). The directionality of the scallops is determined by calculating the angle between the maximum autocorrelation length and streamwise direction. It is found to be relatively consistent for the three Reynolds numbers, at approximately 10 degree to the streamwise direction. The integral length and width scales of the typical scallop are illustrated in the 2-D scallop region using the ellipses shown in Fig. 3.7(b), which are seen to be smaller

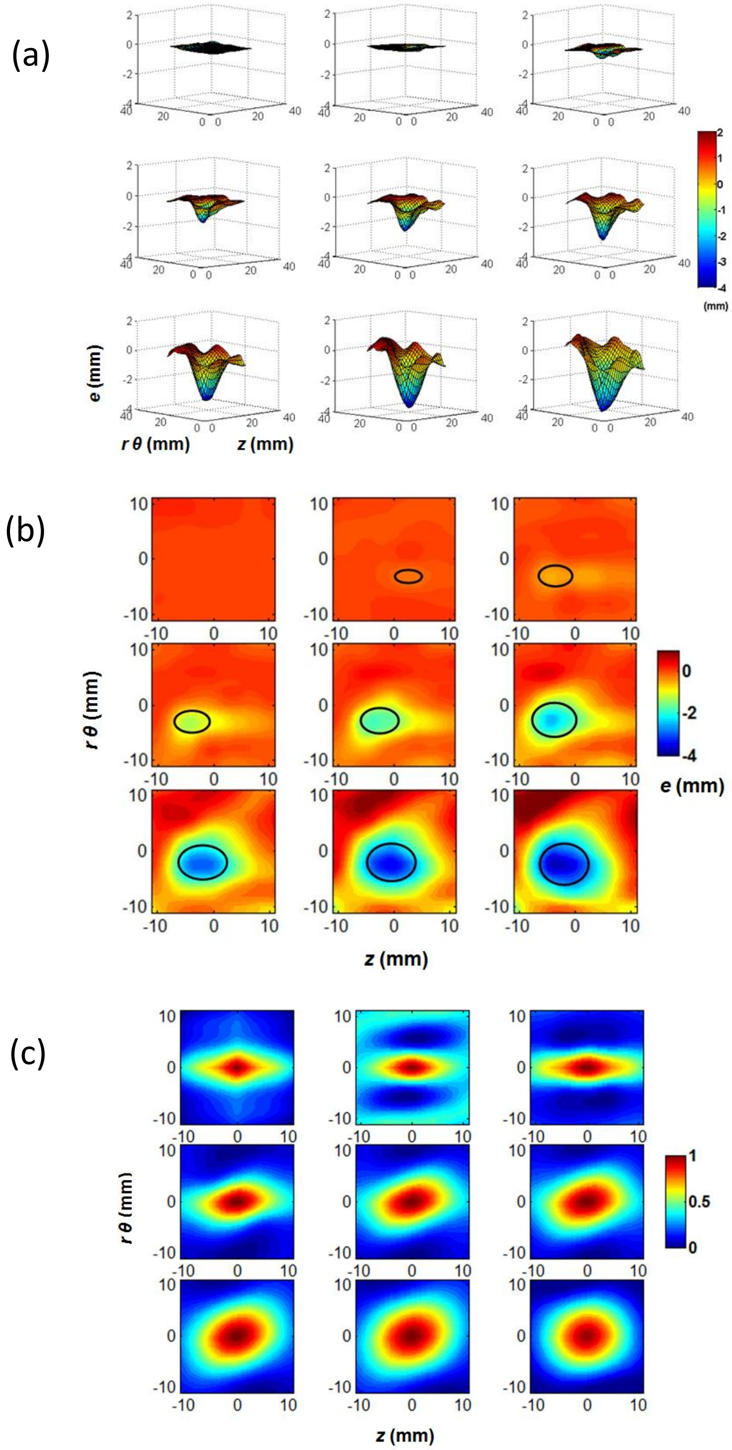

Fig. 3.7: (a) 3-D development of one typical scallop (b) 2-D contour plot in the scallop region (c) Normalized 2-D autocorrelation function applied in this scallop region as a function of time at *Re* = 200,000

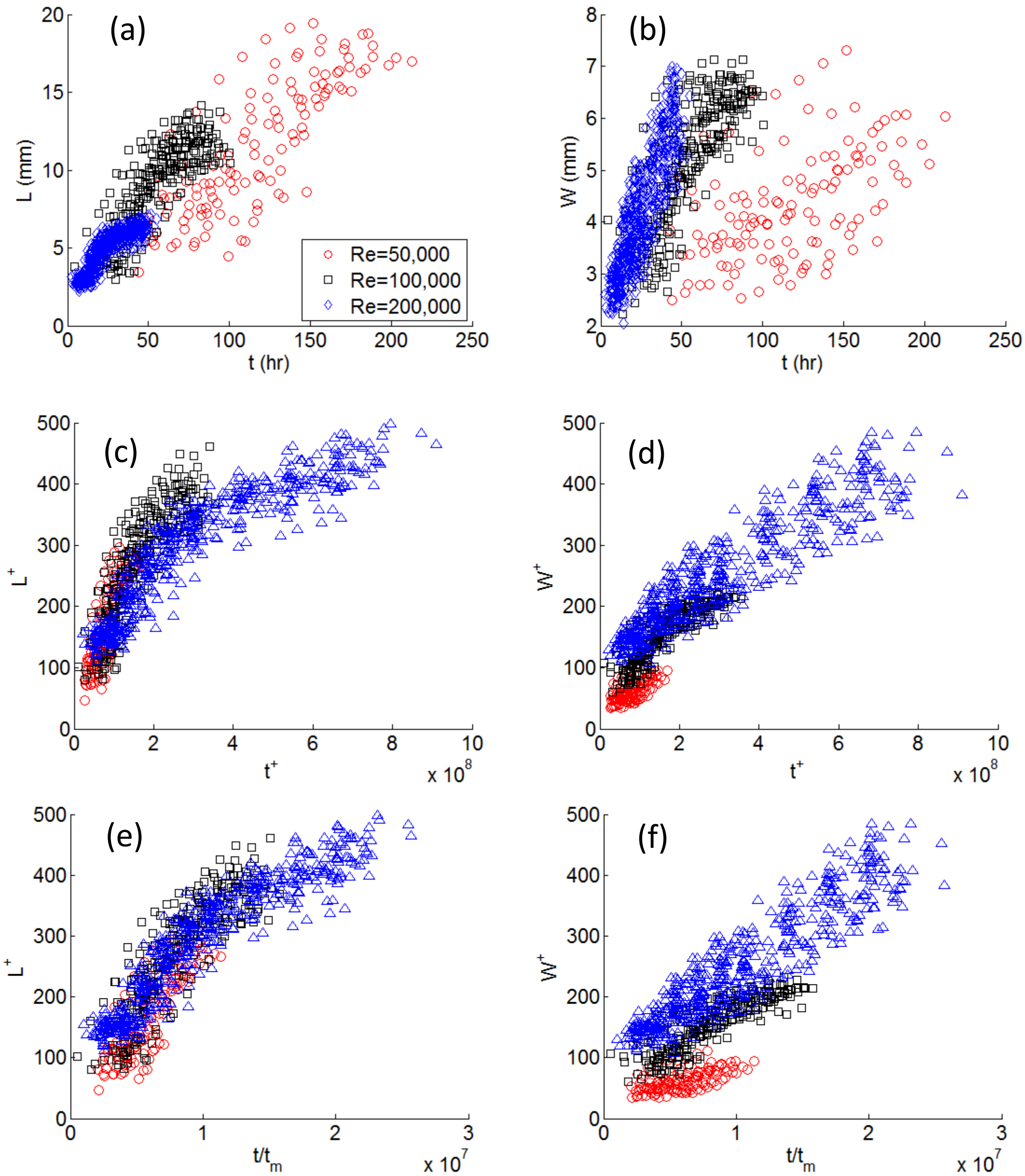

Fig. 3.8: Variation of (a) integral length and (b) width as a function of time, (c) normalized integral length and (d) width as a function of time normalized by inner time and (e) normalized integral length and (f) width as a function of time normalized by mixed time for Reynolds number of 50,000, 100,000 and 200,000

than the actual size. The time evolution of the integral length and width of the scallops obtained from the autocorrelation analysis in each sampling area are shown in Fig. 3.8. The growth of the length scale is opposite to that of the roughness height, initially increasing rapidly before growing more slowly. This change is less apparent for the width, where the change in the growth rate is smaller. There is a better collapse of L^+ with the mixed time scale than the inner time scale, indicating that the outer flow plays a role in the spatial growth of the scallops. The transition between the two growth rates occurs at $t^+ \approx 2 \times 10^8$, and similar to that observed for the roughness height.

The number of scallops is determined by summing the valleys found using the algorithm to compute the peak to valley height of scallops. Only those with a minimum neighboring area of 4×4 mm^2 and minimum height of 10 wall units were counted. The density of scallops, defined as the number of valleys in a unit sampling area, increases with time, with the increase much higher at the higher Reynolds numbers as shown in Fig. 3.9 (a). The density is seen to saturate for the Reynolds number of 200,000 at longer times. The two-dimensional spacing of the scallops is related to the inverse of the density and likely related to the aspect ratio (AR = L/W) of the scallops, particularly as it saturates. Thus, the streamwise spacing of the scallops can be estimated as

$$\lambda_{str}^{+} = \sqrt{AR/{D_s}^{+}} \tag{3.7}$$

where ${D_s}^{+} = D_s * (\nu/u_\tau)^2$. The variation of the normalized streamwise spacing with time normalized by the inner and mixed scales is shown in Fig. 4.9 (b-c). There is a collapses of λ_{str}^{+} for the three Reynolds numbers when plotted against t^+. The streamwise

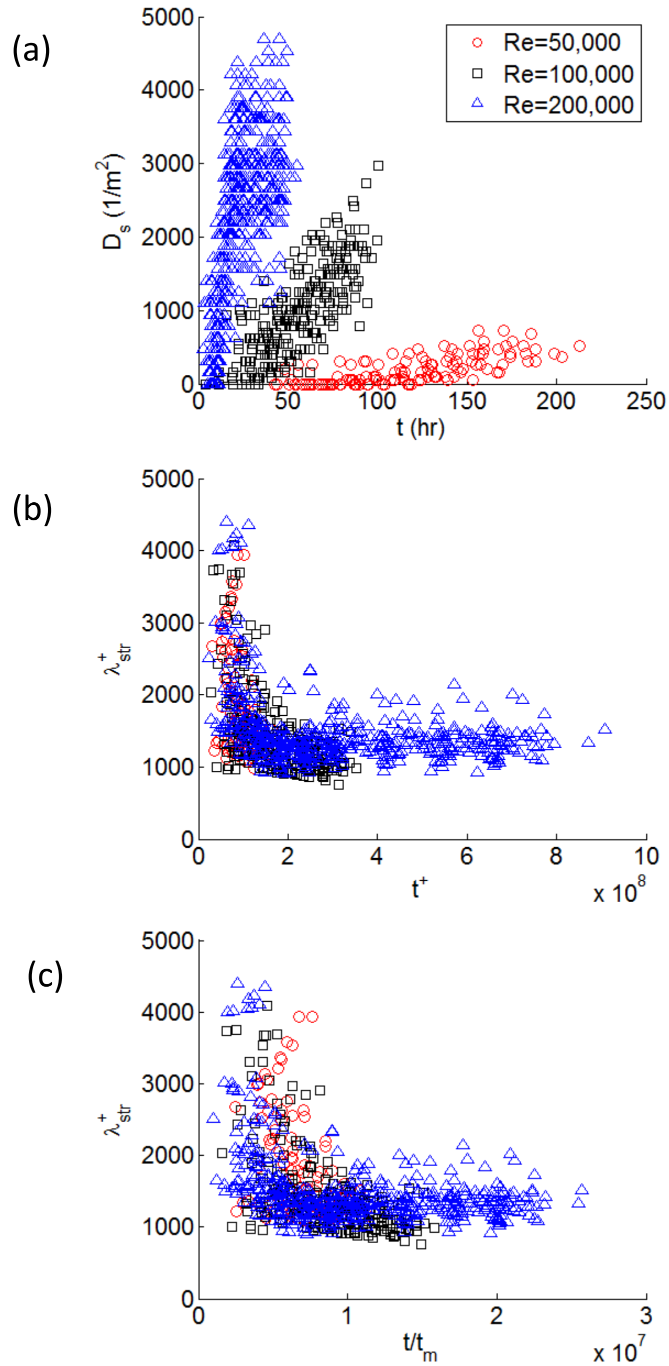

Fig. 3.9: (a) Variation of density of scallops as a function of modified time and normalized streamwise spacing as a function of time normalized by (b) inner time and (c) mixed time for the three Reynolds numbers

spacing decreases rapidly initially and then approaches a nearly constant value of approximately 1000 after $t^{+}\approx 2\times 10^{8}$. This value agrees well with the average streamwise spacing proposed by Thomas [8]. In this case, the streamwise spacing is approximately two times the integral length scale.

A scatter plot of e_{p-v}^{+} with L^{+} and W^{+} is shown in Fig. 3.10, along with the projections on the L^{+}-e_{p-v}^{+} and L^{+}- W^{+} planes. Initially, the length and width grows faster than the roughness height, and then the growth rate reduces as the scallops saturate the surface. The ratio of length to height decreases from about 10 in the early growth period to approximately 1 at the end of the run time for the highest Reynolds number. The ratio of length to width decreases with an increase in Reynolds number. Initially, the length to width ratio is greater than one, and then reduces with time. This is particularly apparent at the highest Reynolds number, where the ratio is again approximately 1 at the end of the run time.

The increase in the height of the roughness is expected to be related to the local wear or mass dissolution. The local wear of the surface due to dissolution in each time period was calculated as the reduction in thickness of the gypsum lining in that period. The cumulative wear (δ) with time was calculated as the summation of the incremental wear within each time period. The change in the non-dimensionalized roughness with t^{+} is shown in Fig. 3.11(a), and the roughness as a function of the local wear in Fig. 3.11(b).

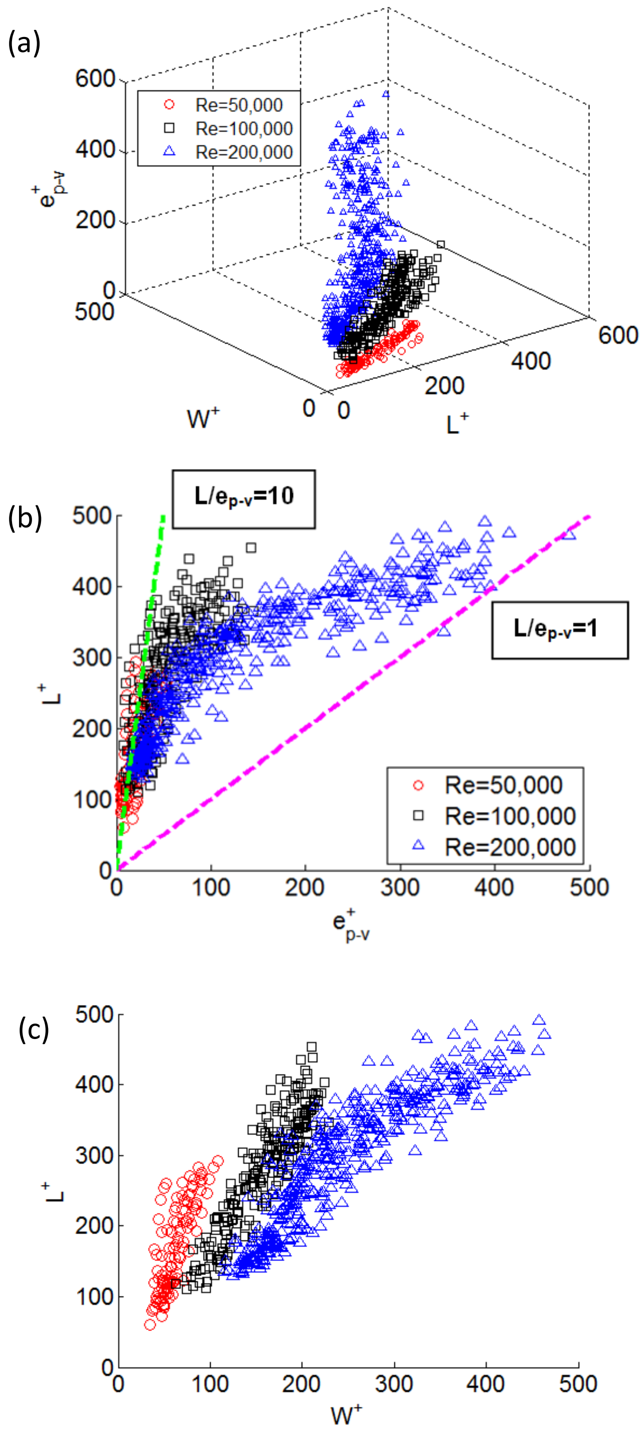

Fig. 3.10: (a) 3-D scatter plot of roughness height with dimensionless integral length and width scales, (b) 2-D plot between length and peak to valley height (c) 2-D plot between integral length and width of scallops

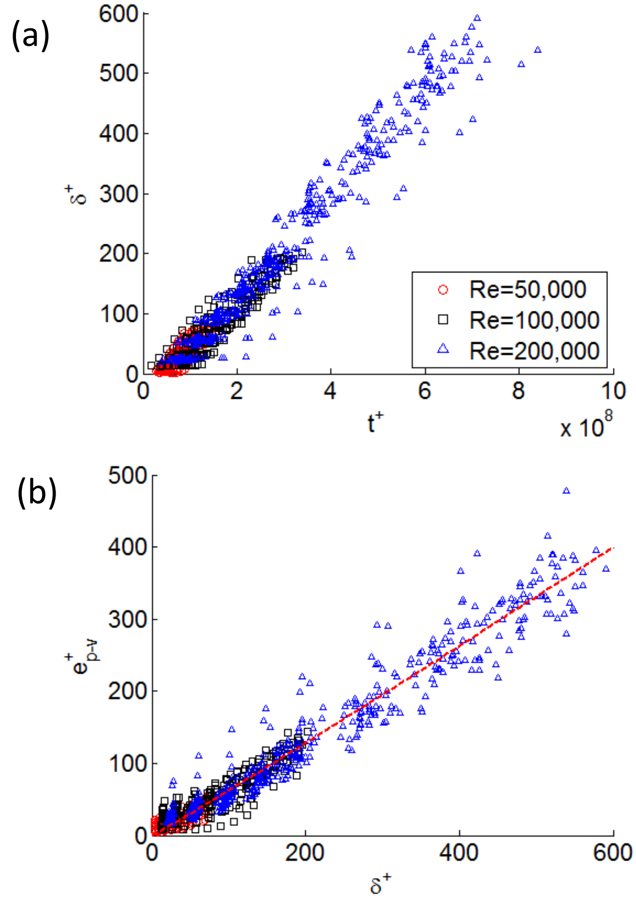

Fig. 3.11: (a) Variation of normalized wear as a function of time normalized by inner scale and (b) Normalized peak to valley roughness height as a function of normalized wear for the three Reynolds numbers

There is a strong relationship between e_{p-v}^{+} and δ^{+}, with a good collapse for the times and Reynolds numbers considered here. A best-fit power function to the data is obtained as

$$e_{p-v}^{+} = 0.54 * \delta^{+1.03} \tag{3.8}$$

3.4 Summary and Conclusions

Experiments were performed to characterize the time evolution of surface roughness on a soluble wall at Reynolds numbers of 50,000, 100,000 and 200,000. The experiments were performed in a closed flow loop using 203 mm diameter pipe test sections that had a dissolving gypsum lining with water as the working fluid. The surface topography was measured periodically using non-destructive X-ray CT scans. The surface roughness develops in the form of scallops, with the density of scallops increasing with time and eventually saturating the surface. The surface roughness was characterized by the rms and peak to valley height, integral length and width scales, aspect ratio and density of scallops. The scallops initiate locally at different times, and an initiation time is introduced within local areas of the surface to provide a common datum to characterize the temporal development of the different roughness parameters. The roughness height was found to collapse well with time when normalized by the turbulent inner scales, indicating that the near-wall turbulence plays a significant role in the roughness development. The roughness height grows at a relatively lower rate initially, and then increases beyond t^{+} of 2×10^{8} at a nearly linear rate. A mixed time scale that combines both the inner and outer scales collapsed the streamwise length scale better, indicating that the outer flow may play a role in the spatial growth of the scallops. The length scale shows a different behavior to the roughness height, with an initial rapid growth period followed by a much slower growth. The ratio of integral length to height decreases with time from large values above 10 at the beginning and reduces to approximately 1 at longer times. The ratio of length to width of the scallops decreases with an increase in Reynolds number. The normalized streamwise spacing estimated from the density is approximately twice the integral length of the scallops and approaches 1000 at longer times, which agrees well with Thomas [8]. There is a strong correlation between the normalized roughness height and wear, with a nearly linear dependence.

Nomenclature

AR	Aspect ratio
C_w	Gypsum concentration at the wall [g/l]
C_b	Gypsum concentration in the bulk flow [g/l]
C_{b0}	Initial gypsum concentration in the bulk flow [g/l]
D	Inner diameter of test section [mm]
D_s	Density of scallops [/m^2]
e	Roughness height [mm]
e_s	Equivalent sand-grain roughness height [m]
$e_{p\text{-}v}$	Peak to valley roughness height [mm]
e_{rms}	RMS roughness height [mm]
f_D	Darcy friction factor
L	Length of roughness element [mm]
Re	Reynolds number
r	Local radius of test section [mm]
r'	Local radius of test section after wavelet [mm]
t	Time from roughness initiation [s]
t_{exp}	Experimental time [s]
t_m	Mixed time scale [s]

t_{mod}	Modified time scale [s]
t^+	Dimensionless time normalized by inner time scale
U	Mean velocity [m/s]
u_τ	Friction velocity [m/s]
W	Width of roughness element [mm]
z	Streamwise distance [mm]

Greek Symbols

δ	Local wear on pipe inner surface [mm]
θ	Crosswise angle in the azimuthal direction [°]
λ_{str}	Streamwise spacing of roughness element [mm]
ν	Kinematic viscosity [m^2/s]
ρ	Gypsum density [kg/m^3]

Subscripts

+	Length scale normalized by wall unit (ν/u_τ)

3.5 References

[1] Dawson, A., Trass, O. 1972. Mass transfer at rough surfaces. *Int. J. Heat Mass Transfer*. 15: 1317-1336.

[2] Lolja, S. A. 2005. Momentum and mass transfer on sandpaper-roughened surfaces in pipe flow. *Int. J. Heat Mass Transfer*. 48: 2209-2218.

[3] Berger, F.P., Hau, K.F.F.L. 1979. Local mass/heat transfer distribution on surfaces roughened with small square ribs. *Int. J. Heat Mass Transfer*. 22: 1645-1656

[4] Postlethwaite, J., Lotz, U. 1988. Mass transfer at erosion-corrosion roughened surfaces. *The Canadian Journal of Chemical Engineering*. 66: 75-78.

[5] Allen, J.R.L. 1971. Bed forms due to mass transfer in turbulent flows: a kaleidoscope of phenomena. *J. Fluid Mechanics*. 49(1): 49-63.

[6] Blumberg, P. N., Curl R. L. 1974. Experimental and theoretical studies of dissolution roughness. *J. Fluid Mechanics*. 65(4): 735-751.

[7] Goodchild, M.F. & Ford, D.C. 1971. Analysis of scallop patterns by simulation under controlled conditions. *Journal of geology*. 79: 52-62.

[8] Thomas, R. M. 1979. Size of scallops and ripples formed by flowing water. *Nature*. 277(25): 281-283.

[9] Burrill, K. A., Cheluget, E. L. 1998. Corrosion of CANDU Outlet Feeder Pipes. *Japan Atomic Industrial Forum on Water Chemistry in Nuclear Power Plants.* 1998 Sept. 7-11.

[10] Dooley, R.B., 2008. Flow accelerated corrosion in fossil and combined cycle/HRSG plants. *PPCHEM*, 68-89.

[11] Achenbach, E. 1976. Mass transfer from bends of circular cross section to air. *Future Engy Production System*. Academic Press. New York, 1: 327-337.

[12] Sparrow, EM. Chrysler, GM. 1986. Turbulent flow and heat transfer in bends of circul cross section: i- heat transfer experiments. *ASME Journal of Heat Transfer*. 108: 40-47.

[13] Wilkin, SJ., Oates, HS., Coney, M. 1983. Mass transfer on straight pipes and 90° bends measured by the dissolution of plaster (1st Edition). *Central Electricity Research Laboratories Report*. TPRD/L/2469/N83.

[14] Mazhar, H., Ewing, D., Cotton, J.S. Ching C.Y. 2013. Experimental investigation of mass transfer in 90° pipe bends using a dissolvable wall technique. *Int. J. Heat Mass Transfer*. 65: 280-288.

[15] Villien, B., Zheng, Y., Lister, D. 2005. Surface Dissolution and the Development of Scallops. *Chem. Eng. Comm*. 192: 125–136.

[16] Wang, D., Huang, Y., Ewing, D., Chow, T., Cotton, J., Noseworthy, M.D., Ching, C.Y., 2015. On the non-destructive measurement of local mass transfer using X-ray computed tomography. *Int. J. Heat Mass Transfer*. 81: 531-541.

[17] Wang D., Le T., Ewing D., Ching C.Y. 2016. Measurement of local mass transfer and the resulting roughness in a large diameter S-bend at high Reynolds number. ASME. *J. Heat Transfer*. 138(6): 062001-7.

[18] Raja, J., Muralikrishnan, B., Fu, S. 2002. Recent advances in separation of roughness, waviness and form. *Precision Engineering*. 26: 222–235.

[19] Chen, X., Raja, J., Simanapalli, S. 1995. Multi-scale analysis of engineering surfaces. *Int. J. Mach. Tools Manufact*. 35(2): 231-238.

[20] Josso, B., Burton, D. R., Lalor, M. J. 2002. Frequency normalised wavelet transform for surface roughness analysis and characterisation. *Wear*. 252: 491–500.

[21] Stout, K. J. et al. 2002. Development of Methods for Characterisation of Roughness in Three Dimensions. Commission of the European Communities.

[22] Thomas, T. R. 1981. Characterization of surface roughness. *Precision engineering*. 3(2): 97-104.

[23] Sobel, I. 1990. An Isotropic 3×3 Gradient Operator. Machine vision for three dimensional scenes, Freeman, H., Academic Pres, NY, 376-379.

[24] Daubechies, I. 1988. Orthonormal Bases of Compactly Supported Wavelets. *Communications on pure and applied mathematics*. 41: 909-996.

[25] Peuker, K., Douglas D. 1975. Detection of surface specific points by local parallel processing of discrete terrain elevation data. *Computer graphics and Image processing*. 4: 375-387.

[26] Colebrook, C. F., White C.M. 1937. Experiments with Fluid friction roughened pipes. *Proc. R. Soc .(A)*. 161.

[27] Nikuradse, J. 1933. Laws of the flow in rough pipes. VDI Forschungsheft. 361. Also NACA TM 1292, 1950.

[28] Zagarola, M.V., Smits, A. J. 1998. Mean-flow scaling of turbulent pipe flow. *J. Fluid Mech.* 373: 33-79.

[29] Shockling, M. A., Allen, J. J., Smits, A.J. 2006. Roughness effects in the turbulent pipe flow. *J. Fluid Mech*. 564: 267-285.

[30] Alfredsson, P. H. & Johansson A. V. 1984. Time scales for turbulent channel flows. *Phys Fluids*. 27(8): 1974-1981.

Chapter 4

The effect of naturally developing roughness on the mass transfer in pipes under different Reynolds numbers

Complete citation:

Wang D., Ewing D., Ching C.Y. 2016. The effect of naturally developing roughness on the mass transfer in pipes under different Reynolds numbers. *In. J. Heat Mass Transfer.* Submitted August 2016.

Relative Contributions:

Wang D.: Performed all experiments, interpretation and analysis of the data and wrote the first draft of the manuscript including all figures and text.

Ewing D.: Assisted in the interpretation and discussion of results.

Ching C. Y.: Supervisor and was responsible for the final draft submittal to the journal.

Abstract

The local mass transfer over dissolving surfaces was measured at pipe Reynolds number of 50,000, 100,000 and 200,000. Tests were run at multiple time periods for each Reynolds number using 203 mm diameter test sections that had gypsum linings dissolving to water in a closed flow loop at a Schmidt number of 1200. The local mass transfer was calculated from the decrease in thickness of the gypsum lining that was measured using X-ray computed tomography (CT) scans. The range of Sherwood numbers for the developing roughness was in good agreement with previous studies. The mass transfer enhancement (Sh/Sh_s) was dependent on both the height and spacing of the roughness scallops. For the developing roughness, two periods of mass transfer were present: (i) an initial period of rapid increase in enhancement when the density of scallops increase till the surface is spatially saturated with the scallops and (ii) a slower period of increase in enhancement beyond this point, where the streamwise spacing is approximately constant and the roughness height grows more rapidly. The mass transfer enhancement was found to correlate well with the parameter $(e_{p-v}/\lambda_{str})^{0.2}$, with a weak dependence on Reynolds number.

4.1 Introduction

Mass transfer due to flow accelerated corrosion results in wall thinning and degradation in piping systems of power generation plants [1-3]. The mass transfer rate, typically at high Schmidt number, in pipes can be affected by a number of factors including the surface roughness. The effect of surface roughness on mass transfer has been characterized using predefined roughness, typically using electrochemical methods [4-9] and dissolving surfaces where roughness forms and develops as the mass transfer occurs [10-15]. Several types of predefined roughness, including V-shaped grooves [4-6], erosion-corrosion roughness [7], sandpaper-rougheness [8] and square rib roughness [9] have been investigated. Dawson and Trass [4] found three roughness regimes for mass transfer over surfaces with V-grooves: (i) smooth for $e^+(= eu_\tau/v)$ < 3, (ii) transition for 3 < e^+ < 25 and (iii) fully rough for e^+ > 25. The maximum mass transfer enhancement was three to four times that in a smooth pipe, and the enhancement relative to the smooth case decreased in the fully rough region. A similar result was found for surfaces with different pitch to height ratios [5, 6]. The mass transfer also decreased with an increase in surface roughness for e^+ > 30 for an erosion-corrosion roughened surface [7], but for $e^+ = 1\sim10$ with sandpaper-roughened roughness [8], indicating each specific type of roughness has its own effect on mass transfer. Local mass transfer with small square-ribs was observed to be less non-uniformly distributed at higher Reynolds numbers and had a different character for different pitch to height ratios [9]. Correlations for the mass transfer rate from rough surfaces have been proposed, both with and without an explicit dependence on the roughness and are given in Table 4.1 [4, 7, 9, 10, 12].

The surface roughness for soluble walls develops with the mass transfer to the bulk flow, which can subsequently affect the mass transfer and vice versa. When the roughness is fully developed, it often takes on a scalloped roughness pattern [16-18]. Thomas [19] proposed that the roughness or scallop spacing would scale with the near-wall turbulence, with a characteristic length scale of approximately 1000 wall units (v/u_τ) for both granular beds and industrial pipes. Measurements of the initial development of the roughness on soluble surfaces showed that both the number and depth of the scallops can vary with time and location [13-16], with higher mass transfer in the

Table 4.1: Correlations for mass transfer over smooth and rough surfaces

Authors	Surface	Reynold number	Correlation
Dawson & Trass [4]	Smooth duct	3,000 ~ 120,000	$Sh_s = 0.0153Re^{0.88}Sc^{0.32}$
	V-grooved duct	3,000 ~ 120,000	$Sh_R/Sh_S = 1.94Sc^{0.09}\epsilon^{+-0.10}$ $(25 < \epsilon^+ < 120)$
Berger & Hau [9]	Smooth pipe	8,000 ~ 200,000	$Sh_s = 0.0165Re^{0.86}Sc^{0.33}$
	Square rib roughened pipe	10,000 ~ 250,000	$Sh_R = 0.281Re^{0.695}Sc^{0.33}$
Postlewaite & Lotz [7]	Smooth Pipe	41,000 ~ 330,000	$Sh_s = 0.0089Re^{0.89}Sc^{0.33}$
	Erosion-corrosion roughened pipes	41,000 ~ 330,000	$Sh_R/Sh_S = 1.64Sc^{0.1}\epsilon^{+-0.14}$ $(\epsilon^+ > 30)$ $Sh_R = 0.0068Re^{0.96}Sc^{0.33}$
Coney [10]	Natural roughness in pipes	Not given	$Sh_R = 0.005ReSc^{0.33}$
Poulson [12]	Analysis of existing experimental results	Not given	$Sh_R = 0.01ReSc^{0.33}$ (upper limit)

regions of larger surface roughness. Differences in the spacing to height ratio of the scallops have also been observed in more complex geometries [15].

Wang et al. [20] recently investigated the development of the roughness scallops with time in pipe flow. They found that the development of the roughness in different Reynolds number pipe flows could be characterized in terms of the non-dimensional time from the local initiation of the scallops. The development of the roughness appeared to occur in two periods: in the first period the length scale of the roughness grew in approximate proportion to the depth until the surface was saturated with the scallops. The number of scallops increased rapidly while the nominal distance between them decreased. In the second period, once the surface was saturated with scallops, the number of scallops did not change and the length grew much more slowly while the depth grew more rapidly. As a result the length to depth ratio of scallops decreased dramatically from 10 to 1. The spacing in this case for developed roughness was approximately 1000 wall units, which agreed with Thomas [19].

The objective of this investigation is to characterize the mass transfer in these two periods and to study how the roughness development observed in Wang et al. [20] affects the mass transfer. The experiments were performed using 203mm diameter straight pipes that had a gypsum lining dissolving to water. Tests were performed over multiple times, and the difference in the thickness of the gypsum lining between each trial in Wang et al. [20] is used to compute the mass transfer. The development of the mass transfer is then correlated to the roughness and compared to previous mass/heat transfer studies.

4.2 Experimental Methodology

The experiments were performed in a flow loop shown schematically in Fig .4.1. The flow passes through a 203mm diameter (*D*) riser with a length of 7.3 m (36*D*) before entering a 4.5*D* straight pipe test section. The flow exits the test section to a 1.4 m (7*D*) pipe leading back to a 1.5 m^3 reservoir. The water temperature was measured at three locations along the loop and maintained at 25±0.5 ℃ using a cooling coil in the reservoir. The electrical conductivity of water was measured by a conductivity probe and recorded. The experiments were performed using three 203 mm inner diameter straight test sections that had 14 mm, 14 mm, and 22 mm thick gypsum linings, with a density of 1580 kg/m^3. The experiments were performed by flowing water through the test sections at Reynolds numbers of 50,000 100,000 and 200,000 within an uncertainty of ±1%. The experiments were performed in a series of eight consecutive trials to capture the time evolution of surface roughness and mass transfer for each Reynolds number. In each case, the test sections were exposed to the flowing water for a set period of time and then the surface was measured. Each test section was then put back into the facility and the process repeated. Details of the test facility and methodology can be found in [20].

The surfaces of the test sections were measured using X-ray CT scans for the unworn initial surface and worn surfaces after each test. A Sobel edge detection [21] method was used to analyze the two-dimensional CT scans, and then the cross sectional profiles were combined into a three-dimensional array of points corresponding to the inner and outer surfaces of the gypsum lining. The inner surfaces were computed on a

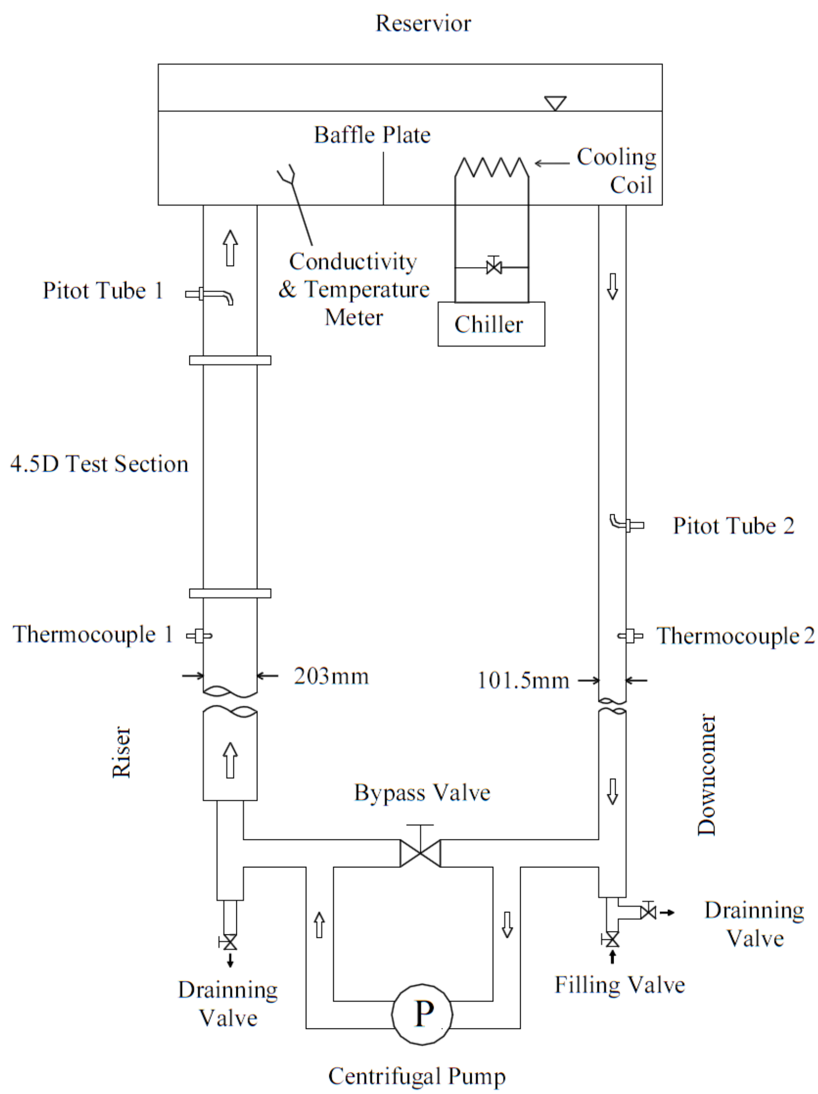

Fig. 4.1: Schematic of test facility

uniform distributed sampling interval of 1×1 mm^2 in axial and circumferential direction. The surfaces at different times were aligned by finding the maximum two-dimensional cross-correlation functions between the surfaces. A 2-D Discrete Wavelet Transform (DWT) was used to decompose the surface details into form variation, roughness, and noise based on different wavelengths using the Daubechies wavelet [22]. The surface roughness was then characterized in smaller sampling areas of 240×80, 160×80, 80×80 mm^2 for Reynolds number at 50,000, 100,000 and 200,000 as discussed in [20].

The mass transfer rates determined from the mass removed between two successive tests were considered here. The mass removed was initially computed based on the change of the inner radius following [23]. The results were compared to a curve fit of the data and it was found that there were large variations in the trial to trial results due to the uncertainty in the alignment of the axis and small distortion in the test sections. The effect of these errors, which were also present in [23], was amplified here due to the small mass removed between the trials, particularly during the initial periods. Thus, the mass transfer was calculated from the change in local thickness of the gypsum lining by subtracting the local inner radius from the local outer radius of the lining, after the wavelet analysis to remove the roughness and noise [20]. The mass transfer coefficient in each time period was computed as

$$h_m = \frac{\rho \Delta\delta}{(C_w - C_{b0})\Delta t} \tag{4.1}$$

where ρ is the density of the dissolvable material, $\Delta\delta$ is the thickness removed (wear) in each time period, Δt is the time of the trial modified to account for the change in flow bulk concentration [20], C_w is the wall concentration, and C_{b0} is the initial bulk concentration. The mass transfer coefficient can be expressed in terms of the Sherwood number ($Sh=h_mD/D_m$) as

$$Sh = \left(\frac{\rho}{C_w - C_{b0}} \frac{D}{D_m}\right) \frac{\Delta\delta}{\Delta t} \tag{4.2}$$

where D is the pipe diameter and D_m is the mass transfer diffusivity. The Sherwood number was then averaged over the same 240×80, 160×80, 80×80 mm^2 sampling areas for the three surfaces as done for the roughness characterization [20]. The uncertainty in the local Sherwood number for the spatially averaged results within each sampling area was approximately ±14% for the higher mass transfer rate and as much as ±30% for the lower rates where less mass is removed, particularly at lower Reynolds numbers.

The roughness parameters, such as roughness height and other length scales, were normalized by the near-wall length scale given by

$$\frac{\nu}{u_\tau} = \frac{D}{Re} * \sqrt{\frac{8}{f_D}} \tag{4.3}$$

where D is the pipe diameter, Re is the Reynolds number and f_D is the Darcy friction factor. The Darcy friction factor is given by the Colebrook equation [24]:

$$\frac{1}{\sqrt{f_D}} = -2.0 \log_{10}\left(\frac{e/D}{3.7}\right) + \frac{2.51}{Re\sqrt{f_D}} \tag{4.4}$$

where e is the equivalent sand-grain roughness height defined by Nikuradse [25]. Here, the equivalent roughness height is evaluated as three times RMS roughness height [26, 27]. The roughness parameters at the mid time between the tests, which were obtained by linear interpolation between the start and end times of the test, was used when correlating the mass transfer to the roughness parameters.

4.3 Results and Discussion

The local Sherwood number distributions over the surface in the different time periods are shown in the contour plots of Fig. 4.2 for the three Reynolds numbers. The local mass transfer was distributed non-uniformly. For the surface at Re = 100,000, two distinct regions of mass transfer were observed, with higher mass transfer in the upstream region. This is due to the different initiation of roughness, caused by a casting seam as found in [20]. The Sherwood number averaged within each sampling area is plotted as a function of the dimensionless peak to valley roughness height within that sampling area in Fig. 4.3. The averaged Sherwood number in each sampling area increases with the roughness height, with a higher Sherwood number at higher Reynolds number. The Sherwood number corresponding to the smooth pipe was difficult to determine from Fig. 4.3. Instead, it was determined by considering the change in Sherwood number with the ratio between roughness height and streamwise spacing (e_{p-v}/λ_{str}) as illustrated in Fig. 5.4. The mass transfer remained approximately constant when the height to spacing ratio was less than 0.01 and the Sherwood number averaged in this period was estimated as the nearly smooth Sherwood number. The resulting Sherwood numbers and the range of local Sherwood numbers are shown in Fig. 4.5. The results for the smooth surface obtained above are close to the correlation of Berger and Hau [26]. The highest Sherwood numbers measured at the three Reynolds numbers are higher than that from the

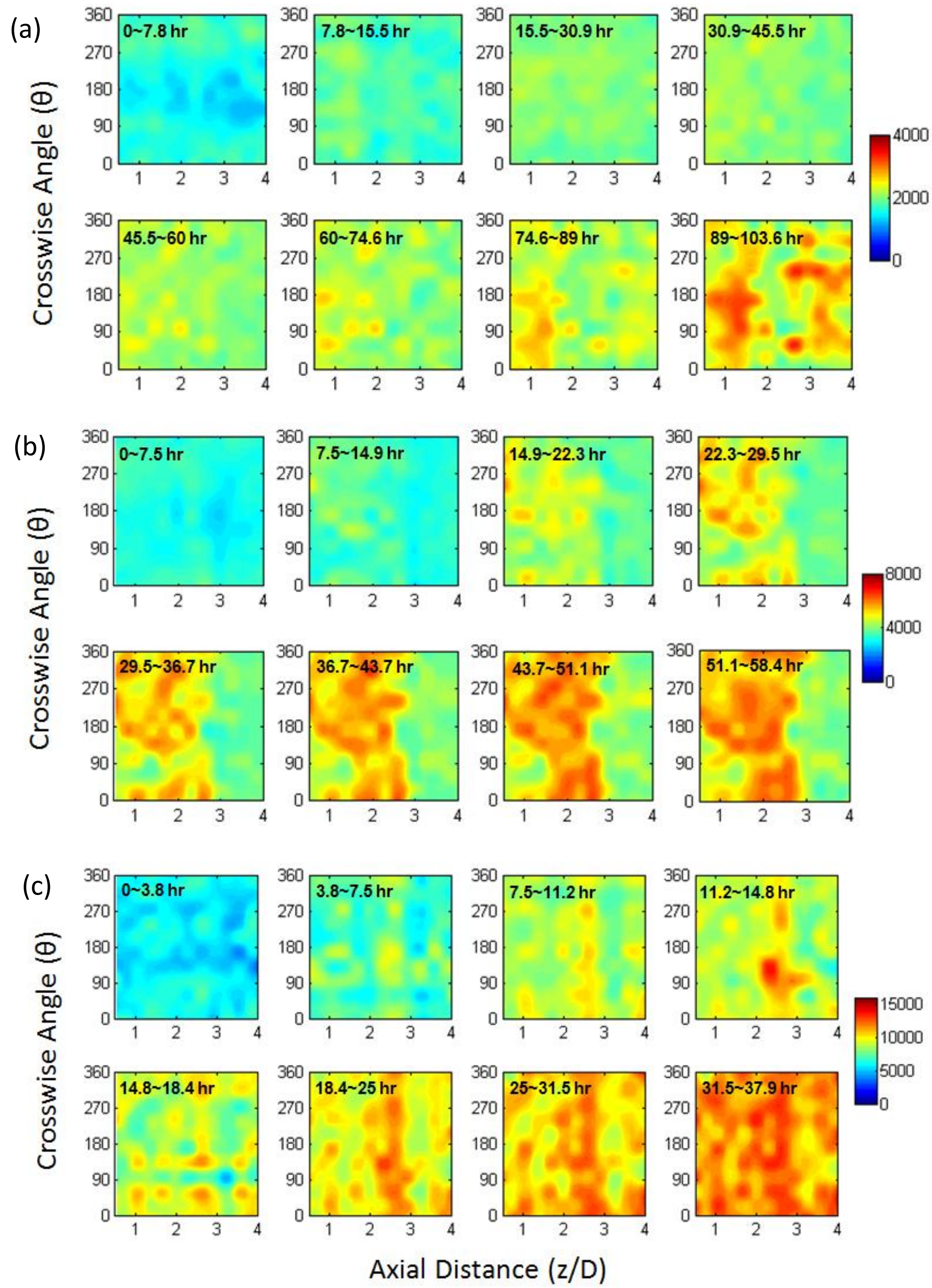

Fig. 4.2: Local distribution of Sherwood number in different time periods for surfaces exposed to flow with (a) *Re* = 50,000 (b) *Re* = 100,000 (c) *Re* = 200,000

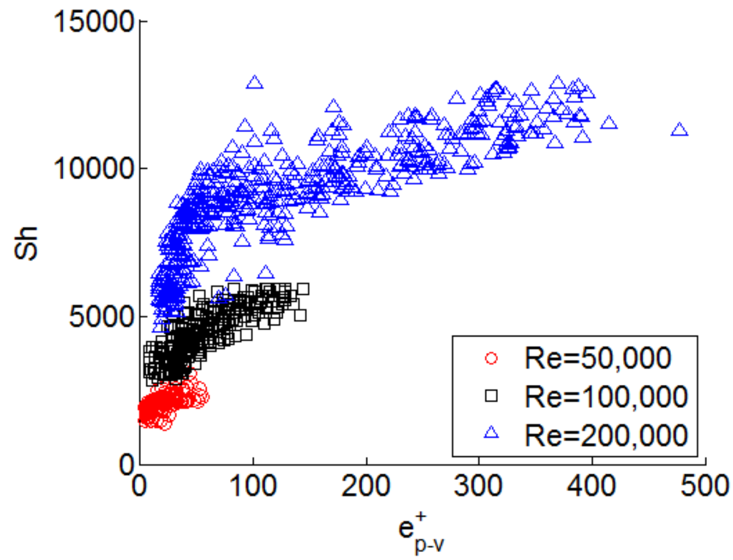

Fig. 4.3: Variation of Sherwood number averaged in sampling areas as a function of normalized peak to valley roughness height for the three Reynolds numbers

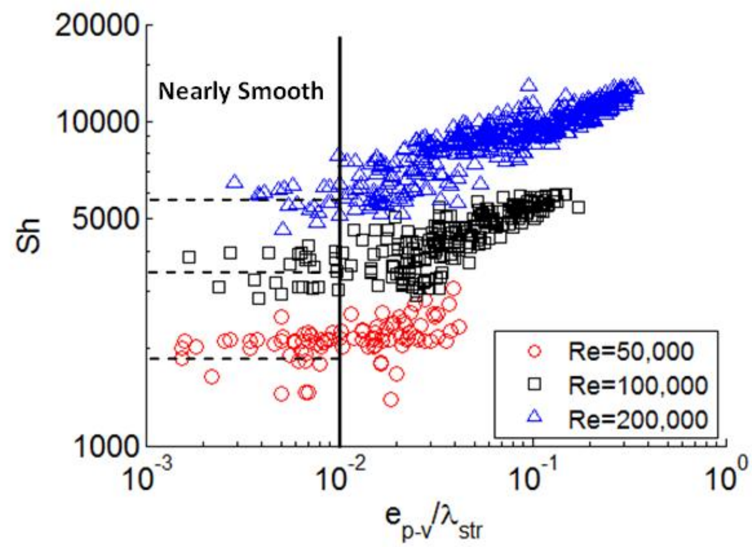

Fig. 4.4: Illustration of estimating Sherwood number in nearly smooth region where the ratio of peak to valley roughness and streamwise spacing is smaller than 0.01

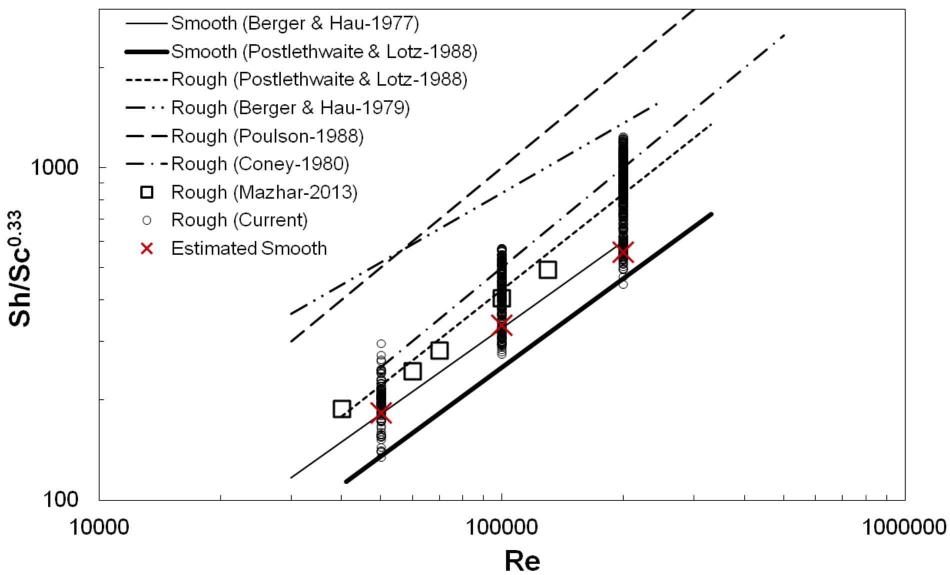

Fig. 4.5: Comparison of the range of mass transfer rates averaged in each sampling area measured in current experiments with previous studies for both smooth and rough surfaces

correlation of Coney [10] for naturally developing roughness, but below the correlation of Berger and Hau [9] for surfaces with square ribs, as seen in Fig. 4.5.

The variation of the mass transfer enhancement or the local Sherwood number relative to the smooth Sherwood number (Sh/Sh_s) with the normalized roughness height is shown in Fig. 4.6. The mass transfer enhancement with e^+_{p-v} is similar for the three Reynolds numbers but differs from the results for predefined roughness, such as the typical result from Dawson and Trass [4]. The maximum enhancement factor in the current experiments approach 2.5, similar to the levels of previous studies [4-8]. The enhancement increases quickly up to $e^+_{p-v} \approx 80$ and more slowly after that up to e^+_{p-v} of 400. The initial period of rapid increase in mass transfer enhancement corresponds to the period where there is a rapid increase in the density of the scallops. The slower increase in mass transfer enhancement period corresponds to the second period where the surface is spatially saturated with the scallops and the streamwise spacing is approximately constant. Once the surface spatially saturates with scallops, the roughness height increases quickly with a nearly linear growth rate [20].

The variation in the mass transfer enhancement with the roughness height to spacing ratio is shown in Fig. 4.7. The results show that the period of large increase in the mass transfer enhancement did correspond to the period of large increase of height to spacing ratio ($e_{p-v}/\lambda_{str} \geq 0.01$). The effect of height to spacing (pitch) ratio on heat transfer has been investigated for artificial repeated rib roughness in previous studies [27-29], where the heat transfer was found to increase with increasing height to pitch ratio

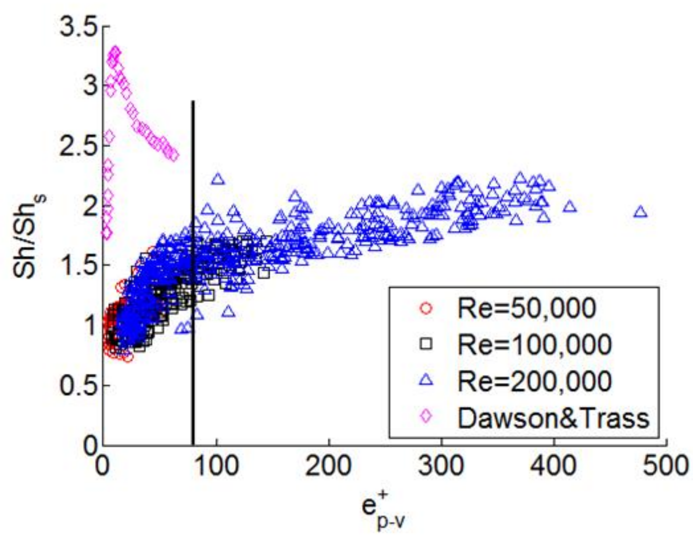

Fig. 4.6: Variation of mass transfer enhancement (*Sh/Sh$_s$*) as a function of normalized peak to valley roughness height and comparison with mass transfer results from Dawson and Trass [4]

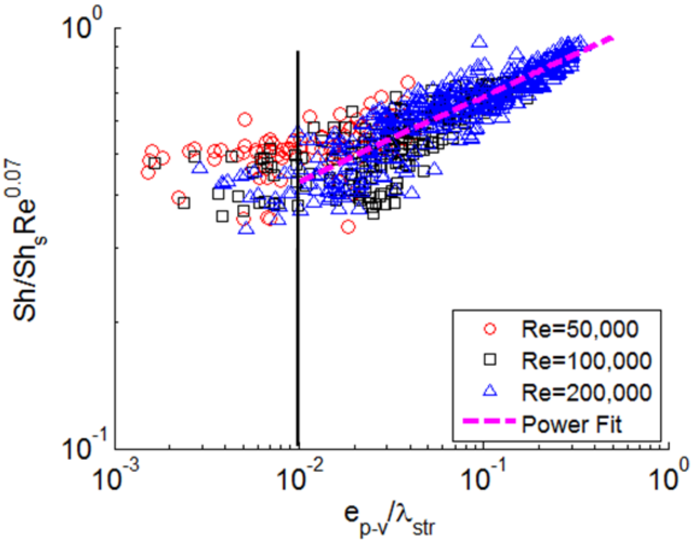

Fig. 4.7: Variation of mass transfer (*Sh/Sh*$_s$) enhancement as a function of height to spacing (pitch) ratio

when the height was kept constant. The maximum heat transfer enhancement for rib roughness was typically found at their minimum pitch to height ratio of 8 ~ 10. Ravigururajan and Bergles [29] proposed a correlation for heat transfer enhancement for ribbed tubes in the form of a simple power law,

$$Nu/Nu_s = Re^{0.036}(e/D)^{0.212}\,(p/D)^{-0.21}(\alpha/90)^{0.29}Pr^{0.024} \tag{4.5}$$

where p is the pitch, D is the diameter and α is the helix angle of rib. It is noted that the effect of rib height and pitch on the heat transfer are opposite but with very similar exponents, and thus to a first approximation can be combined to one parameter. Here, the Sherwood number enhancement could be well correlated for $e_{p-v}/\lambda_{str} \geq 0.01$ by

$$Sh/Sh_s = 1.09\left(e_{p-v}/\lambda_{str}\right)^{0.2}Re^{0.07} \tag{4.6}$$

as shown in Fig. 4.7. There is a weak dependence on the Reynolds number, as a power to 0.07. The Schmidt number dependence of the enhancement was not included because Ravigururajan and Bergles [29] only considered Prandtl numbers up to 37 and it is not clear how their correlation would hold at very high Schmidt or Prandtl numbers. Dawson and Trass [4] suggest a decrease in enhancement with Schmidt number for the predefined surface roughness. The correlation holds for large roughness even as e_{p-v}/λ_{str} approaches 1.

A direct correlation for the Sherwood number in terms of the Reynolds number and roughness parameter e_{p-v}/λ_{str} can be obtained from the current data for $e_{p-v}/\lambda_{str} \geq 0.01$ as shown in Fig. 4.8. The correlation is obtained as

$$Sh = 0.51\left(e_{p-v}/\lambda_{str}\right)^{0.2} Re^{0.84} \tag{4.7}$$

The above correlation can be used for similar naturally developing roughness with the commonly used Schmidt number dependence of $Sc^{0.33}$ as a first approximation.

The height to spacing ratio increases with the roughness height as the roughness develops, even after the surface is saturated with the scallops as shown in Fig. 4.9. The height to spacing ratios collapse for the three Reynolds as a function of normalized roughness height, indicating there is a good correlation between them. The correlation is

$$e_{p-v}/\lambda_{str} = \begin{cases} 0.00027 {e_{p-v}^{+}}^{1.26} & (20 \leq e_{p-v}^{+} < 80) \\ 0.0012 {e_{p-v}^{+}}^{0.92} & (e_{p-v}^{+} \geq 80) \end{cases} \tag{4.8}$$

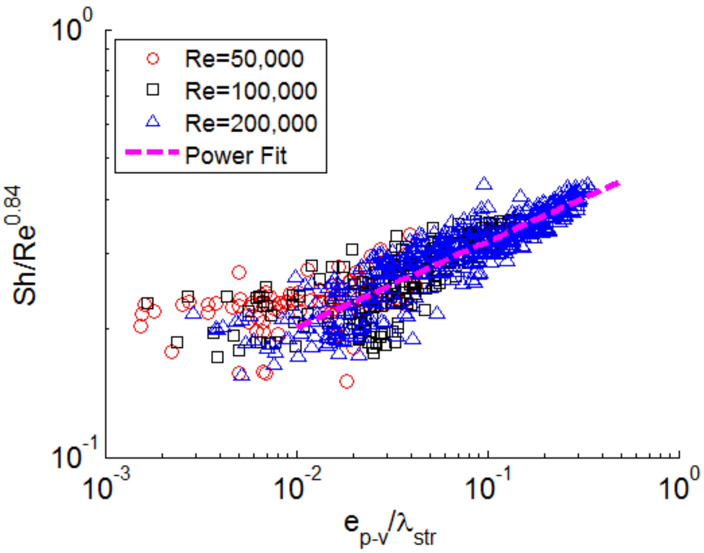

Fig. 4.8: Variation of Sherwood number as a function of height to spacing (pitch) ratio

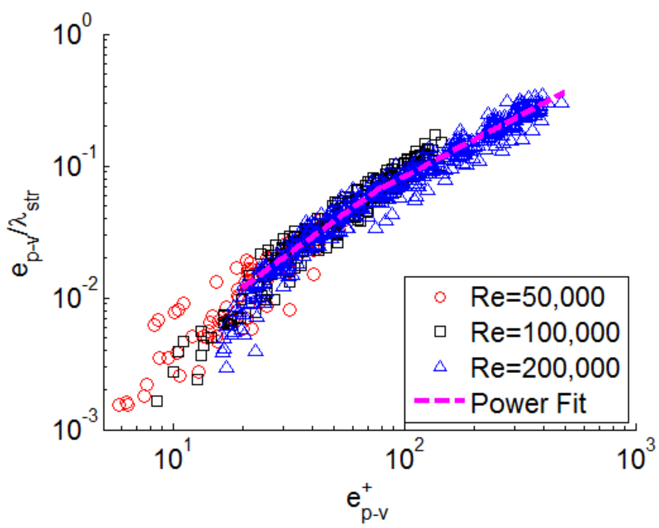

Fig. 4.9: Variation of roughness height to spacing ratio as a function of normalized height with a best fit power correlation between them

as shown in Fig. 4.9. The results here are for roughness that is still developing and longer experimental times would be needed to determine the correlation for fully developed roughness. The effect of Schmidt number on the enhancement also needs further investigation.

4.4 Conclusion

Experiments were performed in 203 mm diameter pipe test sections at Reynolds number of 50,000, 100,000 and 200,000 to study the effect of the developing roughness on mass transfer. A wall dissolving method using gypsum dissolution to water at 25 ℃ was used, with a Schmidt number of 1200. The experiments were performed for multiple time periods and the inner surface topography of the test sections were measured after each time period using X-ray CT scans. The development of the roughness with time due to the mass transfer was characterized in [20]. The local distributions of mass transfer over the surface as the roughness develops were calculated and observed to be non-uniformly distributed. The local mass transfer increased with Reynolds number and as the roughness height increased. The range of Sherwood numbers in the present study was in good agreement with previous studies. The mass transfer enhancement (Sh/Sh_s) was found to be dependent on both the height and spacing of the roughness scallops. For the developing roughness, two periods of mass transfer were present: (i) an initial period of rapid increase in enhancement when the density of scallops increase and the surface gets spatially saturated and (ii) a slower period of increase in enhancement beyond this point, where the streamwise spacing is approximately constant and the roughness height grows more rapidly. Following Ravigururajan and Bergles [29] for heat transfer enhancement in ribbed roughness surfaces, a new correlation for the mass transfer enhancement in naturally developing roughness was developed which showed a $(e_{p-v}/\lambda_{str})^{0.2}$ dependence on the roughness parameters, with a very weak Reynolds number dependence. The height to spacing ratio increases with the roughness height as the roughness develops, even after the surface is saturated with the scallops, with a good correlation between them.

Nomenclature

C_w	Gypsum concentration at the wall [g/l]
C_b	Gypsum concentration in the bulk flow [g/l]
C_{b0}	Initial gypsum concentration in the bulk flow [g/l]
D	Inner diameter of test section [mm]
D_m	Mass transfer diffusivity [m^2/s]
e	Roughness height [mm]
e_{p-v}	Peak to valley roughness height [mm]
e_{rms}	RMS roughness height [mm]
f_D	Darcy friction factor
h_m	Mass transfer coefficient [m/s]
Re	Reynolds number
Sc	Schmidt number
Sh	Sherwood number
u_τ	Friction velocity [m/s]

Greek Symbols

δ	Local wear on pipe inner surface [mm]
λ_{str}	Streamwise spacing of roughness element [mm]
ν	Kinematic viscosity [m^2/s]
ρ	Gypsum density [kg/m^3]

Superscripts

+ Length scale normalized by wall unit (ν/u_τ)

4.5 References

[1] Dooley, R. B., Chexal, V. K. 2000. Flow-accelerated corrosion of pressure vessels in fossil plants. *Int. J. of Pressure Vessels and Piping.* 77: 85-90.

[2] Dooley, R. B. 2008. Flow accelerated corrosion in fossil and combined cycle/HRSG plants. *PPCHEM*, 68-89.

[3] Kain,V., Roychowdhury, S., Ahmedabadi, P., Barua, D. K. 2011. Flow accelerated corrosion: Experience from examination of components from nuclear power plants. *Engineering Failure Analysis*. 18: 2028-2041.

[4] Dawson, A., Trass, O. 1972. Mass transfer at rough surfaces. *Int. J. Heat Mass Transfer*. 15: 1317-1336.

[5] Tantiridge, S., Trass, O. 1984. Mass transfer at geometrically dissimilar rough surfaces. 1984. *The Canadian Journal of Chemical Engineering*. 62: 490-496.

[6] Zhao, W., Trass, O. 1997. Electrochemical mass transfer measurements in rough surface pipe flow: geometrically similar V-shaped grooves. *Int. J. Heat Mass Transfer*. 40(12): 2785-2797.

[7] Postlethwaite, J., Lotz, U. 1988. Mass transfer at erosion-corrosion roughened surfaces. The *Canadian Journal of Chemical Engineering*. 66: 75-78.

[8] Lolja, S. A. 2005. Momentum and mass transfer on sandpaper-roughened surfaces in pipe flow. *Int. J. Heat Mass Transfer*. 48: 2209-2218.

[9] Berger, F.P., Hau, K.F.F.L. 1979. Local mass/heat transfer distribution on surfaces roughened with small square ribs. *Int. J. Heat Mass Transfer*. 22: 1645-1656.

[10] Coney, M.W.E. 1980. Erosion Corrosion: The Calculation of Mass Transfer Coefficients. CEGB Report RD/L/N197/80 CERL.

[11] Blumberg, P. H. 1970. Flutes: a study of stable periodic dissolution profiles resulting from the interaction of a soluble surface and an adjacent turbulent flow. University of Michigan. PhD Thesis.

[12] Poulson, B. 1990. Mass transfer from rough surfaces. *Corrosion Science*. 30: 743-746.

[13] Mazhar, H., Ewing, D., Cotton, J.S. Ching, C.Y. 2014. Mass transfer in dual pipe bends arranged in an S-configuration. *Int. J. Heat Mass Transfer*. 71: 747-757.

[14] Le, T., Ewing, D., Schefski, C., Ching, C.Y. 2014. Mass transfer in back-to-back elbows arranged in an out of plane configuration. *Nuclear Engineering and Design*. 270: 209-216.

[15] Wang D., Le T., Ewing D., Ching C.Y. 2016. Measurement of local mass transfer and the resulting roughness in a large diameter S-bend at high Reynolds number. ASME. *J. Heat Transfer*. 138(6): 062001-7.

[16] Villien, B., Zheng, Y., Lister, D. 2005. Surface Dissolution and the Development of Scallops. *Chem. Eng. Comm.* 192: 125–136.

[17] Allen, J.R.L. 1971. Bed forms due to mass transfer in turbulent flows: a kaleidoscope of phenomena. *J. Fluid Mechanics*. 49(1): 49-63.

[18] Blumberg, P. N., Curl R. L. 1974. Experimental and theoretical studies of dissolution roughness. *J. Fluid Mechanics.* 65(4): 735-751.

[19] Thomas, R. M. 1979. Size of scallops and ripples formed by flowing water. *Nature.* 277(25): 281-283.

[20] Wang D., Ewing D., Ching C.Y. 2016. Time evolution of surface roughness in pipes due to mass transfer under different Reynolds numbers.103:661-671.

[21] Sobel, I. 1990. An Isotropic 3×3 Gradient Operator. Machine vision for three dimensional scenes, Freeman, H., Academic Pres, NY, 376-379.

[22] Daubechies, I. 1988. Orthonormal Bases of Compactly Supported Wavelets. *Communications on pure and applied mathematics*. 41: 909-996.

[23] Wang, D., Huang, Y., Ewing, D., Chow, T., Cotton, J., Noseworthy, M.D., Ching, C.Y., 2015. On the non-destructive measurement of local mass transfer using X-ray computed tomography. *Int. J. Heat Mass Transfer*. 81: 531-541.

[24] Colebrook, C. F., White C.M. 1937. Experiments with Fluid friction roughened pipes. *Proc. R. Soc .(A).* 161.

[25] Nikuradse, J. 1933. Laws of the flow in rough pipes VDI Forschungsheft 361. Also NACA TM 1292, 1950.

[26] Berger FP., Hau KFFL. 1977. Mass transfer in turbulent pipe flow measured by the electrochemical method, *Int. J. of Heat Mass Transfer*. 20:1185-1194.

[27] Webb R. L., Eckert E. R. G., Goldstein R. J. 1971. Heat transfer and friction in tubes with repeated-rib roughness. *Int. J. Heat Mass Transfer*. 14: 601-617.

[28] Prasad B. N., Saini J. S. 1988. Effect of artificial roughness on heat transfer and friction factor in a solar air heater. *Solar Energy*. 41(6): 555-560.

[29] Ravigururajan T. S., Bergles A. E. 1996. Development and verification of general correlations for pressure drop and heat transfer in single-phase turbulent flow in enhanced tubes. *Experimental thermal and fluid science*. 13: 55-70.

Chapter 5

Measurement of local mass transfer and the resulting roughness in a large diameter S-bend at high Reynolds number

Complete citation:

Wang D., Le T., Ewing D., Ching C.Y. 2016. Measurement of local mass transfer and the resulting roughness in a large diameter S-bend at high Reynolds number. ASME. *J. Heat Transfer*. 138(6): 062001-7.

Copyright:

Relative Contributions:

Wang D.: Performed all experiments, interpretation and analysis of the data and wrote the first draft of the manuscript including all figures and text.

Le T.: Assisted in Matlab coding for surface alignment.

Ewing D.: Assisted in the interpretation and discussion of results.

Ching C. Y.: Supervisor and was responsible for the final draft submittal to the journal.

Abstract

The local mass transfer and the resulting roughness in a 203mm diameter back to back bend arranged in an S-configuration was measured at a Reynolds number of 300,000. A dissolving wall method using gypsum dissolution to water at 40 ℃ was used, with a Schmidt number of 660. The topography of the unworn and worn inner surface was quantified using non-destructive X-ray Computed Tomography (CT) scans. The local mass transfer rate was obtained from the local change in radius over the flow time. Two regions of high mass transfer were present: (i) along the intrados of the first bend near the inlet and (ii) at the exit of the extrados of the first bend that extends to the intrados of the second bend. The latter was the region of highest mass transfer, and the scaling of the maximum Sherwood number with Reynolds number followed that developed for lower Reynolds numbers. The relative roughness distribution in the bend corresponded to the mass transfer distribution, with higher roughness in the higher mass transfer regions. The spacing of the roughness elements in the upstream pipe and in the two regions of high mass transfer was approximately the same; however, the spacing to height ratio was very different with values of 20, 10 and 6, respectively.

5.1 Introduction

Flow Accelerated Corrosion (FAC), which results in the thinning and weakening of pipe walls in power generation plants, is essentially a three step process: (a) a series of electrochemical reactions at the metal-oxide interface, (b) chemical erosion that dissolves the oxide layer of the carbon steel pipe walls and (c) mass transfer from the wall to the flow [1]. Factors such as geometrical configuration and orientation of the piping components, flow rate, local turbulence, fluid chemistry, surface roughness and piping material can significantly affect FAC [2]. The diffusion-controlled mass transfer is the rate limiting process, thus the control of FAC in practical applications requires the identification of regions with high local mass transfer.

Flow in bends is subject to severe changes in the flow direction and leads to the development of secondary flow, in the form of counter-rotating vortices in the streamwise direction [3-5]. The strong pressure-driven secondary flow results in regions of high local shear stress on the pipe walls, which can directly enhance the mass transfer in those regions [6-9]. Mass transfer in single bends has been studied experimentally using dissolving wall methods with naphthalene sublimation in air [6-7] and gypsum dissolution in water [8-9]. Regions of high mass transfer were found on the inner wall near the inlet of the bend and in the pipe immediately downstream of the bend outlet [6] on the outer wall side.

Bends in many piping systems are commonly attached back to back in different configurations, such as in S-, C- and out of plane configurations. The mass transfer in the downstream bend of back to back bend configurations can be significantly enhanced [10-12]. Poulson and Robinson [10] measured the maximum mass transfer enhancement in 180° bends for r_c/D =2.5 and 7.3 using the wall dissolving method at Reynolds number up to 2.6×10^5 and Sc=568. The mass transfer in S-shape and out of plane back to back bends was investigated using the dissolvable wall technique at Re=40,000 to 130,000 and Sc=1280 [11-12]. The maximum mass transfer location was determined and the relative roughness height e/D was evaluated by analyzing the surface topography obtained from laser scans. The maximum mass transfer in the downstream second bend was found to be 1.5 to 2 times that in a single bend. There is a need for mass transfer measurements at higher Reynolds numbers to verify the Reynolds number scaling of the Sherwood number, making it more reliable for extrapolating the results to high Reynolds numbers typical of power plant operating conditions.

In mass transfer applications, the surface roughness develops naturally due to the mass transfer to the bulk flow, and the resulting roughness can have a significant effect on the mass transfer [13-17]. Experimental studies have been performed to investigate the effect of surface roughness on mass transfer for predefined surface roughness, such as V-grooves [13-15], sandpaper-roughness [16] and square rib roughness [17]. A dissolving wall method offers an advantage in that the surface roughness develops naturally due to the mass transfer, mimicking the roughness occurring in many practical applications.

The objective of this investigation is to develop a non-destructive dissolving wall methodology to investigate local mass transfer and the resulting surface roughness in a 203mm diameter S-shape back to back bend at Re=300,000. The test section was fabricated using a plastic outer shell and a collapsible inner core constructed in part from components that were 3D printed. Gypsum was cast into the gap between the inner core and outer shell to form the inner dissolvable surface of the S-bend. The experiments were performed in a 203mm diameter flow loop with water maintained at 40 ℃ as the working fluid, leading to a Schmidt number of 660. The local mass transfer rates and surface roughness were obtained from the change in topography of the worn and unworn surfaces measured by non-destructive X-ray Computed Tomography (CT) scans, as detailed by Wang et al. [19]. An important advantage of the current method is that it provides a complete surface distribution of the local mass transfer and roughness, which allows to identify regions of high local mass transfer and its correlation to the surface roughness.

5.2 Experimental Methodology

The experiment was performed in a closed flow loop that is described in detail in [19]. Water flows from a 1.5 m^3 reservoir through a 101.5 mm diameter, 9 m long downcomer before entering a centrifugal pump at the bottom of the loop. The flow exits the pump to a 203 mm diameter (D), 9.5m long acrylic riser through a sudden expansion at the bottom of the riser. The flow passes through the riser with a length of 32D before entering the S-shape gypsum lined test section. The flow exits the test section to a 4.5D downstream pipe and a PVC S-bend leading back to the reservoir. The flow rate is adjusted using a variable speed controller for the pump and measured using two Pitot tubes; one in the riser downstream of the test section and the other in the downcomer. The temperature of water throughout the testing time was measured at two locations along the loop: (i) in the main reservoir and (ii) in the downcomer. The water temperature was maintained at 40 ± 1 ℃ using a cooling coil in the reservoir. The electrical conductivity of water was measured by a conductivity probe and recorded on a computer. A calibration test was performed to correlate the concentration of dissolved gypsum to the electrical conductivity of the water at 40 ℃ before the experiment.

The experiment was performed using a 203 mm inner diameter S-shape test section, where the radius of curvature (r_c/D) of the two bends was 1.5, with a 2D long upstream and 1D long downstream pipe sections. The test section was cast using a 3D printed collapsible inner core and outer shell. The outer diameter of the inner core was 203 mm and the outer shell had an inner diameter of 244 mm, which resulted in a gypsum lining of 20.5 mm thickness. The outer shell and inner core were held concentrically during the casting process, using fixtures that included the base plate and end cap. The gypsum was generated by mixing hydrocal ($CaSO_4$•$1/2H_2O$) with water that yields gypsum with a density of 1580 kg/m^3. A small ratio of citric acid was added during the mixing stage to slow the curing process to facilitate the casting. The inner core was removed shortly after casting and the gypsum was left to cure under ambient conditions for approximately 15 days until the weight of the test section reached steady state using a scale accurate to ± 25g.

The mass transfer experiment was performed by flowing water through the test section for a total run time of 8 hours. The topography of the unworn and worn inner surface of the test section was measured using X-ray CT scans before and after the experiment. The term “worn” is used here in the context of mass removal due to diffusion.

Independent experiments performed with different initial bulk concentrations of gypsum in water showed that erosion did not play a role in the mass removal. Details of the methodology can be found in [19]. The image resolution at each cross-section was 1024×1024 pixels, which yielded a physical resolution of 0.6×0.6 mm. The through plane resolution (i.e slice thickness) was 1mm along the test section. A representative section scan is shown in Fig. 5.1(a). The intensity level of the scan was adjusted so that both edges of the gypsum liner and outer shell were captured clearly. The edges at the gypsum liner and outer shell were detected from the images using a Sobel method [20] that finds the edges based on where the gradient of gray scale in the images is maximum, as shown representatively in Fig. 5.1(b). The two-dimensional cross sectional profiles of the test section were combined into a three-dimensional array of points corresponding to the inner and outer surfaces of the gypsum liner, as well as the outer surface of the shell. The reconstructed 3D image of the unworn test section from the CT scans is shown in Fig. 5.1(c). The axis along the center of the test section was initially determined on a best fit of the outer surfaces through the center. The axis was then refined on a best fit of the unworn inner surface to ensure it followed the inner surface.

The unworn and worn surfaces were aligned along the axial direction based on the outer shell surface. The alignment was checked using the deviation of the two outer surfaces of the gypsum liner. The deviation of the unworn and worn outer surfaces is within ±0.5 mm, indicating good alignment of the two sections. The local mean radius was determined by running an average over a larger grid cell to eliminate variations due

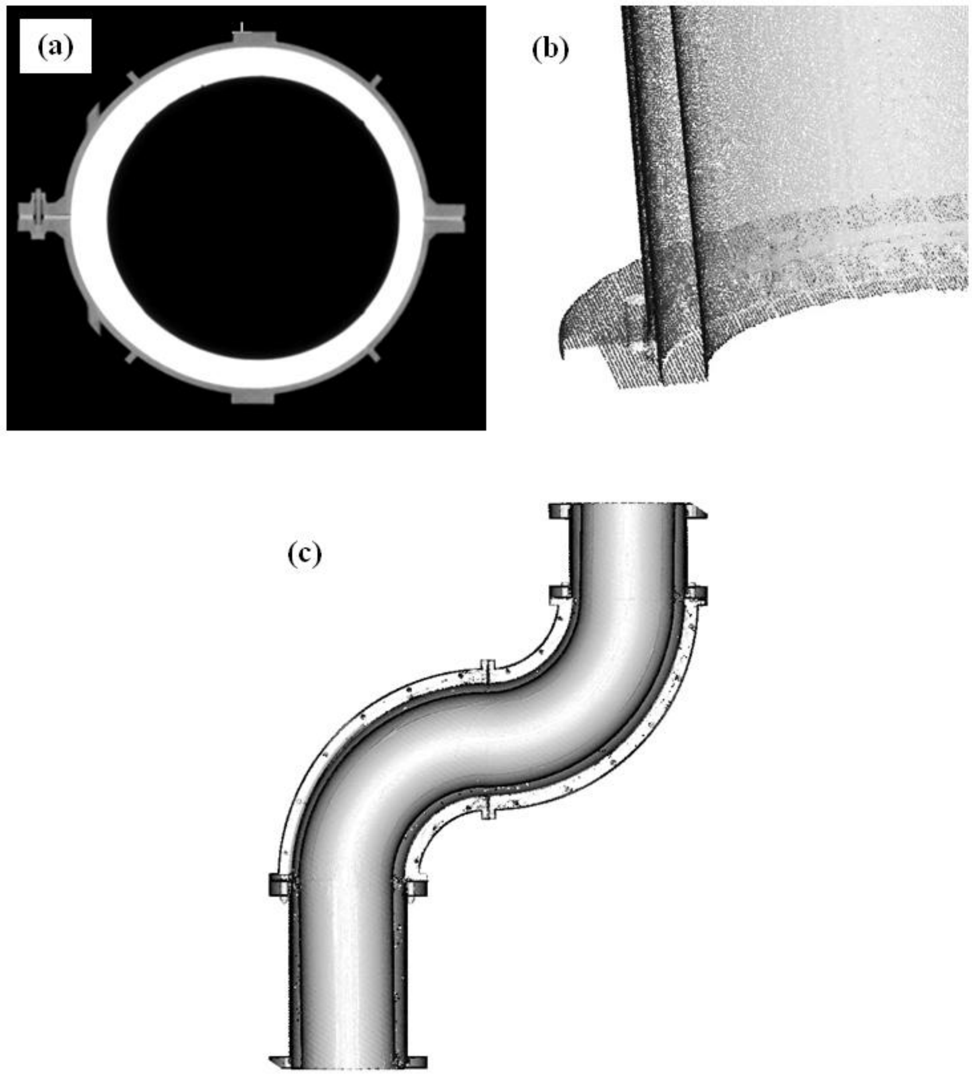

Fig. 5.1: (a) Example of typical CT scan image (b) Point cloud of edges detected from CT scan images after 3D reconstruction (c) Cross section of reconstructed 3-dimensional CT scan image

to local roughness. Three different grid cells of 10×10, 20×20 and 40×40 mm^2 were evaluated. The grid cell of 10×10 mm^2 still encompassed the variations due to local roughness, while the larger grid cell of 40×40 mm^2 was observed to filter the variation of the local mean radius. The cell size of 20×20 mm^2 was found to capture the local variation of the mean radius and is used here to obtain the mean radius for each surface data point.

The local mass transfer coefficient is calculated by

$$h_m = \frac{1}{c_w - c_{b0}} \rho \frac{\partial \delta}{\partial \tilde{t}} \tag{5.1}$$

where δ is the local wear of the inner surface, ρ is the density of gypsum and $\tilde{t}$ is a modified time to account for the change in bulk concentration of the flow during the testing period, given by

$$\tilde{t} = \frac{\int_0^T (c_w - c_b(t))dt}{c_w - c_{b0}} \tag{5.2}$$

The local Sherwood number is calculated as

$$Sh = \frac{h_m D}{D_m} \tag{5.3}$$

where D is the diameter of the test section, and D_m is the mass diffusivity (9.97×10^{-10} m^2/s) of gypsum at 40 ℃. The relative roughness (e/D) of the worn surface was then evaluated following the methodology of Wang et al. [19]. The roughness height was determined by subtracting the local mean radius from the local radius.

The uncertainty in the mass transfer coefficient is due to both a bias error due to any misalignment of the worn and unworn surfaces and a random error. The bias error was quantified from the deviation of the two outer surfaces after alignment. Wang et al. [19] assessed the random error by comparing the CT scan method to other measurement methods, and is used here. The total uncertainty in the mass transfer coefficient in the upstream pipe was estimated to be ±12% at a 95% confidence level. The corresponding uncertainties in the intrados regions of the first bend and second bend were ±14% and ±12%, respectively.

5.3 Results and Discussion

The local Sherwood number distribution over the entire S-bend is shown in Fig. 5.2. The Sherwood number in the upstream pipe is nearly uniform before it increases towards the inlet of the first bend intrados. Two regions of significant mass transfer can be identified: (i) along the intrados of the first bend near the inlet and (ii) towards the exit of the first bend extrados that extends to the inlet of the second bend intrados. The latter region is the maximum mass transfer region, consistent with the results of [11]. The change in the local mass transfer rate in the bends was characterized in detail by examining azimuthal profiles of the local Sherwood number (*Sh*). Representative profiles along the two bends are shown in Fig. 5.3. Here, z/D is defined as the dimensionless streamwise distance along the centerline, starting from the inlet of the first bend, and thus z/D is negative in the upstream pipe, while φ is the angle around each bend. The mass transfer is relatively uniform at z/D=-1 in the upstream pipe. The *Sh* along the intrados of the first bend (θ=-90°) increases significantly near the inlet. This region of high Sherwood number occurs at $\varphi_1 \approx 5° \sim 25°$, and is centered around the inner radius with a

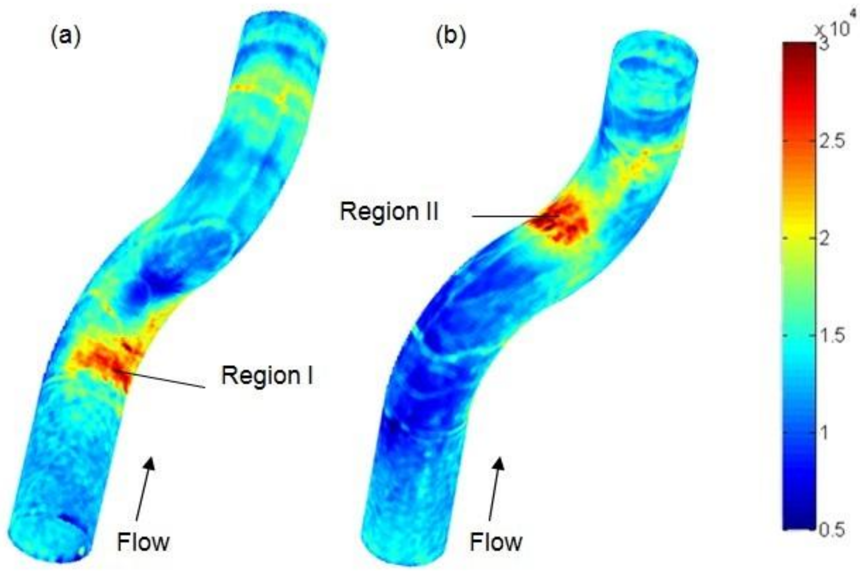

Fig. 5.2: Local Sherwood number contours over the entire test section viewed along (a) the intrados of the first bend and (b) the extrados of the first bend

span of approximately ±45°. It is thought that this is due to the acceleration of the flow into the bend and similar to that observed in a single bend [6, 9]. The high mass transfer region then shifts towards the side walls, consistent with the results of [11], likely due to flow separation and subsequent deceleration of the flow. The Sherwood number along the first bend extrados (θ=90°) decreases from the upstream pipe and then increases gradually along the first bend, likely due to the secondary flow shifting from the intrados towards the extrados along the first bend [3]. This continues into the second bend with a high Sherwood number on the second bend intrados between $\varphi_2 \approx 5° \sim 20°$ that spans approximately ±45° around the inner radius of the bend. This is similar to the results in [11] and is attributed to the superimposition of vortices generated from the first bend and

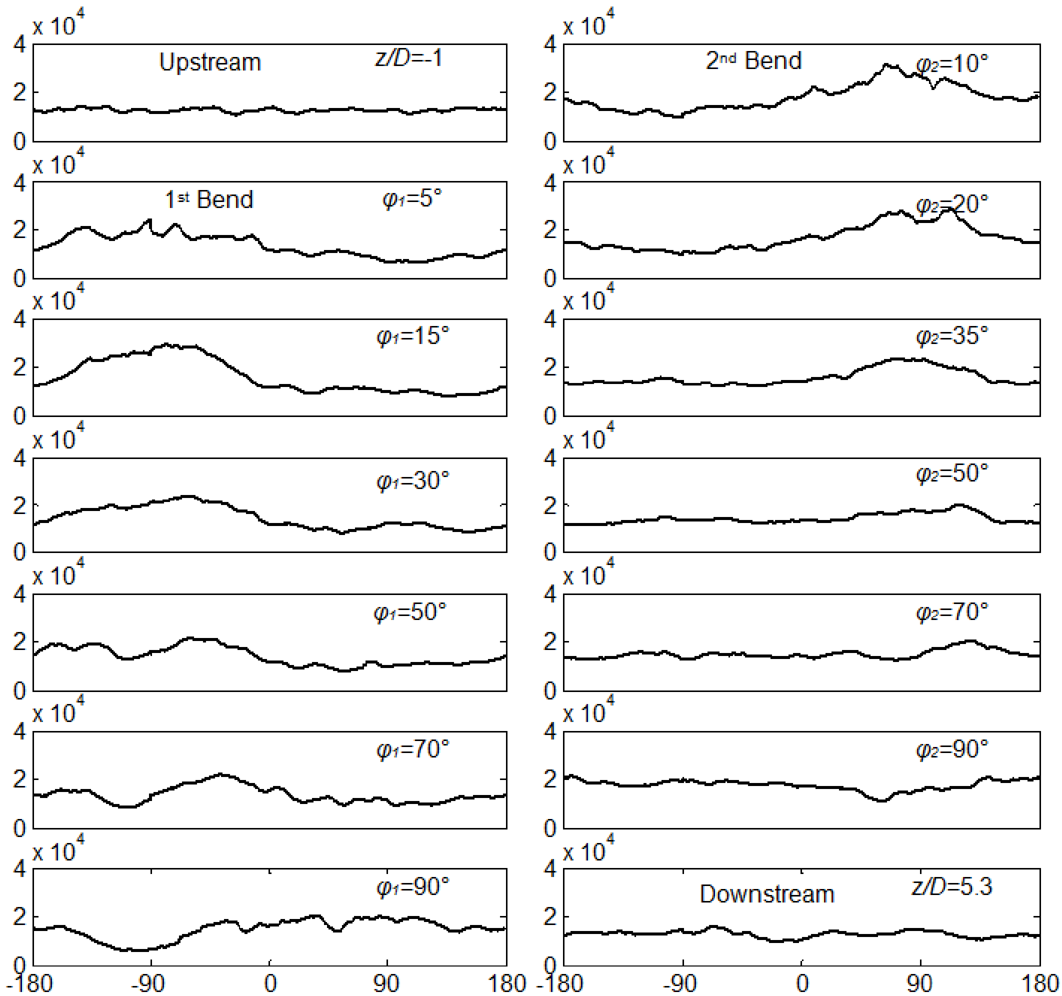

Fig. 5.3: Azimuthal profiles of Sherwood number at typical streamwise locations

acceleration caused by the curvature of the second bend. The *Sh* decreases through the latter part of the second bend and approaches the fully developed pipe value in the downstream pipe, as seen in the profile at z/D=5.3.

The current mass transfer results at Re=300,000 is compared with those at lower Reynolds numbers obtained using 25.4 mm diameter test sections [11], and shown in Fig. 5.4. The averaged *Sh* in the upstream pipe and the maximum *Sh* in the S-bend are shown here. The *Sh* is typically correlated to $Sc^{0.33}$, and this relation is used here. The *Sh* in the upstream pipe in both cases were in reasonable agreement with the correlation of [21]. However, the results here were above the correlation while most of those in [11] were slightly below the correlation. The maximum *Sh* in the S-bend of the current study was in reasonable agreement with the Reynolds number scaling of $Re^{0.93}$ [11] and suggests that this scaling extends to much higher Reynolds numbers than previously determined. The mass transfer enhancement (Sh/Sh_{pipe}) in the two regions of high mass transfer on the first and second bend is approximately 2.1 and 2.6, respectively. The maximum mass transfer enhancement here of 2.6 in this study is lower than 3.2 found by [11], but this could be due to the higher pipe *Sh* obtained from the upstream pipe in this study.

The relatively large diameter of the test section and the resolution of the CT scans allows the examination of the roughness that develops on the surfaces due to mass transfer to the flow. The roughness that develops on the surface is an important parameter as it can have a causal effect on the mass transfer. Images of the surface from the CT scan in the three regions of interest, corresponding to the upstream pipe and the high mass transfer regions on the intrados of the first and second bend, are shown in Fig. 5.5.

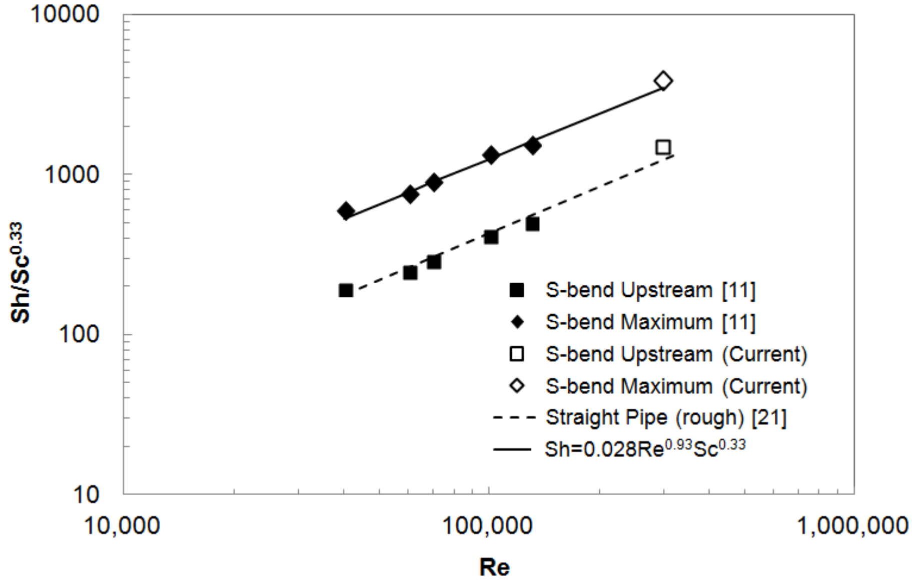

Fig. 5.4: Variation of the local maximum and upstream Sherwood number with Reynolds number in S-bend

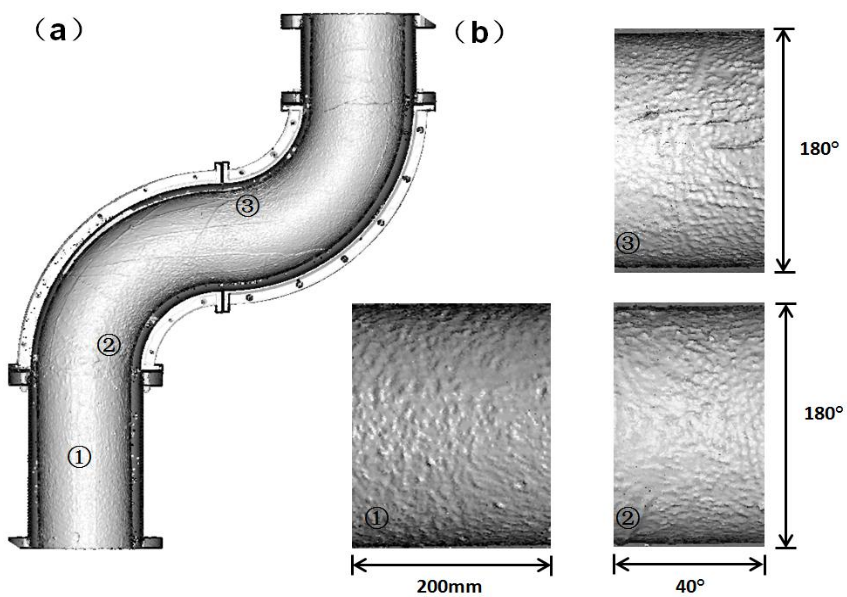

Fig. 5.5: (a) The entire 3D reconstructed worn surface contour from CT scan (b) View of ①: Upstream pipe ($-1.4<z/D<-0.4, -90°<\theta<90°$); ②: High mass transfer region I in the first bend ($0°<\varphi_1<40°, -180°<\theta<0°$); ③: High mass transfer region II in the second bend ($0°<\varphi_2<40°, 0°<\theta<180°$)

The developed roughness is very similar to the scalloping pattern that has been observed in the carbon steel piping systems of power generation plants due to flow accelerated corrosion [22]. The absolute roughness height (*e*) used to characterize the surface roughness was determined by evaluating the deviations of the roughness peaks and valleys from the local mean surface. The difference between the mean values of the local maxima and minima within the averaging area about each point was used to obtain the absolute roughness height [19]. This is more clearly seen in the azimuthal profiles of the local deviation at three typical streamwise locations of z/D=-1, φ_1=15° and φ_2=10° presented in Fig. 5.6. The distribution of the relative roughness (e/D) over the entire surface of the S-bend is shown in Fig. 5.7. The relative roughness along the upstream pipe is relatively uniform beyond the entrance region, with a value of about 2×10^{-3}. Two regions of high relative roughness can be identified: (i) near the inlet of the intrados of the first bend and (ii) at the inlet of the intrados of the second bend, the latter of which is higher. These two regions of high relative roughness correspond to the two regions of high mass transfer identified earlier, and indicate a strong correlation between the surface roughness and mass transfer. The values of the relative roughness in the two regions of high mass transfer are 4×10^{-3} and 7×10^{-3}, respectively. These values are smaller than that found by [11] in a 25.4 mm diameter S-bend at lower Reynolds numbers (40,000 to 130,000).

The streamwise and circumferential spacing of the roughness peaks or scallops here were quantified by determining and mapping the peaks over the area of interest. The peaks were determined using an algorithm that compared each data point of the wear to

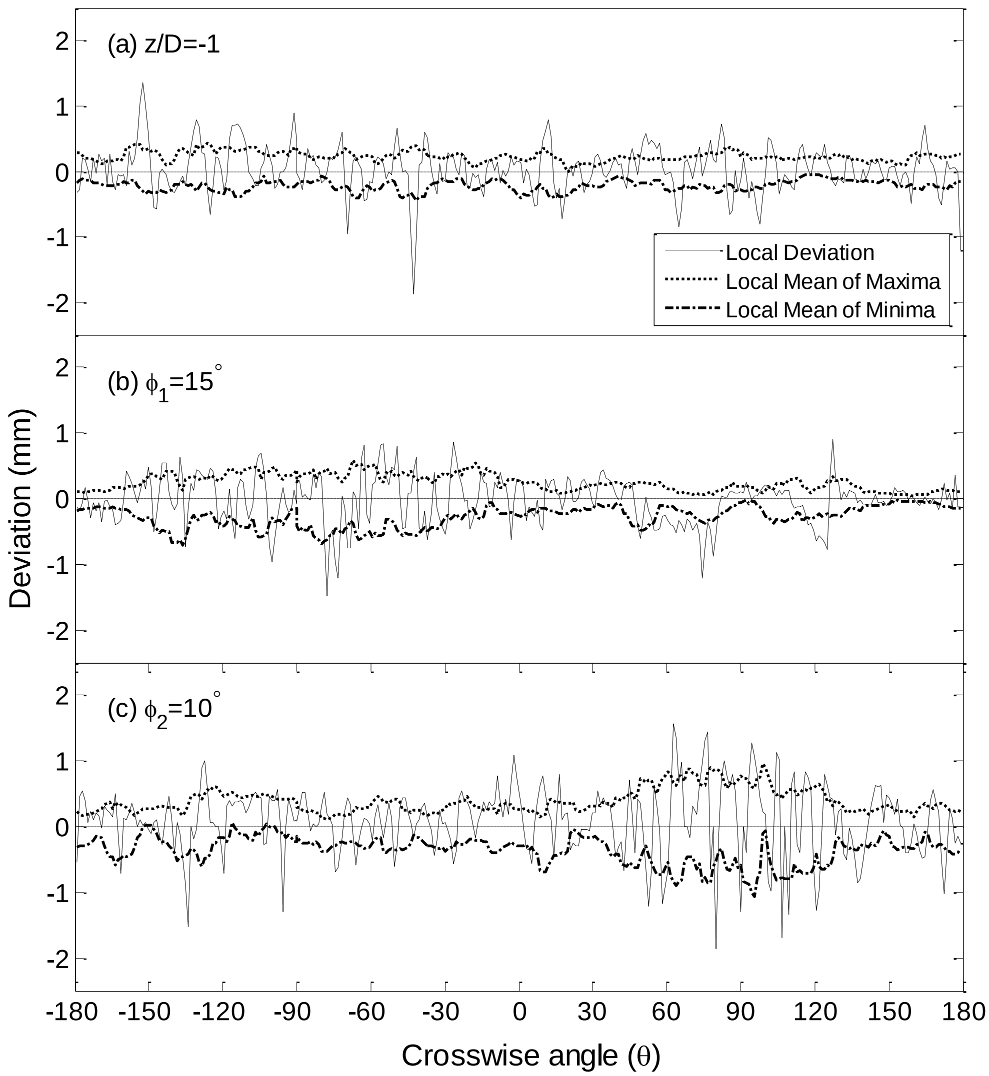

Fig. 5.6: Azimuthal profiles of local deviation on the worn rough surface at three typical streamwise locations: (a) z/D=-1; (b) φ_1=15 °; (c) φ_2=10 °

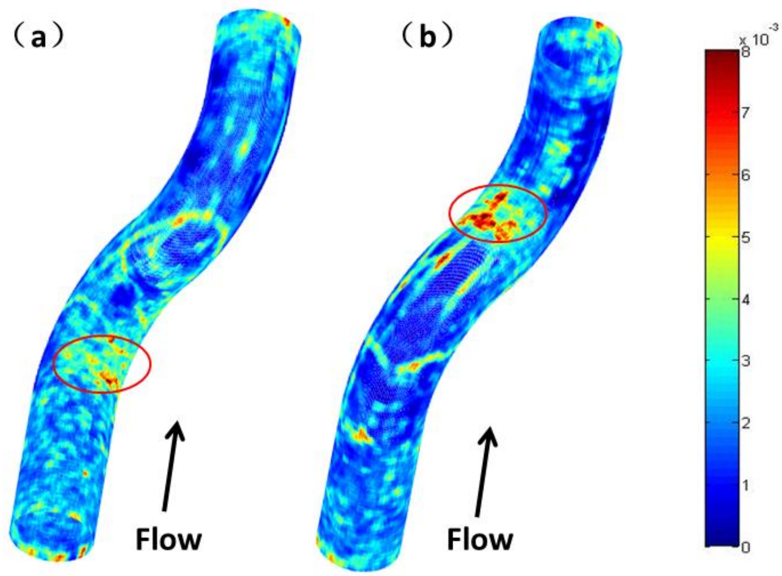

Fig. 5.7: Relative roughness (*e/D*) contours over the entire test section viewed along (a) the intrados of the first bend and (b) the extrados of the first bend

Table 5.1: Streamwise and circumferential spacing of peak to valley roughness in the upstream pipe and the regions of high mass transfer in the first and second bends

Region	e (mm)	λ_z (mm)	λ_Θ(mm)	λ_z/e	λ_Θ/e
Upstream pipe	0.45	8.8	8.4	19	20
First bend (90°)	0.81	7.9	9.0	10	10
Second bend (90°)	1.40	8.0	8.8	6	6

its neighboring values. The average spacing between the roughness peaks or scallops in these three regions are presented in Table 5.1. The spacing in the streamwise and circumferential directions are nearly the same, and similar in the three regions examined above, and illustrated in Fig. 5.8. Thomas [23] proposed that the roughness spacing would scale with the near-wall turbulence, with a characteristic length scale of (ν/u_*) and found a value of $1000\nu/u_*$ for a range of pipe or channel data. The ratio of scallop spacing (λ) to the wall unit (ν/u_*) in the upstream pipe for the current experiment is approximately 750, where the friction velocity was estimated from the Moody diagram [24], and is in reasonable agreement with the results of Thomas [23]. The ratio of the spacing to the roughness height, however, was very different in the three regions with values of 20, 10 and 6 in the upstream pipe, first and second bend, respectively, as evident in Fig. 5.8.

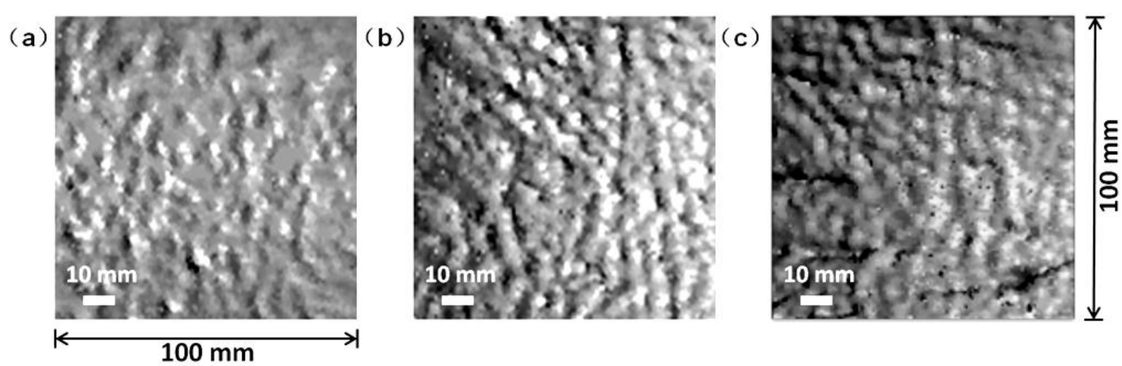

Fig. 5.8: Enlarged view of surface roughness in (a) Upstream pipe (b) High mass transfer region I in the first bend (c) High mass transfer region II in the second bend for illustration of streamwise and circumfirential spacing distributions of peak to valley roughness.

5.4 Conclusion

The mass transfer and resulting roughness in a 203 mm diameter S-shape back to back bend was experimentally measured at a Reynolds number of 300,000 and Schmidt number of 660 using a dissolving wall technique. A gypsum lined test section was used with water at 40 ℃ as the working fluid. The inner surface topography of the unworn and worn test section was quantified using non-destructive X-ray Computed Tomography scans. The mass transfer rates were determined from the change in local radius of the test section with time. Two regions of high mass transfer were found, consistent with previous studies at lower Reynolds numbers using 25.4 mm diameter test sections: (i) at the inlet (5°~25°) of first bend intrados and (ii) at the inlet (5°~15°) of second bend intrados, with the latter being the region of highest mass transfer in the back to back bend. The maximum Sherwood number in the S-bend followed a similar trend as the lower Reynolds number cases [11], and suggests that the Reynolds number scaling of $Re^{0.93}$ extends to higher Reynolds numbers. The maximum mass transfer enhancement (Sh/Sh_{pipe}) relative to the upstream pipe is 2.6. This is slightly lower than the experimental results of [11] at lower Reynolds numbers, and could be due to the slightly higher pipe Sherwood number obtained in this study. To fully ascertain the effect of Reynolds number, however, additional experiments at different Reynolds numbers are needed, and will be performed in a future study. The relative roughness distribution in the bend showed some correspondence to the mass transfer distribution, with higher roughness in the higher mass transfer regions. The relative roughness (e/D) in the upstream pipe and in the two regions of high mass transfer in the bend was approximately 2×10^{-3}, 4×10^{-3}, and 7×10^{-3}, respectively. The average spacing of the roughness peaks in the streamwise and circumferential directions is nearly the same, and approximately 750 wall units (ν/u_*) in the pipe. However, the spacing to height ratio of the roughness in the upstream pipe, and regions of high mass transfer in the first and second bend was different, with values of 20, 10 and 6, respectively.

The current mass transfer results show the locations within the S-bend that are most susceptible to wall thinning due to FAC. This would be of significance to the power plant industry to better plan their inspection locations and schedules for pipe wall thinning in bend geometries of the piping systems. The extension of the correlation for the maximum Sherwood number with Reynolds number to a much higher Reynolds number than before also provides greater confidence in predicting the balance of piping system life of power plants.

The current non-destructive measurement methodology is well suited to investigate the evolution of the surface roughness due to the mass transfer to the bulk flow. As a follow up to this study, tests will be performed over multiple time intervals at different Reynolds numbers, and the surface topography mapped at the end of each time interval. The local surface roughness and mass transfer will be evaluated for each run time interval, and used to understand the causal effect between the evolving roughness and the mass transfer.

Nomenclature

C_w	Gypsum concentration at the wall [g/l]
C_b	Gypsum concentration in the bulk flow [g/l]
C_{b0}	Initial gypsum concentration in the bulk flow [g/l]
D	Diameter of bend cross section [m]
D_m	Mass diffusivity [m^2/s]
e	Roughness height [m]
h_m	Mass transfer coefficient [m/s]
Re	Reynolds number
r_c	Radius of curvature of the bend [m]
Sh	Sherwood number
Sc	Schmidt number
$\tilde{t}$	Modified time scale [s]
z/D	Dimensionless streamwise distance

Symbols

ρ	Gypsum density [kg/m^3]
φ_1	Angle of curvature along the first bend [°]
φ_2	Angle of curvature along the second bend [°]
θ	Angle in the azimuthal direction [°]
δ	Local wear on pipe inner surface [mm]

5.5 References

[1] Pietralik, J.M., Schefski, C.S. 2011. Flow and mass transfer in bends under flow-accelerated corrosion wall thinning conditions. Journal of Engineering for Gas Turbines and Power. 133(1) 012902: 1-7.

[2] Poulson, B. 1999. Complexities in predicting erosion corrosion. Wear. 233-235(1999): 497-504.

[3] Enayet, M.M., Gibson, M.M., Taylor, A. M. K.P., Yianneskis, M. 1982. Laser-Doppler measurements for laminar and turbulent flow in pipe bend, Int. J. Heat Fluid Flow. 3(4): 213–220.

[4] Sudo, K., Sumida, M., Hibara, H. Experimental investigation on turbulent flow in a circular-sectioned 90-degree bend. Experimental in Fluids. 25(1998): 42-49.

[5] El-Gammal, M., Mazhar, H., Cotton, J.S., Schefski, C., Pietralik, J., Ching, C.Y. 2010. The hydrodynamic effects of single phase flow on flow accelerated corrosion in a 90 °elbow. Nuclear Engineering and Design. 240:1589–1598.

[6] Achenbach, E. 1976. Mass transfer from bends of circular cross section to air. Future Energy Production System. Academic Press. New York, 1: 327-337.

[7] Sparrow, EM. Chrysler, GM. 1986. Turbulent flow and heat transfer in bends of circular cross section: i- heat transfer experiments. ASME Journal of Heat Transfer. 108: 40-47.

[8] Wilkin, SJ., Oates, HS., Coney, M. 1983. Mass transfer on straight pipes and 90° bends measured by the dissolution of plaster (1st Edition). Central Electricity Research Laboratories Report. TPRD/L/2469/N83.

[9] Mazhar, H., Ewing, D., Cotton, J.S. Ching C.Y. 2013. Experimental investigation of mass transfer in 90° pipe bends using a dissolvable wall technique. Int. J. Heat Mass Transfer. 65: 280-288.

[10] Poulson, B., Robinson, R. 1988. The local enhancement of mass transfer at 180 degree bend. Int. J. Heat Mass Transfer. 31(6):1289-1297.

[11] Mazhar, H., Ewing, D., Cotton, J.S. Ching, C.Y. 2014. Mass transfer in dual pipe bends arranged in an S-configuration. Int. J. Heat Mass Transfer. 71: 747-757.

[12] Le, T., Ewing, D., Schefski, C., Ching, C.Y. 2014. Mass transfer in back-to-back elbows arranged in an out of plane configuration. Nuclear Engineering and Design. 270: 209-216.

[13] Dawson, A., Trass, O. 1972. Mass transfer at rough surfaces. Int. J. Heat Mass Transfer. 15: 1317-1336.

[14] Tantiridge, S., Trass, O. 1984. Mass transfer at geometrically dissimilar rough surfaces. 1984. The Canadian Journal of Chemical Engineering. 62: 490-496.

[15] Zhao, W., Trass, O. 1997. Electrochemical mass transfer measurements in rough surface pipe flow: geometrically similar V-shaped grooves. Int. J. Heat Mass Transfer. 40(12): 2785-2797.

[16] Lolja, S. A. 2005. Momentum and mass transfer on sandpaper-roughened surfaces in pipe flow. Int. J. Heat Mass Transfer. 48: 2209-2218.

[17] Berger, F.P., Hau, K.F.F.L. 1979. Local mass/heat transfer distribution on surfaces roughened with small square ribs. Int. J. Heat Mass Transfer. 22: 1645-1656.

[18] Grifoll, J., Farriol, X., Giralt Francesc. 1986. Mass Transfer at smooth and rough surfaces in a circular Couette flow. Int. J. Heat Mass Transfer. 29(12): 1911-1918.

[19] Wang, D., Huang, Y., Ewing, D., Chow, T., Cotton, J., Noseworthy, M.D., Ching, C.Y., 2015. On the non-destructive measurement of local mass transfer using X-ray computed tomography. Int. J. Heat Mass Transfer. 81: 531-541.

[20] Sobel, I. 1990. An Isotropic 3×3 Gradient Operator. Machine vision for three dimensional scenes, Freeman, H., Academic Pres, NY, 376-379.

[21] Postlethwaite, J., Lotz, U. 1988. Mass transfer at erosion-corrosion roughened surfaces. The Canadian Journal of Chemical Engineering. 66: 75-78.

[22] Dooley, R.B., 2008. Flow accelerated corrosion in fossil and combined cycle/HRSG plants. PPCHEM, 68-89.

[23] Thomas, R. M. 1979. Size of scallops and ripples formed by flowing water. Nature, 277(25): 281-283.

[24] Moody, L.F. 1944. Friction factors for pipe flow. *Transaction of the ASME*. 66: 671-84.

Chapter 6

Development of surface roughness and its effect on mass transfer in an S-shaped back to back bend at Reynolds number of 200,000

Complete citation:

Wang D., Ewing D., Ching C.Y. 2016. Development of surface roughness and its effect on mass transfer in an S-shaped back to back bend at Reynolds number of 200,000. *In. J. Heat Mass Transfer.* Submitted August 2016.

Relative Contributions:

Wang D.: Performed all experiments, interpretation and analysis of the data and wrote the first draft of the manuscript including all figures and text.

Ewing D.: Assisted in the interpretation and discussion of results.

Ching C. Y.: Supervisor and was responsible for the final draft submittal to the journal.

Abstract

Experiments were performed to investigate the local development of roughness and its effect on mass transfer in an S-shaped bend at Reynolds number of 200,000. The tests were performed over four consecutive time periods using a 203 mm diameter test section with a dissolving gypsum lining to water in a closed flow loop at a Schmidt number of 1200. The surface roughness and mass transfer over the test periods were measured using X-ray CT scans of the surface. Two regions of high mass transfer are found: along the intrados of the first and second bend. The surface roughness in these two regions, characterized by the height-to-spacing ratio, grows more rapidly than in the upstream pipe. There is an increase in the mass transfer with time, which corresponds well with the local increase in the height-to-spacing ratio of the roughness. The two regions of high mass transfer enhancement in the bend can be attributed to both a roughness effect and a geometry effect. The geometry effect was determined by normalizing the local mass transfer with that in a straight pipe with equivalent surface roughness. The mass transfer enhancement due to the geometry effect was found to be relatively constant for the two high mass transfer regions, with a value of approximately 1.5.

6.1 Introduction

Flow accelerated corrosion (FAC) is a piping degradation mechanism that will result in pipe wall thinning due to the dissolution of the magnetite oxide layer on carbon steel surfaces to the bulk flow [1]. To identify and mitigate FAC, locations of high mass transfer in the piping systems must be identified. The local mass transfer rates can depend on a number of factors, including the surface roughness and local flow and turbulence due to the local piping geometry. Flow in bends is subject to severe changes in the flow direction and leads to regions where the flow is accelerated into the bend and development of secondary flows, in the form of counter-rotating vortices in the streamwise direction [2, 3]. Both the acceleration of the flow into the bend and the pressure-driven secondary flow results in regions of high local shear stress on the pipe walls, which can directly enhance the mass transfer in those regions [4-8]. Mass transfer in single bends has been studied experimentally using dissolving wall methods, with high mass transfer regions on the inner wall near the bend inlet and in the pipe immediately downstream of the bend outlet on the outer wall side [7-8].

Bends in many piping systems are commonly attached back to back in different configurations, where the second bend can be at a different twist angle relative to the first. The mass transfer in the downstream bend of back to back bend configurations can be significantly enhanced [9-11]. The mass transfer in 0°(S), 90°(out of plane) and 180° (C) back to back bends were measured using a dissolving gypsum wall to water method at Reynolds numbers up to 130,000 [9-11]. The maximum mass transfer enhancement was found for the S-bend, followed by the out of plane and C- bend. The surface topography was measured after sectioning the test sections by laser scans, and the regions of high mass transfer were found to correspond to regions of high roughness. Recently, Wang at al. [12] measured the mass transfer and the resulting surface roughness in an S-bend at Re=300,000 and Sc=660 using non-destructive X-ray CT scans. The two regions of high mass transfer along the S-bend were found to have smaller spacing-to-height ratios of the roughness elements or scallops than in the upstream pipe.

In dissolving walls, the surface roughness develops due to mass transfer to the bulk flow and thereafter enhances the mass transfer by influencing the near-wall turbulent flow [13-17]. Most studies on the effect of surface roughness on mass transfer has been investigated for predefined roughness, such as V-grooves [13-15], sandpaper-roughness [16] and square rib roughness [17]. In these studies, only a limited range of roughness pitch to height ratios was studied and the mass transfer enhancement was primarily correlated to the roughness height. On dissolving walls, surface roughness develops naturally and the roughness can be characterized by multiple length scales, including the height, length and width of the roughness elements and the spacing between the elements [18-20]. Wang et al. [21] found the height to pitch ratio of the roughness elements was an important parameter, and developed a correlation for the mass transfer enhancement due to roughness in straight pipes in terms of this parameter.

Unlike in straight pipes, the mass transfer in bend configurations is enhanced by both local flow conditions due to the geometry effect and the developing roughness effect. The objective of this study is to investigate the roughness development in an

203mm diameter S-shape back to back bend and elicit the effect of geometry and roughness on mass transfer, especially in the high mass transfer regions. The local mass transfer rates and surface roughness were obtained from the change in topography of gypsum lined inner surfaces of a 203 mm diameter S-bend measured by X-ray Computed Tomography (CT) scans. The local mass transfer in four consecutive time tests were measured and correlated to the corresponding local roughness. The mass transfer enhancement in the bends was then correlated in terms of the roughness height to spacing ratio.

6.2 Measurement Methodology

The experiments were performed in a vertical flow loop shown in Fig. 6.1. Water flows from a 1.5 m^3 reservoir through a 101.5 mm diameter, 9 m long downcomer before entering a centrifugal pump at the bottom of the loop. The flow exits the pump to a 203 mm diameter (*D*), 9.5m long acrylic riser through a sudden expansion at the bottom of the riser. The flow passes through the riser with a length of 32*D* before entering the S-shape gypsum lined test section. The flow exits the test section to a 4.5*D* downstream pipe and a PVC S-bend leading back to the reservoir. The flow rate is adjusted using a variable speed controller for the pump and measured using two Pitot tubes; one in the

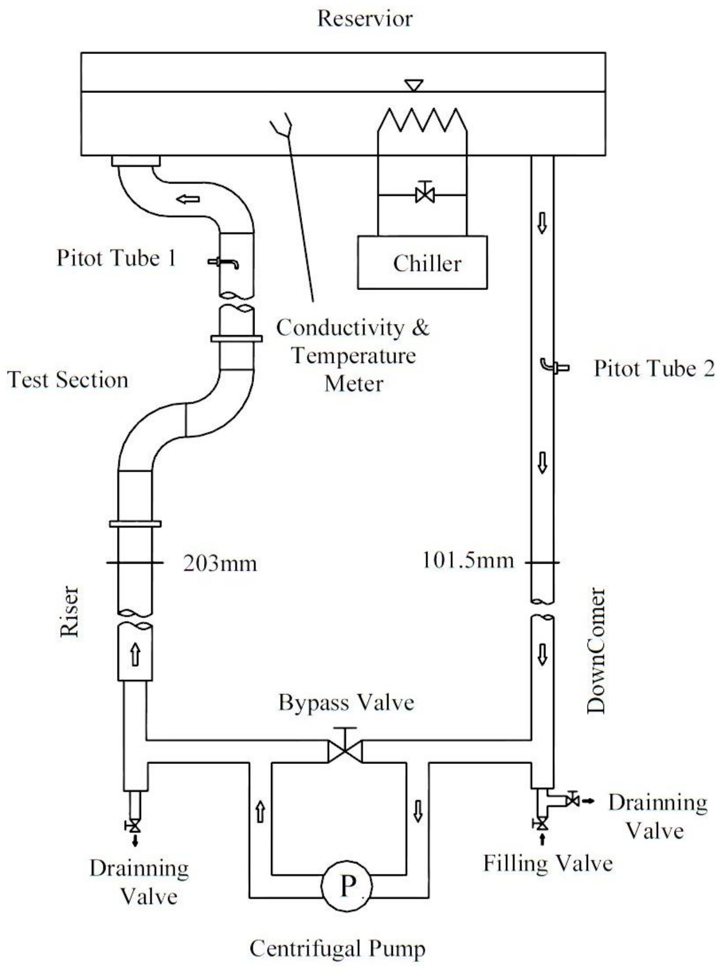

Fig. 6.1: Schematic diagram of experimental flow loop

riser downstream of the test section and the other in the downcomer. The temperature of water throughout the testing time was measured at two locations along the loop: (i) in the main reservoir and (ii) in the downcomer. The water temperature was maintained at 25±0.5 ℃ using a cooling coil in the reservoir. The electrical conductivity of water was measured by a conductivity probe and recorded on a computer. A calibration test was performed to correlate the concentration of dissolved gypsum to the electrical conductivity of the water at 25 ℃ before the experiment.

The experiment was performed using a 203 mm inner diameter S-shape test section, where the radius of curvature (r_c/D) of the two bends was 1.5, with a 2*D* long upstream and 1*D* long downstream pipe sections. The test section was cast using a 3D printed collapsible inner core and outer shell. The outer diameter of the inner core was 203 mm and the outer shell had an inner diameter of 244 mm, which resulted in a gypsum lining of 20.5 mm thickness. The outer shell and inner core were held concentrically during the casting process, using fixtures that included the base plate and end cap. The gypsum was generated by mixing hydrocal ($CaSO_4$•1/2H_2O) with water that yields gypsum with a density of 1580 kg/m^3. A small ratio of citric acid was added during the mixing stage to slow the curing process to facilitate the casting. The inner core was removed shortly after casting and the gypsum was left to cure under ambient conditions for approximately 15 days until the weight of the test section reached steady state using a scale accurate to ±25g.

The mass transfer experiments were performed by running water through the test sections for a series of four six hour tests, for a total run time of 24 hours. The inner surface topography and the thickness of the gypsum lining of the test section was measured using X-ray CT scans before and after each experiment. The image resolution at each cross-section was 1024×1024 pixels, which yielded a physical resolution of 0.5×0.5 mm. The through plane resolution (i.e slice thickness) was 1mm along the test section. The change in the topography of the inner surface was captured through a series of image processing routines: edge detection, three-dimensional reconstruction and coordinate system alignment, which are described in detail in [12]. The local wear of the inner surface due to dissolution was calculated from the decrease of the thickness of the gypsum lining after a series of wavelet filtering to remove noise and roughness [21]. The local mass transfer coefficient is calculated by

$$h_m = \frac{1}{c_w - c_{b0}} \rho \frac{\partial \delta}{\partial \tilde{t}} \tag{6.1}$$

where δ is the local wear of the inner surface, ρ is the density of gypsum and $\tilde{t}$ is a modified time to account for the change in bulk concentration of the flow during the testing period, given by

$$\tilde{t} = \frac{\int_0^T (c_w - c_b(t))dt}{c_w - c_{b0}} \tag{6.2}$$

The local Sherwood number is calculated as

$$Sh = \frac{h_m D}{D_m} \tag{6.3}$$

where D is the diameter of the test section, and D_m is the mass diffusivity (7.42×10^{-10} m^2/s) of gypsum at 25 ℃.

The surface roughness was quantified from the surface topography of the inner surface using wavelet analysis [20]. Following the approach of [21] for straight pipes, the surface roughness was characterized over smaller sampling areas of 80mm x 80mm to capture the local variation of roughness over the surface. Multiple roughness parameters were quantified to characterize the surface roughness, including RMS height, peak to valley height and density (spacing) of roughness elements. The mass transfer and Sherwood number was then evaluated over the same sampling areas. The roughness parameters at the mid time between the tests, which were obtained by linear interpolation between the start and end times of the test, was used when correlating the mass transfer to the roughness parameters.

6.3 Results and Discussion

A schematic showing the coordinate systems for the S-shape back to back bend is shown in Fig. 6.2 to illustrate the orientations for the different sections. The local distribution of mass transfer, represented by the Sherwood number, over the entire surface of the S-bend for the last time period as a representative case is shown in Fig. 6.3. A planar view of the local distribution of the Sherwood number for the four test periods is shown in Fig. 6.4. The results show two regions of high mass transfer: one along the intrados of the first bend (-90°) and the other along the intrados of the second bend (90°), which agrees with previous studies [10, 12]. The mass transfer in the first bend is higher than that in the second, particularly near the inlet, which differs from previous results [11]. The streamwise variation of Sherwood number averaged in each sampling area

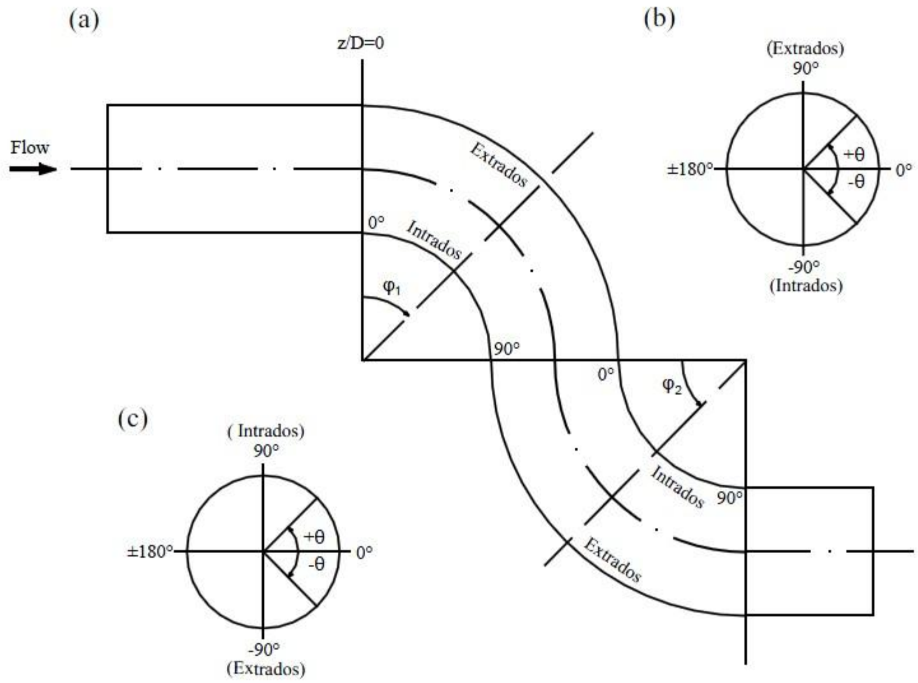

Fig. 6.2: Schematic of the test section showing the section planes relative to (a) Streamwise direction (b) Circumferential direction in the first bend (c) Circumferential direction in the second bend

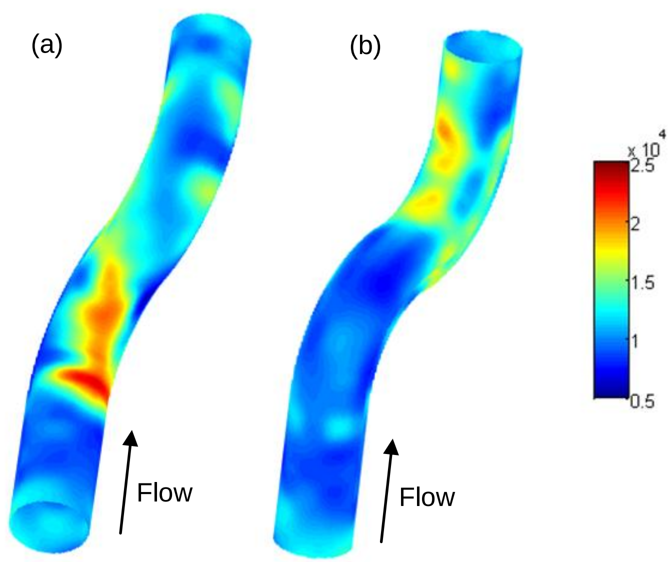

Fig. 6.3. Three-dimensional contours of local Sherwood number over the entire inner surface of the S-bend in last period (14.3~19hr): (a) along first bend intrados (b) along second bend intrados

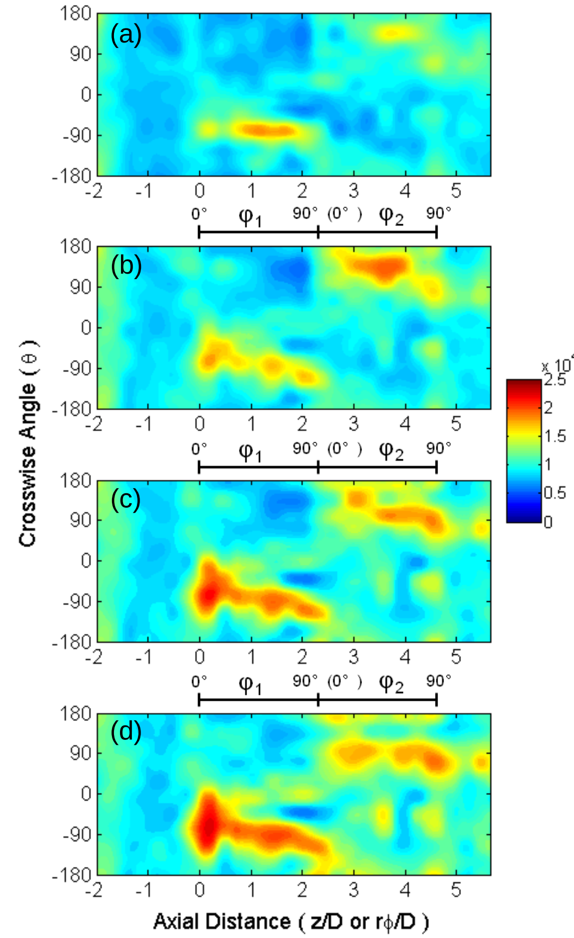

Fig. 6.4. Contours of local Sherwood number over the entire inner surface of the S-bend in four time (modified time) periods: (a) 0~4.9hr (b) 4.9~9.7hr (c) 9.7~14.3hr (d) 14.3~19hr

along four crosswise angles (-180°, -90°, 0° and 90°) of the S-bend for the four time periods are shown in Fig. 6.5. The mass transfer along the first bend intrados (-90°) increased rapidly in the first bend. It then decreased until the entrance to the second bend, and remained relatively constant beyond that. The mass transfer along the first bend extrados (90°) grew quite slowly until the second bend intrados, at which location there is an increase and subsequent gradual decrease towards the downstream section. The mass transfer also increased with time, prominently near the inlet in both bends. The mass transfer along the two side walls of the S-bend (-180° and 0°) was relatively uniform and similar to each other. The increase in mass transfer with time in the bends was greater than that in the upstream pipe, which could be partly attributed to a relatively higher rate of roughness development in the bend.

The azimuthal variations of Sherwood number at different streamwise locations along the S-bend with time are shown in Fig. 6.6. The two high mass transfer regions found in the first and second bend span about ±90° in the widest region. The high mass transfer region in the first bend intrados moved towards the second bend along the two side walls and merge together at the second bend intrados, resulting in the second high mass transfer region. This is also evident in Fig. 6.3, and in good agreement with Wang et al. [12]. The mass transfer increased more rapidly with time in the two high mass transfer regions.

Contours of the peak to valley height (e_{p-v}) of the surface roughness over the entire inner surface of the S-bend for the unworn and four worn surfaces at the different modified times are shown in Fig. 6.7. Initial defects due to the casting were found in

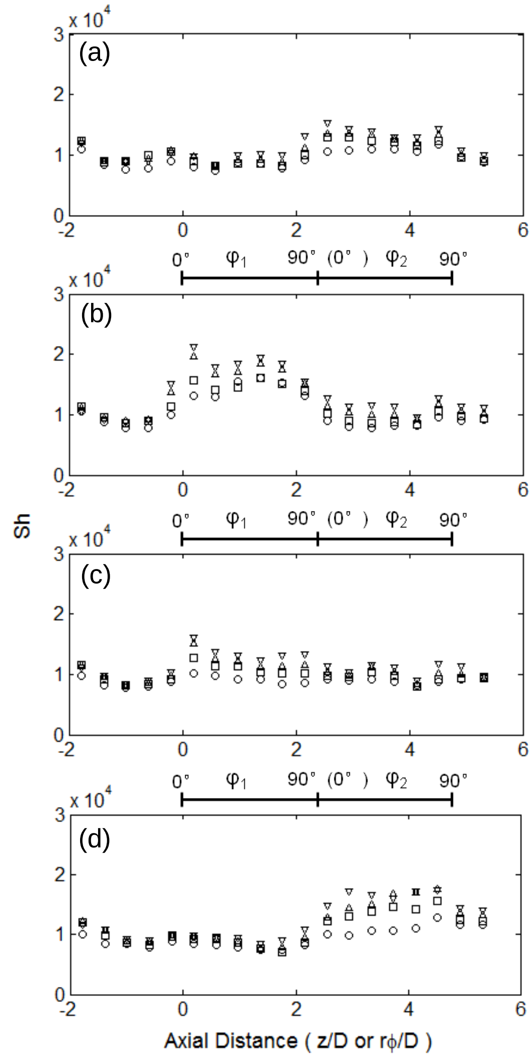

Fig. 6.5. Streamwise variations of Sherwood number along four crosswise angles: (a)-180 °(b) -90 °(c) 0 °and (d) 90 °of the S-bend in four time periods (Circle:0~4.9hr, Square:4.9~9.7hr, Triangle: 9.7~14.3hr; Inverted triangle: 14.3~19hr)

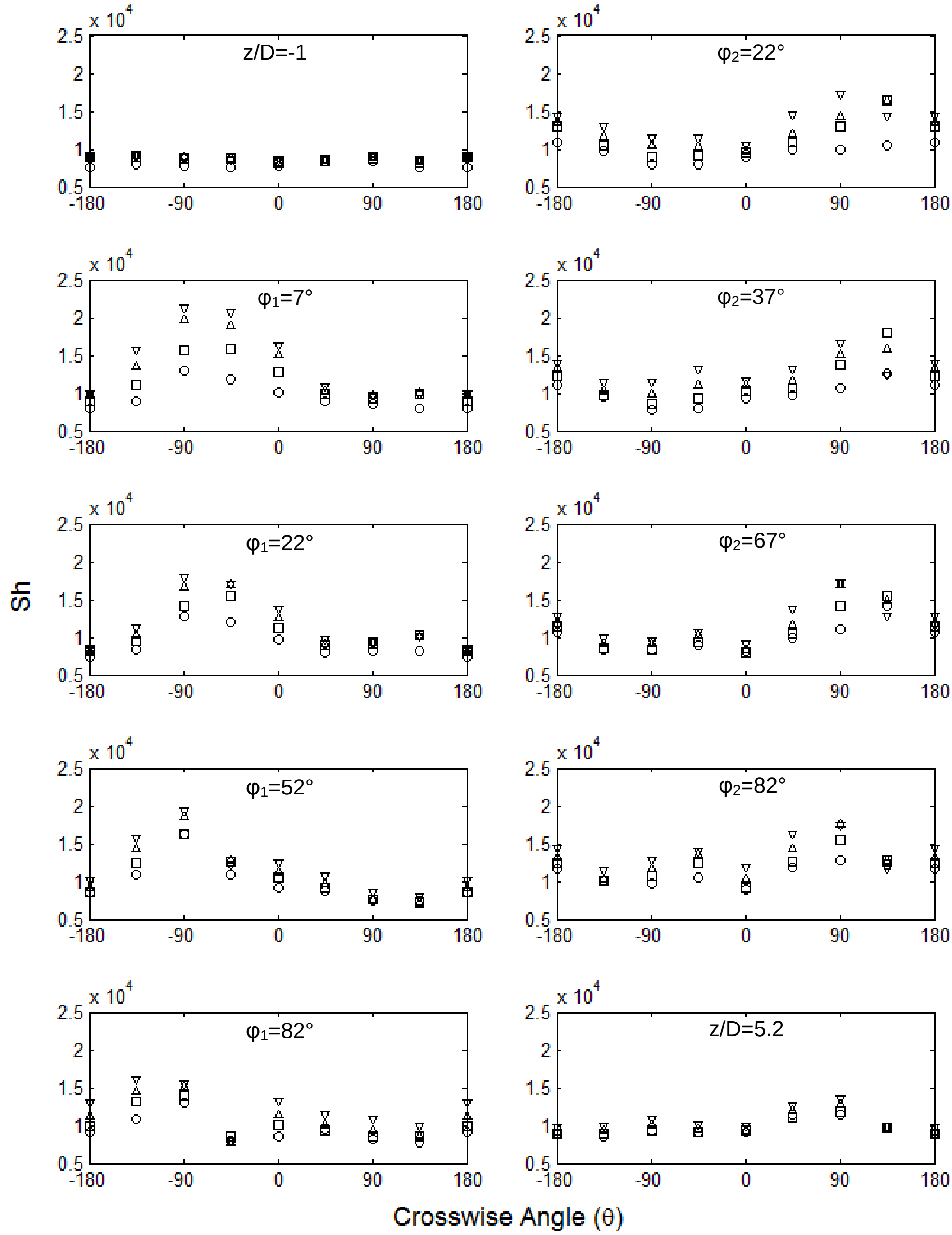

Fig. 6.6. Azimuthal variations of Sherwood number at different streamwise locations along the S-bend in four time periods (symbols as in Fig. 5)

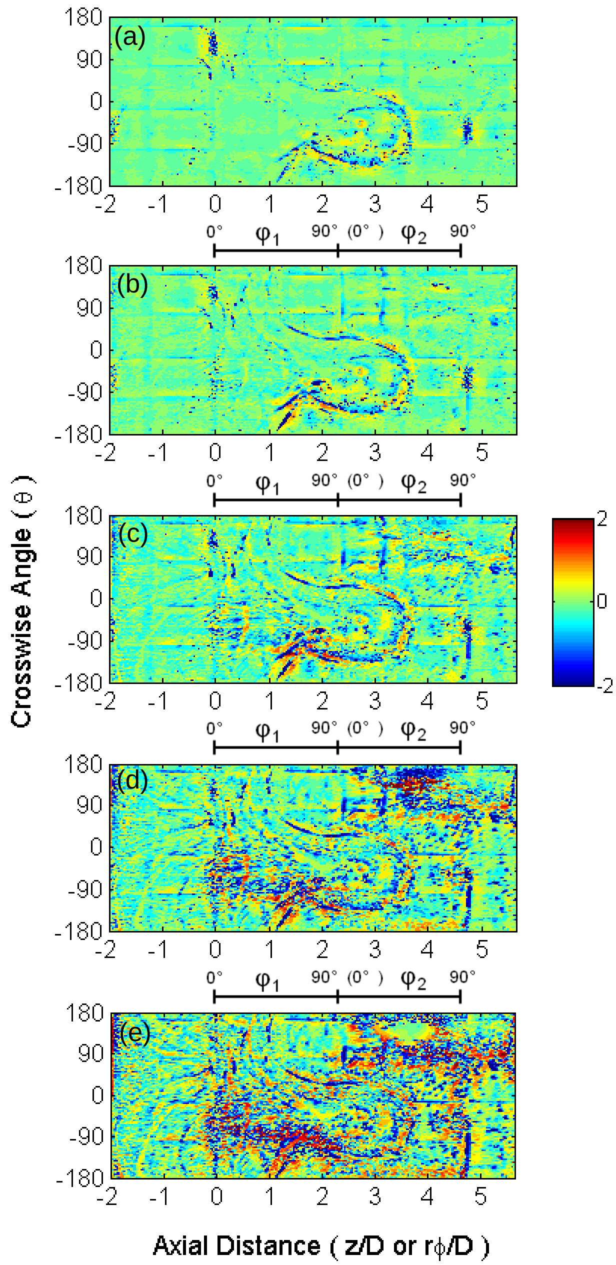

Fig. 6.7. Contours of surface roughness over the entire inner surface of the S-bend for the four tests: (a) Unworn (b) 4.9hr (c) 9.7hr (d) 14.3hr (e) 19hr

several areas from the unworn surface, particularly in the first bend. The areas of high surface roughness are seen to correspond to the areas with high mass transfer, as found in Fig. 6.3. The roughness was observed to develop more rapidly in the two high mass transfer regions, extending to the downstream areas.

The streamwise variations of peak to valley height (e_{p-v}) and streamwise spacing (λ_{str}) of the roughness along four crosswise angles (-180°, -90°, 0° and 90°) are shown in Fig. 6.8 and Fig. 6.9, respectively. In general, e_{p-v} increased with time at all locations. The roughness height developed rapidly near the first and second bend intrados (-90° and 90°) with the highest growth rates, which correspond to the regions of high mass transfer. The roughness height in the upstream pipe was lower than that in the bend, with a relatively slower growth rate. The streamwise spacing decreased with time and reached a limiting value, indicating the surface saturates with the roughness elements in a relatively short time period. The streamwise spacing was relatively uniform along the side walls (-180° and 0°) of the S-bend once the surface saturated with the roughness. The roughness spacing was smaller along the intrados of the first and second bend, which also corresponded to the regions where the roughness height increased quickly. The variations of the ratio of peak to valley height to the streamwise spacing (e_{p-v}/λ_{str}) are shown in Fig. 6.10 along the four crosswise angles. Two regions with high e_{p-v}/λ_{str} are clearly seen: one along the intrados of the first bend and the other along the intrados of second bend. These two regions correspond to the high mass transfer regions found in Fig. 6.5.

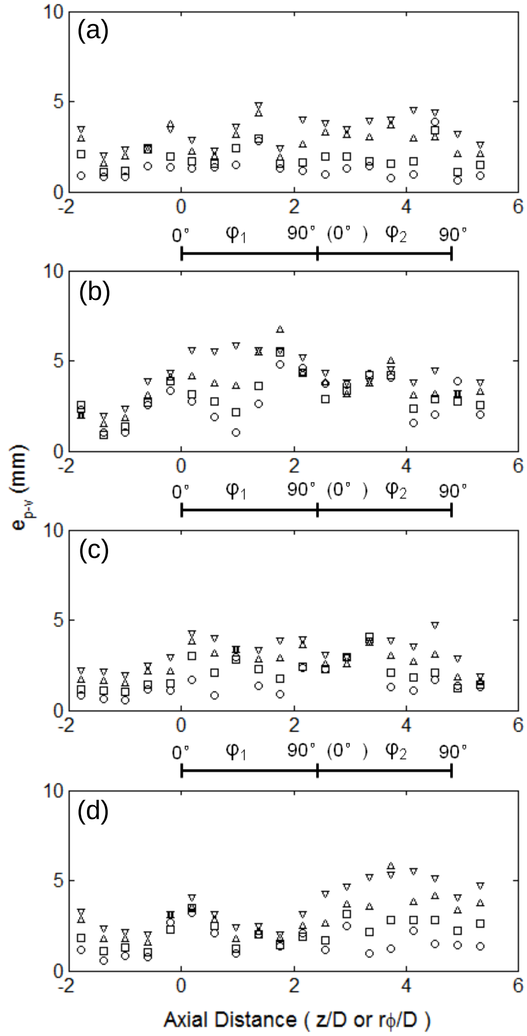

Fig. 6.8. Streamwise variations of peak to valley roughness height along four crosswise angles: (a)-180 °(b) -90 °(c) 0 °and (d) 90 °of the S-bend at different modified times (Circle: t=4.9hr, Square: t=9.7hr, Triangle: t=14.3hr; Inverted triangle: t=19hr)

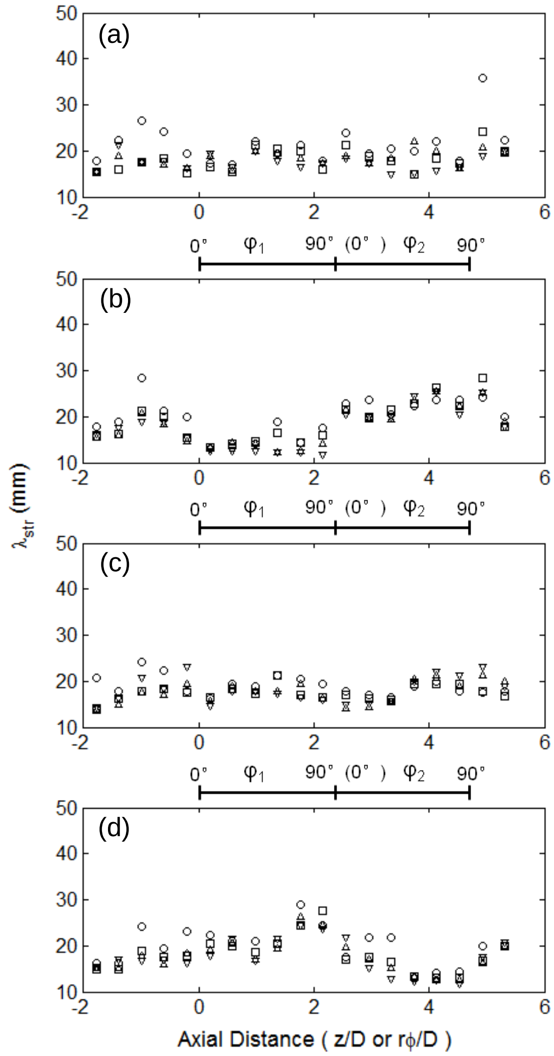

Fig. 6.9. Streamwise variations of streamwise spacing along four crosswise angles: (a)-180 °(b) -90 °(c) 0 °and (d) 90 ° of the S-bend at different modified times (symbols as in Fig. 6.8)

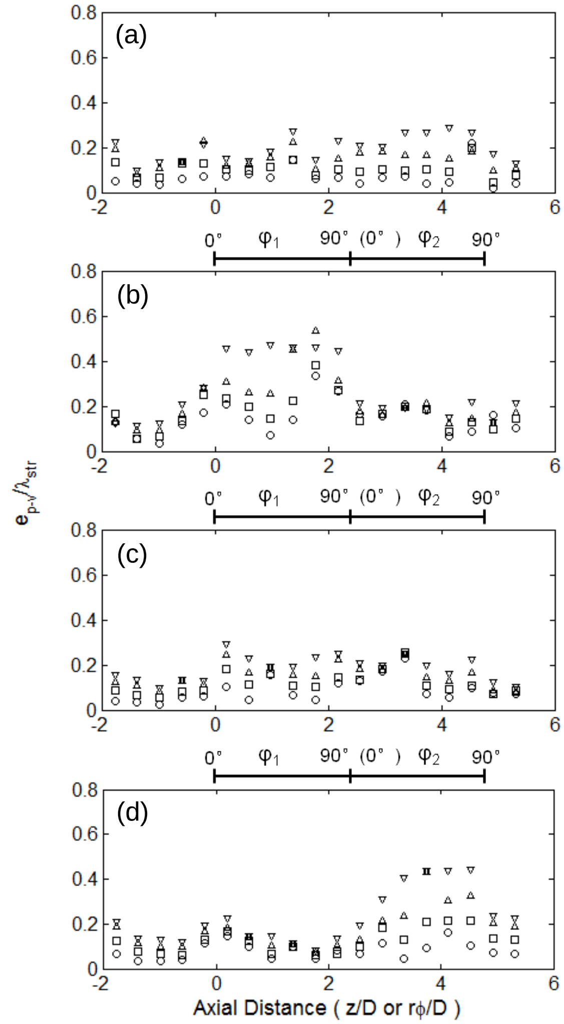

Fig. 6.10. Streamwise variations of height-to-spacing ratio along four crosswise angles: (a)-180 °(b) -90 °(c) 0 °and (d) 90 °of the S-bend at different modified times (symbols as in Fig. 8)

Wang et al. [21] developed a correlation for the effect of roughness on mass transfer in straight pipes as

$$Sh_{pipe} = 0.51\left(e_{p-v}/\lambda_{str}\right)^{0.2} Re^{0.84} \tag{6.4}$$

In bends, the mass transfer is enhanced due to both the developing roughness and local flow due to the bend geometry. The mass transfer within the bend normalized by that in a straight pipe with equivalent local surface roughness (Sh/Sh_{eq}) can be interpreted as that due to the geometry effect of the bend. The streamwise variations of Sh/Sh_{eq} along the four azimuthal locations for the different time periods are shown in Fig. 6.11, where Sh_{eq} is estimated from equation (6.4). There is reasonable collapse of Sh/Sh_{eq} for the different times at all locations, with higher values at the intrados of the first and second bend which can be attributed to the geometry effect. This can be quantified by plotting Sh/Sh_{eq} in the four local sampling areas corresponding to each of the high mass transfer regions along the intrados of first and second bend against e_{p-v}/λ_{str}, as shown in Fig. 6.12. The value is nearly constant and approximately 1.5 for both regions, indicating the mass transfer enhancement due to the geometry effect in these two regions is similar.

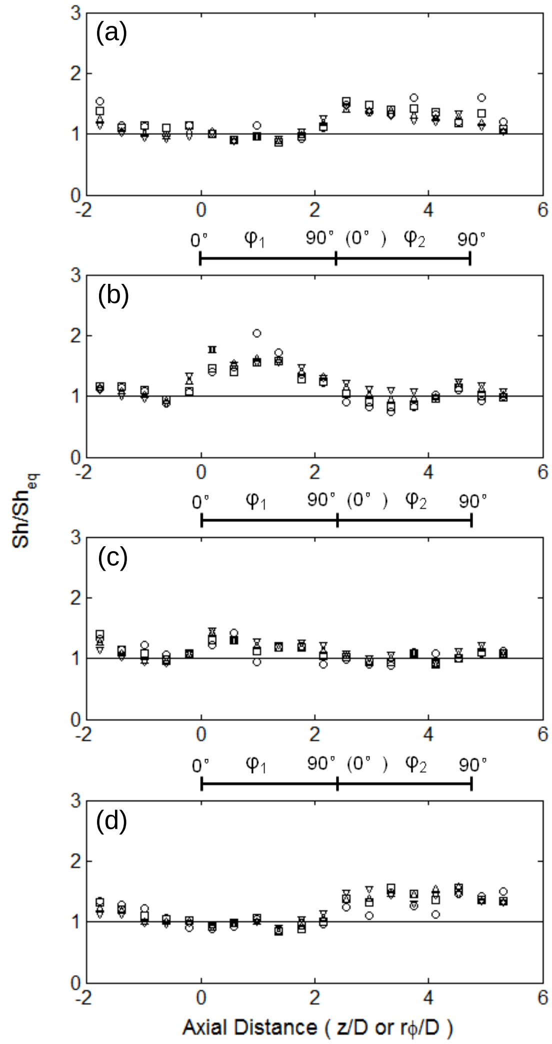

Fig. 6.11. Streamwise variations of Sherwood number normalized by Sherwood number with equivalent roughness in pipes [21] (Sh/Sh_{eq}) along four crosswise angles: (a)-180 ° (b) -90 °(c) 0 °and (d) 90 °of the S-bend at different modified times (symbols as in Fig. 5)

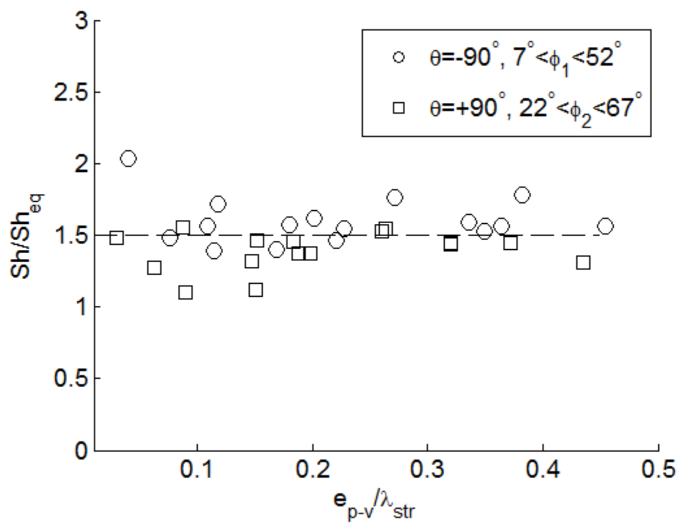

Fig. 6.12. Variations of Sh/Sh_{eq} with height-to-spacing ratio in the high mass transfer regions along first bend intrados and second bend intrados

6.4 Conclusions

The local development of the surface roughness and mass transfer in a 203 mm diameter back to back bend arranged in an S configuration was measured at a Reynolds number of 200,000. A gypsum lined test section was used which dissolved to flowing water in a closed flow loop at a Schmidt number of 1200. Tests were performed for a series of four six hour tests for a total test time of 24 hours. The topography of the inner surface and the thickness of the gypsum lining were measured using X-ray CT scans before and after each experiment. Two regions of high mass transfer are present in the bend: one along the intrados of the first bend and the other along the intrados of the second bend, with the former being higher than the latter. The two regions of high mass transfer correspond to regions of relatively higher roughness within the bend. The height to spacing ratio of the roughness along the intrados of the first and second bend sections increased more rapidly than in the upstream pipe. The mass transfer enhancement in these two regions can be attributed to both a roughness effect and a geometry effect. The local mass transfer within the bend was normalized by that in a pipe with an equivalent surface roughness, the ratio of which can be interpreted as the enhancement due to the geometry effect. The mass transfer enchantment due to the geometry effect for the two high mass transfer regions was found to be similar and approximately 1.5.

Nomenclature

C_w	Gypsum concentration at the wall [g/l]
C_b	Gypsum concentration in the bulk flow [g/l]

C_{b0}	Initial gypsum concentration in the bulk flow [g/l]
D	Inner diameter of test section [mm]
D_m	Mass transfer diffusivity [m^2/s]
$e_{p\text{-}v}$	Peak to valley roughness height [mm]
h_m	Mass transfer coefficient [m/s]
Re	Reynolds number
r	Radius of bend curvature [mm]
Sc	Schmidt number
Sh	Sherwood number
Sh_{pipe}	Sherwood number in straight pipes
Sh_{eq}	Sherwood number for equivalent roughness
t	Experimental time [s]
$\tilde{t}$	Modified time [s]
z/D	Dimensionless streamwise distance

Greek Symbols

δ	Local wear on pipe inner surface [mm]
θ	Angle in the azimuthal direction [°]
λ_{str}	Streamwise spacing of roughness element [mm]
ρ	Gypsum density [kg/m^3]
φ_1	Angle of curvature along the first bend [°]
φ_2	Angle of curvature along the second bend [°]

6.5 References

[1] Pietralik, J.M., Schefski, C.S. 2011. Flow and mass transfer in bends under flow-accelerated corrosion wall thinning conditions. Journal of Engineering for Gas Turbines and Power. 133(1) 012902: 1-7.

[2] Enayet, M.M., Gibson, M.M., Taylor, A. M. K.P., Yianneskis, M. 1982. Laser-Doppler measurements for laminar and turbulent flow in pipe bend, Int. J. Heat Fluid Flow. 3(4): 213–220.

[3] Sudo, K., Sumida, M., Hibara, H. Experimental investigation on turbulent flow in a circular-sectioned 90-degree bend. Experimental in Fluids. 25(1998): 42-49.

[4] El-Gammal, M., Mazhar, H., Cotton, J.S., Schefski, C., Pietralik, J., Ching, C.Y. 2010. The hydrodynamic effects of single phase flow on flow accelerated corrosion in a 90 ° elbow. Nuclear Engineering and Design. 240:1589–1598.

[5] Achenbach, E. 1976. Mass transfer from bends of circular cross section to air. Future Energy Production System. Academic Press. New York, 1: 327-337.

[6] Sparrow, EM. Chrysler, GM. 1986. Turbulent flow and heat transfer in bends of circular cross section: i- heat transfer experiments. ASME Journal of Heat Transfer. 108: 40-47.

[7] Wilkin, SJ., Oates, HS., Coney, M. 1983. Mass transfer on straight pipes and 90 ° bends measured by the dissolution of plaster (1st Edition). Central Electricity Research Laboratories Report. TPRD/L/2469/N83.

[8] Mazhar, H., Ewing, D., Cotton, J.S. Ching C.Y. 2013. Experimental investigation of mass transfer in 90 ° pipe bends using a dissolvable wall technique. Int. J. Heat Mass Transfer. 65: 280-288.

[9] Le, T., Ewing, D., Schefski, C., Ching, C.Y. 2014. Mass transfer in back-to-back elbows arranged in an out of plane configuration. Nuclear Engineering and Design. 270: 209-216.

[10] Chen, X., Le, T., Ewing, D., Ching, C. Y. 2016. Effect of bend separation distance on the mass transfer in back‐to‐back pipe bends arranged in a 180° configuration. Heat Mass Transfer. (DOI:10.1007/s00231-016-1774-9)

[11] Mazhar, H., Ewing, D., Cotton, J.S. Ching, C.Y. 2014. Mass transfer in dual pipe bends arranged in an S-configuration. Int. J. Heat Mass Transfer. 71: 747-757.

[12] Wang D., Le T., Ewing D., Ching C.Y. 2016. Measurement of local mass transfer and the resulting roughness in a large diameter S-bend at high Reynolds number. ASME. J. Heat Transfer. 138(6): 062001-7.

[13] Dawson, A., Trass, O. 1972. Mass transfer at rough surfaces. Int. J. Heat Mass Transfer. 15: 1317-1336.

[14] Tantiridge, S., Trass, O. 1984. Mass transfer at geometrically dissimilar rough surfaces. 1984. The Canadian Journal of Chemical Engineering. 62: 490-496.

[15] Zhao, W., Trass, O. 1997. Electrochemical mass transfer measurements in rough surface pipe flow: geometrically similar V-shaped grooves. Int. J. Heat Mass Transfer. 40(12): 2785-2797.

[16] Lolja, S. A. 2005. Momentum and mass transfer on sandpaper-roughened surfaces in pipe flow. Int. J. Heat Mass Transfer. 48: 2209-2218.

[17] Berger, F.P., Hau, K.F.F.L. 1979. Local mass/heat transfer distribution on surfaces roughened with small square ribs. Int. J. Heat Mass Transfer. 22: 1645-1656.

[18] Villien, B., Zheng, Y., Lister, D. 2005. Surface dissolution and the development of Scallops. Chem. Eng. Comm. 192: 125–136.

[19] Thomas, R. M. 1979. Size of scallops and ripples formed by flowing water. Nature. 277(25): 281-283.

[20] Wang, D., Ewing, D., Ching, C.Y. 2016. Time evolution of surface roughness in pipes due to mass transfer under different Reynolds numbers. Int. J. Heat Mass Transfer. 103:661-671.

[21] Wang, D., Ewing, D., Ching, C.Y. 2016. The effect of naturally developing roughness on the mass transfer in pipes under different Reynolds numbers. Int. J. Heat Mass Transfer. (under review)

[22] Poulson, B. 1990. Mass transfer from rough surfaces. Corrosion Science. 30: 743-746.

Chapter 7

Summary and Conclusions

7.1 Summary and Conclusions

A novel measurement methodology to measure the mass transfer and the resulting roughness using X-ray CT scans was developed. In this method, test sections with a gypsum lining dissolving to water in a closed flow loop was used. The surface topography and the thickness of the gypsum lining is obtained by reconstruction of the full 3-D image from the CT scans before and after the test. The methodology was validated by measuring the mass transfer and roughness in a 203mm diameter straight pipe test section and comparing to measurements from traditional methods that included ultrasonic sensors, coordinate measurement machine (CMM) and laser scan techniques. Measurements for both the mass transfer and the roughness parameters were in good agreement with these traditional methods. Key advantages of the X-ray CT scan measurement methodology are that it provides detailed local data over the entire surface, can be used for complex piping geometries and is non-intrusive. The latter feature allows to capture the developing roughness on a soluble surface and the corresponding mass transfer.

Experiments were performed using the X-ray CT scan measurement methodology to characterize the development of roughness and its effect on mass transfer in straight pipes at Reynolds number of 50,000, 100,000 and 200,000. Gypsum lined test sections dissolving to water were used at Schmidt number of 1200. The high Schmidt number corresponds to that for the diffusion of the iron magnetite layer of carbon steel piping in water, and thus provides an analogous mass transfer environment to flow accelerated corrosion in power generation plants. The scalloped pattern roughness was observed to initiate locally and develop with time. The surface roughness was characterized by the rms and peak to valley height, integral length and width scales, aspect ratio and density of scallops. The scallops are found to initiate locally and eventually the surface gets saturated with the scallops. The growth rate of the scallops was found to collapse well when normalized by the turbulent inner time scale, indicating that the near-wall turbulence plays a significant role in the roughness development. There is an initial relatively slow growth rate in the roughness height, followed by a higher nearly linear growth rate. The density of scallops increases with time rapidly and eventually spatially saturates the surface. The normalized streamwise spacing when the surface is saturated ai approximately 1000 wall units, which agrees well with Thomas (1979). The mass transfer enhancement (Sh/Sh_s) was dependent on both the height and spacing of the roughness scallops. For the developing roughness, two periods of mass transfer were present: (i) an initial period of rapid increase in enhancement when the density of scallops increase till the surface is spatially saturated with the scallops and (ii) a slower period of increase in enhancement beyond this point, where the streamwise spacing is approximately constant and the roughness height grows more rapidly. The mass transfer enhancement was found to correlate well with the parameter $(e_{p-v}/\lambda_{str})^{0.2}$, with a weak dependence on Reynolds number.

The measurement technique was extended to a more complex piping geometry: a back-to-back bend arranged in an S configuration. Experiments were performed using a 203 mm diameter test section that had a radius of curvature of 1.5 times the diameter. Tests were run for 4 consecutive time periods at Reynolds number of 200,000 to determine the local development of the roughness within the bend geometry and its effect on mass transfer. In bends, the mass transfer is enhanced both by the local flow conditions due to the bend geometry and due to the developing roughness. An additional test was performed at a Reynolds number of 300,000. There were two regions of high mass transfer: one along the intrados of the first bend and the other along the intrados of the second bend, which agrees with previous studies. The two regions of high mass transfer correspond to regions of relatively higher roughness within the bend. The height to spacing ratio of the roughness along the intrados of the first and second bend sections increased more rapidly than in the upstream pipe. The mass transfer enhancement in these two regions can be attributed to both a roughness effect and a geometry effect. The local mass transfer within the bend was normalized by that in a pipe with an equivalent surface roughness, the ratio of which can be interpreted as the enhancement due to the geometry effect. The mass transfer enchantment due to the geometry effect for the two high mass transfer regions was found to be similar and approximately 1.5.

7.2 Research Contributions

The contributions of this thesis can be summarized as:

1. A novel non-destructive measurement technique was developed to characterize the development of surface roughness and mass transfer over a soluble surface using X-ray CT scans. The measurement methodology is non-intrusive and provides local quantitative data over the entire surface, and can be used to investigate mass transfer in complex piping geometries. This method is unique and first in the world.
2. Data reduction techniques were developed to characterize the time evolution of naturally developing roughness on soluble surfaces using the X-ray CT scans. The developing surface roughness was quantified for straight pipes at Reynolds numbers of 50,000, 100,000 and 200,000, and is the first study to report this quantitatively.
3. The mass transfer enhancement due to roughness was found to depend on both the height and spacing of the roughness elements. A new correlation was developed for the mass transfer enhancement in straight pipes due to roughness in terms of the height to spacing ratio as $(e_{p-v}/\lambda_{str})^{0.2}$, with a weak Reynolds number dependence.
4. The mass transfer enhancement in a back to back bend in a S configuration was found to depend on both the local flow condition due to the bend geometry and the developing roughness. The development of surface roughness was greater in regions of the bend section than in the upstream pipes. There is a good correlation between mass transfer enhancement and height to spacing ratio of the roughness.

7.3 Recommendations for Future Work

Due to limitations of preparing and performing experiments at such a large scale, the present experiments were only performed for a limited number of Reynolds numbers and only one for the S bend configuration. Additional run times to reach a fully developed roughness state will be very useful to determine if the roughness and mass transfer reach limiting values. Experiments at additional Reynolds numbers will provide data to improve the correlations developed in this study. Since the measurement methodology is suited for different piping geometries, experiments can be performed to determine the effect of having the second bend at different twist angles relative to the first to determine the geometry effect. Studies could also be performed to determine the development of roughness and its effect on mass transfer in common piping singularities such as orifices, nozzle and T-junctions.

Appendix A

Calculation of the modified time

A dissolving wall method using gypsum test sections dissolving to water was used in a closed flow loop to study mass transfer. As a result, the bulk concentration (C_b) in the loop increases over the course of the experimental time due to the dissolution of the gypsum (calcium sulfate) to the bulk flow. To account for the change in driving potential ($\Delta C = C_w - C_b$), the experimental time is modified to take this into account. The change in concentration of the bulk flow was measured and monitored by a conductivity probe in the reservoir of the flow loop. A calibration test was performed before the experiments to correlate the conductivity to the concentration.

A typical example showing the change of conductivity, bulk concentration (C_b) and concentration difference ($C_w - C_b$) for a gypsum straight pipe test section running 25 ° water at Re=200,000 and Sc=1200 for eight hours is shown in Fig A.1.

The relationship between the mass transfer and concentration is defined as

$$\rho d\delta = h_m(C_w - C_b)\, dt$$

Thus, the modified time to obtain the equivalent mass transfer with the initial bulk concentration is given by

$$\int_0^{t_{exp}} (c_w - c_b(t))dt = (c_w - c_{b0})t_{mod}$$

which leads to

$$t_{mod} = \frac{\int_0^{t_{exp}} (c_w - c_b(t))dt}{c_w - c_{b0}}$$

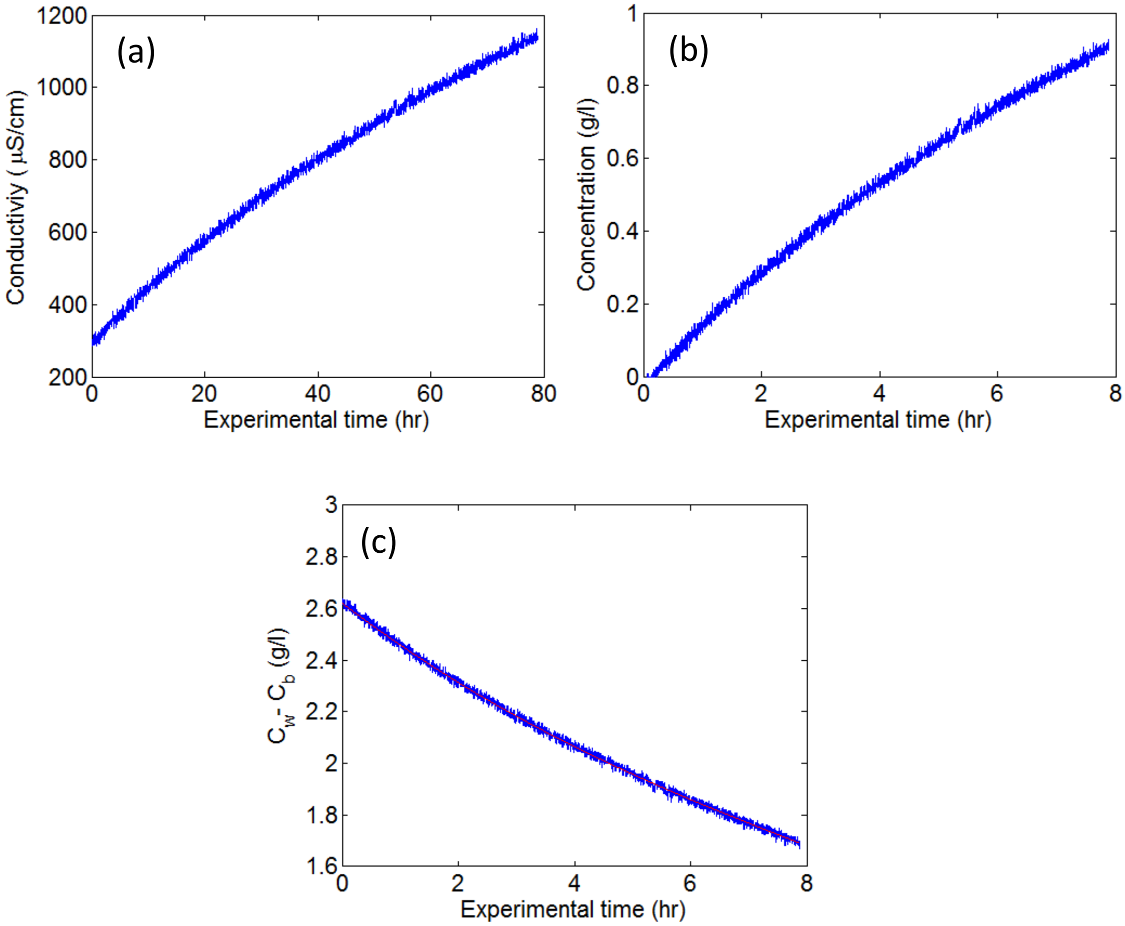

Fig. A.1: Variations of the (a) conductivity, (b) concentration and (c) concentration difference with time measured in the reservoir for a straight pipe test section running water for 8 hours at Re=200,000

Appendix B

Supplementary figures of Chapter 3

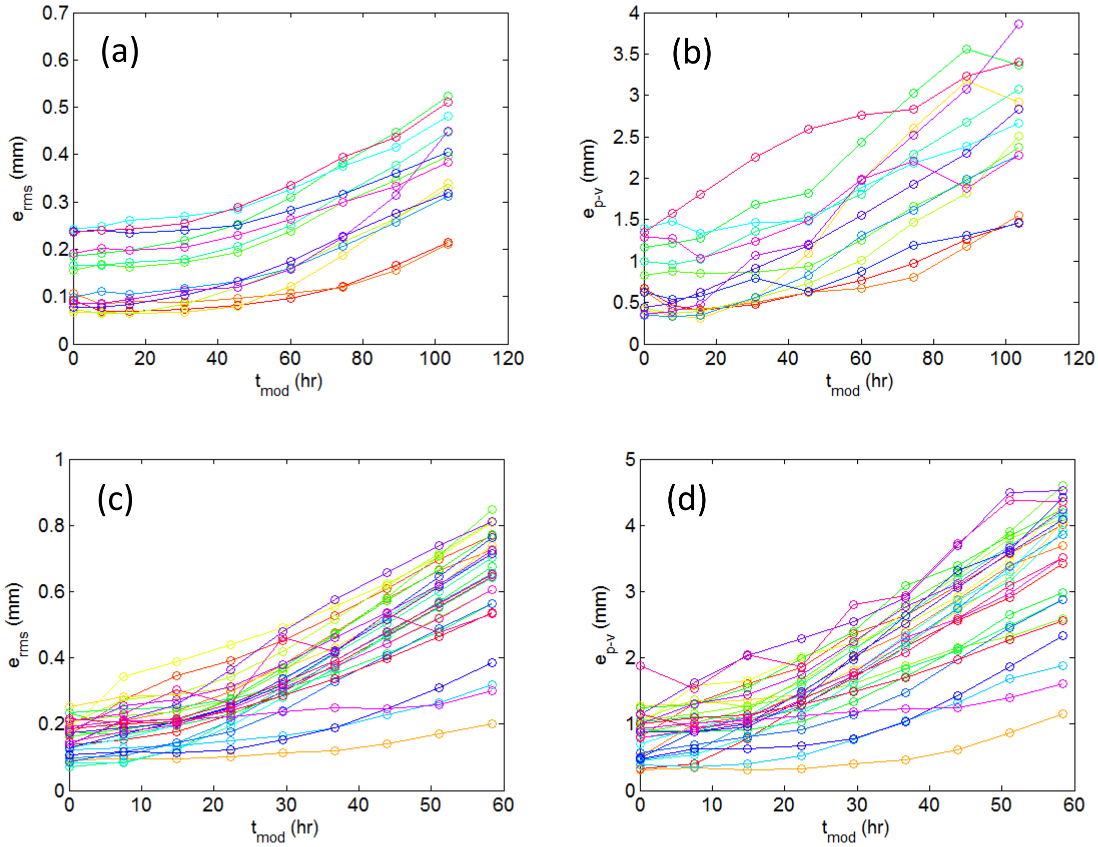

Fig. B.1: Variations in the RMS and peak to valley roughness height as a function of modified time in different sampling areas for: (a) RMS height for *Re* = 50,000, (b) P-V height for *Re* = 50,000, (c) RMS height for *Re* = 100,000, (d) P-V height for *Re* = 100,000

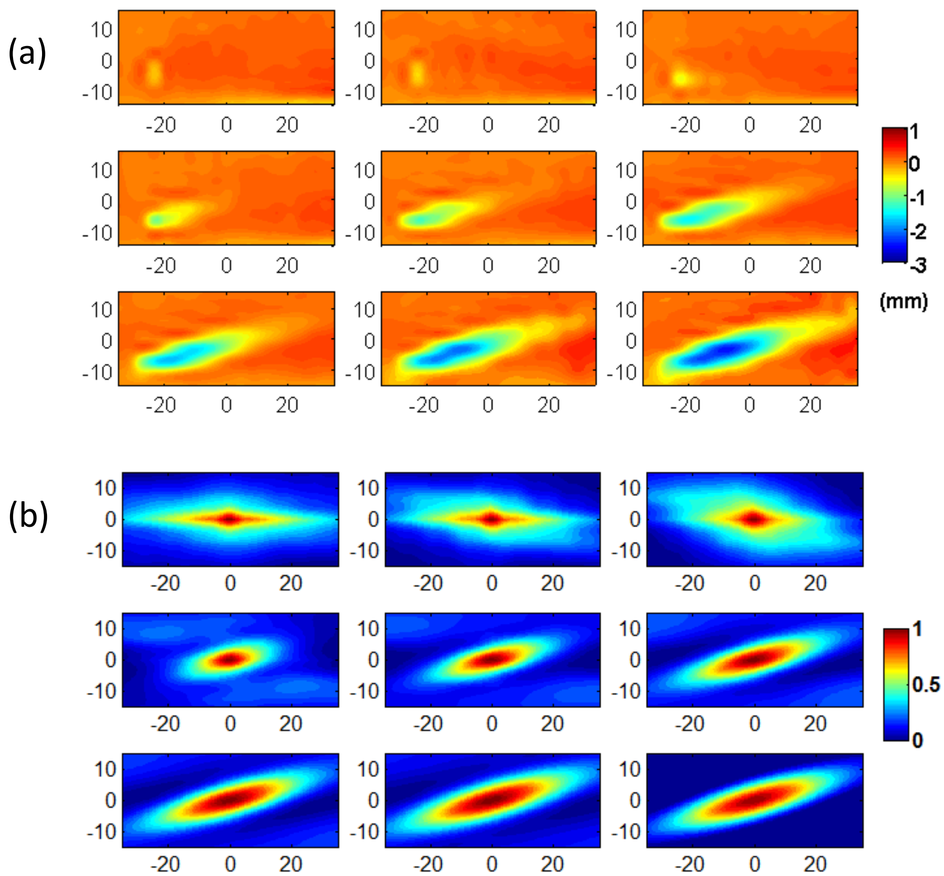

Fig. B.2: (a) Roughness deviation in one typical scallop region as a function of experimental time (b) Normalized 2D autocorrelation function applied in this scallop region at *Re* = 50,000

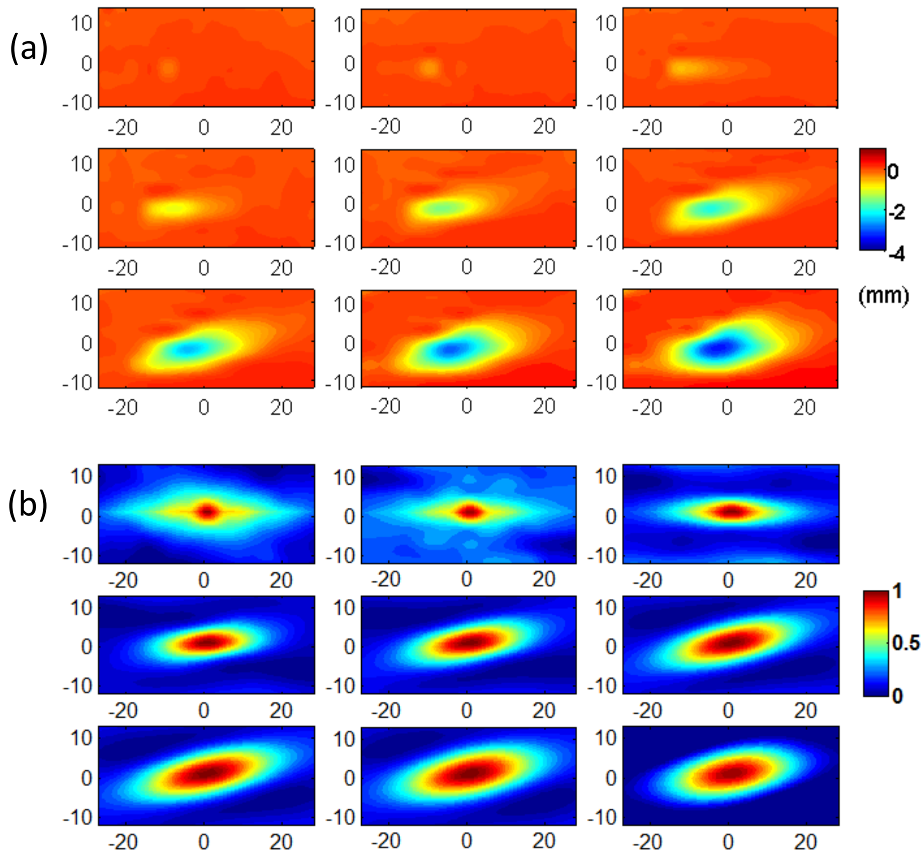

Fig. B.3: (a) Roughness deviation in one typical scallop region as a function of experimental time (b) Normalized 2D autocorrelation function applied in this scallop region at Re = 100,000

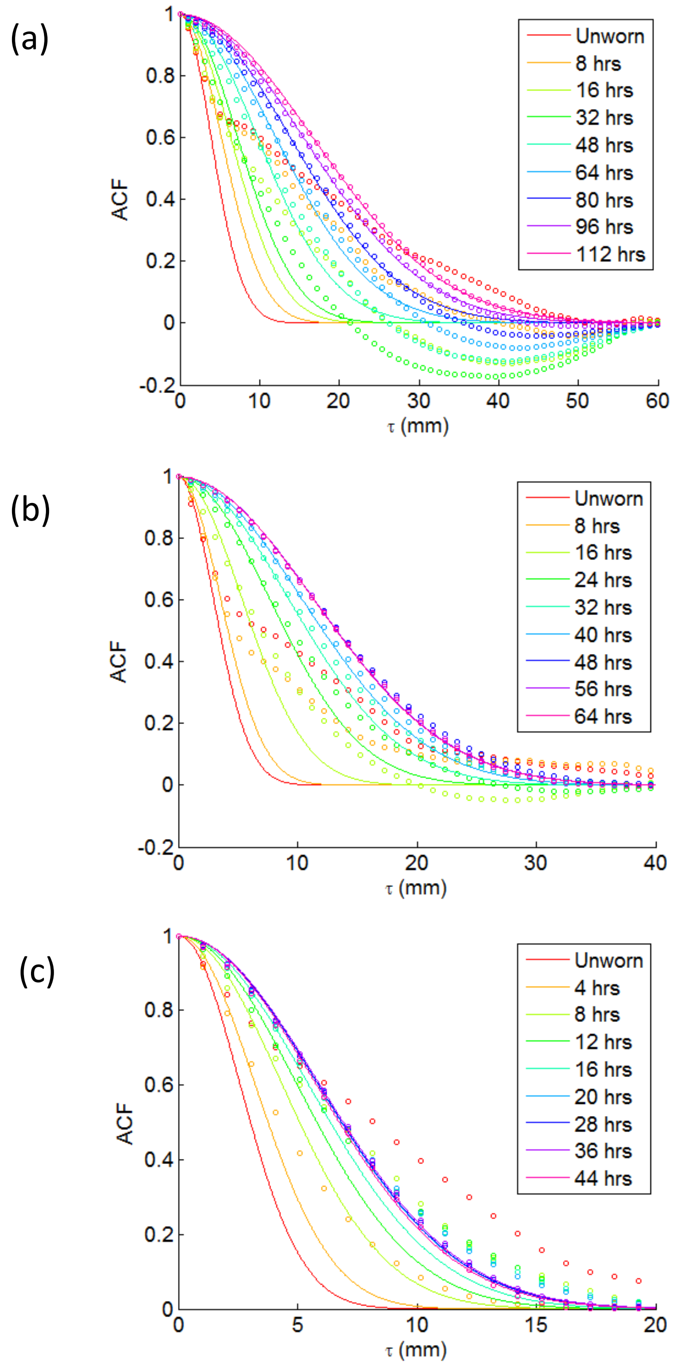

Fig. B.4: 1-D Gaussian curve fitting of data along maximum autocorrelation length direction from normalized 2-D autocorrelation function in one typical scallop region at different time for three Reynolds number: (a) *Re* = 50,000, (b) *Re* = 100,000, (c) *Re* = 200,000

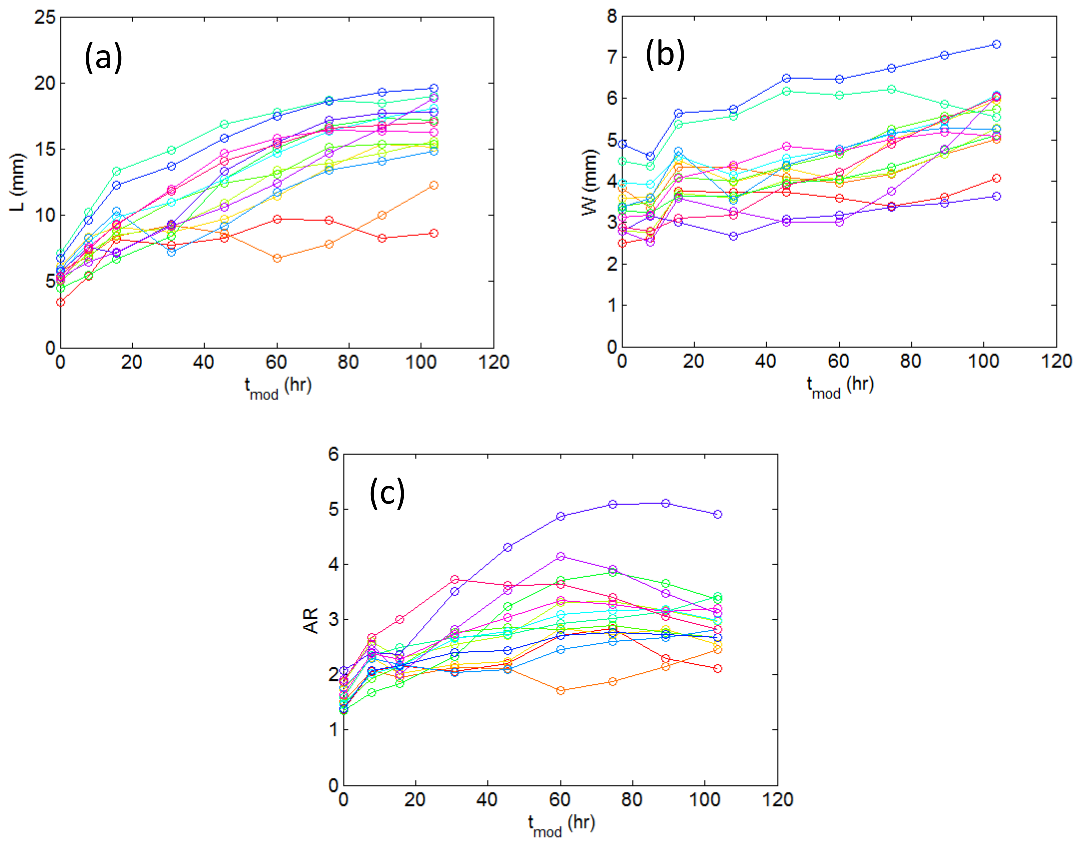

Fig. B.5: (a) Integral length (b) Integral width and (c) Aspect ratio obtained from ACF in different sampling areas (represented in different colored curves) as a function of modified time for *Re* = 50,000

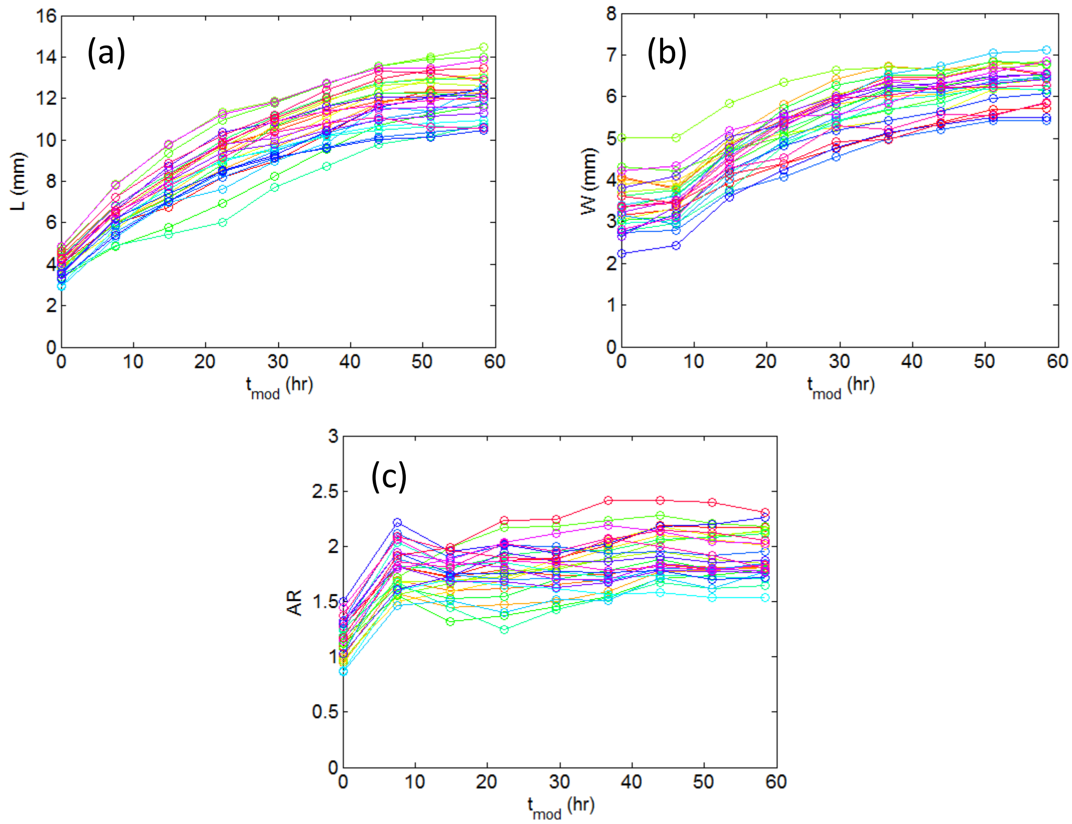

Fig. B.6: (a) Integral length (b) Integral width and (c) Aspect ratio obtained from ACF in different sampling areas (represented in different colored curves) as a function of modified time for *Re* =100,000

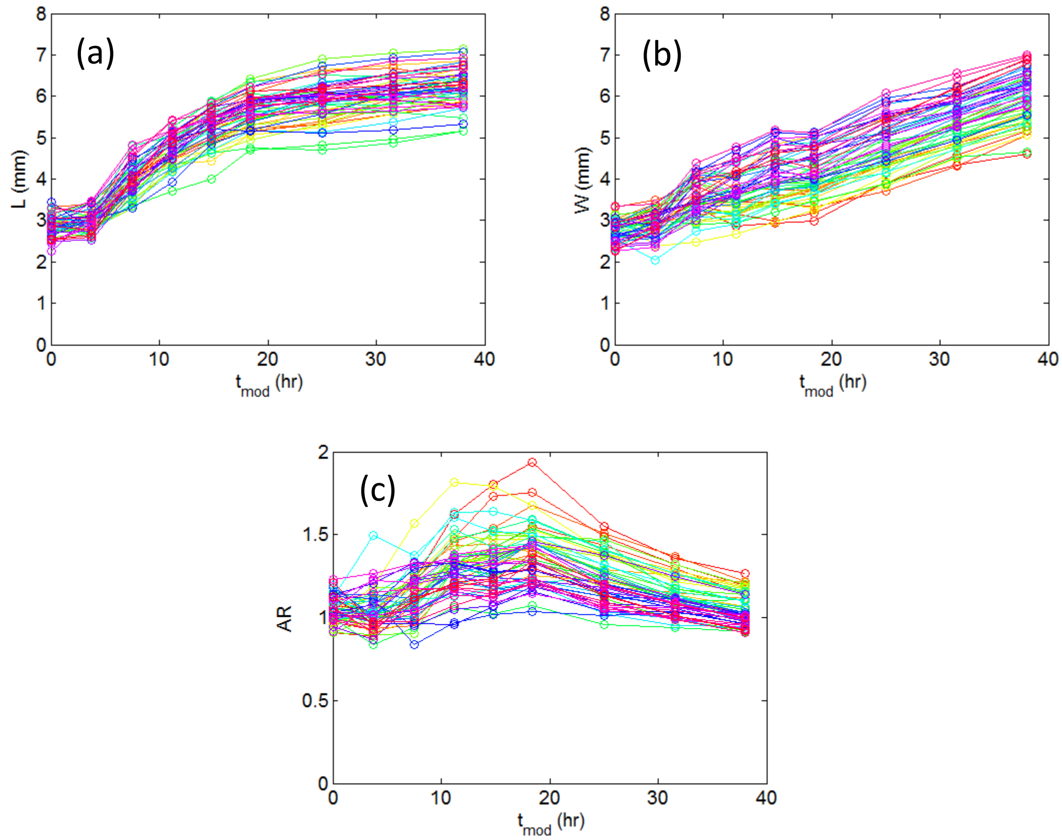

Fig. B.7: (a) Integral length (b) Integral width and (c) Aspect ratio obtained from ACF in different sampling areas (represented in different colored curves) as a function of modified time for *Re* =200,000

Appendix C

Supplementary figures of Chapter 5

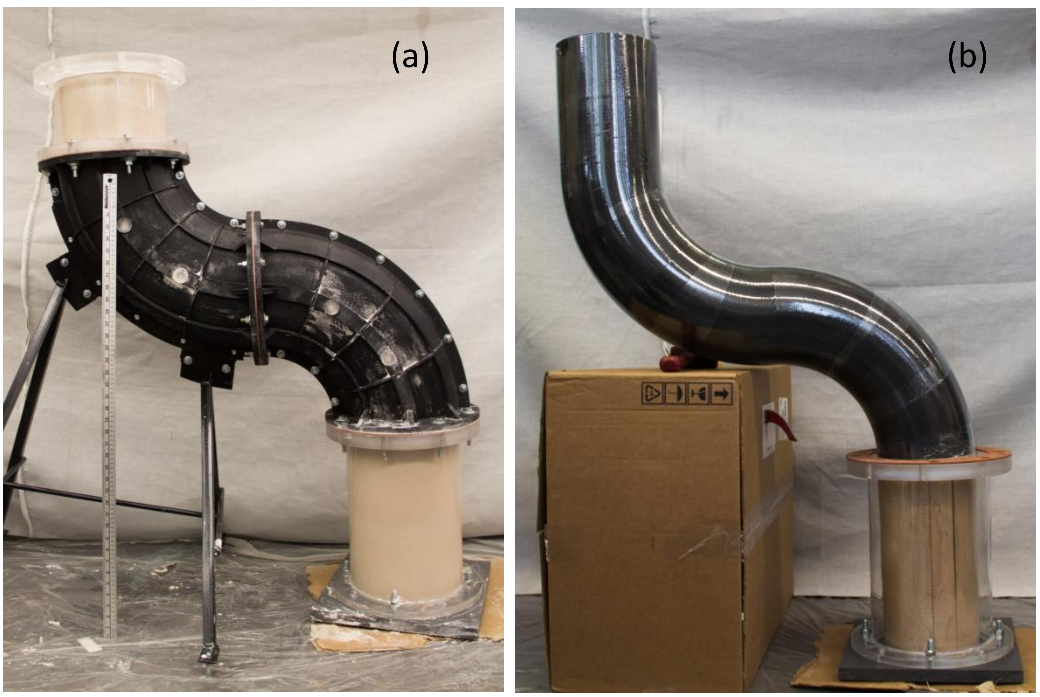

Fig. C.1: Picture of (a) manufactured gypsum test section and (b) inner core for casting of S-bend test section

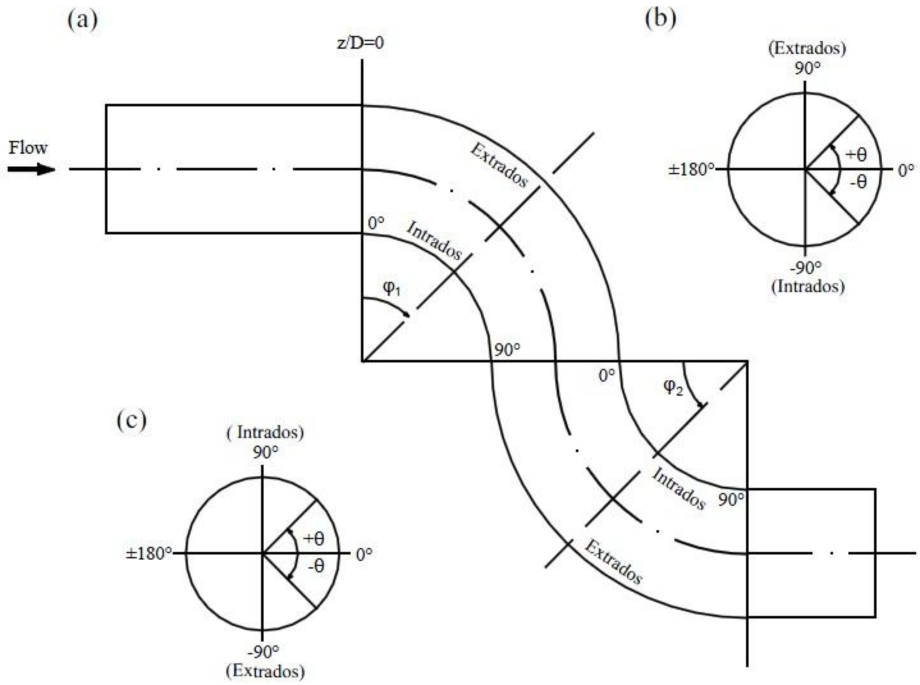

Fig. C.2: Schematic of the test section showing the section planes relative to (a) Streamwise direction (b) Circumferential direction in the first bend (c) Circumferential direction in the second bend

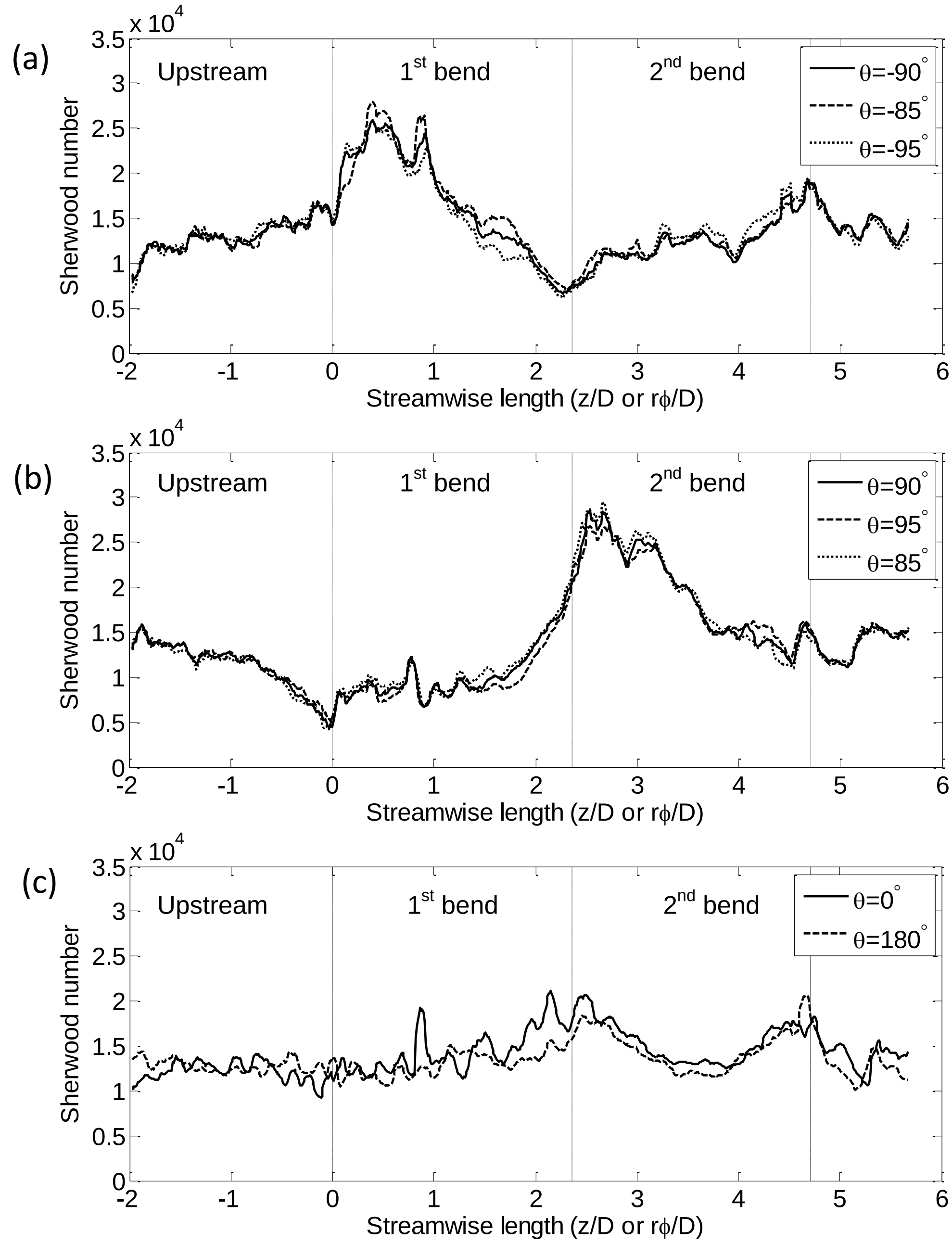

Fig. C.3: Streamwise profiles of local Sherwood number along (a) the first bend intrados (θ=-90±5°) (b) the first bend extrados (θ=90±5°) (c) first bend side walls (θ=0° and 180°)

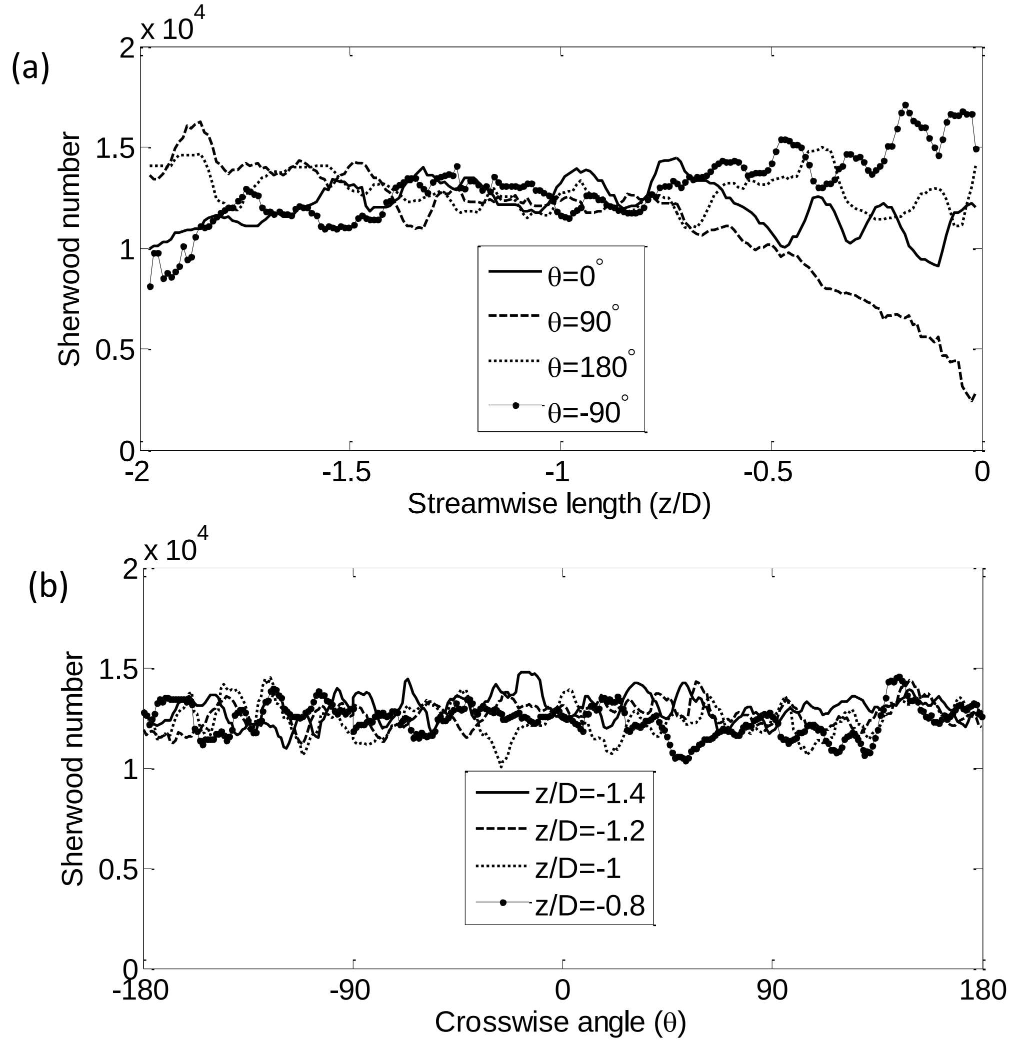

Fig. C.4: Local Sherwood number profiles in the upstream pipe along (a) streamwise direction at different azimuthal locations (θ=0 °, 90 °, 180 °, -90 °) and (b) azimuthal direction at different streamwise locations (z/D=-1.4, -1.2, -1, -0.8)

Appendix D

Matlab routines of data reduction

This appendix lists the main Matlab routines of data reduction process to obtain mass transfer and characterize corresponding surface roughness from CT scan images. The representative data processing codes are listed below using an example of straight pipes at Re=200,000.

D.1 Edge detection of CT scan images

Code Filename: Edgedetection.m

```
%This program find the edges in the CT scanned images of pipe section
close all;
clear all;
clc;
tic

numImg=919;  % number of CT images Slice 1 from outlet! TS3-5
count=0;
%Preallocation memory
x=zeros(1,20000000);
y=zeros(1,20000000);
z=zeros(1,20000000);
fileloop=2;

for k=1:numImg
   if  fileloop==1;  %  unworn Fig No.:1~913
       str1='C:\Users\Daq\Desktop\CT scan data\36in Long Straight Pipe\Test Section 
3_Scan 1_36 inch_Unworn_Aug 8-2014/CT29056.';
       str2='.dcm';
       strname=strcat(str1,num2str(k),str2);
   else     %
```

```
      str1='C:\Users\Daq\Desktop\CT scan data\36in Long Straight Pipe\Test Section
3_Scan 9_36 inch_Worn_Jan 7-2016/CT7775.';
      str2='.dcm';
      strname=strcat(str1,num2str(k),str2);
   end
   OringalFig = dicomread(strname);

   [FindEdge,threhold]=edge(OringalFig,'Sobel',0.0018);

   FinalEdge=medfilt2(FindEdge,[2,2]);
   for i=1:1024
      for j=1:1024
         if FinalEdge(i,j)==1
            count=count+1         %initiating count
            x(count)=i*0.2636719;   % TS3  worn resolution  (27x27cm)
            y(count)=j*0.2636719;
            z(count)=k*1;
         end
      end
   end
end

%   output all the data ponits detected.
outputmatrix=[x(1:count)' y(1:count)' z(1:count)'];
dlmwrite('PointCloud_worn.out', outputmatrix,'delimiter', '\t', 'newLine', 'pc');
toc
```

D.2 First edge separation for outer edge of the gypsum liner

Code Filename: EdgeSeperation.m

```
%This program separates the inner edge of the gypsum from the outer edge of the pipe
section.
close all
clear
clc

tic
fileID = fopen('pc_worn.txt');
C = textscan(fileID, '%f %f %f',...
   'delimiter',',','EmptyValue',-Inf);
fclose(fileID);
```

```
pc = [C{1} C{2} C{3}];

%Preallocation of memory for x,y,z,r and theta
x = zeros(length(pc),1);
y = zeros(length(pc),1);
z = zeros(length(pc),1);
phi = zeros(length(pc),1);
R = zeros(length(pc),1);
theta = zeros(length(pc),1);

%converting cartesian coordinate to polar coordinate
for i=1:length(pc)
    x(i)=pc(i,1);
    y(i)=pc(i,2);
    z(i)=pc(i,3);
end

r = sqrt(x.^2+y.^2);
for i=1:length(pc)
    if x(i)>=0 && y(i)>=0
        theta(i) = asind(y(i)/r(i));    % 1st Quadrant
    elseif x(i)<0 && y(i)>=0
        theta(i) = 180-asind(y(i)/r(i));    %2nd Quadrant
    elseif x(i)<0 && y(i)<0
        theta(i) = 180-asind(y(i)/r(i));    %3rd Quadrant
    else
        theta(i) = 360+asind(y(i)/r(i));    %4th Quadrant
    end
end

Dpipe=203.2;

figure;
plot(z/Dpipe,r/Dpipe)
xlabel('Streamwise (z/D)')
ylabel('Radius (r/D)')
axis([0 4.5 0.45 0.9])

%Gridding and indentifying 1st(hydrocal inner) and 2nd (hydrocal outer + outer shell)
%formulating a grid size having 1mm by 1mm resolution
zStart = 10; %z starts at 1 mm into the pipe
zEnd = 900; %z ends at 910 mm into the pipe
thetRes = 1; %1mm
```

```
zRes = 1; %1mm
CirN = round(pi*Dpipe/thetRes); %number of elements in the circumferential direction
StrN = round((zEnd-zStart)/zRes); %number of elements in the streamwise direction

zgridding = zeros(CirN,StrN);
for i = 1:CirN
   zgridding(i,:) = linspace(zStart,zEnd,StrN);
end

thetagridding = zeros(CirN,StrN);
for i = 1:StrN
   thetagridding(:,i) = linspace(0,360,CirN)';
end

dz = (zgridding(1,2)-zgridding(1,1))/2;
dt = (thetagridding(2,1)-thetagridding(1,1))/2;
pipethick = 20; %pipe nominal thickness for the unworn TS3-3
thres = pipethick/2; %half the nominal thickness
thres_oe = 3;       % Wall Thickness of PC pipe

zsortedpc = sortrows([theta z r],2);
rsorted = zsortedpc(:,3); thetasorted = zsortedpc(:,1); zsorted = zsortedpc(:,2);

rOUTavg = zeros(CirN,StrN); rINavg = zeros(CirN,StrN); rSHELavg =
zeros(CirN,StrN);
for j = 1:StrN
   zind = find(zgridding(1,j)-dz<=zsorted & zsorted<=zgridding(1,j)+dz);
   for i = 1:CirN
      ind = find(zgridding(i,j)-dz<=zsorted(zind(1):zind(length(zind))) &
zsorted(zind(1):zind(length(zind)))<=zgridding(i,j)+dz & ...
         thetagridding(i,j)-dt<=thetasorted(zind(1):zind(length(zind))) &
thetasorted(zind(1):zind(length(zind)))<=thetagridding(i,j)+dt);
      %countIN = 0; countOUT = 0; rIN = 0; rOUT = 0; %initiate count and radius
      rDummy = rsorted(ind+zind(1)-1);
      rINavg(i,j) = mean(rDummy(rDummy<min(rDummy)+thres/2)); %inner edge
      rOUT = rDummy(rDummy>min(rDummy)+thres+5);
      rOUTavg(i,j) =  mean(rOUT(rOUT<min(rOUT)+thres_oe)); %outer edge
      rSHELavg(i,j) = mean(rOUT(rOUT>=min(rOUT)+thres_oe)); %shell edge
   end
end
indNaN = find(isnan(rSHELavg)==1);
rSHELavg(indNaN) = 127; %rough estimate shell=127
indNaN = find(isnan(rOUTavg)==1);
```

```
rOUTavg(indNaN) = 123.5; %rough estimate hydrocal = 123.5

figure;
contourf(zgridding,thetagridding,rINavg)
xlabel('streamwise z/D')
ylabel('Theta')
figure;
contourf(zgridding,thetagridding,rOUTavg)
xlabel('streamwise z/D')
ylabel('Theta')

figure;
contourf(zgridding,thetagridding,rSHELavg)
xlabel('streamwise z/D')
ylabel('Theta')

figure;
for zindex=50:10:850
   plot(thetagridding(:,1),rINavg(:,zindex))
   hold on;
end

figure;
for zindex=50:10:850
   plot(thetagridding(:,1),rOUTavg(:,zindex))
   hold on;
end

figure;
for zindex=50:10:850
   plot(thetagridding(:,1),rSHELavg(:,zindex))
   hold on;
end

theta_vec = reshape(thetagridding,CirN*StrN,1); z_vec =
reshape(zgridding,CirN*StrN,1); rOUT_vec = reshape(rOUTavg,CirN*StrN,1);
rSHEL_vec = reshape(rSHELavg,CirN*StrN,1);
dlmwrite('outeredge.txt', [theta_vec z_vec rOUT_vec],'delimiter', '\t', 'newLine', 'pc');
dlmwrite('shelledge.txt', [theta_vec z_vec rSHEL_vec],'delimiter', '\t', 'newLine', 'pc');
toc
```

D.3 First alignment based on outer edge

Code Filename: Alignment.m

```
%This program aligns the pipe section based on the outer edge
clear all
close all
clc
tic

load 'pc_worn.txt'   %read in original point cloud
pc_x = pc_worn(:,1); pc_y = pc_worn(:,2); pc_z = pc_worn(:,3);

load 'outeredge.txt'
outedge = outeredge;

%defining S-pipe parameters
Dpipe = 8*25.4;

zStart = 10; %z starts at 10 mm into the pipe
zEnd = 900; %z ends at 390 mm into the pipe
thetRes = 1; %1mm
zRes = 1; %1mm
CirN = round(pi*Dpipe/thetRes); %number of elements in the circumferential direction
StrN = round((zEnd-zStart)/zRes); %number of elements in the streamwise direction
z = reshape(outedge(:,2),CirN,StrN);
theta = reshape(outedge(:,1),CirN,StrN);
r = reshape(outedge(:,3),CirN,StrN);

% convert cylindrical coordinate to cartisian coordinate
x_cart = zeros(CirN,StrN);y_cart = zeros(CirN,StrN);z_cart = zeros(CirN,StrN);
for i=1:StrN
    x_cart(:,i) = cosd(theta(:,i)).*r(:,i);
    y_cart(:,i) = sind(theta(:,i)).*r(:,i);
    z_cart(:,i) = z(:,i);
end
figure;
mesh(x_cart,y_cart,z_cart)

%Rz = sqrt(x_cart.^2+y_cart.^2); %Distance from the Z axis
zLine = z_cart(1,:)';

%Shift and rotation alignment of x and y axis based on straight pipe
nIter = 4;      %max number of iterations
counting = 0;
```

```
while counting < nIter
   lines = 80;     % # of lines used for correction (1/4 of the circle for resolution) 80 for
316; 160 for 638
   Ls = 30;       % skipped disorded lines (flanges)
   counting = counting +1;

   %offset in x axis (shift and rotation)
   localShiftx = ones(StrN,1); %preallocation of memory
   for n = 1+Ls:StrN-Ls
      sum = 0;
      for m = 1:round(lines/2)
         sum = sum + (r(m,n) - r(round(CirN/2)-m+1,n))/cosd(theta(m,n)) + (r(CirN-m,n) -
r(round(CirN/2)+m,n))/cosd(theta(m,n));
      end
      localShiftx(n,1) = sum/2/lines;
   end
   shiftconsideredx = localShiftx(1+Ls:StrN-Ls);
   zconsidered = zLine(1+Ls:StrN-Ls);

   %calculate the slope of the correction by 1st order fit
   px = polyfit(zconsidered, shiftconsideredx,1);
   lineSlopex = px(1,1);
   lineShiftx = px(1,2);
   anglex = atand(lineSlopex);
   fitValx = polyval(px,zconsidered);

   %coordinate system shift and rotation
   cartX = x_cart.*cosd(anglex)-z_cart.*sind(anglex)-lineShiftx;
   cartY = y_cart;
   cartZ = x_cart.*sind(anglex)+z_cart.*cosd(anglex);

   %updating cylindrical coordinate
   %updating r
   r = sqrt(cartX.^2+cartY.^2);
   zLine(1+Ls:StrN-Ls) = cartZ(1,1+Ls:StrN-Ls);

   %Updating theta
   for j=1:StrN
      for i=1:CirN
         if cartX(i,j)>=0 && cartY(i,j)>=0
            theta(i,j) = asind(cartY(i,j)/r(i,j));    % 1st Quadrant
         elseif cartX(i,j)<0 && cartY(i,j)>=0
            theta(i,j) = 180-asind(cartY(i,j)/r(i,j));    %2nd Quadrant
```

```
            elseif cartX(i,j)<0 && cartY(i,j)<0
                theta(i,j) = 180-asind(cartY(i,j)/r(i,j));    %3rd Quadrant
            else
                theta(i,j) = 360+asind(cartY(i,j)/r(i,j));    %4th Quadrant
            end
        end
    end

    %updating z
    z = cartZ;

    % updating cartesian coordinate from new cylindrical coordinate
    for i=1:StrN
        x_cart(:,i) = cosd(theta(:,i)).*r(:,i);
        y_cart(:,i) = sind(theta(:,i)).*r(:,i);
        z_cart(:,i) = z(:,i);
    end

    %alignment of original point cloud  'pc.txt'
    cartXpc = pc_x.*cosd(anglex)-pc_z.*sind(anglex)-lineShiftx;
    cartYpc = pc_y;
    cartZpc = pc_x.*sind(anglex)+pc_z.*cosd(anglex);
    pc_x = cartXpc;
    pc_y = cartYpc;
    pc_z = cartZpc;

    figure(counting)
    subplot(1,2,1)
    plot(zconsidered,localShiftx(1+Ls:StrN-Ls),':r',zconsidered,fitValx,'b')
    title('Shift in X direction')
    xlabel('Z/D down stream')
    ylabel('mm')
    set(gcf,'color','white')

    %offset in y axis  (shift and ratation)
    localShifty = ones(StrN,1);   %preallocation of memory
    for n = 1+Ls:StrN-Ls
        sum = 0;
        for m = 1:lines
            sum = sum + (r(round(CirN/4)-round(lines/2)+m,n) - r(CirN-
round(CirN/4)+round(lines/2)-m,n))/cosd(theta(round(CirN/4)-round(lines/2)+m,n)-90);
        end
        localShifty(n,1) = sum/2/lines;
```

```
end
shiftconsideredy = localShifty(1+Ls:StrN-Ls);
zconsidered = zLine(1+Ls:StrN-Ls);

%calculate the slope of the correction by 1st order fit
py = polyfit(zconsidered, shiftconsideredy,1);
lineSlopey = py(1,1);
lineShifty = py(1,2);

angley = -atand(lineSlopey);
fitValy = polyval(py,zconsidered);

%coordinate system shift and rotation
cartX = x_cart;
cartY = y_cart.*cosd(-angley)-z_cart.*sind(-angley)-lineShifty;
cartZ = y_cart.*sind(-angley)+z_cart.*cosd(-angley);

%updating cylindrical coordinate
% updating r
r = sqrt(cartX.^2+cartY.^2);
zLine(1+Ls:StrN-Ls) = cartZ(1,1+Ls:StrN-Ls);

%Updating theta
for j=1:StrN
   for i=1:CirN
      if cartX(i,j)>=0 && cartY(i,j)>=0
         theta(i,j) = asind(cartY(i,j)/r(i,j));    % 1st Quadrant
      elseif cartX(i,j)<0 && cartY(i,j)>=0
         theta(i,j) = 180-asind(cartY(i,j)/r(i,j));    %2nd Quadrant
      elseif cartX(i,j)<0 && cartY(i,j)<0
         theta(i,j) = 180-asind(cartY(i,j)/r(i,j));    %3rd Quadrant
      else
         theta(i,j) = 360+asind(cartY(i,j)/r(i,j));    %4th Quadrant
      end
   end
end

%updating z
z = cartZ;

% updating cartesian coordinate from new cylindrical coordinate
for i=1:StrN
   x_cart(:,i) = cosd(theta(:,i)).*r(:,i);
```

```
        y_cart(:,i) = sind(theta(:,i)).*r(:,i);
        z_cart(:,i) = z(:,i);
    end
    Rz = sqrt(x_cart.^2+y_cart.^2); %Distance from the Z axis

    %alignment of original point cloud
    cartXpc = pc_x;
    cartYpc = pc_y.*cosd(-angley)-pc_z.*sind(-angley)-lineShifty;
    cartZpc = pc_y.*sind(-angley)+pc_z.*cosd(-angley);

    pc_x = cartXpc;
    pc_y = cartYpc;
    pc_z = cartZpc;

    figure(counting)
    subplot(1,2,2)
    plot(zconsidered,localShifty(1+Ls:StrN-Ls),':r',zconsidered,fitValy,'b')
    title('Shift in Y direction')
    xlabel('Z/D down stream')
    ylabel('mm')
end

dlmwrite('pc_oea.txt',[cartXpc,cartYpc,cartZpc],'delimiter', '\t', 'newLine', 'pc');
toc
```

D.4 Second edge separation for inner and outer edges

Code Filename: Inneredge_oea.m

```
% This program separates the inner edge of the gypsum from the outer edge of the pipe
section. Need file 'pc_oea.txt'

clear all
close all
clc

tic
load 'pc_oea.txt'
pc = pc_oea;

%defining  parameters
Dpipe = 8*25.4;
```

```
%Preallocation of memory for x,y,z,r and theta
x = zeros(length(pc),1);
y = zeros(length(pc),1);
z = zeros(length(pc),1);
phi = zeros(length(pc),1);
R = zeros(length(pc),1);
theta = zeros(length(pc),1);

%converting cartesian coordinate to polar coordinate
for i=1:length(pc)
   x(i)=pc(i,1);
   y(i)=pc(i,2);
   z(i)=pc(i,3);
end

r = sqrt(x.^2+y.^2);
for i=1:length(pc)
   if x(i)>=0 && y(i)>=0
      theta(i) = asind(y(i)/r(i));    % 1st Quadrant
   elseif x(i)<0 && y(i)>=0
      theta(i) = 180-asind(y(i)/r(i));    %2nd Quadrant
   elseif x(i)<0 && y(i)<0
      theta(i) = 180-asind(y(i)/r(i));    %3rd Quadrant
   else
      theta(i) = 360+asind(y(i)/r(i));    %4th Quadrant
   end
end

plot(z/Dpipe,r/Dpipe)
xlabel('Streamwise (z/D)')
ylabel('Radius (r/D)')
%axis([0 8 0 0.9])

%Gridding and indentifying 1st(hydrocal inner) and 2nd (hydrocal outer + outer shell)
%formulating a grid size having 1mm by 1mm resolution
zStart = 10; %z starts at 1 mm into the pipe
zEnd = 900; %z ends at 910 mm into the pipe
thetRes = 1; %1mm
zRes = 1; %1mm
CirN = round(pi*Dpipe/thetRes); %number of elements in the circumferential direction
StrN = round((zEnd-zStart)/zRes); %number of elements in the streamwise direction

zgridding = zeros(CirN,StrN);
```

```
for i = 1:CirN
   zgridding(i,:) = linspace(zStart,zEnd,StrN);
end

thetagridding = zeros(CirN,StrN);
for i = 1:StrN
   thetagridding(:,i) = linspace(0,360,CirN)';
end

%Edge detection based on thickness threshold (half the nominal thickness)
%Interpolating the radius by averaging the radius within the cell
%zgridding-+dz and thetagridding-+dt
dz = (zgridding(1,2)-zgridding(1,1))/2;
dt = (thetagridding(2,1)-thetagridding(1,1))/2;
pipethick = 20; %pipe nominal thickness
thres = pipethick/2; %half the nominal thickness
thres_oe = 3; %thickness of the pipe

zsortedpc = sortrows([theta z r],2);
rsorted = zsortedpc(:,3); thetasorted = zsortedpc(:,1); zsorted = zsortedpc(:,2);

rOUTavg = zeros(CirN,StrN); rINavg = zeros(CirN,StrN); rSHELavg =
zeros(CirN,StrN);
for j = 1:StrN
   zind = find(zgridding(1,j)-dz<=zsorted & zsorted<=zgridding(1,j)+dz);
   for i = 1:CirN
      ind = find(zgridding(i,j)-dz<=zsorted(zind(1):zind(length(zind))) &
zsorted(zind(1):zind(length(zind)))<=zgridding(i,j)+dz & ...
         thetagridding(i,j)-dt<=thetasorted(zind(1):zind(length(zind))) &
thetasorted(zind(1):zind(length(zind)))<=thetagridding(i,j)+dt);
      %countIN = 0; countOUT = 0; rIN = 0; rOUT = 0;%initiate count and radius
      rDummy = rsorted(ind+zind(1)-1);
      rINavg(i,j) = mean(rDummy(rDummy<min(rDummy)+thres/2)); %inner edge
      rOUT = rDummy(rDummy>min(rDummy)+thres);
      rOUTavg(i,j) =  mean(rOUT(rOUT<min(rOUT)+thres_oe)); %outer edge
      rSHELavg(i,j) = mean(rOUT(rOUT>=min(rOUT)+thres_oe)); %shell edge

   end
end

%% Plot the results
figure;
subplot(2,3,1);
```

```
contourf(zgridding/Dpipe,thetagridding,rINavg,40)
xlabel('streamwise z/D')
ylabel('Theta')
% caxis([99 110]);
subplot(2,3,2);
contourf(zgridding/Dpipe,thetagridding,rOUTavg,40)
xlabel('streamwise z/D')
ylabel('Theta')
% caxis([115 120]);
subplot(2,3,3);
contourf(zgridding/Dpipe,thetagridding,rSHELavg,40)
xlabel('streamwise z/D')
ylabel('Theta')
% caxis([119 124]);

subplot(2,3,4);
for zindex=50:10:850
    plot(thetagridding(:,1),rINavg(:,zindex))
    hold on;
end
% ylim([99 110]);

subplot(2,3,5);
for zindex=50:10:850
    plot(thetagridding(:,1),rOUTavg(:,zindex))
    hold on;
end
% ylim([121 127]);

subplot(2,3,6);
for zindex=50:10:850
    plot(thetagridding(:,1),rSHELavg(:,zindex))
    hold on;
end
% ylim([124 130]);

%% Output
theta_vec = reshape(thetagridding,CirN*StrN,1); z_vec =
reshape(zgridding,CirN*StrN,1); rIN_vec = reshape(rINavg,CirN*StrN,1);
rOUT_vec = reshape(rOUTavg,CirN*StrN,1); rSHEL_vec =
reshape(rSHELavg,CirN*StrN,1);
dlmwrite('inneredge_oea.txt', [theta_vec z_vec rIN_vec],'delimiter', '\t', 'newLine', 'pc');
dlmwrite('outeredge_oea.txt', [theta_vec z_vec rOUT_vec],'delimiter', '\t', 'newLine', 'pc');
```

```
dlmwrite('shelledge_oea.txt', [theta_vec z_vec rSHEL_vec],'delimiter', '\t', 'newLine',
'pc');
toc
```

D.5 Second alignment based on inner edge

Code Filename: Alignment_ie.m

```
clear all
close all
clc
tic

pc = dlmread('C:\Users\Daq\Desktop\TS3 Roughness\Unworn\pc_oea.txt');   %read in
original point cloud
pcw = dlmread('C:\Users\Daq\Desktop\TS3 Roughness\Worn_8\pc_oea.txt');
pc_x = pc(:,1); pc_y = pc(:,2); pc_z = pc(:,3); %unworn
pcw_x = pcw(:,1); pcw_y = pcw(:,2); pcw_z = pcw(:,3); %worn

load 'C:\Users\Daq\Desktop\TS3 Roughness\Unworn\inneredge_oea.txt'
edge = inneredge_oea;

%defining  parameters
Dpipe = 8*25.4;

zStart = 10; %z starts at 10 mm into the pipe
zEnd = 900; %z ends at 900 mm into the pipe
thetRes = 1; %1mm
zRes = 1; %1mm
CirN = round(pi*Dpipe/thetRes); %number of elements in the circumferential direction
StrN = round((zEnd-zStart)/zRes); %number of elements in the streamwise direction
z = reshape(edge(:,2),CirN,StrN);
theta = reshape(edge(:,1),CirN,StrN);
r = reshape(edge(:,3),CirN,StrN);

figure;
contourf(theta,z,r);

r=[r(4:CirN,:);r(1:3,:)];  % rotation 1.67degree for unworn
figure;
contourf(theta,z,r);

% convert cylindrical coordinate to cartisian coordinate
```

```
x_cart = zeros(CirN,StrN);y_cart = zeros(CirN,StrN);z_cart = zeros(CirN,StrN);
for i=1:StrN
   x_cart(:,i) = cosd(theta(:,i)).*r(:,i);
   y_cart(:,i) = sind(theta(:,i)).*r(:,i);
   z_cart(:,i) = z(:,i);
end
figure;
mesh(x_cart,y_cart,z_cart)

%Rz = sqrt(x_cart.^2+y_cart.^2); %Distance from the Z axis
zLine = z_cart(1,:)';

%Shift and rotation alignment of x and y axis based on straight pipe
nIter = 4;      %max number of iterations
counting = 0;
while counting < nIter
   lines = 160;     % # of lines used for correction (1/4 of the circle for resolution) 80 for
316; 160 for 638
   Ls = 20;        % skipped disorded lines (flanges)
   counting = counting +1;

   %offset in x axis (shift and rotation)
   localShiftx = ones(StrN,1); %preallocation of memory
   for n = 1+Ls:StrN-Ls
      sum = 0;
      for m = 1:round(lines/2)
         sum = sum + (r(m,n) - r(round(CirN/2)-m+1,n))/cosd(theta(m,n)) + (r(CirN-m,n) -
r(round(CirN/2)+m,n))/cosd(theta(m,n));
      end
      localShiftx(n,1) = sum/2/lines;
   end
   shiftconsideredx = localShiftx(1+Ls:StrN-Ls);
   zconsidered = zLine(1+Ls:StrN-Ls);

   %calculate the slope of the correction by 1st order fit
   px = polyfit(zconsidered, shiftconsideredx,1);
   lineSlopex = px(1,1);
   lineShiftx = px(1,2);
   anglex = atand(lineSlopex);
   fitValx = polyval(px,zconsidered);

   %coordinate system shift and rotation
   cartX = x_cart.*cosd(anglex)-z_cart.*sind(anglex)-lineShiftx;
```

```
cartY = y_cart;
cartZ = x_cart.*sind(anglex)+z_cart.*cosd(anglex);

%updating cylindrical coordinate
%updating r
r = sqrt(cartX.^2+cartY.^2);
zLine(1+Ls:StrN-Ls) = cartZ(1,1+Ls:StrN-Ls);

%Updating theta
for j=1:StrN
   for i=1:CirN
      if cartX(i,j)>=0 && cartY(i,j)>=0
         theta(i,j) = asind(cartY(i,j)/r(i,j));    % 1st Quadrant
      elseif cartX(i,j)<0 && cartY(i,j)>=0
         theta(i,j) = 180-asind(cartY(i,j)/r(i,j));    %2nd Quadrant
      elseif cartX(i,j)<0 && cartY(i,j)<0
         theta(i,j) = 180-asind(cartY(i,j)/r(i,j));    %3rd Quadrant
      else
         theta(i,j) = 360+asind(cartY(i,j)/r(i,j));    %4th Quadrant
      end
   end
end

%updating z
z = cartZ;

% updating cartesian coordinate from new cylindrical coordinate
for i=1:StrN
   x_cart(:,i) = cosd(theta(:,i)).*r(:,i);
   y_cart(:,i) = sind(theta(:,i)).*r(:,i);
   z_cart(:,i) = z(:,i);
end

%alignment of origional unworn and worn point cloud
cartXpc = pc_x.*cosd(anglex)-pc_z.*sind(anglex)-lineShiftx;
cartYpc = pc_y;
cartZpc = pc_x.*sind(anglex)+pc_z.*cosd(anglex);

cartXpcw = pcw_x.*cosd(anglex)-pcw_z.*sind(anglex)-lineShiftx;
cartYpcw = pcw_y;
cartZpcw = pcw_x.*sind(anglex)+pcw_z.*cosd(anglex);

pc_x = cartXpc; pcw_x = cartXpcw;
```

```
pc_y = cartYpc; pcw_y = cartYpcw;
pc_z = cartZpc; pcw_z = cartZpcw;

figure(counting)
subplot(1,2,1)
plot(zconsidered,localShiftx(1+Ls:StrN-Ls),':r',zconsidered,fitValx,'b')
title('Shift in X direction')
xlabel('Z/D down stream')
ylabel('Wear/D')
set(gcf,'color','white')

%offset in y axis
localShifty = ones(StrN,1);   %preallocation of memory
for n = 1+Ls:StrN-Ls
    sum = 0;
    for m = 1:lines
        sum = sum + (r(round(CirN/4)-round(lines/2)+m,n) - r(CirN-
round(CirN/4)+round(lines/2)-m,n))/cosd(theta(round(CirN/4)-round(lines/2)+m,n)-90);
    end
    localShifty(n,1) = sum/2/lines;
end
shiftconsideredy = localShifty(1+Ls:StrN-Ls);
zconsidered = zLine(1+Ls:StrN-Ls);

%calculate the slope of the correction by 1st order fit
py = polyfit(zconsidered, shiftconsideredy,1);
lineSlopey = py(1,1);
lineShifty = py(1,2);

angley = -atand(lineSlopey);
fitValy = polyval(py,zconsidered);

%coordinate system shift and rotation
cartX = x_cart;
cartY = y_cart.*cosd(-angley)-z_cart.*sind(-angley)-lineShifty;
cartZ = y_cart.*sind(-angley)+z_cart.*cosd(-angley);

%updating cylindrical coordinate
% updating r
r = sqrt(cartX.^2+cartY.^2);
zLine(1+Ls:StrN-Ls) = cartZ(1,1+Ls:StrN-Ls);

%Updating theta
```

```
for j=1:StrN
   for i=1:CirN
      if cartX(i,j)>=0 && cartY(i,j)>=0
         theta(i,j) = asind(cartY(i,j)/r(i,j));    % 1st Quadrant
      elseif cartX(i,j)<0 && cartY(i,j)>=0
         theta(i,j) = 180-asind(cartY(i,j)/r(i,j));    %2nd Quadrant
      elseif cartX(i,j)<0 && cartY(i,j)<0
         theta(i,j) = 180-asind(cartY(i,j)/r(i,j));    %3rd Quadrant
      else
         theta(i,j) = 360+asind(cartY(i,j)/r(i,j));    %4th Quadrant
      end
   end
end

%updating z
z = cartZ;

% updating cartesian coordinate from new cylindrical coordinate
for i=1:StrN
   x_cart(:,i) = cosd(theta(:,i)).*r(:,i);
   y_cart(:,i) = sind(theta(:,i)).*r(:,i);
   z_cart(:,i) = z(:,i);
end
Rz = sqrt(x_cart.^2+y_cart.^2); %Distance from the Z axis

%alignment of origional point cloud
cartXpc = pc_x;
cartYpc = pc_y.*cosd(-angley)-pc_z.*sind(-angley)-lineShifty;
cartZpc = pc_y.*sind(-angley)+pc_z.*cosd(-angley);

cartXpcw = pcw_x;
cartYpcw = pcw_y.*cosd(-angley)-pcw_z.*sind(-angley)-lineShifty;
cartZpcw = pcw_y.*sind(-angley)+pcw_z.*cosd(-angley);

pc_x = cartXpc; pcw_x = cartXpcw;
pc_y = cartYpc; pcw_y = cartYpcw;
pc_z = cartZpc; pcw_z = cartZpcw;

figure(counting)
subplot(1,2,2)
plot(zconsidered,localShifty(1+Ls:StrN-Ls),':r',zconsidered,fitValy,'b')
title('Shift in Y direction')
xlabel('Z/D down stream')
```

```
    ylabel('Wear/D')

end
fprintf(' The shift in x direction is %3.5f mm. \n', lineShiftx);
fprintf(' The rotation about y axis is %3.5f degree. \n', anglex);
fprintf(' The shift in y direction is %3.5f mm. \n', lineShifty);
fprintf(' The rotation about x axis is %3.5f degree. \n', angley);
% fprintf(' The shift in z direction is %3.5f mm. \n', lineShiftz);
% fprintf(' The rotation about z axis is %3.5f degree. \n', zrot);

% Output and write
dlmwrite('C:\Users\Daq\Desktop\TS3
Roughness\Worn_8\pc_worn_iea.txt',[cartXpcw,cartYpcw,cartZpcw],'delimiter', '\t',
'newLine', 'pc');
toc
```

D.6 Third (last) edge separation for inner and outer edges

Code Filename: Alignment_ie.m

```
%This program separates the inner edge of the gypsum from the outer edge of the pipe
section.
clear all
close all
clc

tic
load 'pc_worn_iea.txt'
pc = pc_worn_iea;

%defining  parameters
Dpipe = 8*25.4;

%Preallocation of memory for x,y,z,r and theta
x = zeros(length(pc),1);
y = zeros(length(pc),1);
z = zeros(length(pc),1);
phi = zeros(length(pc),1);
R = zeros(length(pc),1);
theta = zeros(length(pc),1);

%converting cartesian coordinate to polar coordinate
for i=1:length(pc)
```

```
        x(i)=pc(i,1);
        y(i)=pc(i,2);
        z(i)=pc(i,3);
end

r = sqrt(x.^2+y.^2);
for i=1:length(pc)
    if x(i)>=0 && y(i)>=0
        theta(i) = asind(y(i)/r(i));    % 1st Quadrant
    elseif x(i)<0 && y(i)>=0
        theta(i) = 180-asind(y(i)/r(i));    %2nd Quadrant
    elseif x(i)<0 && y(i)<0
        theta(i) = 180-asind(y(i)/r(i));    %3rd Quadrant
    else
        theta(i) = 360+asind(y(i)/r(i));    %4th Quadrant
    end
end

figure;
plot(z/Dpipe,r/Dpipe);
xlabel('Streamwise (z/D)')
ylabel('Radius (r/D)')
%axis([0 8 0 0.9])

%Gridding and indentifying 1st(hydrocal inner) and 2nd (hydrocal outer + outer shell)
%formulating a grid size having 1mm by 1mm resolution
zStart = 10; %z starts at 10 mm into the pipe
zEnd = 900; %z ends at 900 mm into the pipe
thetRes = 1; %1mm
zRes = 1; %1mm
CirN = round(pi*Dpipe/thetRes); %number of elements in the circumferential direction
StrN = round((zEnd-zStart)/zRes); %number of elements in the streamwise direction

zgridding = zeros(CirN,StrN);
for i = 1:CirN
    zgridding(i,:) = linspace(zStart,zEnd,StrN);
end

thetagridding = zeros(CirN,StrN);
for i = 1:StrN
    thetagridding(:,i) = linspace(0,360,CirN)';
end
```

```
%Edge detection based on thickness threshold (half the nominal thickness)
%Interpolating the radius by averaging the radius within the cell
%zgridding-+dz and thetagridding-+dt
dz = (zgridding(1,2)-zgridding(1,1))/2;
dt = (thetagridding(2,1)-thetagridding(1,1))/2;
pipethick = 20; %pipe nominal thickness -----original thickness: 22mm
thres = pipethick/2; %half the nominal thickness
thres_oe = 3; %thickness of the pipe  3mm maybe too high to get too much noises

zsortedpc = sortrows([theta z r],2);
rsorted = zsortedpc(:,3); thetasorted = zsortedpc(:,1); zsorted = zsortedpc(:,2);

rOUTavg = zeros(CirN,StrN); rINavg = zeros(CirN,StrN); rSHELavg =
zeros(CirN,StrN);
for j = 1:StrN
   zind = find(zgridding(1,j)-dz<=zsorted & zsorted<=zgridding(1,j)+dz);
   for i = 1:CirN
      ind = find(zgridding(i,j)-dz<=zsorted(zind(1):zind(length(zind))) &
zsorted(zind(1):zind(length(zind)))<=zgridding(i,j)+dz & ...
           thetagridding(i,j)-dt<=thetasorted(zind(1):zind(length(zind))) &
thetasorted(zind(1):zind(length(zind)))<=thetagridding(i,j)+dt);
      %countIN = 0; countOUT = 0; rIN = 0; rOUT = 0;%initiate count and radius
      rDummy = rsorted(ind+zind(1)-1);
      rINavg(i,j) = mean(rDummy(rDummy<min(rDummy)+thres/2)); %inner edge
      rOUT = rDummy(rDummy>min(rDummy)+thres);
      rOUTavg(i,j) =  mean(rOUT(rOUT<min(rOUT)+thres_oe)); %outer edge
      rSHELavg(i,j) = mean(rOUT(rOUT>=min(rOUT)+thres_oe)); %shell edge
   end
end

%% Plot the results
figure;

subplot(2,3,1);
contourf(zgridding/Dpipe,thetagridding,rINavg,40)
xlabel('streamwise z/D')
ylabel('Theta')
% caxis([99 110]);
subplot(2,3,2);
contourf(zgridding/Dpipe,thetagridding,rOUTavg,40)
xlabel('streamwise z/D')
ylabel('Theta')
% caxis([115 120]);
```

```
subplot(2,3,3);
contourf(zgridding/Dpipe,thetagridding,rSHELavg,40)
xlabel('streamwise z/D')
ylabel('Theta')
% caxis([119 124]);

subplot(2,3,4);
for zindex=50:10:850
plot(thetagridding(:,1),rINavg(:,zindex))
hold on;
end
% ylim([99 110]);

subplot(2,3,5);
for zindex=50:10:850
plot(thetagridding(:,1),rOUTavg(:,zindex))
hold on;
end
% ylim([121 127]);

subplot(2,3,6);
for zindex=50:10:850
plot(thetagridding(:,1),rSHELavg(:,zindex))
hold on;
end
% ylim([124 130]);

%% Output and write
theta_vec = reshape(thetagridding,CirN*StrN,1); z_vec =
reshape(zgridding,CirN*StrN,1); rIN_vec = reshape(rINavg,CirN*StrN,1);
rOUT_vec = reshape(rOUTavg,CirN*StrN,1); rSHEL_vec =
reshape(rSHELavg,CirN*StrN,1);
dlmwrite('inneredge_iea.txt', [theta_vec z_vec rIN_vec],'delimiter', '\t', 'newLine', 'pc');
dlmwrite('outeredge_iea.txt', [theta_vec z_vec rOUT_vec],'delimiter', '\t', 'newLine', 'pc');
dlmwrite('shelledge_iea.txt', [theta_vec z_vec rSHEL_vec],'delimiter', '\t', 'newLine',
'pc');
toc
```

D.7 Calculation of modified time using conductivity

Code Filename: Modified_time.m

```
% Calculate modified time baed on 25 degree conductivity-concentration calibrition
factor 970 for 40 instead of 861 for 25 (changed with a full correlation)

%gypsum properties
clc;clear;close all
Cw = 2.6; GypDens = 1580; Co = 0; D = 7.42e-10;

conductivity = xlsread('2015-12-15 TS3-8-Conductivity.xlsx');% time unit is second
figure;
plot (conductivity(:,2),conductivity(:,3));

% Convert the conductivity top concentration with linear correlation!
% concen=0.0011*cond-0.3487
concentration=[conductivity(:,2)/3600 conductivity(:,3)*0.0011-0.3487];
dlmwrite('concentration profile.txt',concentration,'delimiter', '\t','newline', 'pc');

% use Polynomial curve fitting to fit the concentration profile
concentration_fit = polyfit(concentration(:,1),Cw-concentration(:,2),3);
concentration_val = polyval(concentration_fit,concentration(:,1));
figure;
plot (concentration(:,1),concentration(:,2));
figure;
plot (concentration(:,1),Cw-concentration(:,2));
hold on
plot (concentration(:,1),concentration_val(:,1),'-r');

tmod = polyval(polyint(concentration_fit),8)/(Cw-Co)

% estimate wear using the final concentration
% factoir=1.63 based on calculation at Notebook page 61
wear_estimate=concentration(length(concentration(:,2)),2)*1.63
```

D.8 Characterization of roughness height

Code Filename: TS3_Roughness_height.m

```
clear all
close all
clc
tic

%% 1. Define Parameters
```

```
% needs to be changed with different cases
Re=200000;
Threshold=0;
Threshold2=0.2;
Viscosity= 0.894e-6;        % m2/s

Dpipe = 8*25.4;
zStart = 10;    %z starts at 10 mm into the pipe
zEnd = 900;     %z ends at 900 mm into the pipe
thetRes = 1;    %1mm
zRes = 1;       %1mm
CirN = round(pi*Dpipe/thetRes);    %number of elements in the circumferential direction
StrN = round((zEnd-zStart)/zRes);  %number of elements in the streamwise direction

for CaseNo=1:9
  if CaseNo==1;
    Modified_time=0;
    strname='C:\Users\Daq\Desktop\TS3 Roughness\Unworn\inneredge_iea.txt';
    worn = dlmread(strname);
    Rw_original = rot90(reshape(worn(:,3),CirN,StrN),2);
    Rw_aligned1=Rw_original;
    Rw=Rw_aligned1(:,10:880);

  elseif CaseNo==2;
    Modified_time=3.77;
    strname='C:\Users\Daq\Desktop\TS3 Roughness\Worn_1\inneredge_iea.txt';
    worn = dlmread(strname);
    Rw_original = rot90(reshape(worn(:,3),CirN,StrN),2);
    % Alignment
    Rw_aligned1=[Rw_original(2:CirN,:);Rw_original(1,:)];
    Rw=Rw_aligned1(:,11:881);

  elseif CaseNo==3;
    Modified_time=7.51;
    strname='C:\Users\Daq\Desktop\TS3 Roughness\Worn_2\inneredge_iea.txt';
    worn = dlmread(strname);
    Rw_original = rot90(reshape(worn(:,3),CirN,StrN),2);
    % Alignment
    Rw_aligned1=[Rw_original(7:CirN,:);Rw_original(1:6,:)];
    Rw=Rw_aligned1(:,12:882);

  elseif CaseNo==4;
    Modified_time=11.17;
```

```
    strname='C:\Users\Daq\Desktop\TS3 Roughness\Worn_3\inneredge_iea.txt';
    worn = dlmread(strname);
    Rw_original = rot90(reshape(worn(:,3),CirN,StrN),2);
    % Alignment
    Rw_aligned1=[Rw_original(5:CirN,:);Rw_original(1:4,:)];
    Rw=Rw_aligned1(:,12:882);

  elseif CaseNo==5;
    Modified_time=14.79;
    strname='C:\Users\Daq\Desktop\TS3 Roughness\Worn_4\inneredge_iea.txt';
    worn = dlmread(strname);
    Rw_original = rot90(reshape(worn(:,3),CirN,StrN),2);
    % Alignment
    Rw_aligned1=[Rw_original(8:CirN,:);Rw_original(1:7,:)];
    Rw=Rw_aligned1(:,13:883);

  elseif CaseNo==6;
    Modified_time=18.36;
    strname='C:\Users\Daq\Desktop\TS3 Roughness\Worn_5\inneredge_iea.txt';
    worn = dlmread(strname);
    Rw_original = rot90(reshape(worn(:,3),CirN,StrN),2);
    % Alignment
    Rw_aligned1=[Rw_original(10:CirN,:);Rw_original(1:9,:)];
    Rw=Rw_aligned1(:,13:883);

  elseif CaseNo==7;
    Modified_time=24.98;
    strname='C:\Users\Daq\Desktop\TS3 Roughness\Worn_6\inneredge_iea.txt';
    worn = dlmread(strname);
    Rw_original = rot90(reshape(worn(:,3),CirN,StrN),2);
    % Alignment
    Rw_aligned1=[Rw_original(6:CirN,:);Rw_original(1:5,:)];
    Rw=Rw_aligned1(:,15:885);

  elseif CaseNo==8;
    Modified_time=31.53;
    strname='C:\Users\Daq\Desktop\TS3 Roughness\Worn_7\inneredge_iea.txt';
    worn = dlmread(strname);
    Rw_original = rot90(reshape(worn(:,3),CirN,StrN),2);
    % Alignment
    Rw_aligned1=[Rw_original(CirN,:);Rw_original(1:CirN-1,:)];
    Rw=Rw_aligned1(:,15:885);
```

```
elseif CaseNo==9;
    Modified_time=37.98;
    strname='C:\Users\Daq\Desktop\TS3 Roughness\Worn_8\inneredge_iea.txt';
    worn = dlmread(strname);
    Rw_original = rot90(reshape(worn(:,3),CirN,StrN),2);
    % Alignment
    Rw_aligned1=[Rw_original(6:CirN,:);Rw_original(1:5,:)];
    Rw=Rw_aligned1(:,15:885);

end

theta = reshape(worn(:,1),CirN,StrN);
z = reshape(worn(:,2),CirN,StrN);   %Reverse z-asix to make z=0 starts from inlet
using fliplr

MeanRadius=mean2(Rw(:,100:800))
index_Rw = find(Rw>115 | Rw<101);
Rw(index_Rw) = MeanRadius;
Meanradius_log(CaseNo,1)=MeanRadius;

%% 2. Decomposition using Wavelet Analysis (2d-dwt)

% wavedec2
[c,l] = wavedec2(Rw(:,100:800),8,'db5');

% wrcoef2
co = cell(10,1);
for i=1:7
    ca0 = wrcoef2('a',c,l,'db5',i);
    co{i,1}=ca0;
end

% small roughness + noise
noise=co{2,1}-Rw(:,100:800);

% big roughness: scallops
roughness=co{6,1}-co{2,1};  % Reversed for real situation positive value for peak,
gegative for valleys(scallops)!

% surface form
form=co{6,1};
```

```
%% only show valleys showing scallop development
rough_separation1=-roughness;
ind_rough=find(rough_separation1>=Threshold2);
rough_separation1(ind_rough)=1;
ind_smooth=find(rough_separation1<Threshold2);
rough_separation1(ind_smooth)=0;

%% 5. Calculate Time Scale

% use global roughness RMS height to darcy estimate friction factor
Roughness_RMS=sqrt(mean2(roughness.^2));   % RMS

% valculate wall unit
E_D=3*Roughness_RMS/(2*MeanRadius);
Fric_Factor = colebrook(Re,E_D);
Wall_unit=2*MeanRadius/Re*(sqrt(8/Fric_Factor));   %mm
Wall_unit_log(CaseNo,1)=Wall_unit;   %mm

% log time
Time(CaseNo,1)=Modified_time; % hourk

% Time normalized with inner time scale
Inner_time_scale = (Wall_unit/1000)^2/Viscosity;    % Unit: s
Time_inner(CaseNo,1)=Modified_time*3600/Inner_time_scale;

% Time normalized with mixed time scale
Velocity=Re*Viscosity/(2*MeanRadius/1000);      % Unit: m
Outer_time_scale=2*MeanRadius/1000/Velocity;         % Unit: s
Mixed_time_scale = sqrt(Inner_time_scale*Outer_time_scale);      % Unit: s
Time_mixed(CaseNo,1)=Modified_time*3600/Mixed_time_scale;

%% 6. Evaluate roughness using sampling box 150 X 75

roughness_block_mean=zeros(638,701);
roughness_block_RMS=zeros(638,701);
roughness_block_Peak_valley=zeros(638,701);

peak_judge=zeros(638,701);
peak_value=zeros(638,701);
valley_judge=zeros(638,701);
valley_value=zeros(638,701);
```

```
index=0;
% sweep from matrix end
for i=1:80:481         % Block Size
   for    j=1:80:561
      index=index+1;
      % Calculate RMS  (Rq)
      roughness_block_RMS(i:i+79,j:j+79)=sqrt(mean2(roughness(i:i+79,j:j+79).^2));

roughness_block_RMS_vector(index,CaseNo)=sqrt(mean2(roughness(i:i+79,j:j+79).^2))
;

      % Calculte skewness

roughness_vector=reshape(roughness(i:i+79,j:j+79),numel(roughness(i:i+79,j:j+79)),1);
      Skewness(index,CaseNo)=skewness(roughness_vector);
      Kurtosis(index,CaseNo)=kurtosis(roughness_vector);

      interval=4;

      % find valleys
      for ii=i+interval:i+79;
         for  jj=j+interval:j+79;
            valley_judge_interval=zeros(interval,1);   % thershold: -10*Wall_unit for
finding density of peaks
            for interval=1:4
               if roughness(ii,jj) < 0 && roughness(ii,jj) < roughness(ii-interval,jj-
interval) && roughness(ii,jj) < roughness(ii-interval,jj)  ...
                     && roughness(ii,jj) < roughness(ii-interval,jj+interval) &&
roughness(ii,jj) < roughness(ii,jj-interval) &&...
                     roughness(ii,jj) < roughness(ii,jj+interval) && roughness(ii,jj) <
roughness(ii+interval,jj-interval)&& roughness(ii,jj)...
                     < roughness(ii+interval,jj) && roughness(ii,jj) <
roughness(ii+interval,jj+interval);
                  valley_judge_interval(interval,1)=1;
               end
            end
            if sum(valley_judge_interval)==interval;

valley_judge(ii,jj)=1;valley_value(ii,jj)=valley_judge(ii,jj)*roughness(ii,jj);

            end
         end
      end
```

```
valley_sorted=sort(reshape(valley_value(i+interval:i+79,j+interval:j+79),numel(valley_value(i+interval:i+79,j+interval:j+79)),1));

    if sum(sum(valley_judge(i+interval:i+79,j+interval:j+79)))==0;      % Consider if matrix is empty
       meanvalley=NaN;
    else
       meanvalley=mean(valley_sorted(1:5));
    end

    % find peaks

    for ii=i+interval:i+79;
       for  jj=j+interval:j+79;
          if roughness(ii,jj) > 0 && roughness(ii,jj) > roughness(ii-interval,jj-interval) && roughness(ii,jj) > roughness(ii-interval,jj)  ...
                && roughness(ii,jj) > roughness(ii-interval,jj+interval) && roughness(ii,jj) > roughness(ii,jj-interval) &&...
                roughness(ii,jj) > roughness(ii,jj+interval) && roughness(ii,jj) > roughness(ii+interval,jj-interval)&& roughness(ii,jj)...
                > roughness(ii+interval,jj) && roughness(ii,jj) > roughness(ii+interval,jj+interval);
             peak_judge(ii,jj)=1;
             peak_value(ii,jj)=peak_judge(ii,jj)*roughness(ii,jj);
          end
       end
    end


peak_sorted=sort(reshape(peak_value(i+interval:i+79,j+interval:j+79),numel(peak_value(i+interval:i+79,j+interval:j+79)),1),'descend');

    % Estiamte density for dominant roughness feature

Density(index,CaseNo)=sum(sum(valley_judge(i+interval:i+79,j+interval:j+79)))/(0.75*0.75);

    if sum(sum(peak_judge(i+interval:i+79,j+interval:j+79)))==0;      % Consider if matrix is empty
       meanpeak=NaN;
    else
       meanpeak=mean(peak_sorted(1:5));
```

```
        end

        % Obtain peak-valley height by summation
        roughness_block_P2V_vector(index,CaseNo)=meanpeak - meanvalley;

      end
   end


   % Estimate global peak to valley height based on block peak to valleydata

roughness_block_P2V_global(CaseNo)=mean(roughness_block_P2V_vector(:,CaseNo));

   % Estimate global RMS height based on block RMS data

roughness_block_RMS_global(CaseNo)=mean(roughness_block_RMS_vector(:,CaseNo
));

   % roughness_block_RMS_vector=
reshape(roughness_block_RMS,numel(roughness_block_RMS),1);

Modified_time_vector=ones(numel(roughness_block_RMS_vector(:,CaseNo)),1)*Modif
ied_time;

   % roughness_block_RMS_vector=
reshape(roughness_block_RMS,numel(roughness_block_RMS),1);

Modified_time_vector=ones(numel(roughness_block_P2V_vector(:,CaseNo)),1)*Modifi
ed_time;

   % wirite all the time-roughness data to a maxtix
   Time_Roughness_RMS(:,2*CaseNo-1)=Modified_time_vector;
   Time_Roughness_RMS(:,2*CaseNo)=roughness_block_RMS_vector(:,CaseNo)';
%rms

   % wirite all the time-roughness data to a maxtix
   Time_P2V_Roughness(:,2*CaseNo-1)=Modified_time_vector;
   Time_P2V_Roughness(:,2*CaseNo)=roughness_block_P2V_vector(:,CaseNo)';
%peak to valley

end

%% 7. Plot all the data using RMS roughness
```

```
figure;
for i=1:9
   scatter(Time_Roughness_RMS(:,2*i-1),Time_Roughness_RMS(:,2*i));
   hold on
end
set(gca,'FontSize',14);
ylabel('RMS Roughness Height (mm)');
xlabel('Modified Time (hr)');

cmap=hsv(56);
figure;
for i=1:56
   plot([Time_Roughness_RMS(i,1) Time_Roughness_RMS(i,3)
Time_Roughness_RMS(i,5) Time_Roughness_RMS(i,7)...
      Time_Roughness_RMS(i,9) Time_Roughness_RMS(i,11)
Time_Roughness_RMS(i,13) Time_Roughness_RMS(i,15)
Time_Roughness_RMS(i,17)],...
      [Time_Roughness_RMS(i,2) Time_Roughness_RMS(i,4)
Time_Roughness_RMS(i,6) Time_Roughness_RMS(i,8)...
      Time_Roughness_RMS(i,10) Time_Roughness_RMS(i,12)
Time_Roughness_RMS(i,14) Time_Roughness_RMS(i,16)
Time_Roughness_RMS(i,18)]...
      ,'-o','Color',cmap(i,:));
   hold on
end
set(gca,'FontSize',14);
ylabel('e_{rms} (mm)');
xlabel('t_{mod} (hr)');
ylim([0 2]);

%% 8. Plot all the data using peak_valley roughness
figure;
for i=1:9
   scatter(Time_P2V_Roughness(:,2*i-1),Time_P2V_Roughness(:,2*i));
   hold on
end

set(gca,'FontSize',14);
ylabel('RMS Roughness Height (mm)');
xlabel('t (hr)');

cmap=hsv(56);
figure;
```

```
for i=1:56
   plot([Time_P2V_Roughness(i,1) Time_P2V_Roughness(i,3)
Time_P2V_Roughness(i,5) Time_P2V_Roughness(i,7)...
      Time_P2V_Roughness(i,9) Time_P2V_Roughness(i,11)
Time_P2V_Roughness(i,13) Time_P2V_Roughness(i,15)
Time_P2V_Roughness(i,17)],...
      [Time_P2V_Roughness(i,2) Time_P2V_Roughness(i,4) Time_P2V_Roughness(i,6)
Time_P2V_Roughness(i,8)...
      Time_P2V_Roughness(i,10) Time_P2V_Roughness(i,12)
Time_P2V_Roughness(i,14) Time_P2V_Roughness(i,16) Time_P2V_Roughness(i,18)]...
      ,'-o','Color',cmap(i,:));
   hold on
end
set(gca,'FontSize',14);
ylabel('e_{p-v} (mm)');
xlabel('t_{mod} (hr)');

%% Plot the scallps in non-dimensional form

ii=0;
for i=1:56
   ii=ii+1;
   Roughness_P2V(:,ii)=[Time_P2V_Roughness(i,2) Time_P2V_Roughness(i,4) ...
      Time_P2V_Roughness(i,6) Time_P2V_Roughness(i,8) Time_P2V_Roughness(i,10)
...
      Time_P2V_Roughness(i,12) Time_P2V_Roughness(i,14)
Time_P2V_Roughness(i,16) ...
      Time_P2V_Roughness(i,18)]';
   Time_Experimental(:,ii)=[Time_P2V_Roughness(i,1) Time_P2V_Roughness(i,3)
Time_P2V_Roughness(i,5) Time_P2V_Roughness(i,7)...
      Time_P2V_Roughness(i,9) Time_P2V_Roughness(i,11)
Time_P2V_Roughness(i,13) Time_P2V_Roughness(i,15) Time_P2V_Roughness(i,17)];
end

figure;
cmap=hsv(56);
for i=1:56
   plot(Time_Experimental,Roughness_P2V(:,i),'-o','Color',cmap(i,:));
   hold on
end
% axis([0 10000000 0 0.03]);
set(gca,'FontSize',14);
ylabel('e_{p-v} (mm)');
```

```
xlabel('t (hr)');

%% Try to collapse the data in scallop regions by shifting time

% target function; e/D = 0.022/35 * t or t = 40/0.027 * (e/D) = 1481 * e/D

for i=1:56
   Delta_Time(i,1)= nanmean(Time_Experimental(:,i) - Roughness_P2V(:,i)* 1481/200);
   Time_Experimental_shifted(:,i)= Time_Experimental(:,i) - Delta_Time(i,1);
end

figure;
cmap=hsv(56);
for i=1:56
   plot(Time_Experimental_shifted(:,i),Roughness_P2V(:,i),'-o','Color',cmap(i,:));
   hold on
end
% axis([0 20000000 0 0.03]);
set(gca,'FontSize',14);
ylabel('e_{p-v} (mm)');
xlabel('t (hr)');

figure;
for i=1:56
   scatter(Time_Experimental_shifted(:,i),Roughness_P2V(:,i),'o');
   hold on
end
% axis([0 20000000 0 0.03]);
set(gca,'FontSize',14);
ylabel('e_{p-v} (mm)');
xlabel('t (hr)');

%% Calculate and Plot e+ normalized with wall unit

% use local roughness RMS height to darcy estimate friction factor
for i=1:56
   for   j=1:9

      E_D(i,j)=3*roughness_block_RMS_vector(i,j)/(2*Meanradius_log(j,1));
      Fric_Factor_matrix(i,j) = colebrook(Re,E_D(i,j));
      Wall_unit_matrix(i,j) = 2*Meanradius_log(j,1)/Re*(sqrt(8/Fric_Factor_matrix(i,j)));
%mm
```

```
        % Time normalized with inner time scale
        Inner_time_scale(i,j) = (Wall_unit_matrix(i,j)/1000)^2/Viscosity;    % Unit: s
        Time_inner(i,j)=Time(j,1)*3600/Inner_time_scale(i,j);

        % Time normalized with mixed time scale
        Velocity(i,1)=Re*Viscosity/(2*Meanradius_log(j,1)/1000);      % Unit: m
        Outer_time_scale(j,1)=2*Meanradius_log(j,1)/1000/Velocity(i,1);         % Unit: s
        Mixed_time_scale(i,j) = sqrt(Inner_time_scale(i,j)*Outer_time_scale(j,1));      %
Unit: s
        Time_mixed(i,j)=Time(j,1)*3600/Mixed_time_scale(i,j);

    end
end

for i=1:56
    for  j=1:9
        Roughness_P2V1(j,i)=Time_P2V_Roughness(i,2*j)/Wall_unit_matrix(i,j);
    end
end

figure;
for i=1:56
    scatter(Time_Experimental_shifted(:,i),Roughness_P2V1(:,i),'o');
    hold on
end
% axis([0 10000000 0 0.03]);
set(gca,'FontSize',14);
ylabel('e^+');
xlabel('t (hr)');

%% calculate initiaton time normalized with inner time matrix
Initiation_time_inner=(Time_Experimental_shifted+8)'./Inner_time_scale*3600;
%Matrix size: 12 x 9

%% Plot RMS

roughness_RMS=roughness_block_RMS_vector';
figure;
for i=1:56
    scatter(Time_Experimental_shifted(:,i),roughness_RMS(:,i),'o');
    hold on
end
% axis([0 10000000 0 0.03]);
```

```
set(gca,'FontSize',14);
ylabel('e_{rms} (mm)');
xlabel('t (hr)');

%% Plot Skewness and Kurtosis

% roughness_RMS=';
figure;
for i=1:56
    scatter(Time_Experimental_shifted(:,i),Skewness(i,:),'o');
    hold on
end
% axis([0 10000000 0 0.03]);
set(gca,'FontSize',14);
ylabel('Skewness');
xlabel('t (hr)');

% roughness_RMS=';
figure;
for i=1:56
    scatter(Time_Experimental_shifted(:,i),Kurtosis(i,:),'o');
    hold on
end
% axis([0 10000000 0 0.03]);
set(gca,'FontSize',14);
ylabel('Kurtosis');
xlabel('t (hr)');

%% Output collapsed time-roughness data to a text profile!
dlmwrite('Re=200000_Time_Roughness.txt', Time_Experimental_shifted,'delimiter', '\t',
'newLine', 'pc');
dlmwrite('Re=200000_Time_Roughness.txt', Roughness_P2V,'-append','delimiter', '\t',
'newLine', 'pc');
dlmwrite('Re=200000_Time_Roughness.txt', roughness_RMS,'-append','delimiter', '\t',
'newLine', 'pc');
dlmwrite('Re=200000_Time_Roughness.txt', Inner_time_scale','-append','delimiter', '\t',
'newLine', 'pc');
dlmwrite('Re=200000_Time_Roughness.txt', Mixed_time_scale','-append','delimiter', '\t',
'newLine', 'pc');
dlmwrite('Re=200000_Time_Roughness.txt', Wall_unit_matrix','-append','delimiter', '\t',
'newLine', 'pc');
dlmwrite('Re=200000_Time_Roughness.txt', Skewness','-append','delimiter', '\t',
'newLine', 'pc');
```

```
dlmwrite('Re=200000_Time_Roughness.txt', Kurtosis','-append','delimiter', '\t', 'newLine',
'pc');

Re_200000 = dlmread('Re=200000_Time_Roughness.txt');
toc
```

D.9 Characterization of length and width using autocorrelation

Code Filename: TS3_Size_all_scallops_Block.m

```
% Illustrate the change of scallops with time using typical areas

clear all
close all
clc

tic

%% 1. Define Parameters

% needs to be changed with different cases
Re=200000;
Viscosity= 0.894e-6;        % m2/s

Dpipe = 8*25.4;
zStart = 10;    %z starts at 10 mm into the pipe
zEnd = 900;     %z ends at 900 mm into the pipe
thetRes = 1;    %1mm
zRes = 1;       %1mm
CirN = round(pi*Dpipe/thetRes);    %number of elements in the circumferential direction
StrN = round((zEnd-zStart)/zRes);  %number of elements in the streamwise direction

%% FIND scallop areas using TS#6 for test areas  %try  Ts#9

strname='C:\Users\Daq\Desktop\TS3 Roughness\Worn_8\inneredge_iea.txt';
worn = dlmread(strname);
Rw_original = rot90(reshape(worn(:,3),CirN,StrN),2);
% Alignment
Rw_aligned1=[Rw_original(6:CirN,:);Rw_original(1:5,:)];
Rw=Rw_aligned1(:,15:885);

MeanRadius=mean2(Rw(:,100:800))
```

```
theta = reshape(worn(:,1),CirN,StrN);
z = reshape(worn(:,2),CirN,StrN);

% wavelet_remove noise and waviness, form
% wavedec2
[c,l] = wavedec2(Rw(:,100:800),8,'db5');
% wrcoef2
co = cell(10,1);
for i=1:7
   ca0 = wrcoef2('a',c,l,'db5',i);
   co{i,1}=ca0;
end

% big roughness: scallops
roughness=co{6,1}-co{2,1};  % Reversed for real situation positive value for peak,
gegative for valleys(scallops)!

figure;
[ch,ch]=contourf(z(:,100:800)/Dpipe,theta(:,100:800),roughness,20);
colorbar;
set(gca,'FontSize',14);
ylabel('Crosswise angle ( \theta )')
xlabel('Axial Distance ( z/D )')
axis([0.5 4 0 360])
caxis([-2 2])
set(gca,'YTick',0:90:360,'XTick',0:0.5:4.5);
set(ch,'edgecolor','none');


% Use global roughness RMS height to estimate friction factor and wall unit
Roughness_RMS=sqrt(mean2(roughness.^2));   % RMS
E_D=3*Roughness_RMS/(2*MeanRadius);
Fric_Factor = colebrook(Re,E_D);
Wall_unit=2*MeanRadius/Re*(sqrt(8/Fric_Factor));   %mm

% Searching the whole surface for valleys of scallops
valley_value=zeros(638,701);
valley_judge=zeros(638,701);
interval=8;

% find valleys
for ii=1+interval:638-interval;
   for  jj=1+interval:701-interval;
```

```
      valley_judge_interval=zeros(interval,1);   % thershold: -10*Wall_unit for finding
density of peaks
      for i=1:interval
         if roughness(ii,jj) < -10*Wall_unit && roughness(ii,jj) < roughness(ii-i,jj-i) &&
roughness(ii,jj) < roughness(ii-i,jj)  ...
               && roughness(ii,jj) < roughness(ii-i,jj+i) && roughness(ii,jj) <
roughness(ii,jj-i) &&...
               roughness(ii,jj) < roughness(ii,jj+i) && roughness(ii,jj) < roughness(ii+i,jj-
i)&& roughness(ii,jj)...
               < roughness(ii+i,jj) && roughness(ii,jj) < roughness(ii+i,jj+i);
            valley_judge_interval(i,1)=1;
         end
      end
      if sum(valley_judge_interval)==interval;
         valley_judge(ii,jj)=1;
         valley_value(ii,jj)=valley_judge(ii,jj)*roughness(ii,jj);

      end
   end
end

% Plot Found valleys!
figure;
contourf(z(:,100:800)/Dpipe,theta(:,100:800),valley_value);
set(gca,'FontSize',14);
ylabel('Crosswise angle ( \theta )')
xlabel('Axial Distance ( z/D )')
axis([0.5 4 0 360])
set(gca,'YTick',0:90:360,'XTick',0:0.5:4.5);
set(gcf, 'colormap', gray)

[row col]=find(valley_judge==1);  % matrix order

%% Calulate ACF in found scallop areas and calculate integral length

% Redfine roughneess Cell
roughness=cell(9,1);

for CaseNo=1:9
   if CaseNo==1;
      Modified_time(CaseNo,1)=0;
      strname='C:\Users\Daq\Desktop\TS3 Roughness\Unworn\inneredge_iea.txt';
      worn = dlmread(strname);
```

```
    Rw_original = rot90(reshape(worn(:,3),CirN,StrN),2);
    Rw_aligned1=Rw_original;
    Rw=Rw_aligned1(:,10:880);

elseif CaseNo==2;
    Modified_time(CaseNo,1)=3.77;
    strname='C:\Users\Daq\Desktop\TS3 Roughness\Worn_1\inneredge_iea.txt';
    worn = dlmread(strname);
    Rw_original = rot90(reshape(worn(:,3),CirN,StrN),2);
    % Alignment
    Rw_aligned1=[Rw_original(2:CirN,:);Rw_original(1,:)];
    Rw=Rw_aligned1(:,11:881);

elseif CaseNo==3;
    Modified_time(CaseNo,1)=7.51;
    strname='C:\Users\Daq\Desktop\TS3 Roughness\Worn_2\inneredge_iea.txt';
    worn = dlmread(strname);
    Rw_original = rot90(reshape(worn(:,3),CirN,StrN),2);
    % Alignment
    Rw_aligned1=[Rw_original(7:CirN,:);Rw_original(1:6,:)];
    Rw=Rw_aligned1(:,12:882);

elseif CaseNo==4;
    Modified_time(CaseNo,1)=11.17;
    strname='C:\Users\Daq\Desktop\TS3 Roughness\Worn_3\inneredge_iea.txt';
    worn = dlmread(strname);
    Rw_original = rot90(reshape(worn(:,3),CirN,StrN),2);
    % Alignment
    Rw_aligned1=[Rw_original(5:CirN,:);Rw_original(1:4,:)];
    Rw=Rw_aligned1(:,12:882);

elseif CaseNo==5;
    Modified_time(CaseNo,1)=14.79;
    strname='C:\Users\Daq\Desktop\TS3 Roughness\Worn_4\inneredge_iea.txt';
    worn = dlmread(strname);
    Rw_original = rot90(reshape(worn(:,3),CirN,StrN),2);
    % Alignment
    Rw_aligned1=[Rw_original(8:CirN,:);Rw_original(1:7,:)];
    Rw=Rw_aligned1(:,13:883);

elseif CaseNo==6;
    Modified_time(CaseNo,1)=18.36;
    strname='C:\Users\Daq\Desktop\TS3 Roughness\Worn_5\inneredge_iea.txt';
```

```
        worn = dlmread(strname);
        Rw_original = rot90(reshape(worn(:,3),CirN,StrN),2);
        % Alignment
        Rw_aligned1=[Rw_original(10:CirN,:);Rw_original(1:9,:)];
        Rw=Rw_aligned1(:,13:883);

    elseif CaseNo==7;
        Modified_time(CaseNo,1)=24.98;
        strname='C:\Users\Daq\Desktop\TS3 Roughness\Worn_6\inneredge_iea.txt';
        worn = dlmread(strname);
        Rw_original = rot90(reshape(worn(:,3),CirN,StrN),2);
        % Alignment
        Rw_aligned1=[Rw_original(6:CirN,:);Rw_original(1:5,:)];
        Rw=Rw_aligned1(:,15:885);

    elseif CaseNo==8;
        Modified_time(CaseNo,1)=31.53;
        strname='C:\Users\Daq\Desktop\TS3 Roughness\Worn_7\inneredge_iea.txt';
        worn = dlmread(strname);
        Rw_original = rot90(reshape(worn(:,3),CirN,StrN),2);
        % Alignment
        Rw_aligned1=[Rw_original(CirN,:);Rw_original(1:CirN-1,:)];
        Rw=Rw_aligned1(:,15:885);

    elseif CaseNo==9;
        Modified_time(CaseNo,1)=37.98;
        strname='C:\Users\Daq\Desktop\TS3 Roughness\Worn_8\inneredge_iea.txt';
        worn = dlmread(strname);
        Rw_original = rot90(reshape(worn(:,3),CirN,StrN),2);
        % Alignment
        Rw_aligned1=[Rw_original(6:CirN,:);Rw_original(1:5,:)];
        Rw=Rw_aligned1(:,15:885);

    end

    theta = reshape(worn(:,1),CirN,StrN);
    z = reshape(worn(:,2),CirN,StrN);   %Reverse z-asix to make z=0 starts from inlet
using fliplr

    MeanRadius=mean2(Rw(:,100:800))
    index_Rw = find(Rw>115 | Rw<101);
    Rw(index_Rw) = MeanRadius;
    Meanradius_log(CaseNo,1)=MeanRadius;
```

```
    % 2. Decomposition using Wavelet Analysis (2d-dwt)

    % wavedec2
    [c,l] = wavedec2(Rw(:,100:800),8,'db5');

    % wrcoef2
    co = cell(10,1);
    for i=1:7
        ca0 = wrcoef2('a',c,l,'db5',i);
        co{i,1}=ca0;
    end

    % small roughness + noise
    noise=co{2,1}-Rw(:,100:800);

    % big roughness: scallops
    roughness{CaseNo,1}=co{6,1}-co{2,1};  % Reversed for real situation positive value
for peak, gegative for valleys(scallops)!

    % surface form
    form=co{6,1};

    % 3. find the scallop locations

end

%% Plot autocorrelation for the selected scllop area

% SET Test Area!
for TestNo=1:length(col)

    for CaseNo=1:9
        Test_area{CaseNo,1}=roughness{CaseNo,1}(row(TestNo)-
8:row(TestNo)+8,col(TestNo)-8:col(TestNo)+8);   % 16 x 16 mm
        crr{CaseNo,1}= xcorr2(Test_area{CaseNo,1});
        crr_norm{CaseNo,1}=crr{CaseNo,1}./max(crr{CaseNo,1}(:));
    end


    Upperlimit_fitting=[2 2 3 4 5 6 7 8 8]; ;   % Set No. of points to be fitting [2 2 3 3 4 4 5
6 7];
```

```
  for i=1:9

     for ii=1:33
        x(ii)=ii;
        y(ii)=17+(ii-17)*tan(10/180*pi);   % 10 degree
        v(ii)=crr{i,1}(floor(y(ii)),x(ii))+(crr{i,1}(ceil(y(ii)),x(ii))-
crr{i,1}(floor(y(ii)),x(ii)))*(y(ii)-floor(y(ii)));
     end

     x_axis=(x-17)/cos(10/180*pi);
     v_value=v/max(v);

     myfittype = fittype('exp(-
a*x*x)','dependent',{'y'},'independent',{'x'},'coefficients',{'a'});
     myfit =
fit(x_axis(17:16+Upperlimit_fitting(i))',v_value(17:16+Upperlimit_fitting(i))',myfittype);
     %        hh=plot(myfit);
     %        set(hh,'color',cmap(i,:))
     %        hold on;

     Coef(i,1)=coeffvalues(myfit);
     Length_integral(i,TestNo)=sqrt(pi/Coef(i,1))*0.5;         % The Gaussian integral
     Length_10perc(i,TestNo)=sqrt(2.3/Coef(i,1));            % 10% length scale

  end

  % Plot autocorrelation along 10degree to show the width (Careful!!!)
  Upperlimit_fitting2=[2 2 3 3 4 4 5 6 7]; %[2 2 3 4 5 6 7 8 8];

  %     figure;
  %     cmap=hsv(9);
  for i=1:9

     for ii=1:29
        xx(ii)=ii;
        yy(ii)=17 +(17-ii)*tan(10/180*pi);   % 10 degree
        vv(ii)=crr{i,1}(xx(ii),floor(yy(ii)))+(crr{i,1}(xx(ii),ceil(yy(ii)))-
crr{i,1}(xx(ii),floor(yy(ii))))*(yy(ii)-floor(yy(ii)));
     end

     xx_axis=(xx-17)/cos(10/180*pi);
     vv_value=vv/max(vv);
```

```
        % Curve fit to exponential using first 10 points
        myfittype = fittype('exp(-
a*x*x)','dependent',{'y'},'independent',{'x'},'coefficients',{'a'});
        myfit =
fit(xx_axis(17:16+Upperlimit_fitting2(i))',vv_value(17:16+Upperlimit_fitting2(i))',myfitt
ype);
        %       hh=plot(myfit);
        %       set(hh,'color',cmap(i,:))
        %       hold on;
        %
        Coef2(i,1)=coeffvalues(myfit);
        Width_integral(i,TestNo)=sqrt(pi/Coef2(i,1))*0.5;       % The Gaussian integral
        Width_10perc(i,TestNo)=sqrt(2.3/Coef2(i,1));
    end

end

%% Plot the final results
figure;
cmap=hsv(20);
index=0;
for TestNo=1:50:length(col)
    index=index+1;
    scatter(Modified_time(:,1),Length_integral(:,TestNo));
    hold on;
    set(gca,'FontSize',14);
    xlabel(' Modified Time (hr)');
    ylabel('Gaussian Fit Integral Length (mm)');
end

figure;
index=0;
for TestNo=1:50:length(col)
    index=index+1;
    plot(Modified_time(:,1),Width_integral(:,TestNo));
    hold on;
    set(gca,'FontSize',14);
    xlabel(' Modified Time (hr)');
    ylabel('Gaussian Fit Integral Width (mm)');
end
 toc

%% Find the five mimaximum ACL Length in bigger Block area 80x80
```

```
BlockNo=0;
for i=1:80:481        % Block Size
   for    j=1:80:561
      BlockNo=BlockNo+1;
      count=0;
      for index=1:length(col)
         if row(index)>i && row(index)<i+80 && col(index)>j && col(index)<j+80
            count=count+1;
            Length_integral_Block(count,:)=Length_integral(:,index);
         end
      end

      %        % find the five maximum sizes at the end and record index
      Length_Block_sorted = sortrows(Length_integral_Block,-9);  %sort the rows based
on colume 9 in descending order
      Length_Block_5average(BlockNo,:)=mean(Length_Block_sorted(1:5,:));
   end
end

cmap=hsv(BlockNo);
figure;
for i=1:BlockNo
   plot(Modified_time,Length_Block_5average(i,:),'-o','Color',cmap(i,:));
   hold on;
end
set(gca,'FontSize',14);
xlabel(' t_{mod} (hr)');
ylabel('L (mm)');
ylim([0 8]);
% Find the five mimaximum ACL Width in bigger Block area 80x80

BlockNo=0;
for i=1:80:481        % Block Size
   for    j=1:80:561
      BlockNo=BlockNo+1;
      count=0;
      for index=1:length(col)
         if row(index)>i && row(index)<i+80 && col(index)>j && col(index)<j+80
            count=count+1;
            Width_integral_Block(count,:)=Width_integral(:,index);
         end
      end
```

```
    %     % find the five maximum sizes at the end and record index
    Width_Block_sorted = sortrows(Width_integral_Block,-9);  %sort the rows based
on colume 9 in descending order
    Width_Block_5average(BlockNo,:)=mean(Width_Block_sorted(1:5,:));
  end
end

cmap=hsv(BlockNo);
figure;
for i=1:BlockNo
  plot(Modified_time(1:9,1),Width_Block_5average(i,1:9),'-o','Color',cmap(i,:));
  hold on;
end
set(gca,'FontSize',14);
xlabel(' t_{mod} (hr)');
ylabel('W (mm)');
ylim([0 8]);

% Calculate aspect ratio using the Integral Length scale
Aspect_ratio=Length_Block_5average./Width_Block_5average;

figure;
for i=1:BlockNo
  plot(Modified_time,Aspect_ratio(i,:),'-o','Color',cmap(i,:));
  hold on;
end
set(gca,'FontSize',14);
xlabel(' t_{mod} (hr)');
ylabel('AR');
ylim([0 2]);

%% Output collapsed time-roughness data to a text profile!
dlmwrite('Re=200000_Time_Size.txt', Length_Block_5average','delimiter', '\t', 'newLine',
'pc');
dlmwrite('Re=200000_Time_Size.txt', Width_Block_5average','-append','delimiter', '\t',
'newLine', 'pc');
dlmwrite('Re=200000_Time_Size.txt', Aspect_ratio','-append','delimiter', '\t', 'newLine',
'pc');
 Re_200000 = dlmread('Re=200000_Time_Size.txt');
```

D.10 Characterization of density of scallops

Code Filename: TS3_density.m

```
clear all
close all
clc

tic

%% 1. Define Parameters

% needs to be changed with different cases
Re=200000;
Viscosity= 0.894e-6;        % m2/s

Dpipe = 8*25.4;
zStart = 10;   %z starts at 10 mm into the pipe
zEnd = 900;    %z ends at 900 mm into the pipe
thetRes = 1;   %1mm
zRes = 1;      %1mm
CirN = round(pi*Dpipe/thetRes);    %number of elements in the circumferential direction
StrN = round((zEnd-zStart)/zRes);  %number of elements in the streamwise direction

valley_value_cell=cell(9,1);
valley_judge_cell=cell(9,1);

for CaseNo=1:9
   if CaseNo==1;
      Modified_time=0;
      strname='C:\Users\Daq\Desktop\TS3 Roughness\Unworn\inneredge_iea.txt';
      worn = dlmread(strname);
      Rw_original = rot90(reshape(worn(:,3),CirN,StrN),2);
      Rw_aligned1=Rw_original;
      Rw=Rw_aligned1(:,10:880);

   elseif CaseNo==2;
      Modified_time=3.77;
      strname='C:\Users\Daq\Desktop\TS3 Roughness\Worn_1\inneredge_iea.txt';
      worn = dlmread(strname);
      Rw_original = rot90(reshape(worn(:,3),CirN,StrN),2);
      % Alignment
      Rw_aligned1=[Rw_original(2:CirN,:);Rw_original(1,:)];
```

```
        Rw=Rw_aligned1(:,11:881);

    elseif CaseNo==3;
        Modified_time=7.51;
        strname='C:\Users\Daq\Desktop\TS3 Roughness\Worn_2\inneredge_iea.txt';
        worn = dlmread(strname);
        Rw_original = rot90(reshape(worn(:,3),CirN,StrN),2);
        % Alignment
        Rw_aligned1=[Rw_original(7:CirN,:);Rw_original(1:6,:)];
        Rw=Rw_aligned1(:,12:882);

    elseif CaseNo==4;
        Modified_time=11.17;
        strname='C:\Users\Daq\Desktop\TS3 Roughness\Worn_3\inneredge_iea.txt';
        worn = dlmread(strname);
        Rw_original = rot90(reshape(worn(:,3),CirN,StrN),2);
        % Alignment
        Rw_aligned1=[Rw_original(5:CirN,:);Rw_original(1:4,:)];
        Rw=Rw_aligned1(:,12:882);

    elseif CaseNo==5;
        Modified_time=14.79;
        strname='C:\Users\Daq\Desktop\TS3 Roughness\Worn_4\inneredge_iea.txt';
        worn = dlmread(strname);
        Rw_original = rot90(reshape(worn(:,3),CirN,StrN),2);
        % Alignment
        Rw_aligned1=[Rw_original(8:CirN,:);Rw_original(1:7,:)];
        Rw=Rw_aligned1(:,13:883);

    elseif CaseNo==6;
        Modified_time=18.36;
        strname='C:\Users\Daq\Desktop\TS3 Roughness\Worn_5\inneredge_iea.txt';
        worn = dlmread(strname);
        Rw_original = rot90(reshape(worn(:,3),CirN,StrN),2);
        % Alignment
        Rw_aligned1=[Rw_original(10:CirN,:);Rw_original(1:9,:)];
        Rw=Rw_aligned1(:,13:883);

    elseif CaseNo==7;
        Modified_time=24.98;
        strname='C:\Users\Daq\Desktop\TS3 Roughness\Worn_6\inneredge_iea.txt';
        worn = dlmread(strname);
        Rw_original = rot90(reshape(worn(:,3),CirN,StrN),2);
```

```
        % Alignment
        Rw_aligned1=[Rw_original(6:CirN,:);Rw_original(1:5,:)];
        Rw=Rw_aligned1(:,15:885);

    elseif CaseNo==8;
        Modified_time=31.53;
        strname='C:\Users\Daq\Desktop\TS3 Roughness\Worn_7\inneredge_iea.txt';
        worn = dlmread(strname);
        Rw_original = rot90(reshape(worn(:,3),CirN,StrN),2);
        % Alignment
        Rw_aligned1=[Rw_original(CirN,:);Rw_original(1:CirN-1,:)];
        Rw=Rw_aligned1(:,15:885);

    elseif CaseNo==9;
        Modified_time=37.98;
        strname='C:\Users\Daq\Desktop\TS3 Roughness\Worn_8\inneredge_iea.txt';
        worn = dlmread(strname);
        Rw_original = rot90(reshape(worn(:,3),CirN,StrN),2);
        % Alignment
        Rw_aligned1=[Rw_original(6:CirN,:);Rw_original(1:5,:)];
        Rw=Rw_aligned1(:,15:885);

    end

    theta = reshape(worn(:,1),CirN,StrN);
    z = reshape(worn(:,2),CirN,StrN);   %Reverse z-asix to make z=0 starts from inlet
using fliplr

    MeanRadius=mean2(Rw(:,100:800))
    index_Rw = find(Rw>115 | Rw<101);
    Rw(index_Rw) = MeanRadius;
    Meanradius_log(CaseNo,1)=MeanRadius;

    %% 2. Decomposition using Wavelet Analysis (2d-dwt)

    % wavedec2
    [c,l] = wavedec2(Rw(:,100:800),8,'db5');

    % wrcoef2
    co = cell(10,1);
    for i=1:7
        ca0 = wrcoef2('a',c,l,'db5',i);
        co{i,1}=ca0;
```

```
    end

    % small roughness + noise
    noise=co{2,1}-Rw(:,100:800);

    % big roughness: scallops
    roughness=co{6,1}-co{2,1};  % Reversed for real situation positive value for peak,
gegative for valleys(scallops)!

    % surface form
    form=co{6,1};

    %% 5. Calculate Global Time Scale

    % use global roughness RMS height to darcy estimate friction factor
    Roughness_RMS=sqrt(mean2(roughness.^2));   % RMS

    % calculate wall unit
    E_D=3*Roughness_RMS/(2*MeanRadius);
    Fric_Factor = colebrook(Re,E_D);
    Wall_unit(CaseNo,1)=2*MeanRadius/Re*(sqrt(8/Fric_Factor));   %mm

    % log time
    Time(CaseNo,1)=Modified_time; % hourk

    % Time normalized with inner time scale
    Inner_time_scale = (Wall_unit(CaseNo,1)/1000)^2/Viscosity;    % Unit: s
    Time_inner(CaseNo,1)=Modified_time*3600/Inner_time_scale;

    % Time normalized with mixed time scale
    Velocity=Re*Viscosity/(2*MeanRadius/1000);      % Unit: m
    Outer_time_scale=2*MeanRadius/1000/Velocity;         % Unit: s
    Mixed_time_scale = sqrt(Inner_time_scale*Outer_time_scale);      % Unit: s
    Time_mixed(CaseNo,1)=Modified_time*3600/Mixed_time_scale;

    %% 6. Evaluate roughness using sampling box 150 X 75

    roughness_block_mean=zeros(638,701);
    roughness_block_RMS=zeros(638,701);
    roughness_block_Peak_valley=zeros(638,701);

    % Searching the whole surface for valleys of scallops
    valley_value=zeros(638,701);
```

```
    valley_judge=zeros(638,701);
    interval=4;   %neibouring areas

    % find valleys
    for ii=1+interval:638-interval;
       for  jj=1+interval:701-interval;
          valley_judge_interval=zeros(interval,1);   % thershold: -10*Wall_unit for finding
density of peaks
          for i=1:interval
             if roughness(ii,jj) < -10*Wall_unit(CaseNo,1) && roughness(ii,jj) <
roughness(ii-i,jj-i) && roughness(ii,jj) < roughness(ii-i,jj)  ...
                   && roughness(ii,jj) < roughness(ii-i,jj+i) && roughness(ii,jj) <
roughness(ii,jj-i) &&...
                   roughness(ii,jj) < roughness(ii,jj+i) && roughness(ii,jj) <
roughness(ii+i,jj-i)&& roughness(ii,jj)...
                   < roughness(ii+i,jj) && roughness(ii,jj) < roughness(ii+i,jj+i);
                valley_judge_interval(i,1)=1;
             end
          end
          if sum(valley_judge_interval)==interval;
             valley_judge(ii,jj)=1;
             valley_value(ii,jj)=valley_judge(ii,jj)*roughness(ii,jj);
          end
       end
    end

    % Record locations
    valley_judge_cell{CaseNo,1}=valley_judge;
    valley_value_cell{CaseNo,1}=valley_value;

    % Estiamte density
    Density(CaseNo,1)=sum(sum(valley_judge))/(0.637*0.7);   % 1/m^2

end

%% Plot Density;

figure;
ha=tight_subplot(2,4,[.05 .05],[.15 .1],[.15 .1]);

for CaseNo=1:8
    axes(ha(CaseNo));
```

```
    % Plot Found valleys!
    contourf(z(:,100:800)/Dpipe,theta(:,100:800), valley_value_cell{CaseNo+1,1});
    set(gca,'FontSize',10);

    axis([0.5 4 0 360])
    set(gca,'YTick',0:90:360,'XTick',1:1:4);
    set(gcf, 'colormap', gray);

end

ylabel('Crosswise angle ( \theta )')
xlabel('Axial Distance ( z/D )')

[row col]=find(valley_judge==1);

%% Quantify density in each block 80x80

for CaseNo=1:9
    index=0;
    for i=1:80:481         % Block Size
        for    j=1:80:561
            index=index+1;
            Density_block(CaseNo,index)=
sum(sum(valley_judge_cell{CaseNo,1}(i:i+79,j:j+79)))/(0.08*0.08);

        end

    end
end

%% Plot the time-density

figure;
scatter(Time,Density);
set(gca,'FontSize',14);
xlabel('t_{mod} (hr)');
ylabel('D_v (1/m^2)');
axis([0 40 0 3500])

figure;
scatter(Time_inner,Density);
set(gca,'FontSize',14);
xlabel('t');
```

```
ylabel('D_v (1/m^2)');
% axis([0 40 0 3500])

dlmwrite('Re=200000_Time_Density.txt',Density_block ,'delimiter', '\t', 'newLine', 'pc');

Re_200000 = dlmread('Re=200000_Time_Density.txt');
toc
```

D.11 Calculation of Sherwood number

Code Filename: TS3_Sherwood.m

```
% Calculate wear-Sherwood number based on new sampling area 80x80

clear all
close all
clc

tic

% 1. Define Parameters

% needs to be changed with different cases
Re=200000;
Viscosity= 0.894e-6;        % m2/s

Dpipe = 8*25.4;
zStart = 10;    %z starts at 10 mm into the pipe
zEnd = 900;     %z ends at 900 mm into the pipe
thetRes = 1;    %1mm
zRes = 1;       %1mm
CirN = round(pi*Dpipe/thetRes);    %number of elements in the circumferential direction
StrN = round((zEnd-zStart)/zRes);  %number of elements in the streamwise direction


% 2. Calculate Inner Surface Radius
for CaseNo=1:9
   if CaseNo==1;
      Modified_time(CaseNo,1)=0;
      strname='C:\Users\Daq\Desktop\TS3 Roughness\Unworn\inneredge_iea.txt';
      worn = dlmread(strname);
      Rw_original = rot90(reshape(worn(:,3),CirN,StrN),2);
```

```
    Rw_aligned1=Rw_original;
    Rw=Rw_aligned1(:,10:880);

elseif CaseNo==2;
    Modified_time(CaseNo,1)=3.77;
    strname='C:\Users\Daq\Desktop\TS3 Roughness\Worn_1\inneredge_iea.txt';
    worn = dlmread(strname);
    Rw_original = rot90(reshape(worn(:,3),CirN,StrN),2);
    % Alignment
    Rw_aligned1=[Rw_original(2:CirN,:);Rw_original(1,:)];
    Rw=Rw_aligned1(:,11:881);

elseif CaseNo==3;
    Modified_time(CaseNo,1)=7.51;
    strname='C:\Users\Daq\Desktop\TS3 Roughness\Worn_2\inneredge_iea.txt';
    worn = dlmread(strname);
    Rw_original = rot90(reshape(worn(:,3),CirN,StrN),2);
    % Alignment
    Rw_aligned1=[Rw_original(7:CirN,:);Rw_original(1:6,:)];
    Rw=Rw_aligned1(:,12:882);

elseif CaseNo==4;
    Modified_time(CaseNo,1)=11.17;
    strname='C:\Users\Daq\Desktop\TS3 Roughness\Worn_3\inneredge_iea.txt';
    worn = dlmread(strname);
    Rw_original = rot90(reshape(worn(:,3),CirN,StrN),2);
    % Alignment
    Rw_aligned1=[Rw_original(5:CirN,:);Rw_original(1:4,:)];
    Rw=Rw_aligned1(:,12:882);

elseif CaseNo==5;
    Modified_time(CaseNo,1)=14.79;
    strname='C:\Users\Daq\Desktop\TS3 Roughness\Worn_4\inneredge_iea.txt';
    worn = dlmread(strname);
    Rw_original = rot90(reshape(worn(:,3),CirN,StrN),2);
    % Alignment
    Rw_aligned1=[Rw_original(8:CirN,:);Rw_original(1:7,:)];
    Rw=Rw_aligned1(:,13:883);

elseif CaseNo==6;
    Modified_time(CaseNo,1)=18.40;
    strname='C:\Users\Daq\Desktop\TS3 Roughness\Worn_5\inneredge_iea.txt';
    worn = dlmread(strname);
```

```
        Rw_original = rot90(reshape(worn(:,3),CirN,StrN),2);
        % Alignment
        Rw_aligned1=[Rw_original(10:CirN,:);Rw_original(1:9,:)];
        Rw=Rw_aligned1(:,13:883);

    elseif CaseNo==7;
        Modified_time(CaseNo,1)=24.95;
        strname='C:\Users\Daq\Desktop\TS3 Roughness\Worn_6\inneredge_iea.txt';
        worn = dlmread(strname);
        Rw_original = rot90(reshape(worn(:,3),CirN,StrN),2);
        % Alignment
        Rw_aligned1=[Rw_original(6:CirN,:);Rw_original(1:5,:)];
        Rw=Rw_aligned1(:,15:885);

    elseif CaseNo==8;
        Modified_time(CaseNo,1)=31.43;
        strname='C:\Users\Daq\Desktop\TS3 Roughness\Worn_7\inneredge_iea.txt';
        worn = dlmread(strname);
        Rw_original = rot90(reshape(worn(:,3),CirN,StrN),2);
        % Alignment
        Rw_aligned1=[Rw_original(CirN,:);Rw_original(1:CirN-1,:)];
        Rw=Rw_aligned1(:,15:885);

    elseif CaseNo==9;
        Modified_time(CaseNo,1)=37.89;
        strname='C:\Users\Daq\Desktop\TS3 Roughness\Worn_8\inneredge_iea.txt';
        worn = dlmread(strname);
        Rw_original = rot90(reshape(worn(:,3),CirN,StrN),2);
        % Alignment
        Rw_aligned1=[Rw_original(6:CirN,:);Rw_original(1:5,:)];
        Rw=Rw_aligned1(:,15:885);

    end

    theta = reshape(worn(:,1),CirN,StrN);
    z = reshape(worn(:,2),CirN,StrN);   %Reverse z-asix to make z=0 starts from inlet
using fliplr

    Mean_Rw_inner(CaseNo,1)=mean(nanmean(Rw(:,100:800)));
    Radius_inner{CaseNo,1}=Rw;

end
% 3. Calculate Outer Surface Radius
```

```
for CaseNo=1:9
   if CaseNo==1;
      strname='C:\Users\Daq\Desktop\TS3 Roughness\Unworn\outeredge_iea.txt';
      worn = dlmread(strname);
      Rw_original = rot90(reshape(worn(:,3),CirN,StrN),2);
      Rw_aligned1=Rw_original;
      Rw=Rw_aligned1(:,10:880);

   elseif CaseNo==2;
      strname='C:\Users\Daq\Desktop\TS3 Roughness\Worn_1\outeredge_iea.txt';
      worn = dlmread(strname);
      Rw_original = rot90(reshape(worn(:,3),CirN,StrN),2);
      % Alignment
      Rw_aligned1=[Rw_original(2:CirN,:);Rw_original(1,:)];
      Rw=Rw_aligned1(:,11:881);

   elseif CaseNo==3;
      strname='C:\Users\Daq\Desktop\TS3 Roughness\Worn_2\outeredge_iea.txt';
      worn = dlmread(strname);
      Rw_original = rot90(reshape(worn(:,3),CirN,StrN),2);
      % Alignment
      Rw_aligned1=[Rw_original(7:CirN,:);Rw_original(1:6,:)];
      Rw=Rw_aligned1(:,12:882);

   elseif CaseNo==4;
      strname='C:\Users\Daq\Desktop\TS3 Roughness\Worn_3\outeredge_iea.txt';
      worn = dlmread(strname);
      Rw_original = rot90(reshape(worn(:,3),CirN,StrN),2);
      % Alignment
      Rw_aligned1=[Rw_original(5:CirN,:);Rw_original(1:4,:)];
      Rw=Rw_aligned1(:,12:882);

   elseif CaseNo==5;
      strname='C:\Users\Daq\Desktop\TS3 Roughness\Worn_4\outeredge_iea.txt';
      worn = dlmread(strname);
      Rw_original = rot90(reshape(worn(:,3),CirN,StrN),2);
      % Alignment
      Rw_aligned1=[Rw_original(8:CirN,:);Rw_original(1:7,:)];
      Rw=Rw_aligned1(:,13:883);

   elseif CaseNo==6;
      strname='C:\Users\Daq\Desktop\TS3 Roughness\Worn_5\outeredge_iea.txt';
```

```
        worn = dlmread(strname);
        Rw_original = rot90(reshape(worn(:,3),CirN,StrN),2);
        % Alignment
        Rw_aligned1=[Rw_original(10:CirN,:);Rw_original(1:9,:)];
        Rw=Rw_aligned1(:,13:883);

    elseif CaseNo==7;
        strname='C:\Users\Daq\Desktop\TS3 Roughness\Worn_6\outeredge_iea.txt';
        worn = dlmread(strname);
        Rw_original = rot90(reshape(worn(:,3),CirN,StrN),2);
        % Alignment
        Rw_aligned1=[Rw_original(6:CirN,:);Rw_original(1:5,:)];
        Rw=Rw_aligned1(:,15:885);

    elseif CaseNo==8;
        strname='C:\Users\Daq\Desktop\TS3 Roughness\Worn_7\outeredge_iea.txt';
        worn = dlmread(strname);
        Rw_original = rot90(reshape(worn(:,3),CirN,StrN),2);
        % Alignment
        Rw_aligned1=[Rw_original(CirN,:);Rw_original(1:CirN-1,:)];
        Rw=Rw_aligned1(:,15:885);

    elseif CaseNo==9;
        strname='C:\Users\Daq\Desktop\TS3 Roughness\Worn_8\outeredge_iea.txt';
        worn = dlmread(strname);
        Rw_original = rot90(reshape(worn(:,3),CirN,StrN),2);
        % Alignment
        Rw_aligned1=[Rw_original(6:CirN,:);Rw_original(1:5,:)];
        Rw=Rw_aligned1(:,15:885);

    end

    % Romove NaN values
    Mean_Rw_outer=mean(nanmean(Rw(:,100:800)));

    index_outer = find(isnan(Rw) == 1);
    Rw(index_outer)= Mean_Rw_outer;
    Radius_outer{CaseNo,1}=Rw;

end


%%  4.Calculate Thickness & wear
```

```
for CaseNo=1:9

   Thickness{CaseNo,1} = Radius_outer{CaseNo,1}(:,100:800)-
Radius_inner{CaseNo,1}(:,100:800);

end

for CaseNo=1:8

   Wear{CaseNo,1} = Thickness{CaseNo,1}- Thickness{CaseNo+1,1} ;

   [c,l] = wavedec2(Wear{CaseNo,1},7,'db5');

   % wavelet to remove noise and roughness effect
   for i=1:7
      ca0 = wrcoef2('a',c,l,'db5',i);
      co{i,1}=ca0;
   end

   std_dev=std(co{6,1}(:))*2/mean(co{6,1}(:))  % 2std/mean
   Wear_filtered{CaseNo,1}= co{6,1};

end

% Calculate total wear
for i=1:8
   if i==1
      Wear_total_raw{i,1}=Wear_filtered{1,1};
   else
      Wear_total_raw{i,1}=Wear_filtered{i,1}+Wear_total_raw{i-1,1};
   end
end

% Plot wear contour
figure;
for CaseNo=1:8
   subplot(2,4,CaseNo)
   [ch,ch]=contourf(z(:,100:800)/Dpipe,theta(:,100:800),Wear_total_raw{CaseNo,1},30);
   set(gca,'FontSize',14);

   axis([0.5 4 0 360])
   set(gca,'YTick',0:90:360,'XTick',1:1:4);
```

```
    set(ch,'edgecolor','none');

    caxis([0 10])%     caxis([0 3]);
    set(gca,'FontSize',10);
    pbaspect([1 1 1]);
end
%% Calculate Sherwood number
%gypsum properties
GypDens = 1580;        % gypsum density
Cw = 2.6;  Co = 0;      % Cw = 2.6
Diffu = 7.42e-10;          % D = 7.42e-10 @ 25 degree and 9.97e-10 @ 40 degree

for CaseNo=1:8
    Delta_time=Modified_time(CaseNo+1,1)-Modified_time(CaseNo,1);
    Mean_radius= (Mean_Rw_inner(CaseNo,1)+Mean_Rw_inner(CaseNo+1,1))/2;
    MTC = (Wear_filtered{CaseNo,1}/1000)*GypDens/(Cw-Co)/(Delta_time*3600);
    Sh{CaseNo,1} = MTC*2*Mean_radius/1000/Diffu;
end

% Plot Sh contour
figure;
for CaseNo=1:8
    subplot(2,4,CaseNo)
    [ch,ch]=contourf(z(:,100:800)/Dpipe,theta(:,100:800),Sh{CaseNo,1},30);
    set(gca,'FontSize',14);

    axis([0.5 4 0 360])
    set(gca,'YTick',0:90:360,'XTick',1:1:4);
    set(ch,'edgecolor','none');

    caxis([0 16000])%     caxis([0 3]);
    set(gca,'FontSize',10);
    pbaspect([1 1 1]);
end
%     ylabel('Crosswise angle ( \theta )')
%     xlabel('Axial Distance ( z/D )')
colorbar;

%% Calculate and plot Wear in 80x80 block areas
for CaseNo=1:8
    index=0;
    for i=1:80:481         % Block Size  80x80
        for    j=1:80:561
```

```
            index=index+1;
Wear_average(CaseNo,index)=sqrt(mean2(Wear_filtered{CaseNo,1}(i:i+79,j:j+79).^2));
% Calculate average Sh
        end
    end
end

for i=1:8
    if i==1
        Total_wear_average(i,:)=Wear_average(1,:);
        Total_time(i,:)=sum(Modified_time(i:i+1,1))/2;
    else
        Total_wear_average(i,:)=sum(Wear_average(1:i,:));
        Total_time(i,:)=sum(Modified_time(i:i+1,1))/2;
    end
end

figure;
for   index=1:56
    plot(Total_time(1:8,1),Total_wear_average(1:8,index),'-o');
    hold on;
end
set(gca,'FontSize',14);
ylabel('Wear (mm)')
xlabel('t_{mod} (hr)')

% calculate mean wear std dev
mean(Wear_average')
for i=1:8
    std_dev2=std(Wear_average(i,:))*2/mean(Wear_average(i,:))  % 2std/mean
end
%% Calculate and plot Sh in 80x80 block areas
for CaseNo=1:8
    index=0;

    for i=1:80:481         % Block Size  80x80
        for    j=1:80:561
            index=index+1;
            Sh_average(CaseNo,index)=sqrt(mean2(Sh{CaseNo,1}(i:i+79,j:j+79).^2));
% Calculate average Sh
        end
    end
```

```
end

 figure;
for   index=1:56
   plot(Total_time(1:8,1),Sh_average(1:8,index),'-o');
   hold on;
end
set(gca,'FontSize',14);
ylabel('Sh')
xlabel('t_{mod} (hr)')

Sh_average_vector=reshape(Sh_average(:),numel(Sh_average(:)),1);

% Total_time_matrix=repmat(Total_time,1,56);
Total_time_matrix=repmat(Modified_time(2:9,1),1,56);
%% Output collapsed time-roughness data to a text profile!

dlmwrite('Re=200000_Time_Sh.txt', Sh_average,'delimiter', '\t', 'newLine', 'pc');
dlmwrite('Re=200000_Time_Sh.txt', Total_wear_average,'-append','delimiter', '\t',
'newLine', 'pc');
dlmwrite('Re=200000_Time_Sh.txt', Total_time_matrix,'-append','delimiter', '\t',
'newLine', 'pc');

Re_200000_Time_Sh = dlmread('Re=200000_Time_Sh.txt');

toc
```